

Improving the multiscale morphological and mechanical properties of laser welded Al-Si coated 22MnB5 press- hardened steels

by

Muhammad Shehryar Khan

A thesis
presented to the University of Waterloo
in fulfilment of the
requirement for the degree of
Doctor of Philosophy
in
Mechanical and Mechatronics Engineering

Waterloo, Ontario, Canada, 2023

© Muhammad Shehryar Khan 2023

Examining Committee

The following served on the Examining Committee for this thesis. The decision of the Examining Committee is by majority vote.

External Member: Professor Wenda Tan
 Dept. of Mechanical Engineering,
 University of Michigan

Supervisor(s): Professor Y. Norman Zhou
 Dept. of Mechanical and Mechatronics Engineering,
 University of Waterloo

Professor Elliot Biro
Dept. of Mechanical and Mechatronics Engineering,
University of Waterloo

Internal Member(s): Professor Ehsan Toyserkani
 Dept. of Mechanical and Mechatronics Engineering,
 University of Waterloo

Professor Adrian Gerlich
Dept. of Mechanical and Mechatronics Engineering,
University of Waterloo

Internal-External Member: Professor Walter Duley
 Professor Emeritus, Dept. of Physics and Astronomy,
 University of Waterloo

Author's Declaration

This thesis consists of material all of which I authored or co-authored: see **Statement of Contributions** included in the thesis for details.

This is a true copy of the thesis, including any required final revisions, as accepted by my examining committee.

I understand that my thesis may be made electronically available to the public.

Statement of Contributions

This thesis consists of eight chapters, including the introduction (Chapter 1) and the literature review (Chapter 2) which is a published review paper written by the candidate as the first author. Chapter 3 outlines the experimental methodology and optimization techniques employed during the course of this research, incorporating results from two published journal papers written by the candidate as the first author. Chapters 4 to 7 are the four main research chapters composed of four published journal papers written by the candidate as the first author. The candidate is the primary author of the above-mentioned manuscripts. The vast majority of the work conducted in the lab (except where noted) including (but not limited to) process optimization, experimental design, sample cleaning and preparation, laser welding of the samples, metallographic preparation (mounting, grinding, and polishing etc.), all types of mechanical testing, and microstructural characterization was done by the candidate. The candidate wrote the first draft of all published manuscripts, revised the manuscripts based on input from the co-authors, and revised the manuscripts again during the peer-review process. The following co-authors have contributed to the studies included in this thesis:

Professor Norman Zhou served as the candidate's supervisor, provided funds for research, guided the research direction and progress, and reviewed the manuscripts. Professor Elliot Biro served as the candidate's co-supervisor, overseeing research progress and direction, assisting with data analysis, offering technical guidance, and reviewing the manuscripts.

Dr. Andrew Macwan from ArcelorMittal Dofasco, Hamilton, Canada, acted as the industrial liaison by providing financial support, materials, feedback on the direction of research, and reviewed the manuscripts.

Chapter 2

M Shehryar Khan, MH Razmpoosh, E Biro, Y Zhou (2020) A review on the laser welding of coated 22MnB5 press-hardened steel and its impact on the production of tailor-welded blanks. *Science and Technology of Welding and Joining*. 25:447–467. <https://doi.org/10.1080/13621718.2020.1742472>

The candidate is the primary author of this work and wrote the paper, including any subsequent revisions, except the last section titled, “Fibre laser welding of Zn-coated

22MnB5 PHS”, which was written by Dr. MH Razmpoosh. This section has been excluded entirely from this thesis. All authors reviewed and commented on the paper.

Chapter 3

M Shehryar Khan, S Ali, D Westerbaan, WW Duley, E Biro, Y Zhou (2022) The effect of laser impingement angle on the optimization of melt pool geometry to improve process stability during high-speed laser welding of thin-gauge automotive steels. *Journal of Manufacturing Processes*. 78:242–253. <https://doi.org/10.1016/j.jmapro.2022.04.022>

The candidate is the primary author of this work and wrote the paper, including any subsequent revisions. Mr. D Westerbaan conducted the laser welding experiments used in this study and the candidate assisted in the experimental design and carrying out the experiments. Mr. S Ali and the candidate developed the numerical model together. The simulations were run by Mr. S Ali. The candidate processed the results and acquired the data that was presented in this manuscript. All authors reviewed and commented on the paper.

M Shehryar Khan, SI Shahabad, M Yavuz, WW Duley, E Biro, Y Zhou (2021) Numerical modelling and experimental validation of the effect of laser beam defocusing on process optimization during fiber laser welding of automotive press-hardened steels. *Journal of Manufacturing Processes*. 67:535–544. <https://doi.org/10.1016/j.jmapro.2021.05.006>

The candidate is the primary author of this work and wrote the paper, including any subsequent revisions. Dr. SI Shahabad developed the numerical model used in this study and that section has been excluded from this thesis. Prof. M Yavuz supervised the candidate in his graduate course which provided technical expertise and access to numerical modelling software that was employed in this manuscript. All authors reviewed and commented on the paper.

Chapter 4

M Shehryar Khan, MH Razmpoosh, A Macwan, E Biro, Y Zhou (2021) Optimizing weld morphology and mechanical properties of laser welded Al-Si coated 22MnB5 by surface application of colloidal graphite. *Journal of Materials Processing Technology*. 293:117093. <https://doi.org/10.1016/j.jmatprotec.2021.117093>

The candidate is the primary author of this work and wrote the paper, including all subsequent revisions. Dr. MH Razmpoosh offered technical expertise during the experimental design of this study and assisted with the metallurgical and fractography analysis presented in this manuscript. All authors reviewed and commented on the paper.

Chapter 5

M Shehryar Khan, P Enrique, A Ghatei-Kalashami, JG Lopes, N Schell, JP Oliveira, E Biro, Y Zhou (2022) The influence of in-situ alloying of electro-spark deposited coatings on the multiscale morphological and mechanical properties of laser welded Al-Si coated 22MnB5. *Materials Science and Engineering: A*. 839:142830. <https://doi.org/10.1016/j.msea.2022.142830>

The candidate is the primary author of this work and wrote the paper, including any subsequent revisions. Dr. P Enrique assisted with the application of the electro-spark deposited coatings and the acquisition of some SEM images. Mr. A Ghatei-Kalashami assisted with the acquisition and interpretation of the EBSD data. Mr. JG Lopes, Dr. N Schell, and Prof. JP Oliveira acquired and analyzed the SXRD data in consultation with the candidate. The final synthesis and analysis of the data presented in the manuscript was done entirely by the candidate.

Chapter 6

M Shehryar Khan, A Macwan, E Biro, Y Zhou (2021) α -ferrite Suppression during Fiber Laser Welding of Al-Si Coated 22MnB5 Press-Hardened Steel. *Welding Journal*. 100:213–220 <https://doi.org/10.29391/2021.100.018>

The candidate is the primary author of this work and wrote the paper, including any subsequent revisions. All authors reviewed and commented on the paper.

Chapter 7

M Shehryar Khan, A Ghatei-Kalashami, X Wang, E Biro, Y Zhou (2022) Refining the hierarchical structure of lath martensitic steel by in-situ alloying with nickel: morphology, crystallography, and mechanical properties. *Journal of Materials Science*. 1-28. <https://doi.org/10.1007/s10853-022-07916-z>

The candidate is the primary author of this work and wrote the paper, including any subsequent revisions. Mr. A Ghatei-Kalashami assisted with the acquisition of the EBSD data and conducted the post-processing of the raw data using the MTEX toolbox in MATLAB in consultation with the candidate. Dr. X. Wang assisted with the acquisition and analysis of the TEM results. All authors reviewed and commented on the paper.

The manuscripts listed above have been reprinted in this thesis with the express permission of the publishers holding the copyright to the published papers; permission has been conveyed through the Copyright Clearance Center, Inc. All associated permission letters are available upon request.

Abstract

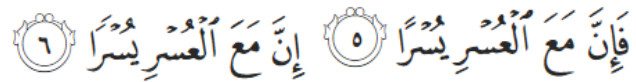
In the automotive industry, the demand for reduced vehicle weight, improved safety and enhanced crashworthiness qualities continues to rise which introduces the need for parts and components with tailored properties. This demand can be met by making use of tailor-welded blanks (TWBs), which allow the production of highly optimized and complex components that are simultaneously lightweight and exceptionally strong. An example of this type of component is the B-pillar which is produced by laser-welding different types of press-hardened steels (PHSs) to offer increased elongation properties where improved energy absorption is required, while also providing an increased yield strength where preservation of structural integrity under high dynamic load is required. Parts produced using TWBs offer many different advantages like weight reduction, part consolidation, and improved part performance.

The laser welding of Al-Si coated PHSs to produce TWBs is known to cause the formation of a softer ferrite phase in the welded joint due to the mixing of the Al-Si coating in the molten weld pool. It has been shown that the formation of this phase is the principal reason for premature failure of these laser-welded joints. Industry is currently removing the Al-Si layer prior to welding using laser ablation but other techniques have been developed to weld through the coating by either using secondary or modified coatings. This thesis reviews the existing literature on the problems associated with the laser welding of Al-Si coated 22MnB5 steel and several recent solutions to this problem will be discussed. As part of this research, several novel solutions to solve the problem of weld softening have been considered. It has been observed that for certain given conditions, welding through a secondary or modified coating made of austenite stabilizing elements decreases the ferrite content and increases the strength of the weld without the need to remove the Al-Si coating prior to welding. The final chapter of this thesis discusses the effect of alloying Ni with 22MnB5 on the morphology, crystallography, and mechanical properties of the steel to offer insights into potential advancements in the development of new press-hardened steels. The thesis concludes with several recommendations for future work.

Keywords: Fiber laser welding; press-hardened steels; ferrite suppression; TWBs; coating ablation; austenite stabilizing elements; hot stamped steel; Al-Si coated 22MnB5

Acknowledgements

Alhamdulillah (Arabic: **الْحَمْدُ لِلَّهِ**, al-Ḥamdu lillāh). All praise and gratitude is for God the Almighty (the most Gracious, the most Merciful) for the countless blessings which cannot be enumerated.



So, verily, with every difficulty, there is relief. Verily, with every difficulty there is relief. (Al-Quran 94:6)

There are so many people who I need to acknowledge and thank for my many successes during my Ph.D. but for the sake of time, I will try to keep this short. First and foremost, I must thank the admissions team at the University of Waterloo who gave this one-time university dropout [1] the chance to restart his academic journey as an undergraduate student in Mechanical Engineering, which reignited my passion for knowledge and learning, eventually leading to this Ph.D. – whoever you are, God bless your soul. I would like to express my deepest appreciation for my graduate supervisors, Prof. Y. Norman Zhou and Prof. Elliot Biro, who have taught me many lessons over the past few years and made me into a researcher who I hope they will be proud of in the future. Thank you for believing in me, supporting me, guiding me and writing countless letters of recommendations for the many different awards and scholarships I applied for. It has been an honor working for Prof. Zhou, who has given me tremendous opportunities to grow and learn – especially the freedom I was given to work on many different and exciting projects on the very cutting edge of advanced materials processing, which ensured that I was always kept on my toes and allowed me to be as productive as I've been during my graduate studies. It is also worth noting that I would likely not have done a Ph.D. if it hadn't been for the support of Prof. Biro, who has taught me more than any other teacher. His technical knowledge and outstanding memory have left me in awe on many occasions and I am tremendously grateful for the many hours I have spent learning from you. I am forever indebted to my graduate supervisors for everything I have learned during my Ph.D. – thank you so much. I would also like to acknowledge the financial support provided by the Natural Sciences and Engineering Research Council (NSERC) of Canada in the form of the prestigious NSERC Postgraduate Scholarship which

afforded me the freedom to explore my scientific and research curiosities, eventually leading to many journal publications, conference papers and technical presentations.

I have had the honor of working with and learning from some of the most brilliant minds in academia and in industry during the course of my graduate studies. I would like to express my sincerest gratitude all of you: Prof. Mike Collins from the University of Waterloo (specifically for introducing me to research and for writing several very important recommendations for me over the years); Prof. Adrian Gerlich from the University of Waterloo (specifically for writing that last minute recommendation that won me the NSERC PGS-D Award); Prof. Walter Duley from the University of Waterloo (specifically for being so generous with his time and knowledge on the many different occasions I have gone to him for help); Dr. Charles Kwan from the University of Waterloo (specifically for preparing and teaching a special reading course on the mechanical metallurgy of steels); Prof. Ehsan Toyserkani from the University of Waterloo; Prof. Mustafa Yavuz from the University of Waterloo; Prof. Marco Alfano from the University of Waterloo; Dr. Frank Goodwin from the International Zinc Association; Mr. Doug Luciani from the CWB Group; Dr. Andrew Macwan and Dr. Erika Bellhouse from ArcelorMittal Dofasco; Dr. Xiang Wang from McMaster University; Mr. Vladimir Yasnogorodski, Mr. Vivek Sengupta, and Mr. Tim Hurley from Lincoln Electric; Dr. Mok-Young Lee from POSCO, Korea; Dr. Gang Song from Dalian University of Technology, China; Dr. Maria Faria from the University of São Paulo, Brazil; Mr. Daniel Westerbaan from the University of Waterloo; Prof. JP Oliveira from the Universidade NOVA de Lisboa, Portugal; Dr. Dulal Saha from the University of Waterloo; Mr. Stephen Utter for always looking out for me; Mr. Stephen Carr for hiring me for the best part-time job a graduate student could ever ask for; Mr. Saad Abdul Rehman for being such an amazing friend; Mr. Sarim Ali for the meaningful discussions and contributions; and many, many others.

I would like to thank all my colleagues and other graduate students at the Center for Advanced Materials Joining (CAMJ): Dr. Hadi Razmpoosh, Dr. Chris DiGiovanni, Dr. Pablo Enrique, Dr. Abdelbaset Midawi, Dr. Luqman Hakim, Ali Ghatei Kalashami, Mostafa AbdelAziz, Yong-Hwan Cho, Shadab Sarmast, Shima Akbarian, Kaiping Zhang, and many others. I am grateful to have worked with such inspiring and dedicated graduate students who allowed me to grow and become better, simply by virtue of being able to work with them. Particularly, I would like to acknowledge Ali Ghatei who has been a tremendous friend and an even better colleague. His rigorous application of fundamental knowledge and willingness to stand by his own principles led to many heated but meaningful discussions that undoubtedly improved the many studies we have collaborated on over the past several years – a partnership I hope will continue to flourish

in the future. I am grateful to have had the opportunity to collaborate with some of the most brilliant minds in the world, and I will always treasure the memories.

A very special thank you to all the technical staff I had the absolute pleasure of working with over the past few years: The folks at the Engineering Machine Shop (shoutout to Mr. Mark Kuntz for always finding a way to accommodate my last-minute requests), WATLab, Dr. Yuquan Ding, Mr. Henry Ma at MSAM, Dr. Carmen Andrei and Mr. Travis Casagrande at CCEM, for their unlimited patience and guidance for the TEM characterization work. I would also like to acknowledge the support of the administrative staff at the University of Waterloo who work tirelessly behind the scenes to ensure things run as smoothly as then can, with a special thanks to Ms. Tanya Yoworski and Ms. Jian Zou. My journey in pursuing this PhD has been enriched by the contributions and support of countless individuals, from my advisors and mentors to my peers and family members. Though I cannot possibly recognize everyone who has played a role in my success, I am forever grateful for their unwavering encouragement and guidance. This achievement is not just mine, but a collective effort of those who have been a part of this journey with me.

I would like to express my sincere gratitude to my extended family and in-laws for their unwavering support, encouragement, and understanding throughout my PhD journey. Their love, patience, and belief in me have been instrumental in helping me achieve this significant milestone. I am truly fortunate to have such a supportive network of family members who have been there for me every step of the way. Thank you from the bottom of my heart.

As a closing remark, I would like to acknowledge the many times I encountered hurdles and roadblocks during the course of this PhD. This thesis stands as a testament to the power of grit and determination, which ultimately led to fruitful results. To anyone facing their own challenges, I encourage you to never let others limit your potential. Be your own advocate and remember the words of the famous quote, "If I am not for myself, who will be for me?"

To my beloved grandparents: for teaching me the importance of hard work and perseverance but most importantly, showering me with infinite love to give me the confidence to take on the challenges of the world.

To my beloved parents: for their countless sacrifices and daily prayers without which this would not have been possible.

To my beloved sisters: for always being my greatest supporters and believing in me, even when the rest of the world had written me off.

To my beloved wife: first, for agreeing to let me do this Ph.D.; and second, for supporting me in a way that made this seem a lot easier than it actually was. You have been instrumental to my success in a way that cannot be described in words.

To my beloved cats, Leo and Dobby: thank you for the countless cuddles.

Table of Contents

Examining Committee	ii
Author's Declaration	iii
Statement of Contributions	iv
Abstract	vii
Acknowledgements	viii
List of Figures	xv
List of Tables	xxvi
List of Abbreviations	xxvii
1 Introduction.....	1
1.1 Background.....	1
1.2 Objectives	2
1.3 Thesis Outline	3
2 Literature Review.....	4
2.1 Lasers and their application in welding	4
2.1.1 Introduction to lasers.....	4
2.1.2 Fiber lasers	5
2.1.3 Laser welding.....	6
2.2 Coated ultra-high strength Mn-B alloyed press-hardened steels	8
2.2.1 Material properties	8
2.2.2 Surface coatings and their characteristics	10
2.3 Hot stamping.....	12
2.4 Laser welding of Al-Si coated 22MnB5	15
2.4.1 Microstructure of the laser welded fusion zone	15
2.4.2 Ferrite evolution in the fusion zone	17
2.4.3 Ferrite distribution in the fusion zone.....	19
2.4.4 Effect of ferrite on the mechanical properties of the FZ.....	21
2.4.5 Existing solutions to mitigate ferrite formation during laser welding	24
3 Experimental methodology and process optimization.....	26
3.1 Material and sample preparation details	26
3.2 Hot stamping details	26

3.3	Mechanical testing	27
3.4	Laser welding details	27
3.5	Optimizing the laser welding process	28
3.5.1	Effect of laser impingement angle on process optimization	28
3.5.2	Effect of laser beam defocusing on process optimization	46
4	Suppressing α -ferrite by simultaneous in-situ ablation of the Al-Si coating and in-situ alloying of the FZ with carbon.....	56
4.1	Experimental details.....	56
4.2	Mechanism for in-situ ablation of the Al-Si coating	57
4.3	Microstructural analysis.....	61
4.4	Mechanical properties	64
4.5	Conclusions.....	69
5	Optimizing FZ mechanical properties by modifying the Al-Si coating using electro-spark deposition to achieve in-situ alloying during laser welding	70
5.1	Experimental details.....	71
5.2	In-situ alloying of the FZ	73
5.3	Microstructural analysis.....	78
5.4	Mechanical properties	90
5.5	Conclusions.....	95
6	Suppressing α -ferrite and strengthening the FZ microstructure through in-situ alloying with nickel	97
6.1	Experimental details.....	97
6.2	Microstructural analysis.....	99
6.3	Mechanical properties.....	106
6.4	Conclusions.....	108
7	Effect of nickel on the morphology, crystallography, and mechanical properties of hot-stamped 22MnB5	109
7.1	Experimental details.....	114
7.2	CALPHAD predications and microstructural analysis	116
7.3	Effect of Ni on morphological hierarchy	121
7.4	Effect of Ni on variant-pairing and transformation mechanism	124

7.5	Effect of Ni on grain orientation and internal strain during martensitic transformation	130
7.6	TEM analysis of lath and coarse martensite	131
7.7	Effect of Ni on the hardness of the steel	136
7.8	Conclusions	139
8	Conclusions and future work	140
8.1	Conclusions	140
8.2	Direction for future research	142
9	Research contributions (Ph.D. work)	144
9.1	Journal publications	144
9.2	Conference papers and presentations	146
9.3	Patents	146
	References	147

List of Figures

Figure 1: Usage of hot-stamped components in a middle-class sedan showing that the key difference between Gen I vehicles compared to Gen II vehicles is the usage of UHSSs which has increased from about 7% to about 33%, respectively. [24]	2
Figure 2: Schematic of the lasing action showing energy absorption from a pumping source and the ejection of a stimulated photon as the excited electron returns to its ground energy level [33].	5
Figure 3: Schematic of high-power pump light being launched into a much larger (in terms of size and numerical aperture) cladding which is significantly easier than trying to pump the light directly into the highly restrictive active core [34].	6
Figure 4: Schematic of conduction and keyhole welding modes [45].	7
Figure 5: Mechanical properties of 22MnB5 in the AR condition and in the PHS condition relative to other grades of steel [73].	9
Figure 6: Base metal microstructure of 22MnB5 press-hardened steel a) As-received condition; b) Hot-stamped condition [75].	9
Figure 7: Flow curves and microstructure evolution of 22MnB5 during HS as it goes from a BCC crystal structure in the as-received state to an FCC crystal structure when fully austenitized and finally achieving a BCT crystal structure following the quenching and forming stage [73].	10
Figure 8: Method for manufacturing hot-dip aluminized steel sheets showing that the steel sheet is continuously dipped in a molten bath of Al-Si and the coating solidifies as the steel leaves the bath [87].	11
Figure 9: Schematic showing the (a) direct hot-stamping method which is the most common method used in the hot-stamping process and the more uncommon (b) indirect hot-stamping method [73].	13
Figure 10: CCT diagram of 22MnB5 pre-coated steel showing that by ensuring a cooling rate higher than 27 K/s a fully martensitic microstructure can be achieved [73].	14
Figure 11: Schematic showing the production of a TWB by HS laser-welded steel sheets to produce a part with tailored properties [73].	15
Figure 12: Micrograph of non-coated 22MnB5 FZ with fully martensitic microstructure [75]. ..	15
Figure 13: Schematic showing (a) the laser welding of Al-Si coated 22MnB5 steel with a cross-section of (b) the molten weld pool showing the mixing pattern of the Al-Si coating and (c) the solidified FZ showing the dual-phase microstructure with ferrite dispersed in a martensitic matrix [25].	16
Figure 14: Representative SEM micrographs of the as-received BM, as-hot-stamped BM and the dual-phase regions in the FZ of the ARW and ARWHS condition [116].	16
Figure 15: Bright-field TEM images of the FZ of ARW sample [116].	17
Figure 16: Bright-field TEM images of the FZ of ARWHS sample [116].	17
Figure 17: Binary Fe-Al phase diagram generated for the chemical composition of 22MnB5 PHS using ThermoCalc [75].	18
Figure 18: EDX line scans showing a spike in Al-content in the ferrite phase found in the (a) ARW and (b) ARWHS samples [75].	19

Figure 19: (a) Optical Microscope image of the FZ in the ARWHS condition with elemental maps made using EPMA for (b) Al and (c) Si [118].	19
Figure 20: Schematic of fluid flow in a molten weld pool showing that when (a) $\delta\gamma\delta T$ is negative (b) molten material inside the weld pool flows from the center of the weld to the boundary and when (c) $\delta\gamma\delta T$ is positive (d) molten material inside the weld pool flows from the boundary to the center of the weld [33].	20
Figure 21: Marangoni Convection Flow in a molten weld pool showing that molten material flows from the center of the weld to the boundaries [122].	20
Figure 22: Nanoindentation study of the different phases present in the weldment for the (a) ARW, (b) ARWHS, and (c) HSW condition. (d) is the bar graph showing the relative difference in nanohardness between the martensite and the ferrite phases present in the different conditions [75].	22
Figure 23: Microhardness map of the FZ with and without the presence of the Al-Si coating in the (a) ARW and (b) ARWHS condition [127].	22
Figure 24: Engineering stress vs. strain curves for different the different conditions under consideration [75].	23
Figure 25: Light micrographs of the failure locations found in the (a) ARBM and ARW condition, (b) HSBM condition, (c) ARWHS condition, and (d) HSW condition [75].	24
Figure 26: Schematic showing the (a) trailing, (b) perpendicular, and (c) leading beam configuration. The laser head was tilted at an angle of 20° in the trailing (i.e., negative 20°) and leading (i.e., positive 20°) beam configurations, respectively.	29
Figure 27: (a) Model geometry domain with the inset showing ultra-fine meshing along the direction of motion of the moving DCG heat source with a coarse mesh in the surrounding area. The combination of mesh sizes shown here reduced the overall computational time needed for the simulation. (b) and (c) show the model geometry being tilted 20° to the left and right of the perpendicular to replicate the effect of tilting the laser heat source in the TBC and LBC, respectively. (d) and (e) show the 2D and 3D schematic of the DCG heat source, respectively, clearly identifying the different variables used in developing the model.	31
Figure 28: Still images of the welding process in the PBC showing rough weld banks indicative of molten material being pushed out of the weld pool leading to observable undercut and elevated weld banks. The plume ejection angle was clearly visible which is known to get smaller as the welding speed increases which causes humping to be observed on the weld surface.	34
Figure 29: 3D laser profile of the (a) top and (b) bottom surfaces of the weld in the PBC showing elevated or rough weld banks that form as a result of the deposition of some molten material from the weld pool. This loss of material leads to the observable undercut at the top and bottom surfaces; although the depth of the defect is almost double at the bottom surface ($\approx 120 \mu\text{m}$) compared to the top ($\approx 60 \mu\text{m}$). 2D height maps of the (c) top and (d) bottom surfaces of the weld in the PBC showing elevated weld banks caused by the deposition of molten material at the weld seam leading to considerable undercut at both the surfaces. Although the depth of the defect was much larger at the bottom surface, the defect was not consistent and appeared to be cyclic in nature. The undercut was not as severe at the top surface but presented itself as a consistent feature of the surface profile and weld geometry. Color scale bars have a unit of μm . (WD: Welding Direction)	35

Figure 30: Isometric view of the heat distribution profile on the surface of the 3D geometry domain along with the optical micrographs of the respective cross-section of the welds in the (a) TBC, the (b) PBC, and the (c) LBC. The green boundary line in the overlay images show that there is an excellent match between the fusion boundary location predicted by the FE model compared to the actual weld cross-sections ensuring that the resulting melt pool geometry predicted by the FE model would give an accurate representation of how the change in melt pool shape and size controlled the volatility in the process that led to defects..... 36

Figure 31: Respective still images of the LW process with images of the longitudinal cross-section of the temperature distribution along with the isothermal view of the molten weld pool boundary in the (a) TBC, (b) PBC, and (c) LBC. The green lines indicate the predicted boundary of the melt pool and the schematic arrows show the predicted flow fields generated in the melt pool based on the CFD model developed by Courtois et al. [138,144]. It can be seen clearly in (a) and (b) that due to the shape, size and temperature of the keyhole combined with the geometry of the molten weld pool, specifically the large convex bend at the back wall, two distinct flows develop in the molten pool leading to the violent turbulence observed in Figure 28 and Figure 32. As the laser beam impingement angle changes to +20° (i.e., the LBC) as shown in (c), the keyhole shape changes which changes the temperature profile and the resulting melt pool geometry, stabilizing the molten liquid flow as shown in Figure 35..... 38

Figure 32: Still images of the welding process using the TBC showing an unstable weld pool leading to perturbations in the molten weld seam and significant spattering which causes defects such as weld humping and high concavity. 39

Figure 33: 3D laser profile of the (a) top and (b) bottom surfaces of the weld in the TBC showing severe concavity and loss of material from within the weld seam. The loss of material was attributed to the high level of spattering observed during the welding process which could be a result of the serious turbulence and humping phenomenon observed in the molten weld pool that was captured using the welding camera. The concavity was much more severe at the bottom surface ($\approx 300 \mu\text{m}$) compared to the top surface ($150 \mu\text{m}$). 2D height maps of the (a) top and (b) bottom surfaces of the weld in the TBC showing the severe loss of material from the weld seam. Color scale bars have a unit of μm . (WD: Welding Direction) 41

Figure 34: Comparison of the cross-section of the weld profiles made in the trailing (shown by the yellow line) and perpendicular beam (shown by the red line) configurations for the (a) top and (b) bottom surfaces. The red region highlights the material that is missing the TBC compared to the PBC which clearly shows the severe concavity observed when welding in the TBC. The yellow region shows the material that is present in the welds made in the TBC and missing in the PBC; it is clear to see that no undercut is present in the TBC, but it is a serious problem in the PBC. 42

Figure 35: Still images of the welding process using the LBC showing a very stable weld pool with almost no visible perturbations in the molten weld seam. 43

Figure 36: 3D laser profile of the (a) top and (b) bottom surfaces of the weld in the LBC showing a weld profile that is free of any serious concavity or undercut defects. In fact, the 3D profiles of the weld suggest that the fluid flow generated in this beam configuration is such that more molten material is deposited and retained in the molten weld seam which causes the weld bead to have a convex profile at the top and bottom surfaces. Despite this accumulation of excess material in the weld bead, very minimal undercut was observed at the top surface ($< 30 \mu\text{m}$) and no undercut was observed at the bottom. 2D height maps of the (c) top and (d) bottom surfaces of the weld

in the LBC showing the elevated weld beads with some cyclic undercut at the top surface and no surface defects at the bottom surface. Color scale bars have a unit of μm . (WD: Welding Direction).....	44
Figure 37: Comparison of the cross-section of the weld surface profiles made in the leading (shown by the yellow line) and perpendicular beam (shown by the red line) configurations for the (a) top and (b) bottom surfaces. The yellow region shows the material that is present in the weld seam for the LBC compared the material that is missing in the PBC. The severe undercut that was observed in the PBC was entirely mitigated when welding in the LBC. The red region in (a) shows the elevated weld banks in the PBC that were not present when welding in the LBC...	45
Figure 38: (a) Still image of the OKM laser welding process showing the keyhole surrounded by the molten weld pool. (b) and (c) show the schematic of the weld cross-section for the fully focused and defocused conditions, respectively.	47
Figure 39: Isometric views along with the respective longitudinal cross-section of the temperature distribution in the (a) fully focused beam condition with a spot size of 0.3 mm, the (b) partially defocused beam condition with a spot size of 0.4 mm, and the (c) fully defocused beam condition with a spot size of 0.5 mm, showing clearly how the melt pool geometry changes as the laser beam is defocused going from full penetration welding in (a) to partial penetration in (c).	47
Figure 40: Comparison of the cross-section of the weld pool geometry given by the numerical model with the experimental results for the (a) fully focused beam condition with a spot size of 0.3 mm showing the X-shaped profile of the FZ, while the (b) partially defocused beam condition with a spot size of 0.4 mm, and the (c) fully defocused beam condition with a spot size of 0.5 mm, showed the Y-shaped profile of the FZ, respectively. The dashed lines show that there is an excellent match between the fusion boundary location predicted by the FE model compared to the actual weld cross-sections.....	48
Figure 41: Still images of the weld zone using the focused beam condition showing a larger, unstable melt pool, some spattering, instability in the weld plume and perturbations in the weld seam. The size of the plasma plume at the top surface is noticeably smaller as some of the plasma escapes through the bottom of the keyhole.....	49
Figure 42: Optical Micrographs showing the improvement in weld geometry with severe concavity being observed in the (a) fully focused condition with a beam spot size of 0.3 mm, the concavity improving (b-d) as the laser beam is defocused by increasing the effective spot size, with almost no concavity (e and f) being observed at a defocusing distance where the beam spot size is about 0.4 mm. As the defocusing distance increases to a point where the spot size is greater than 0.5 mm (g and h), the total energy delivered to the work piece decreases, and partial penetration welds are observed.....	50
Figure 43: Isothermal view of the molten weld pool boundary along with the respective longitudinal cross-section of the temperature distribution with arrows showing the flow fields generated due to the Marangoni convection flow based on the CFD model developed by Courtois et al. [138] in the (a) fully focused beam condition with a spot size of 0.3 mm, the (b) partially defocused beam condition with a spot size of 0.4 mm, and the (c) fully defocused beam condition with a spot size of 0.5 mm. It can be seen clearly in (a) that due to the shape, size and temperature of the keyhole combined with the geometry of the molten weld pool two distinct flows develop in the molten pool leading to the violent turbulence observed in Figure 41. As the laser beam is defocused as shown in (b) and (c), the spot size increases, the power density of the laser decreases, and the keyhole shape changes as the temperature decreases. This decreases the effect	

of the Marangoni convection flow and the liquid in the molten pool becomes less turbulent. As the size of the molten weld pool becomes smaller the liquid flow stabilizes as observed in Figure 44.....	52
Figure 44: Still images of the weld zone using the partially defocused beam condition with a beam spot size of 0.4 mm showing a smaller melt pool, drastic reduction in process instabilities and an increase in the size of the weld plume as no vapor escapes from the bottom of the keyhole....	53
Figure 45: Flow curves for the base metal, and the welds made in the defocused and focused condition showing an improvement of about 8% in the peak load, respectively.	54
Figure 46: Image showing the graphite coating applied to the surface of the Al-Si coated 22MnB5 PHS, and the welds were made through the coated area.	57
Figure 47: EPMA data showing that the Al-content in the FZ decreases as the graphite coating thickness increases, however, C-content increases at higher coating thicknesses.....	58
Figure 48: Zoomed in image of the weld zone showing the outer boundary of the molten weld pool surrounded by the molten Al-Si coating which has a much lower melting point as compared to the substrate.	59
Figure 49: Schematic showing the mechanism of removal of Al-Si coating during the laser welding of graphite coated 22MnB5 steel where (a) is the welding process with no graphite coating, (b) is the process with the graphite coating showing an increase in the amount of molten Al-Si coated sandwiched between the graphite coating and the substrate, and (c and d) is showing how the molten Al-Si coating becomes pressurized and explodes through the graphite coating, respectively.	60
Figure 50: Still images from the welding video showing (a-c) the welding process in the absence of graphite coating, and (d-f) the welding process with the graphite coating, clearly showing the violent ejection of the molten Al-Si coating away from weld pool. The red arrow shows the deformation of the graphite coating due to the internal build-up of pressure that causes the ejection of the molten Al-Si coating.	61
Figure 51: High magnification SEM images of the (a) BM, FB, and FZ in the ARWHS condition showing the difference between the morphology of the BM (which has a fully martensitic microstructure) and the FZ, with (b) and (c) showing magnified images of the dual-phase ferrite-martensite microstructure in the FZ; (d) shows the BM, FB, and FZ in the WGHS condition, with (e) and (f) showing magnified images of the FB and FZ showing significantly reduced ferrite phase concentration in the weld (M: Martensite, F: Ferrite). [Note: (a) is reprinted from Ref. [156], with permission of the American Welding Society (AWS), Miami, FL.]	62
Figure 52: Image analysis of optical micrographs using Clemex Vision Lite showing the phase fraction of ferrite (brown color) and martensite (green color) in the weld microstructure for the (a) ARWHS condition, (b) WGHS condition with a coating thickness of 60 μm , and (c) WGHS condition with a coating thickness of 130 μm . The insets in (a) show the regions where EPMA area scanning was performed to measure the C and Al content in the FZ.....	63
Figure 53: Graph showing the decrease in ferrite phase fraction in the FZ as the graphite coating thickness increases.	63
Figure 54: Fe-Al phase diagrams generated using JMatPro (v. 11.2) for (a) the ARWHS FZ composition showing that at the austenitization temperature of 930°C and an Al content of about 1 wt.% the FZ comprises of austenite and ferrite, and (b) the WGHS FZ composition showing that the addition of C and removal of Al stabilizes the single-phase austenite-region thereby	

- increasing the phase concentration of the martensite at the end of the hot stamping process and the arrow is showing that the FZ microstructure at 930°C and the measured Al content of about 0.6 wt.% is fully austenitic..... 64
- Figure 55: Hardness maps for the BM and FZ of the (a) ARWHS condition showing a significantly softer FZ as compared to the BM, and of the WGHS condition with a (b) 60 μm and (c) 130 μm coating thickness showing that the average FZ hardness increases as the coating thickness increases. 65
- Figure 56: Graph showing the increase in UTS for the WGHS condition as the coating thickness increases with complete strength recovery when a coating thickness of 130 μm is used. Insets are showing the failure location in the FZ due to the high phase concentration of α -ferrite when (a) no graphite coating is applied, (b) 20 μm coating thickness is used, and (c) 60 μm coating thickness is used, respectively; (d) shows the failure location in the BM of the WGHS sample with 130 μm coating thickness. Fracture surfaces for (a), (c) and (d) are shown in Figure 57. 66
- Figure 57: SEM micrographs of the fracture surface of the samples shown in Figure 56. (a) shows the fracture surface of the weld for the ARWHS condition, with (b-d) showing magnified images from within the region outlined in (a), confirming that brittle fracture occurred in this sample by cleavage, which corresponds well to the tensile curve for this sample as shown in (e). (f) shows the fracture surface of the weld for the WGHS condition with a coating thickness of 60 μm , with (g-i) showing magnified images from within the region outlined in (f), confirming that a combination of ductile and brittle fracture occurred in this sample as shown by the small dimples interspersed with cleavage faces, which corresponds well to the tensile curve for this sample as shown in (j). (k) shows the fracture surface of the BM for the WGHS condition with a coating thickness of 130 μm , with (l-n) showing magnified images from within the region outlined in (k), confirming that ductile failure occurred in this sample due to the presence of numerous and relatively larger dimples, which corresponds well to the tensile curve for this sample as shown in (e). The lighter regions in (a), (f), and (k) shown with arrows represent the relative area of the fracture surface that experiences stable plastic deformation before failure. (YS: Yield Strength) 68
- Figure 58: Electro-spark deposition of (a) In625 and (b) WC-10%Co on Al-Si coated 22MnB5 steel in the as received condition. “Splats” of material are deposited from the electrode on to the substrate as the electrode tip rotates and makes contact with the surface, with the white arrows show the coating that has already been deposited. 72
- Figure 59: Still images of the laser welding process for the (a) Al-Si, (b) WC, and (c) In625 coated 22MnB5 steel, clearly showing that the plume size gets smaller when welding through the higher melting temperature secondary coatings. The gray colored arrows are showing how the Al-Si and ESD-modified coatings melt around the molten weld pool and mix into the fusion zone. 73
- Figure 60: CCT diagrams for the bulk composition of the FZ of the (a) ARWHS and (b) WIHS samples. (c) and (d) show the predicted CCT diagrams for the bulk composition of the center of the FZ, and the FB of the WWCHS sample, respectively. The dotted arrow represents a cooling rate of 30 $^{\circ}\text{C}/\text{s}$, with the starting and ending phases observed in each case also shown next to the dotted arrow. Although the Ac_1 and Ac_3 values were almost identical for the FZ and FB regions of the WWCHS sample, the starting microstructure in the FZ post-welding had a fully martensitic morphology because the Al that was diluting into the weld pool was trapped at the FB, which also had a higher W- and C-content that suppressed the formation of ferrite. Therefore,

it can be assumed that during austenitization the FZ microstructure was purely austenitic leading to a fully martensitic microstructure after quenching. (M: Martensite)..... 74

Figure 61: FE-SEM images of the (a, b) Al-Si, (c-d, g) In625, and (e-f, h) WC coatings in the as-received and press-hardened state, respectively, along with the corresponding EDS data for the regions specified in (d) and (f). Computerized tomography (CT) scan images of the Inconel and WC coated samples is also shown to highlight the tomographical differences between the coatings' relative surface texture. The known phases of the as-received Al-Si coating are identified in (a)..... 76

Figure 62: EPMA maps showing the elemental distribution of Al, Fe, W, Co, Ni, and Cr in the (a) WWCHS, and the (b) WIHS samples, respectively. Insets are showing the regions where elemental distribution was measured and the average of these regions has been considered the bulk composition of the sample. The white and red dotted lines in (a) are showing the regions where the largest concentration of WC particles and no WC particles were found, respectively. 78

Figure 63: Optical microscopy showing the differences in microstructure for the (a) ARWHS, (b) WWCHS, and the (c) WIHS samples. The black arrows indicate the regions where high magnification images were taken from and the white insets show the regions of interest that were investigated further using FE-SEM. The figures shown with an associated number were analyzed using image analysis to measure the phase volume fraction of martensite (shown as the black phase) and α -ferrite (shown as the white phase)..... 79

Figure 64: High magnification FE-SEM images of the ARWHS sample at the (a, b) fusion boundary and at the (c, d) center of the weld clearly showing the dual phase ferrite-martensite morphology of the FZ. (LM: lath martensite, LB: lower bainite, AB: acicular bainite, θ : cementite, PAGB: prior austenite grain boundary, MA: Martensite-austenite constituent)..... 81

Figure 65: High magnification FE-SEM images of the WWCHS sample showing the (a, b) fusion boundary, the (c, d) base material to the right of the fusion boundary, the (e, f) edge of the FZ close to the fusion boundary, and the (g, h) center of the FZ. The high magnification inset shows the abundant presence of nanosized WC particles found in the FZ along the FB. The other high magnification inset shows the sparse presence of the ferrite phase dispersed in the martensitic matrix at the center of the FZ. Finally, the inset of an EDS line scan is shown in (f) to confirm the presence of WC nanoparticles at the FB. (LM: lath martensite, LB: lower bainite, CM: coalesced martensite, AB: acicular bainite, θ : cementite, M*: plate martensite, MA: martensite-austenite constituent) 82

Figure 66: EBSD analysis showing the (a) IQP map, (b) IPF, (c) GROD, and (d) LAM maps of the FB region of the WWCHS sample. The PFs for several individual grains along $\{100\}$ are also shown..... 85

Figure 67: High magnification FE-SEM images of the WIHS sample showing the (a, b) fusion boundary, the (c, d) base material to the right of the fusion boundary, the (e, f) right edge of the FZ close to the fusion boundary, and the (g, h) center of the FZ. The high magnification inset shows the abundant presence of coarse and lath martensite found in the FZ along the FB. The other high magnification inset shows a complex phase morphology at the center of the FZ with the presence of lath martensite, various different types of bainite and traces of cementite. (LM: lath martensite, LB: lower bainite, CM*: coarse martensite, AB: acicular bainite, θ : cementite, PM: plate martensite, MA: martensite-austenite constituent, Region shown with the dotted line and marked with an * is lenticular martensite) 86

Figure 68: EBSD analysis showing the (a) IQP map, (b) IPF, (c) GROD, and (d) LAM maps of the FB region of the WWCHS sample. The PFs for several individual grains along {100} are also shown..... 87

Figure 69: SXRD data from the BM, FB, and center of the FZ identifying the different phases observed in these regions for the (a) WC- and (b) Inconel-coated samples. 89

Figure 70: Microhardness maps and line scans, along with the nanoindentation results for the (a) ARWHS, (b) WWCHS, and the (c) WIHS samples. The graph shows the Load vs. Depth graph for the nanoindentation results which provides insight into the mechanical behavior of a given type of phase as it transitions from fully elastic to fully plastic deformation behavior. 91

Figure 71: Characteristic flow curves for the HSBM, ARWHS, WWCHS, and the WIHS samples. The insets show the fracture location for the tested samples along with the OM images of the fractured samples, showing that the ARWHS sample failed catastrophically along the FB while the WIHS sample failed far from the weld in the BM by way of ductile failure, as shown by the red arrows. The white arrows show clear signs of banding on the tensile coupons, clearly indicating that these sample had undergone necking and therefore, failed in a ductile manner.93

Figure 72: Fracture surface analysis of the (a) BM, (b) ARWHS, (c) WWCHS, and the (d) WIHS samples. The white arrows show the regions of the fracture sample that underwent stable plastic deformation before failure. 95

Figure 73: Cross-sectional images of the (a-d) WWCHS, and (e) ARWHS fractured samples. (a) shows that the fracture was initiated at the brittle (b) toe region, with (c) and (d) showing fracture features indicative of brittle and ductile failure, respectively, as shown by the green arrows, confirming that the WWCHS samples underwent a combination of brittle and ductile failure. (e) shows that the crack propagated through the martensitic islands in the FZ of the ARWHS sample that were rich in MA-constituents..... 95

Figure 74: Frame-by-frame images of the welding process showing the weld being made as the laser travels from the non-coated substrate (a, b) to the Ni-coated substrate (c-f). The final image (g) is showing how the Ni-coating was applied to the Al-Si coated 22MnB5 PHS. The weld was made through the area that is covered by the Ni-coating..... 98

Figure 75: EPMA elemental maps for (a) Fe, and (b) Ni showing the dilution of the Ni coating into the FZ for the WNHS condition with the highest concentration of Ni found at the FB whereas the bulk of the FZ has a more even distribution of Ni content. 100

Figure 76: Optical micrographs of the (a) weld microstructure with no Ni addition, (b) Weld microstructure with Ni-coating, and image analysis using Clemex Vision Lite showing the PC of ferrite (gray color) and martensite (green color) in (c) and (d) for both conditions, respectively. 101

Figure 77: Optical micrographs of the (a) weld microstructure with no Ni addition, with high magnification images of the (b) left-side fusion boundary, (c) right-side fusion boundary, and the (d) center of the fusion zone with corresponding images showing the PC of ferrite (black color) and martensite (white color). 102

Figure 78: SEM images of the (a) fusion boundary of the ARWHS condition at the location specified in Figure 77 as well as high magnification images of the (b) base metal showing a fully martensitic microstructure, and the (c) fusion zone showing the ferrite phase embedded in a martensitic matrix. 103

Figure 79: Optical micrographs of the (a) weld microstructure with Ni-coating, with high magnification images of the (b) left-side fusion boundary, (c) right-side fusion boundary, and the (d) center of the fusion zone with corresponding images showing the PC of ferrite (black color) and martensite (white color). 104

Figure 80: SEM images of the (a) fusion boundary of the WNHS condition at the location specified in Figure 79 as well as high magnification images of the (b) base metal showing a fully martensitic microstructure, and the (c) martensitic fusion zone showing a combination of prior martensite characterized by the darker concave morphology and fresh martensite characterized by the lighter convex morphology. 104

Figure 81: Fe-Al phase diagrams generated using JMatPro (v. 11.2) for (a) the ARWHS FZ composition in which there is no Ni and the arrow is showing that at the austenitization temperature of 930°C the FZ microstructure comprises of austenite and ferrite, and (b) the WNHS FZ composition showing that the addition of Ni stabilizes the single-phase austenite-region thereby increasing the PC of the martensite at the end of the hot stamping process and the arrow is showing that the FZ microstructure at 930°C is fully austenitic. 105

Figure 82: Predictive CCT diagrams for the (a) ARWHS FZ composition showing that at a 30°C/s cooling rate the weld microstructure is expected to be a combination of ferrite and martensite, and for the (b) WNHS FZ composition showing that the weld microstructure is expected to be purely martensitic at a 30°C/s cooling rate. 106

Figure 83: Hardness maps for the (a) BM and FZ of the ARWHS condition showing a significantly softer FZ as compared to the BM, and for the (b) BM and FZ of the WNHS condition showing that the average FZ hardness is the same as that of the BM. 107

Figure 84: Flow curves for the hot-stamped BM, ARWHS condition, and WNHS condition with inserts showing the failure location of the ARWHS samples along the FB due to the high PC of α -ferrite present in the FZ, and the failure location of the WNHS samples in the BM. 108

Figure 85: (a-d) In-situ alloying of pure Ni using a high-powered fiber laser to dilute the molten Ni coating into the processed melt pool. The molten Ni flows into the melt pool along the boundary based on the Marangoni convection flow. During the heating stage of hot-stamping, a relatively homogenous distribution of Ni is achieved at the center of the processed zone as the Ni-content gradually increases towards the periphery. (e) EPMA results showing the elemental map of Ni. The Ni content was measured to be ~2 wt.% at the center of the PZ, with a maximum of ~18 wt.% measured at the periphery. The bulk average Ni-content of the entire processed zone was measured to be ~4 wt.%. The outlined region shown in (e) had an average Ni-content of ~8.3 wt.% and was chosen as the region of interest for investigation. 116

Figure 86: LSCM and high magnification differential interference contrast (DIC) images showing the difference in the morphology and phase distribution of the bulk microstructure of the (a-b) BM and (e-f) NABM samples. The CALPHAD predicted phase volume fraction has been shown for the (c-d) BM and (g-h) NABM chemistry shown in Table 12 during the heating and quenching stages of hot-stamping, respectively. 117

Figure 87: High magnification FE-SEM images showing the microstructure of the (a-d) BM, composed mainly of fine lath martensite (α_1') with sparsely distributed islands of lower bainite, and the (e-h) NABM, showing the presence of coarse martensite grains distributed in a fine lath martensite (α_2') matrix, respectively. (CM: Coarse martensite, LB: lower bainite, MA:

- martensite-austenite constituent, and the region marked with an * is lenticular martensite with a clearly visible midrib) 120
- Figure 88: EBSD-IPF maps showing the differences in crystal morphology of the (a) BM and the (d) NABM microstructure, reconstructed using the MTEX toolbox in MATLAB. To predict and show the difference in the prior austenite grain (PAG) size, the EBSD data was plotted for the (b) BM and the (e) NABM samples using the standardized Fe-FCC crystal structure information, showing that the austenite grain sizes (AGS) were much larger for the NABM. The IPF figures with the predicted PAG boundaries are shown in (c) and (f) for the BM and the NABM sample, respectively. 123
- Figure 89: Reconstructed EBSD maps of the (a) BM and (b) NABM showing the packet distribution in the bulk microstructure based on the 4 possible parallel plane orientations that can exist in a given PAG, as summarized in Table 11. The pole figures for individually labelled PAGs were used to index the martensitic variants in each grain. The EBSD maps and the pole figures clearly showed that the NABM had a significantly more ideal martensitic transformation compared to the BM, as evident by the presence of a homogenous distribution of the 4 CP groups (representing individual packets) in each PAG analyzed in the NABM, with all 24 martensitic variants being indexed in each grain. The BM microstructure was composed of PAGs that had an average of about 2 CP groups in each grain and a significantly smaller number of variants were indexed in these grains. 126
- Figure 90: High-magnification IPF maps (and their respective pole figures) of a single austenite grain (labelled as grain 1 in Figure 6) from the (a) BM and (b) NABM, showing the variant-pairing behaviour and variant distribution in each respective grain. The $\{001\}$ PFs clearly show that with the addition of Ni, the packet and block sizes are significantly more refined, with a much more homogeneous distribution of all 24 martensitic variants in each PAG indicating an ideal martensitic transformation with a net transformational strain that is almost purely dilatational..... 129
- Figure 91: Grain reference orientation deviation (GROD) maps of the (a) BM and the (b) NABM showing the differences in orientation heterogeneities that evolve during plastic deformation with the addition of Ni. Grain orientation spread (GOS) maps of the (c) BM and the (d) NABM showing the differences in the average misorientation angles of the lath martensitic structures compared to the grain mean orientation. The strain maps clearly show that the addition of Ni significantly decreases transformational strains in the crystal lattice. 131
- Figure 92: Low magnification (a) HAADF and (b) BF-TEM images of NABM showing the different types of martensitic morphology observed in the sample. (CM: coarse martensite, CM*: carbide-free coarse martensite, and the region marked with an * is lenticular martensite with a clearly visible midrib) 132
- Figure 93: TEM micrograph at low magnification of the (a) BF image showing a region with several CM* crystals surrounded by fine lath martensite. High magnification BF- and DF images showing the lath martensite crystals on the (b, b₁) left and (c, c₁) right of the central CM* crystal, respectively. The DF images along with the SAD pattern shown in (c₂) confirms the presence of thin film-like RA between the martensite laths. The CM* crystal shown in (d) was smaller in size and had a relatively lower (d₁) dislocation density compared to the larger CM* crystal shown in (e), which had a significantly higher (e₁) dislocation density. The SAD patterns for these CM* crystals are shown in (d₂) and (e₂), respectively. The difference in dislocation density shows that these two coarse martensitic crystals are at different stages of autotempering, most likely due to

their difference in size. Since the smaller crystal had autotempered more, faint diffraction spots corresponding to θ were observed as shown by the yellow arrows in (d₂). (CM*: carbide-free coarse martensite, RA: retained austenite, θ : cementite)..... 134

Figure 94: TEM micrographs at (a) Low and (b) high magnification BF and (b1) HAADF images showing the morphology of a single CM crystal that has a very low dislocation density and shows the presence of numerous needle-like θ carbides, as confirmed by the SADP shown in (b₂). (c) High magnification BF images of another CM crystal, with the associated (c₁) SADP confirming the presence of θ carbides. In general, the CM crystals were measured to be less than half the size of the CM* crystals resulting in greater autotempering of the crystals which results in dislocation recovery and encouraged the nucleation of needle-like carbides. (CM: coarse martensite, θ : cementite, CM*: carbide-free coarse martensite) 136

Figure 95: Nanoindentation data showing that the addition of Ni marginally reduced the hardness of the $\alpha 2'$ lath martensite, compared to the $\alpha 1'$ lath martensite found in the BM, most likely due to the decrease in size of the lath martensite crystals which promotes segregation of carbon from the bulk of the lath towards its boundaries making the lattice relatively softer in comparison. The CM crystals found in the NABM had a lower hardness compared to the lath martensite, most likely due to the autotempering of these large crystals that decreases the dislocation density resulting in a lower hardness. The LB found in the BM had the lowest measured hardness compared to the martensitic crystals. The P-h curve shows the deformation behavior response of the $\alpha 2'$ and CM crystals during the indentation test. 138

List of Tables

Table 1: Comparison of various coatings used to protect 22MnB5 grade steel [25].	12
Table 2: Characteristic Mechanical Properties of BM and welded joints [12,74,97,98,118,120]	23
Table 3: Comparison of different methods used to avoid ferrite formation in the FZ during FLW of Al-Si coated 22MnB5 [25]	25
Table 4: Chemical composition of the base material used in the present work (in wt.%).	26
Table 5: Details of the laser welding machine and process setup.	27
Table 6: Identified heat source parameters for different laser welding condition	33
Table 7: Bulk chemical composition of the weld fusion zone in the ARWHS, WWCHS, and WIHS conditions (in wt.%).	74
Table 8: Chemical composition of the weld fusion zone in the ARWHS and WNHS conditions (in wt.%).	99
Table 9: Summary of the ferrite PC found in the ARWHS and WNHS conditions measured using image analysis for the entire FZ.	100
Table 10: Summary of the ferrite PC found in the ARWHS and WNHS conditions measured using image analysis for 3 distinct regions of interest at high magnification.	105
Table 11: 24 crystallographically distinct variants of the K-S orientation relationship, showing that 6 unique variants form on each of the four {111} planes found in the austenite grain [211]. The associated organization of variants into CP and Bain groups is shown to make their identification in packet and block structures simpler to understand. Note that the Bain correspondence can be found in Ref. [219]. The color in brackets represents the color for that CP group used for EBSD analysis, as shown in Figure 89.	113
Table 12: Chemical composition of the base material and the Ni-alloyed BM used in the present work (in wt.%).	115
Table 13: Measurements of PAGS, PS, block width, sub-block width, and lath width acquired from the EBSD and TEM data presented in this study. The measurements have been compared to the data presented for lath martensitic structures for similar PAGS in different steels given in Ref. [223]. The lath width for the 22MnB5 BM was measured from the TEM data presented in Ref. [120]. The measured values are reported with a confidence interval of 95%.	124

List of Abbreviations

3D	Three-dimensional
AB	Acicular bainite
AHSS	Advanced-high strength steel
AR	As received
ARW	As-received welded
ARWHS	As-received Welded then Hot-stamped
bcc	Body-centered cubic
bct	Body-centered tetragonal
BIA	Beam impingement angle
BIW	Body-in-white
BM	Base metal
BOP	Bead-on-plate
BPP	Beam parameter product
BS	Block size
CFD	Computational fluid dynamics
CG	Conical-Gaussian
CKM	Closed keyhole mode
CP	Close-packed
CPP	Close-packed planes
CR	Cooling rate
CW	Continuous-wave
DBTT	Ductile-to-brittle transition temperature
DCG	Double Conical-Gaussian
DF	Dark field
DIC	Digital image correlation
DP	Dual-phase
DP 980	Dual-phase 980
EBSD	Electron backscatter diffraction
EDX	Energy dispersive X-Ray spectroscopy
EELS	Electron-energy-loss spectroscopy
EPMA	Electron probe micro-analyzer
ESD	Electro-spark deposited
FB	Fusion boundary
fcc	Face-centered cubic
FE	Finite element
FE-SEM	Field emission scanning electron microscope
FIB	Focused ion beam
FLW	Fiber laser welding
FM	Fresh Martensite
FZ	Fusion Zone
GA	Galvannealed
GI	Galvanized
GND	Geometrically necessary dislocations
GOS	Grain orientation spread
GROD	Grain reference orientation deviation
HAZ	Heat-affected zone
HS	Hot stamped
HSBM	Hot-stamped base material
HSW	Hot-stamped then welded

IPA	Isopropanol
IPF	Inverse pole figure
IQ	Image quality
K-S	Kurdjumov-Sachs
LAM	Local average misorientation
LB	Lower bainite
LBC	Leading beam configuration
LBW	Laser beam welding
LM	Lath martensite
LME	Liquid metal embrittlement
LSCM	Laser scanning confocal microscope
LW	Laser welding
LWB	Laser-welded blank
MA	Martensite-austenite constituents
M_s	Martensite start temperature
NABM	Ni-alloyed BM
OKM	Open keyhole mode
OR	Orientation relationship
P	Laser power
PAG	Prior austenite grain
PAGB	Prior austenite grain boundaries
PAGS	Prior austenite grain size
PBC	Perpendicular beam configuration
PC	Phase concentration
PF	Pole figure
PHS	Press-hardened steel
PM	Plate martensite
PS	Packet size
PZ	Processed zone
RA	Retained austenite
SXRD	Synchrotron X-Ray diffraction
TBC	Trailing beam configuration
TEM	Transmission electron microscopy
TS	Travel speed
TWB	Tailor-welded blank
UHSS	Ultra-high strength steel
UTS	Ultimate tensile strength
WC	Tungsten-carbide
WGHS	Welded with graphite and then hot stamped
WIHS	Welded with Inconel and then hot-stamped
WNHS	Welded with Ni then Hot-stamped
WWCHS	Welded with WC and then hot-stamped
YS	Yield strength

1 Introduction

1.1 Background

The current demand in the automotive industry for vehicles with high fuel efficiency, improved safety and enhanced crashworthiness characteristics has created the need to build body-in-white (BIW) structures by carefully selecting materials that are lightweight, have high formability for easy manufacturing, offer good crash performance to maintain passenger safety, and provide good weldability to successfully join individual parts into a coherent structure; while maintaining a relatively low cost of production. Therefore, the steel-making industry has been developing new types of steels that are commonly referred to as advanced high strength steels (AHSSs) to meet the existing demand; while also investigating novel methods to join these steels to allow automotive manufacturers to produce lighter and stronger BIW structures for their production cars [2,3].

AHSSs can be classified based on their chemical composition, microstructural features and associated mechanical properties. The strength of the AHSSs varies in the range of 500 to 2000 MPa; with AHSSs exceeding an ultimate tensile strength (UTS) of 800 MPa sometimes being referred to as ultra-high strength steels (UHSSs) [4,5]. The first generation of AHSSs comprised mainly of ferrite-based microstructures such as dual phase (DP) steels, complex phase (CP) steels, and transformation induced plasticity (TRIP) steels [6,7]. The second generation of AHSSs are known as the high-Mn twinning-induced plasticity (TWIP) steels which promoted austenitic-based microstructures [8–11]. Second generation AHSSs are expensive on account of the high-alloying content and are generally considered difficult to work with in the industrial setting. The third generation of AHSSs like the medium-Mn TRIP steels, quench and partitioned steels, and the Mn-B alloyed press-hardened steels (PHSs) which have strength levels exceeding 1.5 GPa and a relatively lower cost have garnered significant attention from the automotive industry. Usage of AHSSs in BIW applications has almost quadrupled in recent years [12–15].

The development of anti-intrusion automotive components made from UHSSs have been given a further boost in terms of crashworthiness qualities, part consolidation, and overall weight reduction by joining them with PHSs to make blanks with tailored properties [16,17]. A variety of automotive chassis components are made from PHSs that include the A-pillar, B-pillar, bumper, rocker and roof rail, and the tunnel as shown in Figure 1 [12,15]. To produce components with the desired tailored properties while making the best use of PHSs, the steels must either have their mechanical properties locally adjusted, for instance through local tempering processes [18,19], or

they must be joined with other grades of PHSs with varying thicknesses and properties [12,20,21]. The most common way to join different types of PHSs to form a laser-welded blank (LWB), which is also sometimes referred to as a tailor-welded blank (TWB), is by using laser welding (LW) [16]. The blanks are then hot stamped (HS) to make the component with the desired geometry, shape and mechanical properties [22,23]. However, the laser welding of PHSs has several issues which will be the primary focus of this research and discussed in detail in later sections.

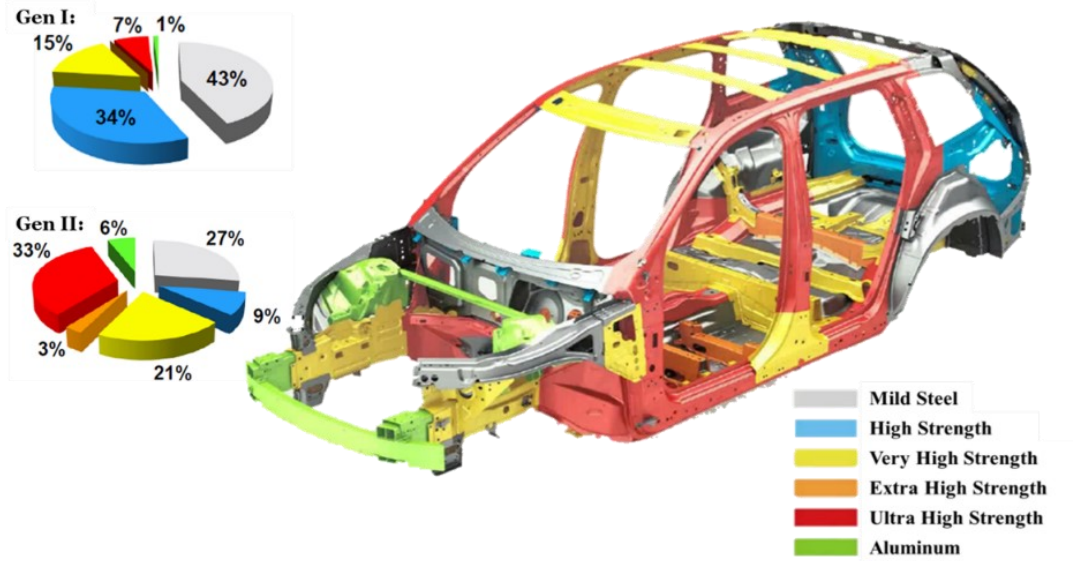


Figure 1: Usage of hot-stamped components in a middle-class sedan showing that the key difference between Gen I vehicles compared to Gen II vehicles is the usage of UHSSs which has increased from about 7% to about 33%, respectively. [24]

1.2 Objectives

The goals of this project ranged from gaining a fundamental understanding of the laser-substrate interaction during the LW of coated PHSs to understanding the effect of welding Al-Si coated 22MnB5 through various types of secondary/modified coatings on the resultant microstructural evolution of the fusion zone (FZ). The ultimate goal was to develop several different novel techniques that improved the mechanical properties of the welded joints to optimize the production of TWBs and improve automotive safety and efficiency. The main objectives are as follows:

- i. To determine the mechanism of microstructural evolution during the LW of coated PHSs, specifically focusing on the FZ softening phenomenon observed during LW of Al-Si coated PHSs.
- ii. To develop a fundamental understanding of the underlying physics and thermodynamic interactions between the high energy laser, the coating, and the steel substrate to successfully optimize the process and attain desirable FZ properties.

- iii. To develop and investigate techniques that improve the mechanical properties of the FZ – e.g., alloying austenite stabilizing elements into the FZ or the in-situ ablation of the protective coating during the welding process.
- iv. To adapt the developed techniques to control the alloying content of the weld pool and improve the mechanical properties of laser welded Al-Si coated PHSs.
- v. To characterize the morphological differences in the microstructure of the modified laser welded fusion zone and investigate the relationship between the processing-microstructure-mechanical properties of the given system.

The significance of this work and the novel findings presented in this thesis have directly benefitted the Canadian automotive industry by providing crucial information on how to improve the laser welding of coated PHSs. The research also holds the potential to facilitate the evolution of PHSs that will help keep the Canadian steel industry competitive in the global market in the years to come.

1.3 Thesis Outline

This thesis consists of eight chapters including a chapter on experimental methodology and process optimization and four main research chapters. Chapter one is an introduction to this thesis, focusing on the background and objectives of this research. Chapters two through seven are adapted from published manuscripts as explained in the Statement of Contributions.

Chapter two is a comprehensive review of the literature available on the laser welding of Al-Si coated 22MnB5. Chapter three discusses the experimental methodology and process optimization techniques that were employed during the course of this research to ensure mechanical defects caused during laser welding were minimized/eliminated. Chapter four was the first main research chapter in which colloidal graphite coatings were used to achieve in situ ablation of the Al-Si coating during laser welding while simultaneously alloying the FZ with carbon to eliminate softening in the weld. Chapter five focused on using electro-spark deposition as a coating modification technique to modify the Al-Si coating with alloying elements that suppressed the formation of α -ferrite in the FZ. Chapter six presented the findings from a study in which the FZ was strengthened using in situ alloying with Ni. Chapter seven was an in-depth discussion on the characterization of the morphology and crystallography of the Ni-alloyed FZ to analyze the effect of Ni on the hierarchical nature of the lath martensitic microstructure and its effect on mechanical properties. Finally, chapter eight summarizes the major conclusions and provides recommendations for future work and discusses new research opportunities.

2 Literature Review

* This chapter is composed of a published review paper [25] as outlined in the Statement of Contributions.

2.1 Lasers and their application in welding

2.1.1 Introduction to lasers

Light amplification by stimulated emission of radiation, or simply “LASER”, was an idea proposed by Schawlow and Townes [26], which relied on the phenomenon of stimulated emission that was first predicted by Einstein [27]. Although, a laser is made up of light there are some key characteristics of a laser that make it different from ordinary light [28]:

- i) Lasers are highly monochromatic – the beam of a laser is made up of a narrow range of wavelengths within a single-color portion of the light spectrum.
- ii) Lasers are highly coherent – the beam consists of waves with a constant phase difference which means that the crests and troughs of successive waves overlap with each other.
- iii) Lasers are directional – the beam travels in a single direction within a narrow cone of divergence.
- iv) Lasers are highly focused – the beam can be focused to a very small spot size delivering a power intensity significantly higher than any other energy source.

Maiman demonstrated the first functioning ruby laser [29] proving that the lasing action predicted by Einstein was, in fact, possible. The main idea of how lasers work goes back to Einstein’s study of radiation, when he hypothesized that the energy of excitation is released from an excited material when it is struck by a photon of radiation [30]. Stimulated photons (i.e., the building blocks of a laser) are generated when an active medium that has been excited to a high-energy level returns to its more stable low-energy state [31]. This “lasing” action can be achieved when the electrons of a dopant element (i.e., usually a small amount of some transition or rare earth element) have been selectively excited to a higher energy level using a “pumping source” in a given active material (e.g., optical fibers in the case of fiber lasers or a single crystal in the case of solid-state lasers), return to their normal (or ground) energy level as shown in Figure 2 [31,32]. The stimulated photon is coherent (i.e., it travels in the same direction) and it is in phase with the stimulating photon [30].

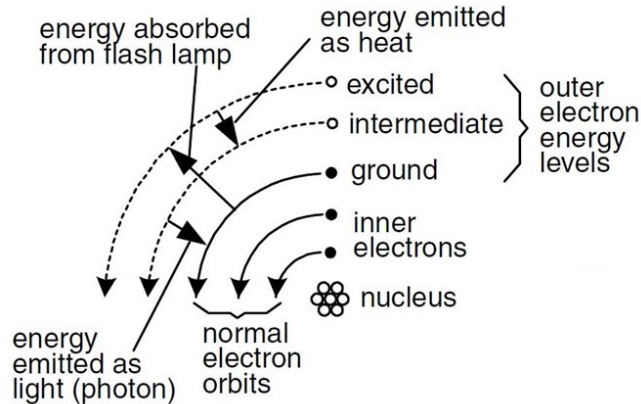


Figure 2: Schematic of the lasing action showing energy absorption from a pumping source and the ejection of a stimulated photon as the excited electron returns to its ground energy level [33].

A phenomenon known as population inversion (i.e., more atoms or molecules in the excited state than in the lower energy state) allows for the amplification of the stimulated emission phenomenon which can be achieved as long as the lifetime of the lower energy state is shorter than the excited state [30]. By fulfilling the condition of population inversion, the number of collisions between the stimulating photons and the active medium can be increased, which increases the density of the stimulated (or the in-phase) photons [31].

There are many different types of lasers, and they can be categorized in a number of different ways based on the parameters that lead to the generation of the laser beam. The most common way to classify laser types is based on the physical state of the active medium and accordingly the main types of lasers are as follows [28]: gas, excimer, semiconductor (or diode), liquid dye, and solid-state. All the different types of lasers follow the same working principle of generating light using stimulated emissions, but they share some similar features, such as: an active medium capable of population inversion, some sort of optical cavity that offers control over (and enhancement of) the optical field, and an energy (or a “pumping”) source. From amongst the various different types of lasers, fiber lasers are the newest addition under the solid-state laser technology umbrella and have been shown to have superior overall performance, particularly in terms of output power stability and they have unmatched beam quality at high output powers [34].

2.1.2 Fiber lasers

Compared to the other types of lasers, fiber lasers offer significantly improved thermal management by eliminating thermal lensing (which is a common occurrence in solid-state crystal lasers) due to the large surface to volume ratio [34]. According to Zervas and Codemard [34], fiber lasers offer a much more controlled spatial distribution of the signal which leads to high beam stability and quality, which in turn reduces the cavity and transmission losses, significantly improving wall-plug efficiency. Furthermore, Toyserkani et al. [28] praise fiber lasers in comparison to their counterparts for their easy integration into industrial processes for a number

of reasons other than the ones already mentioned: standard wall-plug operation, single-mode fiber delivery line, exceptionally high reliability and repetition rate, as well as the added benefit of a maintenance-free operation.

The active medium that provides the gain in fiber lasers are the doped cores of various types of fibers. The cores are generally doped with active rare-earth elements such as ytterbium, erbium, etc. [34]. The optical cavity is formed in one of two ways: using bulk mirrors placed on either end of the fiber [34] or by using fiber Bragg gratings engraved directly into the fiber core [35,36]. The pumping action is achieved by combining semiconductor diode lasers that convert electrical energy into light energy that is then launched into the core or the cladding of the fiber as shown in Figure 3 [34].

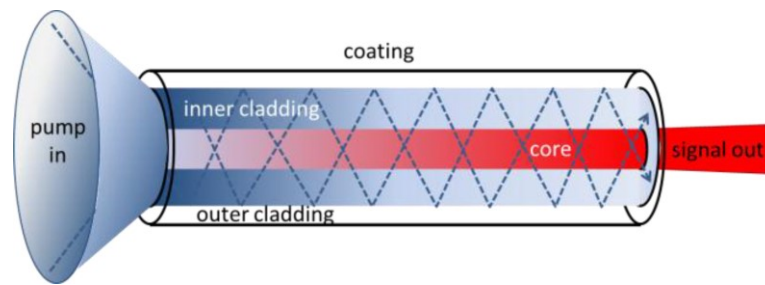


Figure 3: Schematic of high-power pump light being launched into a much larger (in terms of size and numerical aperture) cladding which is significantly easier than trying to pump the light directly into the highly restrictive active core [34].

2.1.3 Laser welding

Laser welding is a fusion joining process in which two or more solids of similar or dissimilar nature are joined together due to the absorption of incident radiation in a spatially localized volume. The resultant molten pool traverses along the seam between the components being joined as the high-powered laser moves along the surface of the substrate, effectively fusing the solids together as the weld pool solidifies [37,38]. Precise laser welding is accomplished by striking a balance between the heating and cooling of the area being welded, which is normally a function of the absorptivity of the laser radiation and the dissipation of heat within the substrate [37]. There are two main modes of laser welding: the less popular (in terms of usage in welding applications) conduction mode [39–41] and the more widely used keyhole mode [41–44]. The main difference between the two modes of welding is that the surface of the molten weld pool remains intact during conduction welding, whereas in keyhole mode the surface is forced open, in the shape of a keyhole, to allow the laser beam to enter the molten weld pool in penetration (or keyhole) welding as shown in Figure 4 [37].

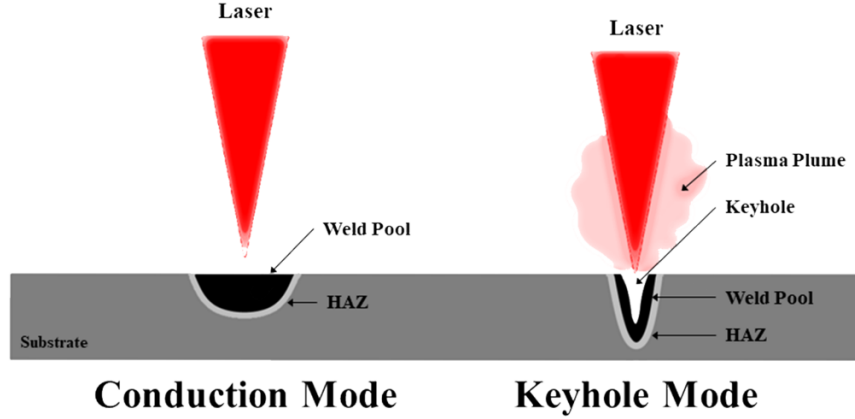


Figure 4: Schematic of conduction and keyhole welding modes [45].

Conduction welding occurs when the power density of the laser is insufficient to vaporize the material at a given welding speed and it usually happens when the beam is out of focus as seen in Figure 4 [38]. Welds made using conduction mode are less likely to carry defects such as porosity due to gas entrapment as the process limits agitation of the system as the laser radiation does not create a vapor column in the substrate that can generate a volatile fluid flow in the melt pool [37]. On the other hand, penetration welding offers sufficient energy per unit area to vaporize the material being welded creating a narrow vapor column in the shape of a keyhole which acts like an optical black body entrapping the laser radiation allowing for the system to achieve higher welding speeds [38,45]. Keyhole formation in steels can be achieved with a beam intensity of 10^3 W/mm² while at power intensities between 10^4 and 10^5 W/mm² the weld penetration increases drastically allowing the formation of narrow and deep welds without compromising the welding speed [31]. At a power intensity exceeding 10^5 W/mm² the keyhole becomes highly unstable leading to the expulsion of molten and vaporized material which severely compromises the weld geometry and its mechanical properties [31,46].

One of the main advantages of laser welding is the ability to optimize weld properties by careful manipulation of the laser-substrate interaction [37]. The welding efficiency, which is defined as the coefficient of power transfer, η :

$$\eta = \frac{\text{Laser power absorbed by workpiece}}{\text{Incident laser power}}, \quad (1)$$

is very low before the formation of the keyhole, but approaches unity once the threshold for keyhole formation has been passed and the keyhole has been established [37]. The melting efficiency, ε , relates the rate of melting to the incident laser power where:

$$\varepsilon = \frac{vt(2r_l)\Delta H_m}{P}, \quad (2)$$

where P is the incident laser power, v is the welding speed, t is the sheet thickness, r_l is the laser beam radius, and ΔH_m is the heat content of the metal at the melt temperature as defined by Swift-

Hook and Gick [47]. It is easy to confirm that even when the welding efficiency is 100%, ϵ never approaches unity [37]. In fact, the maximum theoretical value of the melting efficiency is 48% for penetration welds [47]. According to Duley [37], both η and ϵ can be enhanced as long as the absorption coefficient, α , can be increased before arriving at the keyhole formation threshold. A number of ways have been suggested that can help enhance α [37,48,49]:

- i) Application of an absorbent coating that improves the absorptivity of the substrate [50,51]
- ii) Surface roughening or texturizing [52]
- iii) Surface preheating

Other methods that have been suggested to improve welding efficiency include beam polarization [37,53], beam combination and split-beam techniques [37,54–57], beam walking [37], beam defocusing and configuration (i.e. trailing, leading or perpendicular) [58–63], and arc-augmented laser welding [37,64–69].

2.2 Coated ultra-high strength Mn-B alloyed press-hardened steels

2.2.1 Material properties

As the need for parts with complex shapes, good formability, toughness, and impact resistance increases, the traditional high strength low alloy steels do not meet the present day requirements of the automotive industry as their strength is limited and they are relatively expensive [70]. The usage of boron steel sheets has been recognized as an excellent alternative to more traditional grades of UHSSs due to the ability of boron to act as a strong hardening agent with excellent hardenability while still allowing for the steel to have good formability – which allows the steel to be hot formed quite effectively. A boron addition of 30 ppm to low alloy steels gives a hardenability increase equivalent to 0.6 wt% Mn or 0.7 wt% of Cr or 0.5 wt% of Mo or 1.5 wt% of Ni [71]. Boron-alloyed steels such as 22MnB5, 27MnCrB5, and 37MnB4 grades are the most widely used PHSs that produce a fully martensitic structure when utilizing a water-cooled die during quenching [72]. Amongst these, 22MnB5 is the most commonly used grade for automotive hot stamping (HS) applications [12] due to the fact that after HS, it exhibits a yield strength of 1100 MPa and a UTS of about 1500 MPa, as shown in Figure 5 [72]. 22MnB5 will be the primary PHS grade that is focused on as part of this research.

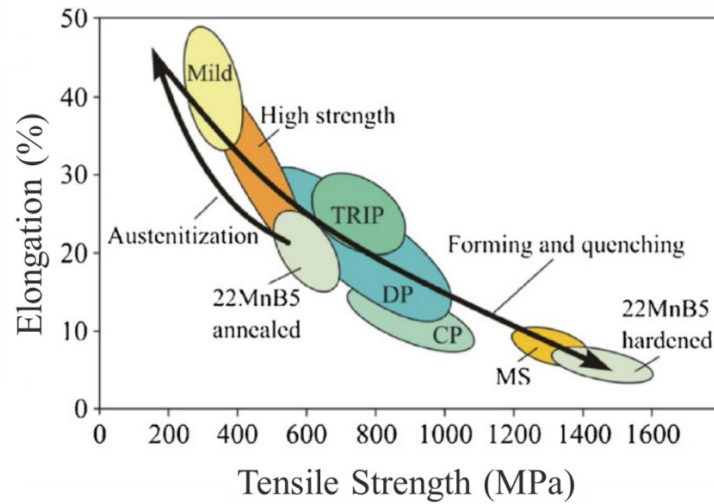


Figure 5: Mechanical properties of 22MnB5 in the AR condition and in the PHS condition relative to other grades of steel [73].

The typical microstructure of boron-alloyed steel in the as-received condition comprises ferrite, pearlite, and a small amount of martensite located at the ferrite grain boundaries as shown in Figure 6 (a). The typical morphology of the material in the hot-stamped condition is that of lath martensite as shown in Figure 6 (b). In general, it is observed that the laths are parallel to each other with some of the laths containing distributed carbides which is thought to be a consequence of autotempering [74].

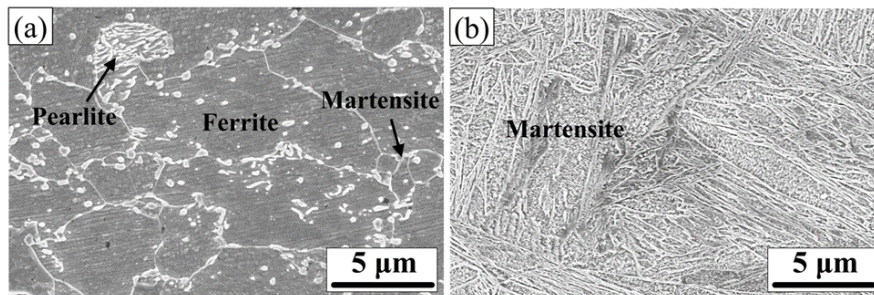


Figure 6: Base metal microstructure of 22MnB5 press-hardened steel a) As-received condition; b) Hot-stamped condition [75].

The addition of very small quantities of boron, typically ranging around from 10 – 30 ppm, to low alloy steels boosts the hardenability of the steel [76]. The reason for this increase in hardenability is attributed to the segregation of boron to the austenite grain boundaries. Boron segregation changes the austenite grain boundary characteristics (grain boundary surface energy modification [77,78] and leads to the formation of $Fe_{23}(CB)_6$ intermetallic particles [79,80] which delays the heterogeneous nucleation of ferrite at the austenite grain boundaries [76,81,82]. The effect of manganese is also important as it is an effective hardening agent that helps delay most austenite decomposition reactions [83]. The two alloying elements together help to push the

CCT diagram (shown in Figure 10) to the right by decreasing the minimum cooling rate necessary to form a fully martensitic microstructure by avoiding the nose of the ferrite and bainite curves during quenching at the end of the HS process. The transformation of 22MnB5 from a primarily ferritic (bcc) microstructure to austenite (fcc) during the heating stage and then to martensite (bct) during the rapid quenching stage can be seen in Figure 7.

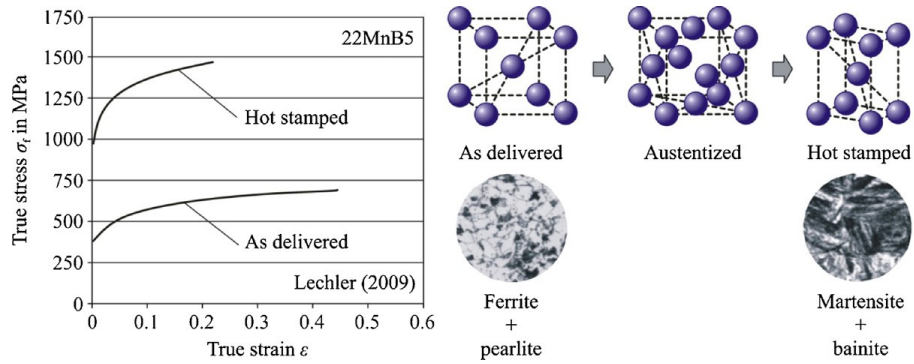


Figure 7: Flow curves and microstructure evolution of 22MnB5 during HS as it goes from a BCC crystal structure in the as-received state to an FCC crystal structure when fully austenitized and finally achieving a BCT crystal structure following the quenching and forming stage [73].

2.2.2 Surface coatings and their characteristics

Surface oxidation and corrosion is an issue for all components made of steel. PHSs are no exception to that rule with the oxidation of the steel surface becoming more rapid and aggressive at the elevated forming temperatures during the HS process [84]. Uncoated 22MnB5 is plagued with the formation of oxide scale on the surface due to thermal oxidation at elevated austenitization temperatures. Previously, chromium shot blasting was used to blast away the oxide scale which left behind a thin Fe-Cr layer that helped prevent further oxidation and corrosion, and eliminated the need to reapply an oil coating [83]. Recently, 22MnB5 steel has been made available with surface coatings that provided some type of barrier or sacrificial protection as well as protection against decarburization during the heating stage. The most common and widely used coating is the Al-Si coating, and the coated PHS is sold under the trade name of Usibor® 1500P (aka Usibor® AluSi). The coating is applied through a process known as hot-dip-aluminizing [85]. However, as the electrochemical potential of the Al-Si-Fe coating is so close to that of the base material, there is not enough of a chemical potential difference required to provide adequate sacrificial protection and therefore, it is primarily used to provide barrier protection against oxidation as well as decarburization. The core focus of this research will be on the Al-Si coated Usibor® 1500P.

Hot-dip aluminizing is carried out in the form of a continuous process (as shown in Figure 8) where the base metal steel sheet (4) is guided into a hot-dip Al-Si plating (aka aluminizing) bath (1). The coating thickness is adjusted by a gas-wiping mechanism (3) as the steel sheet moves into a cooling unit (5) which solidifies the coating-metal layer providing the

finished coated steel (6). The substrate is usually aluminized by dipping it in a molten aluminum bath held at a temperature of about 680 °C. The composition of the molten bath is approximately 88 wt% Al, 10 wt% Si and 2 wt% Fe [86].

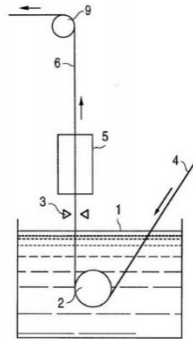
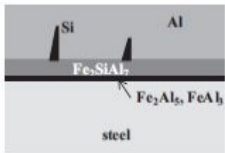
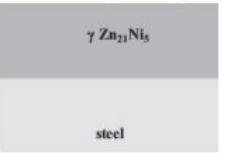
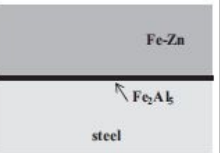
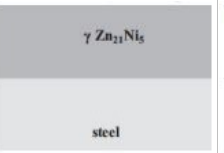
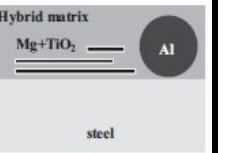


Figure 8: Method for manufacturing hot-dip aluminized steel sheets showing that the steel sheet is continuously dipped in a molten bath of Al-Si and the coating solidifies as the steel leaves the bath [87].

The addition of Si to the aluminized coating is to form an intermetallic inhibition layer of Fe_2SiAl_7 between the coating and the steel substrate. The Fe_2SiAl_7 layer prevents the formation of brittle intermetallics at temperatures below 550°C [88]. During the HS process, the service temperature is much higher than 550°C so the Fe-Al intermetallic phase formation reaction is much faster. However, in the absence of silicon it was observed that there is rapid growth of the brittle Fe_2Al_5 intermetallic phase into the steel substrate forming a wavy coating-steel interface at elevated temperatures [89]. The Fe_2Al_5 phase is extremely detrimental to coating adhesion and material formability since the phase is quite hard and brittle. Si is very effective at controlling the inward protrusions of the intermetallic phase into the steel substrate leading to a flat coating-substrate interface and much improved coating properties [86].

Alternative coatings such as the Zn-based galvanized (GI) Zn-Al_{0.2%} and galvanized (GA) Zn-Fe_{10%} coatings are also used to protect PHSs [84,90,91]. However, the Zn-based coatings come with their own set of problems with the most relevant being Liquid Metal Embrittlement (LME) [25,92]. LME is a phenomenon that is generally observed between two metals with low mutual solubility, specifically when an aggressive (or reactive) liquid metal comes into contact with a susceptible substrate in the presence of a tensile load [93,94]. During the press-hardening process liquid zinc from the coating seeps into the exposed grain boundaries of the steel substrate, resulting in material decohesion as LME-cracks are formed and propagated through the thickness of the substrate. Apart from the more mainstream coatings some zinc-nickel alloy coatings as well as some hybrid coatings have been tested for PHS applications. Fan et al. [86] provided an excellent summary of the different types of coatings used for HS applications as well as a list of their advantages and disadvantages. A more up-to-date summary of different types of coatings is provided in Table 1.

Table 1: Comparison of various coatings used to protect 22MnB5 grade steel [25].

	Aluminized (Al-Si) Coating	Galvanized (GI) Coating	Galvannealed (GA) Coating	Zn-Ni Alloy Coating	Hybrid Coating
Pre-Press-Hardening Coating Structure [95]					
Primary Purpose	<ul style="list-style-type: none"> •Provides excellent barrier protection 	<ul style="list-style-type: none"> •Provides sacrificial and barrier protection 	<ul style="list-style-type: none"> •Provides sacrificial and barrier protection 	<ul style="list-style-type: none"> •Provides sacrificial and barrier protection 	<ul style="list-style-type: none"> •Provides sacrificial and barrier protection
Advantages	<ul style="list-style-type: none"> •No need for phosphating •Good formability •Good oxidation resistance •Relatively cost effective 	<ul style="list-style-type: none"> •Cathodic protection •Relatively cost effective 	<ul style="list-style-type: none"> •Cathodic protection •Limited LME 	<ul style="list-style-type: none"> •Cathodic protection •No LME •High melting temperature 	<ul style="list-style-type: none"> •Cathodic protection •No observed LME
Disadvantages	<ul style="list-style-type: none"> •Liquid Al adhesion •Brittleness of coating 	<ul style="list-style-type: none"> •High LME risk •Removal of oxides •Liquid Zn adhesion •Brittleness of coating 	<ul style="list-style-type: none"> •Brittleness of coating •Higher processing time •Relatively higher cost compared to GI 	<ul style="list-style-type: none"> •Coating is complicated to engineer •Higher production cost 	<ul style="list-style-type: none"> •Higher production cost •Brittle intermetallics can lead to cracking and delamination •Post PH coating microstructure difficult to control
Paintability	<ul style="list-style-type: none"> •Excellent 	<ul style="list-style-type: none"> •Good after oxide-removal and phosphating 	<ul style="list-style-type: none"> •Excellent 	<ul style="list-style-type: none"> •Reported issues with electrophoretic primer 	<ul style="list-style-type: none"> •Good
Laser Welding Impact	<ul style="list-style-type: none"> •Weld weakening due to coating dilution leading to ferrite formation in the weld-zone 	<ul style="list-style-type: none"> •Coating vaporization 	<ul style="list-style-type: none"> •Increased LME susceptibility 	<ul style="list-style-type: none"> •Unknown 	<ul style="list-style-type: none"> •Unknown
Resistance Spot Welding Impact	<ul style="list-style-type: none"> •Excellent weldability 	<ul style="list-style-type: none"> •Presence of surface oxides complicates the RSW process •Heating cycle needs to be optimized for good results 	<ul style="list-style-type: none"> •Excellent weldability •Coating is prone to LME susceptibility in certain welding conditions 	<ul style="list-style-type: none"> •Weldability is generally considered to be better than GA and GI coatings 	<ul style="list-style-type: none"> •Third generation hybrid coatings are known to offer good weldability
Main References	[18,22,26,27,34,35,46–49,50]	[84,86,104–109]	[84,86,104–106,109]	[86,106,110]	[86,111]

2.3 Hot stamping

Developed in Sweden in 1977 by a company called Plannja, HS was first used as a process to manufacture sawblades and lawn mower blades [112]. The first known use of the HS technology in the automotive industry was by Saab Automobile AB in 1984 [112]. The technology was slow to catch on with only 3 million parts produced in 1987; however, in a span of 20 years production of hot-stamped parts had increased to 107 million parts/year in 2007 [112].

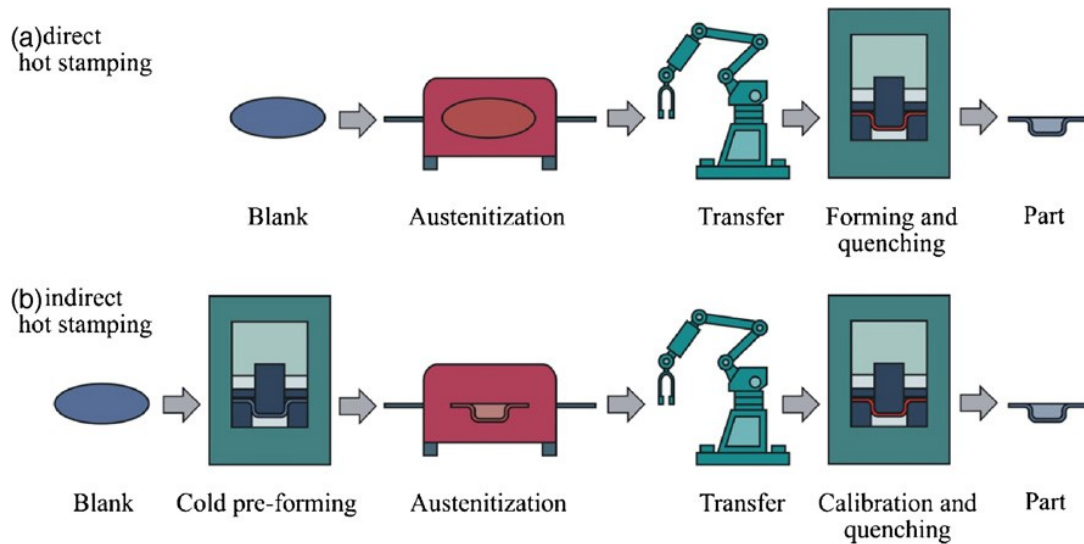


Figure 9: Schematic showing the (a) direct hot-stamping method which is the most common method used in the hot-stamping process and the more uncommon (b) indirect hot-stamping method [73].

There are two main methods of HS as shown in Figure 9. The most commonly used method for HS is known as the direct HS method (Figure 9 a). This method requires the blank to be heated up to its automatization temperature ($T > A_{c3}$ or 850°C to 950°C) and held for about 4-10 minutes, after which the blank is rapidly transferred to the HS press where it is simultaneously quenched and formed using a water-cooled die for about 6-10 seconds [12] to ensure that no bainite or ferrite forms in the microstructure [72]. If the cooling rate exceeds the critical cooling rate required for a complete diffusionless transformation of austenite to martensite, an ultra-high strength, fully martensitic steel will be achieved (i.e., UTS $\sim 1500\text{-}2000$ MPa) as shown by the continuous cooling transformation (CCT) curve in Figure 10 [113].

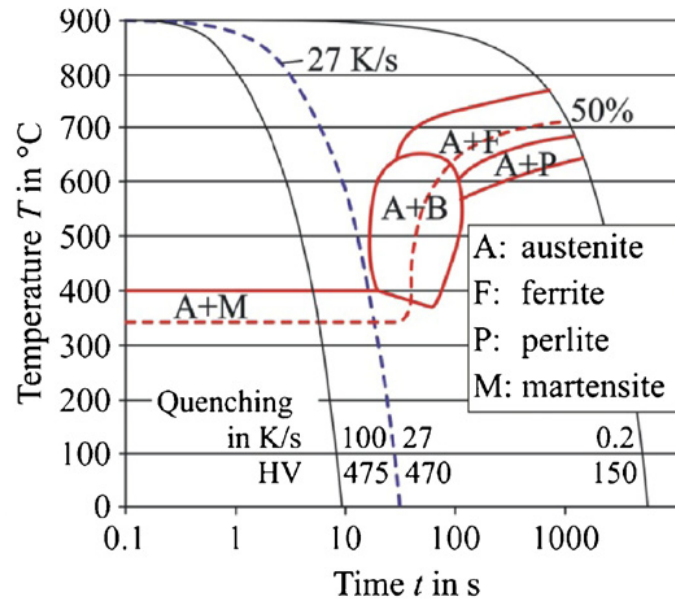


Figure 10: CCT diagram of 22MnB5 pre-coated steel showing that by ensuring a cooling rate higher than 27 K/s a fully martensitic microstructure can be achieved [73].

The most common method to produce vehicle components with tailored properties is known as TWBs. The technology was first invented by Floyd Kerby [114]. In this method, two or more types of steel with varying thicknesses are joined together using LW and, in the case of TWBs made of PHSs, are then hot formed into the required part using the direct HS approach as shown in Figure 11. The benefits of using this technology are listed as follows:

- i) The technology significantly simplifies the manufacturing process which saves time and reduces production costs.
- ii) By joining different types of steels together with varying thicknesses the part can be optimized by reducing its weight and improving its performance.
- iii) Two or three separate parts can potentially be consolidated into one single component.
- iv) In general, using TWBs leads to a material cost reduction.

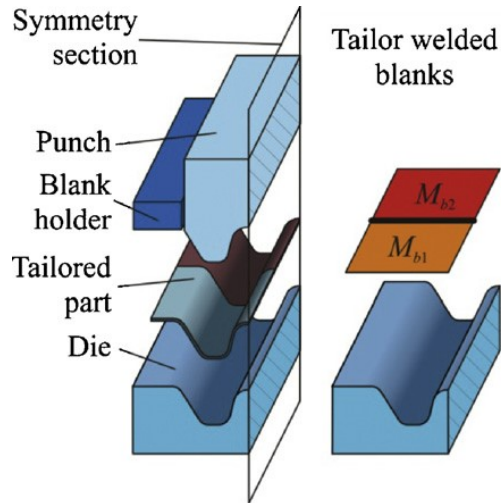


Figure 11: Schematic showing the production of a TWB by HS laser-welded steel sheets to produce a part with tailored properties [73].

2.4 Laser welding of Al-Si coated 22MnB5

2.4.1 Microstructure of the laser welded fusion zone

When 22MnB5 steel is welded in the absence of a surface coating, the fusion zone (FZ) is shown to have a martensitic microstructure as shown in Figure 12. This means that the weldment has a similar microstructure and physical properties as the base metal in the hot-stamped condition.

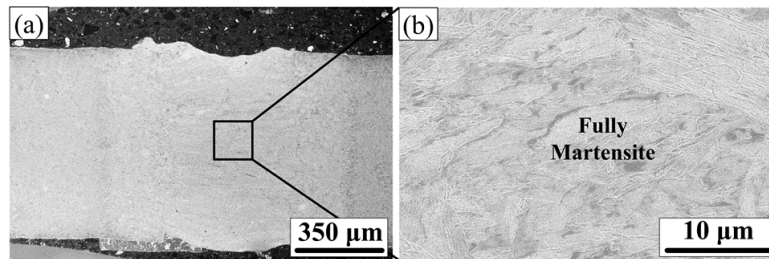


Figure 12: Micrograph of non-coated 22MnB5 FZ with fully martensitic microstructure [75].

However, due to the corrosion and oxidation susceptibility of the 22MnB5 steel grade, automakers typically use PHSs with a protective Al-Si coating. During LW of Al-Si coated 22MnB5 PHS, the coating melts and mixes into the molten weld pool as shown in Figure 13 (a) and (b) [115]. This leads to the formation of a dual-phase region in the FZ comprising of ferrite and martensite in both the as-received welded (ARW) and the as-received welded then hot-stamped (ARWHS) condition as shown in Figure 13 (c).

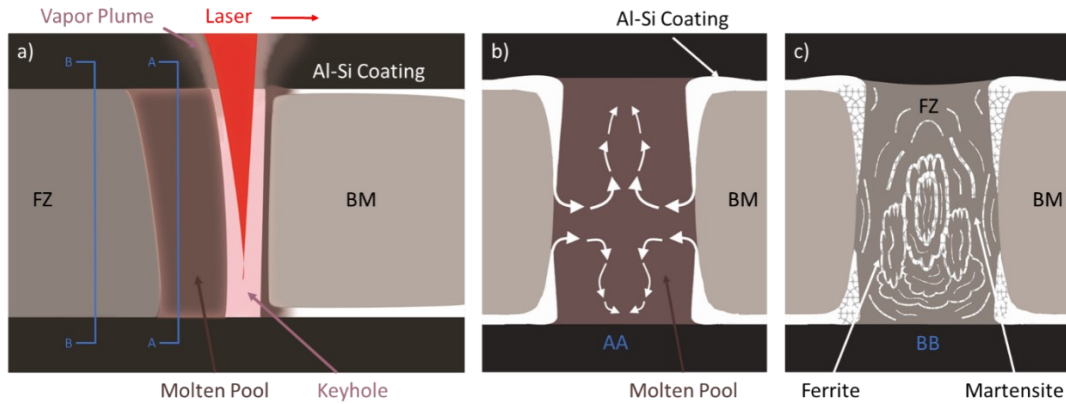


Figure 13: Schematic showing (a) the laser welding of Al-Si coated 22MnB5 steel with a cross-section of (b) the molten weld pool showing the mixing pattern of the Al-Si coating and (c) the solidified FZ showing the dual-phase microstructure with ferrite dispersed in a martensitic matrix [25].

Figure 14 shows the representative SEM micrographs illustrating the (a) ferritic-pearlitic complex-phase region in the as-received BM, the (b) fully martensitic microstructure in the press-hardened BM, the (c) combination of high-temperature δ -ferrite and α_1' martensite phase in the FZ of the ARW material, and the (d) combination of low-temperature α -ferrite and α_2' martensite phase in the FZ of the ARWHS material.

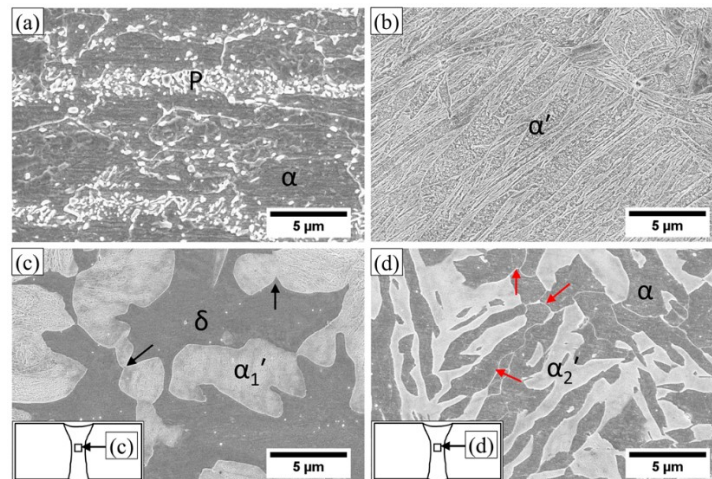


Figure 14: Representative SEM micrographs of the as-received BM, as-hot-stamped BM and the dual-phase regions in the FZ of the ARW and ARWHS condition [116].

Bright-field transmission electron microscopy (TEM) was used to show that the dual-phase region seen in the weldment was a combination of high-temperature δ -ferrite and martensite in the ARW condition, and the microstructure is composed of the low-temperature α -ferrite and martensite phase in the ARWHS condition. Figure 15 shows the bright-field TEM images of the FZ in the ARW sample showing: (a) a mixture of δ -ferrite and martensite (α_1') phase, (b) lower bainite microconstituents, and diffraction patterns of (c) δ -ferrite in $[\bar{1}11]$ projection, (d) α_1' in $[001]$ projection, and the (e) orientation relationship between δ and α_1' . Figure 16 shows the

bright-field TEM images of the FZ of the ARWHS sample showing: (f) a mixture of α -ferrite and martensite (α_2') phase, (g) magnified view of α - α_2' interface, and the diffraction patterns of (h) α -ferrite in $[012]$ projection, and (i) α_2' in $[\bar{1}\bar{1}\bar{1}]$ projection.

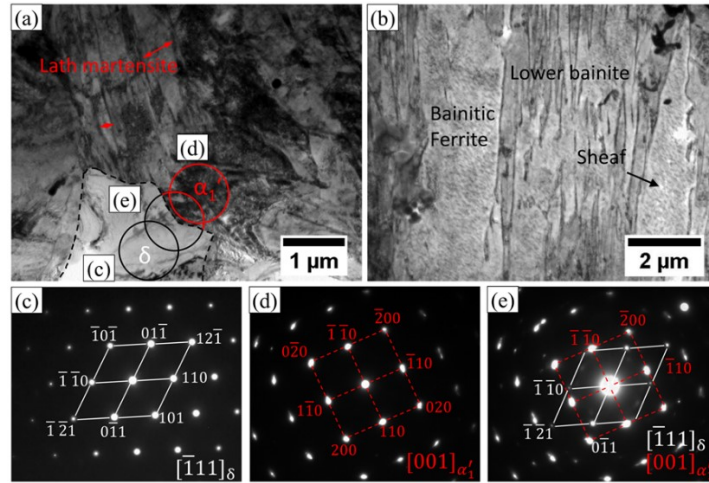


Figure 15: Bright-field TEM images of the FZ of ARW sample [116].

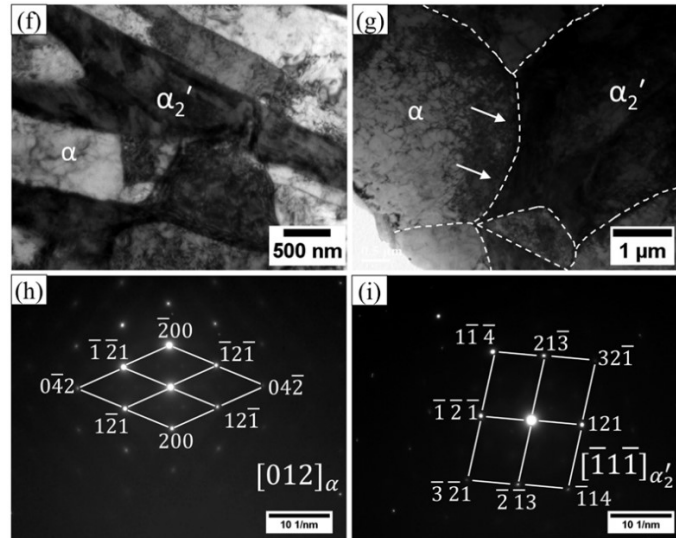


Figure 16: Bright-field TEM images of the FZ of ARWHS sample [116]

2.4.2 Ferrite evolution in the fusion zone

According to Martin et al. [117] aluminum is a strong ferrite stabilizer that plays a role in shrinking the single-phase austenite region while causing an expansion of the two-phase ferrite-austenite region on the Fe-Al phase diagram. In fact, it has been reported that an Al-content of greater than 1.2 wt.% can inhibit the formation of the austenite phase [68]. Figure 17 shows the Fe-Al phase diagram that confirms that during cooling, the δ -ferrite phase forms first from the liquid phase (L), after which a peritectic reaction ($\delta + L \rightarrow \delta + \gamma$) completely transforms the L-

phase to austenite which implies that as long as the Al-content in the weld is greater than about 0.3 wt%, the final microstructure in the FZ will be a combination of ferrite and martensite, given that the cooling rate is high enough for martensite formation.

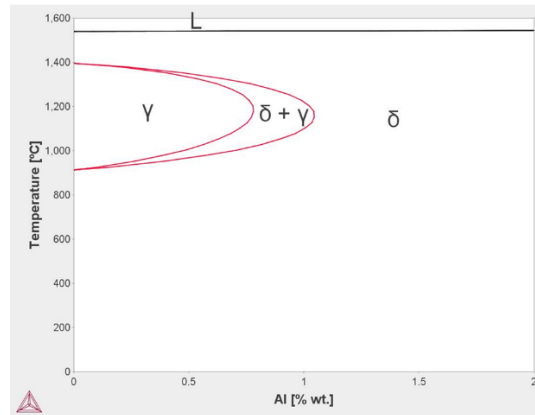


Figure 17: Binary Fe-Al phase diagram generated for the chemical composition of 22MnB5 PHS using ThermoCalc [75].

It is important to confirm that it is indeed the addition of Al in the weld zone that leads to the formation of the ferrite phase. Figure 18 (a) and (b) shows the energy dispersive X-ray spectroscopy (EDX) analysis of the FZ in the ARW and ARWHS condition, respectively. The line-scans confirm that there is a spike in the Al-content when moving from the martensite phase to the ferrite phase which suggests that the formation of the ferrite phase is directly related to the local concentration of Al at the given site. Furthermore, elemental mapping with an electron probe micro-analyzer (EPMA) can be used to confirm that the ferrite phase has a high local concentration of Al as shown in Figure 19 (a) and (b). On average, it has been shown that the local Al-wt.% in the ferrite phase in the ARWHS condition ranges from about 1.7 to 2.5% [74].

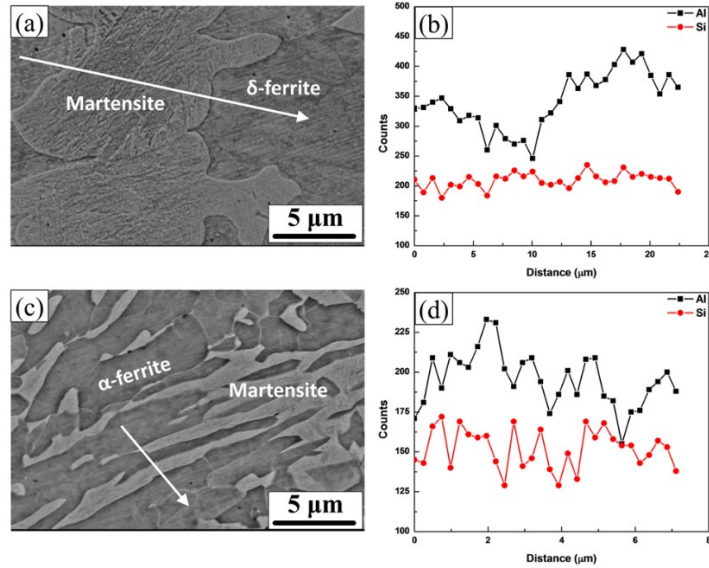


Figure 18: EDX line scans showing a spike in Al-content in the ferrite phase found in the (a) ARW and (b) ARWHS samples [75].

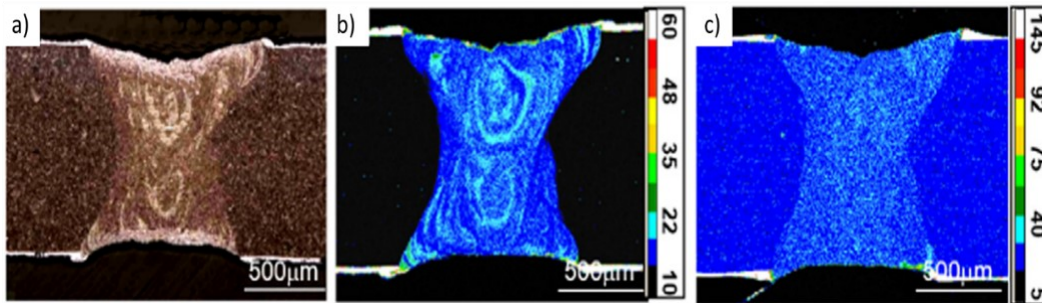


Figure 19: (a) Optical Microscope image of the FZ in the ARWHS condition with elemental maps made using EPMA for (b) Al and (c) Si [118].

2.4.3 Ferrite distribution in the fusion zone

The ferrite location in the ARW condition has been shown to be concentrated along the fusion boundary [74]. The Marangoni convection flow can be used to explain the flow of material in the molten weld pool during welding. The flow in a molten weld pool is a function of the surface tension (γ) between the phases and the temperature (T) as shown in Figure 20. Fe and Al both have a negative temperature coefficient of surface tension (i.e., $\delta\gamma/\delta T$ is negative) which implies that the molten material inside the weld pool flows from the center of the weld to the boundary as shown in Figure 20 (b) [119].

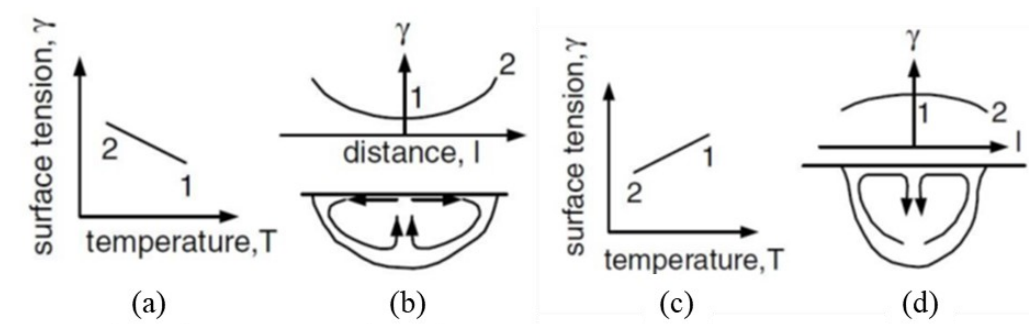


Figure 20: Schematic of fluid flow in a molten weld pool showing that when (a) $\delta\gamma/\delta T$ is negative (b) molten material inside the weld pool flows from the center of the weld to the boundary and when (c) $\delta\gamma/\delta T$ is positive (d) molten material inside the weld pool flows from the boundary to the center of the weld [33].

The convection circulation in the molten weld pool is such that liquid metal flows from the center of the weld where the temperature of the system is at a maximum due to the presence of the keyhole (i.e., the hottest area of the weld) to the weld boundary where the temperature is at the lowest [120]. This temperature differential provides the driving force that leads to the fluid flow pattern shown by the red arrows in Figure 21. Therefore, it can be argued that the molten Al-Si coating flows into the weld along the fusion boundary as it is sucked in due to the fluid flow driven by the Marangoni effect, and due to the extremely high cooling ($\sim 10,000$ °C) during laser welding, it becomes trapped as the molten weld pool quickly solidifies [121].

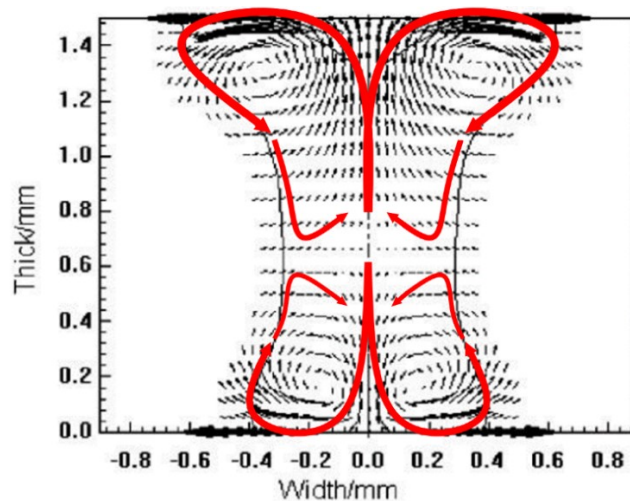


Figure 21: Marangoni Convection Flow in a molten weld pool showing that molten material flows from the center of the weld to the boundaries [122].

It was noted by Saha et al. that a relatively higher Al-content is observed in the ARW condition compared to ARWHS condition because the aluminum is concentrated primarily along the fusion boundary [74]. During the HS process the aluminum has time to diffuse through the weld at the high austenitization temperatures. For this reason, Al-content was observed to be more evenly distributed throughout the weld and the local Al-content in the ferrite phase was found to

be lower in the ARWHS condition [123]. However, Saha notes that the ferrite phase concentration (PC) is higher (about 40%) in the ARWHS condition compared to the ARW condition (about 20%) despite an apparent reduction in Al-content in the FZ [74]. It has been suggested that the growth of the δ -ferrite phase during laser welding is limited and kept in check due to the large compressive stress imposed on it by the formation and growth of the martensite plates [124]. However, during austenitization, the martensite decomposes, releasing the compressive stress which leads to the formation of a more abundant (and relatively unstressed) α -ferrite phase by way of recrystallization. Since the mechanical properties of the FZ are tied directly to its morphology, it can be assumed that as the ferrite content in the weld increases, its mechanical properties will tend to worsen, and the strength of the weld would decrease.

2.4.4 Effect of ferrite on the mechanical properties of the FZ

The ferrite phase in steels is softer and more ductile than the martensite phase found in PHS. Figure 22 shows the nano-indentation study of the different phases present in the FZ of the (a) ARW, (b) ARWHS, and (c) Hot-Stamped then Welded (HSW) conditions. It was observed that the hardness of the martensite phase ranged from 7.1 to 7.9 GPa and that of the ferrite phase ranged from 4.5 to 4.9 GPa, for all three sample conditions. Interestingly, it was noted that the lowest nanohardness for the martensite phase was observed in the ARWHS sample (7.1 ± 0.6 GPa) which was attributed to the lower cooling rate in the HS condition and the presence of the smaller martensite crystals with a relatively lower internal stress [74]. Figure 23 shows the characteristic microhardness profile across the FZ in the (a) ARW and (b) ARWHS condition with and without the presence of the Al-Si coating. It has been reported that the as-received BM hardness for 22MnB5 steel is about 250 HV and the Hot-Stamped BM (HSBM) hardness ranges from about 500 to 550 HV [102,115,125,126]. The FZ hardness is observed to be lower in both the ARW and ARWHS conditions when the welds are made through the Al-Si coating compared to when the Al-Si coating is removed prior to welding [96,102].

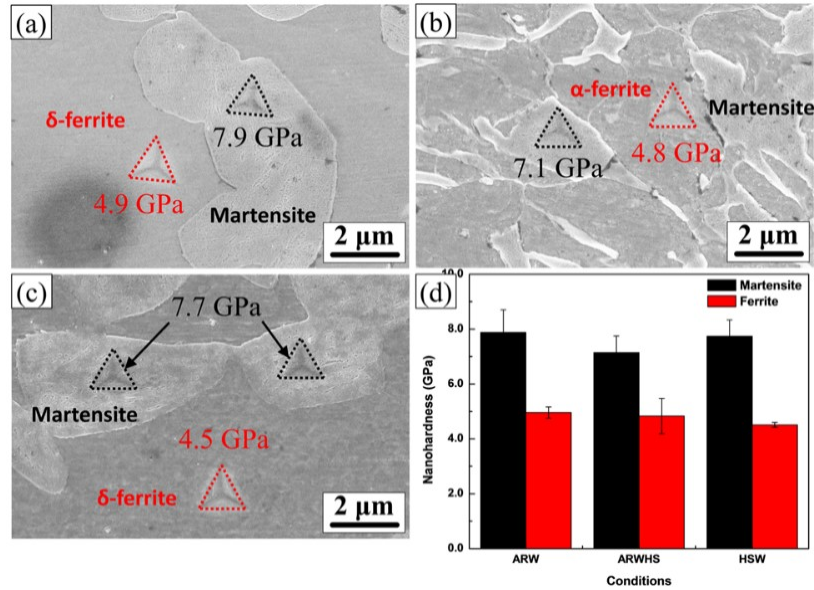


Figure 22: Nanoindentation study of the different phases present in the weldment for the (a) ARW, (b) ARWHS, and (c) HSW condition. (d) is the bar graph showing the relative difference in nanohardness between the martensite and the ferrite phases present in the different conditions [75].

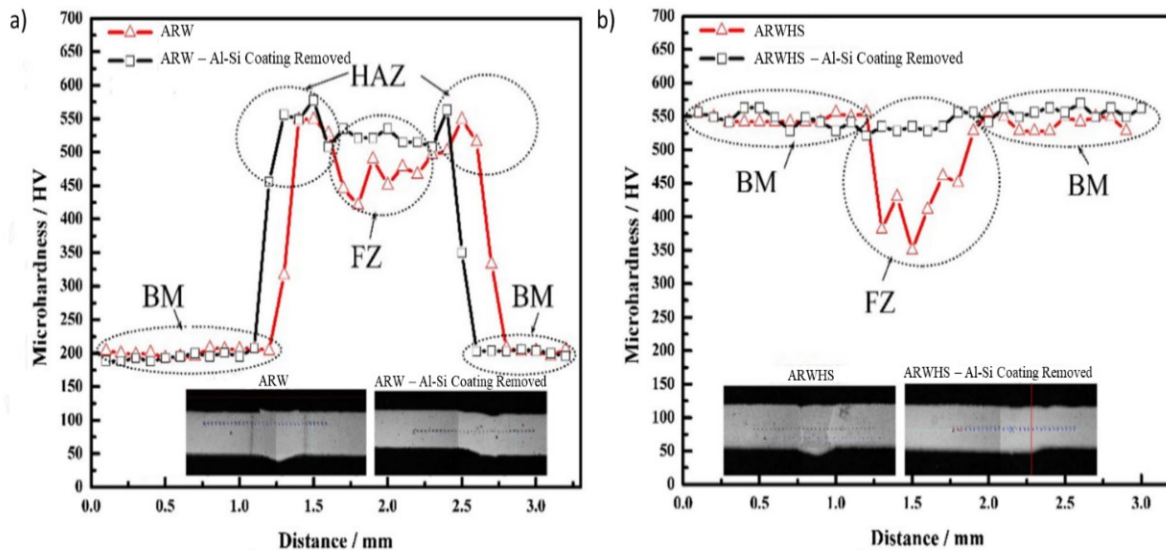


Figure 23: Microhardness map of the FZ with and without the presence of the Al-Si coating in the (a) ARW and (b) ARWHS condition [127].

Figure 24 shows the characteristic engineering stress-strain curves for the different samples of interest. For the as-received samples, the yield strength and the UTS of the ARW sample showed a negligible difference when compared to the as-received BM (ARBM). In the case of the hot-stamped samples, the non-welded sample (i.e., HSBM) was seen to have the highest UTS and engineering strain, whereas both the welded samples (i.e., HSW and ARWHS) exhibited a much lower UTS while also showing a significant loss in elongation. The lower hardness observed in

the FZ of these samples indicates that the load-carrying capacity of the FZ was compromised which leads to catastrophic failure in the weldment.

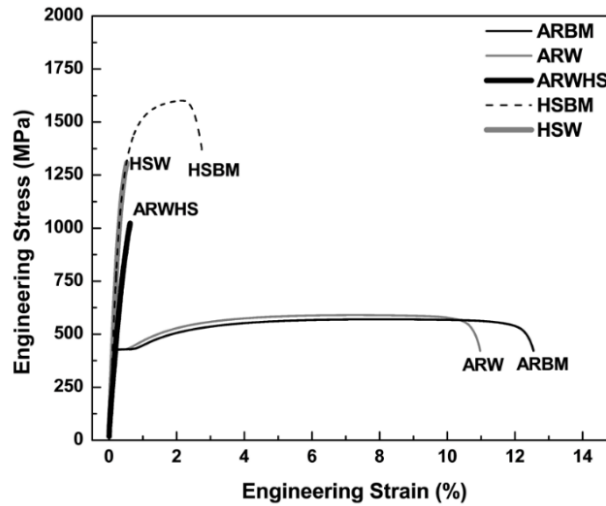


Figure 24: Engineering stress vs. strain curves for different the different conditions under consideration [75].

The mechanical properties of the BM and the welded samples in different conditions were collected from the available literature [12,74,102,103,123,125] and the details have been summarized in Table 2. The tensile samples in the ARBM and the ARW condition both failed in the BM as the UTS of 22MnB5 PHS in the as-received condition is about 585 MPa which is significantly lower than the strength of the martensitic FZ. However, due to the presence of the weld itself in the ARW sample which changes the geometric homogeneity of the workpiece, the joint elongation is reduced and therefore, the sample exhibits lower elongation and fails sooner compared to the ARBM condition. For the hot-stamped samples, the HSBM has the highest UTS of about 1550 MPa and the highest engineering strain of about 4% which is to be expected due to the fully martensitic microstructure [74,102,115,126]. In comparison, the ARWHS sample shows that the engineering strain is measured at just about 0.77% and the UTS is measured at about 1100 MPa [74,102]. This loss in mechanical properties of the joint can be explained by the presence of the dual-phase ferrite and martensite FZ microstructure which leads to a lower hardness of the weld compared to the BM, which leads to a loss in strength and ductility.

Table 2: Characteristic mechanical properties of BM and welded joints [12,74,102,103,123,125].

Sample Condition	UTS (MPa)	Elongation (%)	Joint Efficiency (%)	Fracture Locations
ARBM	585 ± 15	20 ± 3	100	BM
ARW	585 ± 22	13.3 ± 3	99	BM
HSBM	1527 ± 26	3.6 ± 0.1	100	BM
ARWHS	1129 ± 75	0.84 ± 0.1	74	FZ

Figure 25 shows the failure conditions in the (a) ARBM and ARW condition, (b) HSBM condition, (c) ARWHS condition, and (d) HSW condition. It can be seen that welding in the as-received condition has no significant impact on the mechanical properties of the joint, as failure occurs in the BM in both the ARW and ARBM conditions. However, in the ARWHS condition, failure is seen to initiate at the fusion boundary (FB) and then propagates through the FZ following the network of low-strength α -ferrite dispersed through the weldment. The joint efficiency in the ARWHS condition is about 74% which is extremely poor when compared to the HSBM. Similarly, the joint fails in the FB in the HSW condition, which can be explained by the presence of the δ -ferrite phase along the boundary of the weld and the presence of the heat affected zone (HAZ) surrounding the FZ.

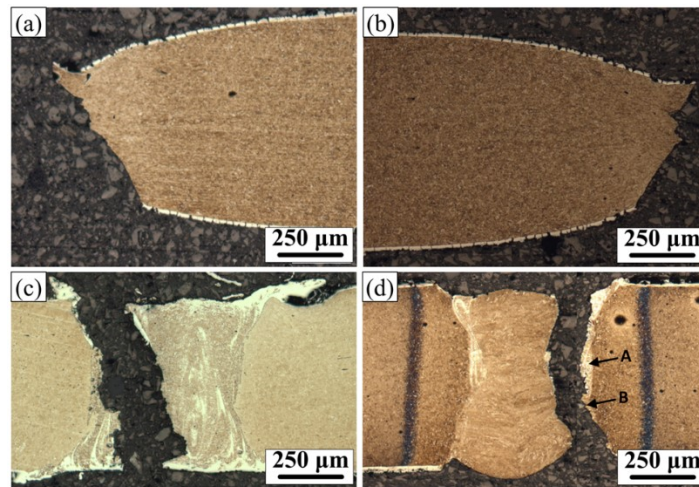


Figure 25: Light micrographs of the failure locations found in the (a) ARBM and ARW condition, (b) HSBM condition, (c) ARWHS condition, and (d) HSW condition [75].

2.4.5 Existing solutions to mitigate ferrite formation during laser welding

To date, several different methods have been developed to mitigate the issue of FZ weakening during FLW of Al-Si coated 22MnB5 PHS and a summary is provided in Table 3, which draws a comparison between the various solutions. It is interesting to note that the most widely used method in industry today continues to be one of the first methods developed for solving this problem over ten years ago, which is the ablation of the Al-Si coating using a pulsed laser prior to welding [96]. Although this method continues to be the most widely used, it does not mean that it is currently the most efficient method that can be employed to solve this problem. Due to the cost and complexity of using laser ablation, there remains a drive to this day to find a solution that is more affordable and easier to implement. Recent breakthroughs in improving weld properties using methods that range from optimizing and adapting the welding process to changing the alloying composition of the FZ clearly show that there is a demand to find methods which solve the problem of the formation of ferrite in the FZ of Al-Si coated 22MnB5 laser-welded joints in a way that is relatively easier and more affordable compared to laser ablation.

Table 3: Comparison of different methods used to avoid ferrite formation in the FZ during FLW of Al-Si coated 22MnB5 [25]

	Mechanical Scraping	Laser Ablation	Laser-Arc Hybrid Welding; Arc Pre-treatment	Dual-beam Laser Welding	Filler Wire/ Interlayer with Austenite Stabilizing Element
Primary Purpose	<ul style="list-style-type: none"> Mechanical removal of coating 	<ul style="list-style-type: none"> Vaporization of Al-Si coating using high energy light source 	<ul style="list-style-type: none"> Increasing the size of the molten weld pool to decrease coating dilution and improve chemical homogeneity in the weld 	<ul style="list-style-type: none"> Increasing the size of the molten weld pool to decrease coating dilution and improve chemical homogeneity in the weld 	<ul style="list-style-type: none"> Addition of austenite stabilizing element to suppress ferrite formation and increase the martensite fraction in the weldment
Methodology	<ul style="list-style-type: none"> Using abrasive or scraping tool 	<ul style="list-style-type: none"> Ablation of Al-Si coating using pulsed Q-Switch lasers 	<ul style="list-style-type: none"> Laser welding combined with at least one electric arc to fully weld the workpiece Local heating of weld-line vicinity using a micro-TIG machine 	<ul style="list-style-type: none"> Collateral dual-beam module with a 1:1 ratio for symmetrical configuration was used to produce larger welds compared to a single-beam setup 	<ul style="list-style-type: none"> Direct addition of filler wire into the molten weld pool Using an interlayer made of an austenite stabilizing element at the welding interface
Advantages	<ul style="list-style-type: none"> Relatively inexpensive Low process complexity 	<ul style="list-style-type: none"> Currently, the most widely used method in industry Leaves behind Fe-Al intermetallic layer for continued corrosion resistance Process can be used in tandem with laser welding setup 	<ul style="list-style-type: none"> Stabilizes the keyhole and improves fluid flow in the molten weld pool Increases the size of the molten weld pool reducing dilution MIG-Laser Hybrid uses filler wire that improves weld chemistry 	<ul style="list-style-type: none"> Stabilizes the keyhole and improves fluid flow in the molten weld pool Increases the size of the molten weld pool reducing dilution 	<ul style="list-style-type: none"> Controlling the properties of the weld by changing weld chemistry rather than the process Can be more cost-effective compared to methods changing the process A much wider array of potential solutions can be found Adding interlayers or coatings to surfaces being welded can be relatively easy
Disadvantages	<ul style="list-style-type: none"> Time consuming Lack of control over process 	<ul style="list-style-type: none"> Expensive Process dynamics can complicate the manufacturing process Can be more time-consuming 	<ul style="list-style-type: none"> Expensive Process dynamics can complicate the manufacturing process Process parameters can be more difficult to optimize Needs more work to establish process efficacy 	<ul style="list-style-type: none"> Expensive Process dynamics can complicate the manufacturing process Process parameters can be more difficult to optimize Needs more work to establish process efficacy 	<ul style="list-style-type: none"> Requires large body of experimental work Measuring low alloy compositions can be challenging Repeatability and reliability can be an issue Slight changes in chemical composition can have drastic effects on final weld properties
Final Weld Properties	<ul style="list-style-type: none"> Finer lath martensite and negligible ferrite in FZ post-PH High strength recovery in the de-coated specimen 	<ul style="list-style-type: none"> Complete strength and hardness recovery in the weld zone No failure in weld seam during 3-point-bend test and crush test No change in corrosion resistance properties 	<ul style="list-style-type: none"> Complete recovery of tensile strength Improvement in elongation properties Arc pre-treatment leads to slight improvement in strength with much improved weld homogeneity 	<ul style="list-style-type: none"> 90% recovery of strength, hardness and elongation properties Fracture was successfully shifted from the FZ to the BM 	<ul style="list-style-type: none"> Using high carbon filler wire can lead to brittle fracture in the weld Complete recovery in strength, hardness and elongation properties for both filler wire and interlayer methods
Year Developed	N/A	2009	2011; 2015	2019	2017; 2019
Main References	[102]	[96,128]	[68,69,123]	[57]	[103,129,130]

3 Experimental methodology and process optimization

* Section 3.5 is on the optimization of the laser welding process using numerical modelling and experimental validation, incorporating results from published studies [61–63] as outlined in the Statement of Contributions.

3.1 Material and sample preparation details

Al-Si coated 22MnB5 steel (1.5 mm thick) was used primarily as the base material (BM) for this study and the nominal chemical composition of the material is shown in Table 4. The samples were prepared for metallographic analysis using conventional metallographic grinding and polishing up to a final 1 μm polishing step and the samples were etched with 2.5% Nital solution. The Zeiss UltraPlus field emission scanning electron microscope (FE-SEM) was used to observe high magnification images of the coating microstructure, FZ morphology, and the fracture surfaces of the welds in the various conditions of interest. Clemex Vision Lite Image Analysis software (v. 8.0.197) was used to analyze the FZ and BM microstructure to quantify the phase concentration of ferrite and martensite in the different samples. The JEOL JXA-8230 electron probe micro-analyzer (EPMA) was used for elemental analysis to determine the alloying content of the elements of interest in the FZ of the samples. The raw data for the CCT diagrams was generated using commercial CALPHAD software, JMatPro (v. 11.2), and the data was plotted using OriginPro 2021b (9.85).

Table 4: Chemical composition of the base material used in the present work (in wt.%).

Sample Condition	C	Mn	B	Si	Cr	Ti	Mo	P	Al	Fe
BM	0.23	1.22	0.0032	0.27	0.20	0.04	0.02	0.01	0.04	bal.

3.2 Hot stamping details

All the samples investigated in this thesis were welded and then hot-stamped (unless otherwise stated) by heating them in a continuous electrically heated furnace for 6 minutes to an austenitization temperature of 930 $^{\circ}\text{C}$ and then quenched instantaneously using a water-cooled die at a cooling rate of approximately 30 $^{\circ}\text{C}/\text{s}$, to ensure a fully martensitic microstructure in the as-received hot-stamped base material (HSBM).

3.3 Mechanical testing

Hardness was measured using the Clemex CMT (v. 8.0.197) with an indenter load of 200 gf and a 10 s dwell time, with each indent spaced two and a half times the size of the indent. The hardness properties of the different phases were characterized using an Anton Parr RST3 and a NHT3 nanoindentation tester. Nanoindentation hardness measurements were made with a standard Berkovich tip under the load control mode with a maximum load of 30 mN. The loading and unloading rates were set to 60 mN/min with a dwell time of 5s for each indent. Full- and sub-sized tensile coupons were cut from the welded and hot stamped samples using a water jet cutter in accordance to the ASTM E8/E8M standard [131]. The Instron 4206 was used to pull a total of 4 tensile coupons for each condition to ensure statistical relevance of the reported results. The samples were pulled with a displacement speed of 1 mm/minute and an optical extensometer was used to measure the strain. All errors have been reported as a confidence interval with a significance of 0.05 (i.e., a confidence level of 95%) for the mean value for each condition.

3.4 Laser welding details

A robotic IPG Photonics Ytterbium-doped (YLS-6000-S2) continuous-wave fiber laser was used to weld 1.5 mm thick Al-Si coated 22MnB5 grade PHS in the bead-on-plate (BOP) configuration, unless otherwise stated. The nominal laser spot size at a focal length of 200 mm was ~ 0.35 mm in the fully focused condition, and the beam was randomly polarized with a beam parameter product (BPP) of 4.5 mm*mrad. The laser welding system has a maximum deliverable power of 6 kW with the robot capable of welding at speeds higher than 20 m/min. The details of the laser system can be found in Table 5 and further details can be found in Ref. [132]. For the studies presented in this thesis, laser power (P) was generally kept constant at 4 kW and the travel speed (TS) was kept constant at 6 m/min, unless otherwise stated. To observe the material-laser interaction, the laser welding process was filmed from the side using a XIRIS XVC-1000 welding camera at a speed of 90 fps and at an angle of depression of $\sim 45^\circ$ using special UV and IR filters to observe the melt pool, plasma plume and spattering. All welds were made perpendicular to the rolling direction of the steel. A high-pressure air knife was used during laser welding, which directed a stream of clean, dry air towards the weld zone to suppress the plasma plume and remove any residual gases or impurities that may be present on the surface of the material or in the surrounding atmosphere, creating a clean and stable environment for the laser beam to operate. No shielding gas was used during laser welding.

Table 5: Details of the laser welding machine and process setup.

Laser Type	Make	Model	Focal Length (mm)	Beam Spot Size, \varnothing (mm)	Laser Impingement Angle, θ	Laser Defocus (mm)
Ytterbium Laser System	IPG Photonics	YLS-6000-S2	200	0.35	+ 20°	Variable

3.5 Optimizing the laser welding process

Due to the fully martensitic nature of the BM in the hot-stamped (HS) condition, the mechanical properties of the welded joints are known to be highly sensitive to defects like concavity or undercut in the FZ. To minimize the formation of welding defects while keeping the processing parameters constant (i.e., constant TS and P), the laser was defocused, and the laser impingement angle was modified. Two detailed numerical models were constructed which were experimentally validated to understand the effect of laser impingement angle [61,62] and laser defocusing [63] on the optimization of the laser welding process.

3.5.1 Effect of laser impingement angle on process optimization

Three different beam impingement angles (BIAs) were used as part of this study (i.e., leading, trailing, and perpendicular) as shown in Figure 26 [61]. The welding conditions for all three cases were identical with a laser power of 4 kW and a welding speed of 14 m/min. The laser head was tilted at an angle of 20° to either side of the normal as shown in Figure 26 (a and c), referred to as the trailing beam configuration (TBC) and the leading beam configuration (LBC), respectively. The perpendicular beam configuration (PBC), where the beam was kept perfectly perpendicular to the workpiece, is shown in Figure 26 (b) and this was used as the base configuration to which the other two configurations were compared. In OKM laser welding, the presence of the keyhole acts as an effective blackbody for the laser radiation, minimizing the effect of reflections that may damage the components in the laser head, eliminating the need to introduce a small tilt angle (i.e., < 5°) during experimentation.

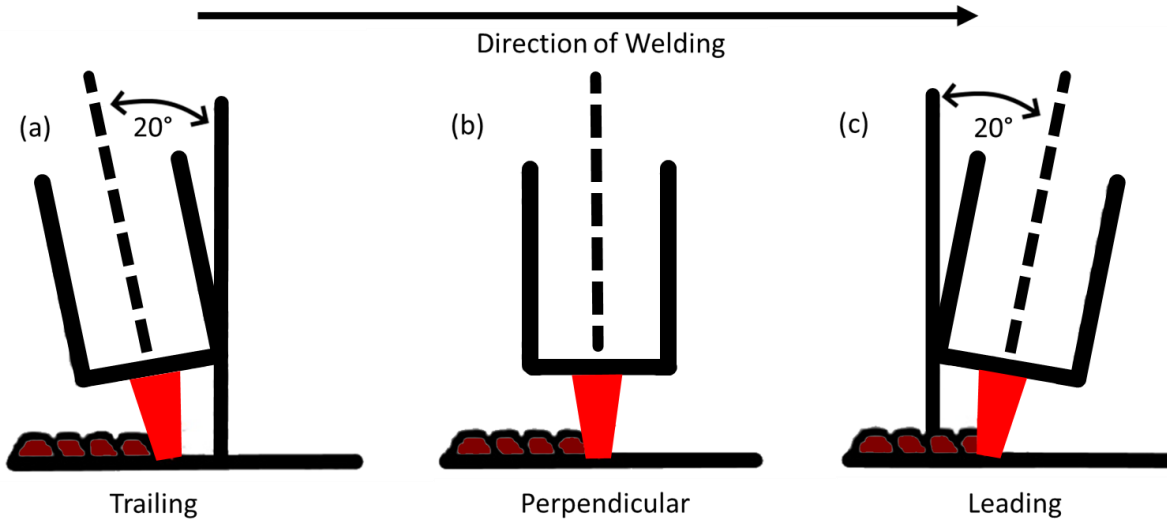


Figure 26: Schematic showing the (a) trailing, (b) perpendicular, and (c) leading beam configuration. The laser head was tilted at an angle of 20° in the trailing (i.e., negative 20°) and leading (i.e., positive 20°) beam configurations, respectively.

3.5.1.1 Finite element modelling

Finite element (FE) analysis was used to investigate the influence of changing the laser BIA on the melt pool geometry during the laser welding process. COMSOL Multiphysics[®] was used to develop a 3D thermal model that captured the effect of tilting the laser beam. To minimize the computational time required to run the simulation, a small-scale domain geometry was modeled as shown in Figure 27 (a). A uniform cuboid mesh was created for the geometry domain with an extremely fine mesh ($50\ \mu\text{m}$ in size) being used adjacent to the direction of laser movement with a coarser mesh being employed in other areas to improve the accuracy of the simulation while simultaneously decreasing computational time. The model geometry domain was created as a replica of the $1.2\ \text{mm}$ thick BM used in this study, with a $15\ \mu\text{m}$ thick GA coating on the BM surface, as shown by the inset in Figure 27 (a). To investigate the effect of changing the laser impingement angle on the predicted melt pool geometry, the 3D model domain was tilted 20° to the left and right of the perpendicular to simulate the effect of an angled laser beam in the TBC and LBC, as shown in Figure 27 (b) and (c), respectively. To avoid laser defocusing when the heat source moved in the x-direction (longitudinally) during the tilted-case simulation, the laser intensity equation was adjusted temporally to account for the increment or decrement in the z-direction relative to the total height and the tilt angle of the geometry domain. The well-known 3D conical Gaussian (CG) volumetric heat source [133–136] developed for laser welding applications was used for this study to predict the melt pool geometry, and the cross-sectional FZ boundary was validated using the experimental results. Two CG heat sources were incorporated together into a double-conical Gaussian (DCG) heat source, as shown in Figure 27 (d & e), to obtain a more continuous and smoother temperature distribution and melt pool geometry.

The thermo-physical properties of the Zn-coated DP980 grade steel (including thermal conductivity, specific heat, and density) were taken from the Material Database in the commercially available SORPAS[®] welding simulation software. To minimize the computational time required to run the simulations, the following assumptions were made regarding the numerical model:

- Material properties are considered to be isotropic and homogenous except for the thermal conductivity.
- Thermophysical properties are dependent on temperature via interpolation using the anisotropically enhanced thermal conductivity approach proposed by Kamara et al. [137].
- The Gaussian conical heat source moves at a constant speed relative to the time steps and the total geometry height in the x and z-directions.
- The proposed liquid flow in the molten weld pool was based on the CFD models presented by Courtois et al. [138].
- Surface effects (including surface tension), shielding gas pressure, vaporization and plume pressure effects were excluded from the FE model.

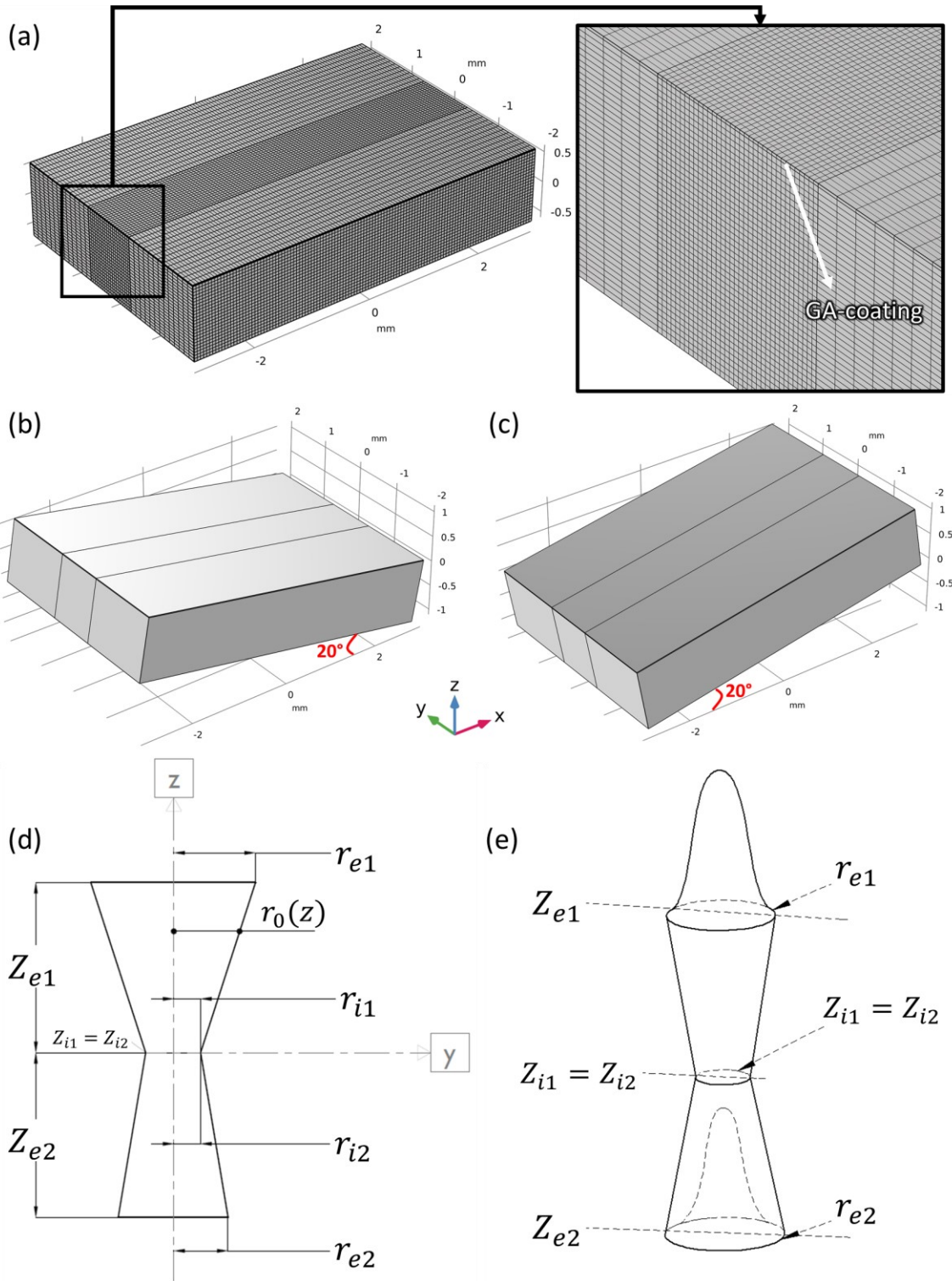


Figure 27: (a) Model geometry domain with the inset showing ultra-fine meshing along the direction of motion of the moving DCG heat source with a coarse mesh in the surrounding area. The combination of mesh sizes shown here reduced the overall computational time needed for the simulation. (b) and (c) show the model geometry being tilted 20° to the left and right of the perpendicular to replicate the effect of tilting the laser heat source in the TBC and LBC, respectively. (d) and (e) show the 2D and 3D schematic of the DCG heat source, respectively, clearly identifying the different variables used in developing the model.

The governing equation regarding the conservation of energy was given by [139]:

$$\rho c_p \left(\frac{\delta T}{\delta t} \right) + \rho c_p u \cdot \nabla T = \vec{\nabla} \cdot (k \vec{\nabla} T) + Q_{laser} \quad (3)$$

where T is the temperature (K), t is time (s), ρ is the density (kg/m³), c_p is the specific heat capacity at constant pressure, u is the velocity field defined by translational motion (assumed to be 0 in this study), k is the thermal conductivity and Q_{laser} is the energy heat source represented by the laser.

Convective heat transfer was based on Newton's law and was considered on all open surfaces, expressed as:

$$q_c = h_c(T_{ext} - T) \quad (4)$$

where q_c [W/m²] is the convective heat loss, h_c [W/m² K] is the convective heat transfer coefficient, T_{ext} [K] is the surface temperature of the model geometry, and T is the ambient temperature taken to be 293 K.

The radiative heat loss from each surface of the geometrical domain was obtained using:

$$q_r = \sigma_{sb} \varepsilon (T_{ext}^4 - T^4) \quad (5)$$

where, σ_{sb} [W/m² K⁴] is the Stefan-Boltzmann constant and ε is the emissivity.

The intensity of heat for the top cone of the 3D CG model, as shown schematically in Figure 27 (d) and (e), was expressed mathematical as [140]:

$$I_{top}(x, y, z, t) = q_0 \cdot \exp\left(-2 \frac{(x + x_t)^2 + y^2}{r_0^2}\right) \quad (6)$$

$$r_0(z) = r_{e1} + \frac{z + z_t}{h} (r_{e1} - r_{i1}) \quad (7)$$

$$h = Z_{e1} - Z_{i1} \quad (8)$$

$$x_t = v \cdot \delta t \quad (9)$$

$$z_t = v_z \cdot \delta t = \frac{L \cdot \sin(\theta_{tilt})}{t_{total}} \cdot \delta t \quad (10)$$

where, q_0 is the maximum heat intensity, r_{e1} and r_{i1} are the cone radii for the top and bottom of the top CG heat source profile, h represents the height of the top 3D CG heat source, δt is the step-time v is the welding speed, L is the length of the geometry, θ_{tilt} is the angle of tilt (corresponding to 0° in the PBC case), and t_{total} is the total time. As the value of z increases,

the amplitude of the volumetric heat source decreases. The heat intensity profile for the bottom cone was calculated similarly, as explained in detail elsewhere [63].

The equation for the total energy of the laser was expressed as [141]:

$$Q_{laser} = \int_h^0 \int_{-\infty}^{+\infty} \int_{-\infty}^{+\infty} q_0 \cdot \exp\left(-2 \frac{x^2 + y^2}{r_0^2}\right) dx dy dz \quad (11)$$

where, Q_{laser} is the total energy delivered by the laser [J], and q_0 is the maximum value for the heat intensity, given by:

$$q_0 = \frac{2\alpha P}{V_{cone}} = \frac{6\alpha P}{\pi(h)(r_{e1}^2 + r_{e1}r_{i1} + r_{i1}^2)} \quad (12)$$

Table 6 shows the identified parameters for each laser beam configuration. The center radius of the DCG heat source in the TBC and LBC was estimated using Snell's law to account for the effect of beam tilt. Figure 27 (d) and (e) show the complete schematic of the 2D and 3D DCG heat source explaining all the parameters. Additionally, the volume of the predicted melt pool for the different beam configurations was evaluated using the volume integration of the material at the temperature greater than or equal to the isothermal temperature at every time step. The isothermal contour for the melt pool boundary was selected to be 1506 °C (1780 K). At the welding speed of 14 m/min, full maturity of the melt pool in the FE simulation was achieved at a distance of about 2.8 mm from the starting edge of the model domain which was an excellent match with the experimental results. As such, all the results, including the calculation of the melt pool volume, extraction of the isothermal contour showing the melt pool geometry, and the predicted FZ geometry were taken when the heat source was 2.8 mm from the starting edge of the model domain.

Table 6: Identified heat source parameters for different laser welding condition

Configuration	Z_{e1} (mm)	Z_{i1} / Z_{i2} (mm)	Z_{e2} (mm)	r_{e1} (mm)	r_{i1} / r_{i2} (mm)	r_{e2} (mm)
TBC	0.615	0	-0.6	0.35	fn. of tilt angle	0.21
PBC	0.615	0	-0.6	0.35	0.2	0.31
LBC	0.615	0	-0.6	0.35	fn. of tilt angle	0.26

3.5.1.2 Perpendicular beam configuration

The welding process was first observed in the PBC as this is the most common setup used in industrial LW applications. Several still frames from the video recording of the welding process in sequential order are shown in Figure 28. The images clearly show some spattering (Figure 28 (a) and (f)) and the weld seam was pronounced by elevated “weld banks” suggestive of material being removed from the molten weld pool and being deposited at the seams as recast material. The loss of material from the molten weld pool generally leads to the formation of defects such as concavity and undercut leading to an undesirable weld geometry.

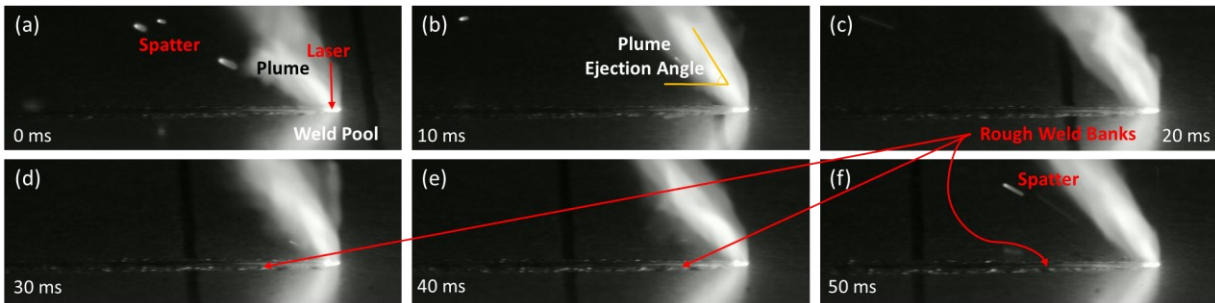


Figure 28: Still images of the welding process in the PBC showing rough weld banks indicative of molten material being pushed out of the weld pool leading to observable undercut and elevated weld banks. The plume ejection angle was clearly visible which is known to get smaller as the welding speed increases which causes humping to be observed on the weld surface.

Using laser-assisted 3D profilometry, the top and bottom surfaces of the weld were analyzed, and a 3D surface profile was generated as shown in Figure 29. The 3D figures helped visualize the surface quality of the weld and they made it clear that there was considerable undercut observed at the weld boundaries – although, as shown in Figure 29 (b), the undercut was much more significant at the bottom surface where its maximum depth was measured at approximately 120 μm compared to the top (Figure 29 (a)) where the maximum depth was measured at about 60 μm . The 3D surface profiles also confirmed the presence of elevated or rough weld banks which helped explain the presence of the undercut observed at the boundaries. The impact and extent of the surface defects was more clearly observable by looking at the 2D height map of the surface profile shown in Figure 29. The height maps showed that even though the undercut was less severe at the top surface (Figure 29 (c)), it was consistent and ran along the boundary of the entire length of the weld bead. On the other hand, the height map also showed that even though the depth of undercut was much larger at the bottom surface, the defect was cyclic in nature occurring at periodic intervals along the weld boundary.

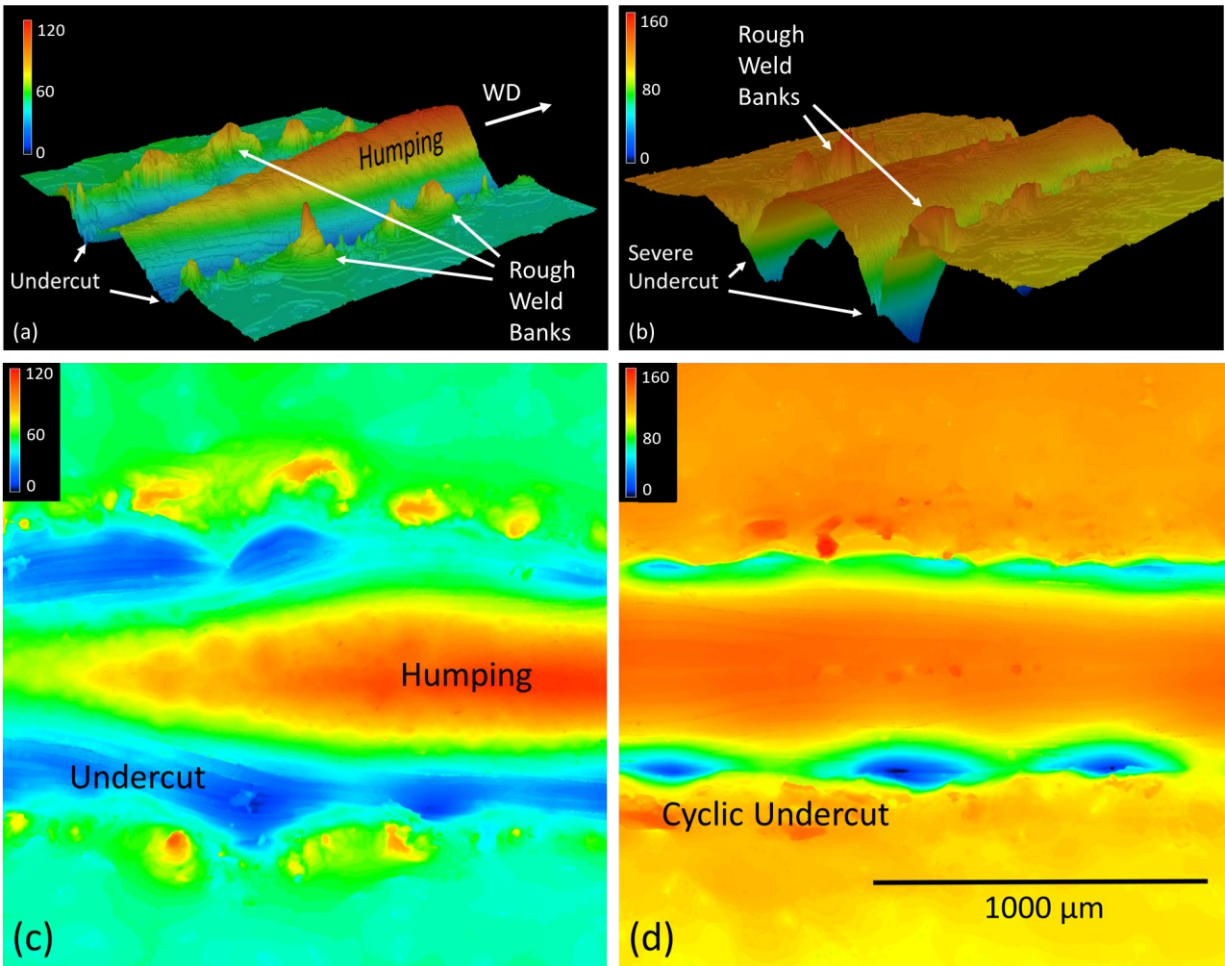


Figure 29: 3D laser profile of the (a) top and (b) bottom surfaces of the weld in the PBC showing elevated or rough weld banks that form as a result of the deposition of some molten material from the weld pool. This loss of material leads to the observable undercut at the top and bottom surfaces; although the depth of the defect is almost double at the bottom surface ($\approx 120 \mu\text{m}$) compared to the top ($\approx 60 \mu\text{m}$). 2D height maps of the (c) top and (d) bottom surfaces of the weld in the PBC showing elevated weld banks caused by the deposition of molten material at the weld seam leading to considerable undercut at both the surfaces. Although the depth of the defect was much larger at the bottom surface, the defect was not consistent and appeared to be cyclic in nature. The undercut was not as severe at the top surface but presented itself as a consistent feature of the surface profile and weld geometry. Color scale bars have a unit of μm . (WD: Welding Direction)

The cross-section of the weld, shown in Figure 30 (b), had an X-shaped geometry which is characteristic of a fully focused laser beam that has the focal point somewhere in the middle of the sheet thickness creating a keyhole that resembles the shape of a catenoid. In OKM, the vapor column extends through the sheet thickness because of the recoil pressure generated by the vaporized metal in the keyhole that actively escapes from the top and bottom surfaces of the keyhole as the laser moves forward, vaporizing newer material. The vaporized material in the keyhole continues to be heated by the laser beam which creates a plasma that accelerates towards either surface as it gets hotter and with more material being vaporized, the plasma begins to pressurize as it exits through the two ends of the keyhole causing it to become wider compared to the center, giving the weld its characteristic X-shaped weld geometry [63]. The heat-affected zone

(HAZ) was found to be the largest for this sample, almost having a barrel-like appearance with the widest region being at the center of the weld, measuring at around 235 μm . This is typical for X-shaped laser welds that are narrower at the center of the fusion zone FZ which also happens to be the hottest part of the weld causing the HAZ to be larger at this location [63]. Furthermore, the X-shaped weld cross-section also confirmed the presence of undercut at the top and bottom surfaces of the weld. The volume of the melt pool, as predicted by the numerical model, was the largest for the PBC being calculated at 0.197 mm^3 , as shown in Figure 31 (b).

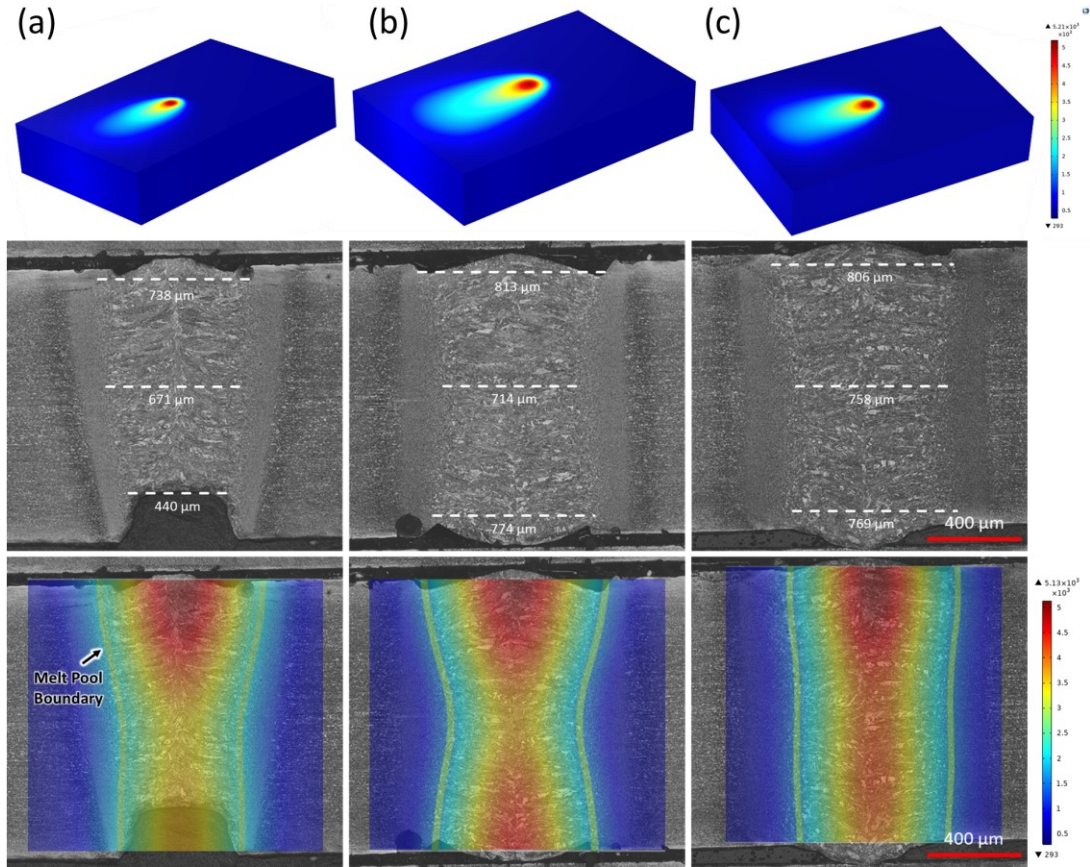


Figure 30: Isometric view of the heat distribution profile on the surface of the 3D geometry domain along with the optical micrographs of the respective cross-section of the welds in the (a) TBC, the (b) PBC, and the (c) LBC. The green boundary line in the overlay images show that there is an excellent match between the fusion boundary location predicted by the FE model compared to the actual weld cross-sections ensuring that the resulting melt pool geometry predicted by the FE model would give an accurate representation of how the change in melt pool shape and size controlled the volatility in the process that led to defects.

Another clearly observable phenomenon was the humping that was seen at the top surface in Figure 29 (a) and (c). Humping is commonly observed in high-speed LW applications due to the angle at which the plume is ejected from the keyhole, which becomes smaller as the travel speed increases [60], as shown in Figure 28 (b). This is inherently due to the fact that at high welding speeds the bottom of the keyhole usually lags behind the top of the keyhole which changes the shape of the keyhole by adding a trailing curvature to the catenoid [142,143]. The angle of

plasma ejection follows this curvature so as the welding speed increases, the curvature of the keyhole increases which in turn increases the angle at which the plasma is ejected. Since the fluid flow around the keyhole is driven primarily by the Marangoni effect [25,32] which is dependent on the surface tension between the phases and (as with any other type of convective flow) is driven by the temperature differential between one part of the fluid relative to the other [119], it can be said that the larger the shape distortion of the keyhole, the smaller the angle of plasma ejection, and the larger the magnitude of the displacement of the molten fluid surrounding the keyhole opening which is forced to flow to the rear of the molten weld pool at a higher velocity [60]. This also creates an x-shaped molten weld pool, as shown in Figure 31 (b), which causes two distinct and opposing Marangoni-driven flows to exist which causes turbulence in the weld pool. Furthermore, the tilt angle of the plasma plume caused the formation of a wave in the molten weld pool as the high velocity fluid being pushed outward and away from the keyhole wall collides with the back flow as shown in Figure 31 (b). Due to the extremely high cooling rate during LW of thin sheet steels [25], the molten pool solidifies quickly and the weld bead has a wave-like surface profile commonly referred to as humping. The cyclic formation of humps on the top surface means that there is less material available at the bottom surface which would explain the more severe cyclic undercut that was observed at the bottom surface of the weld in the PBC as shown in Figure 29 (b).

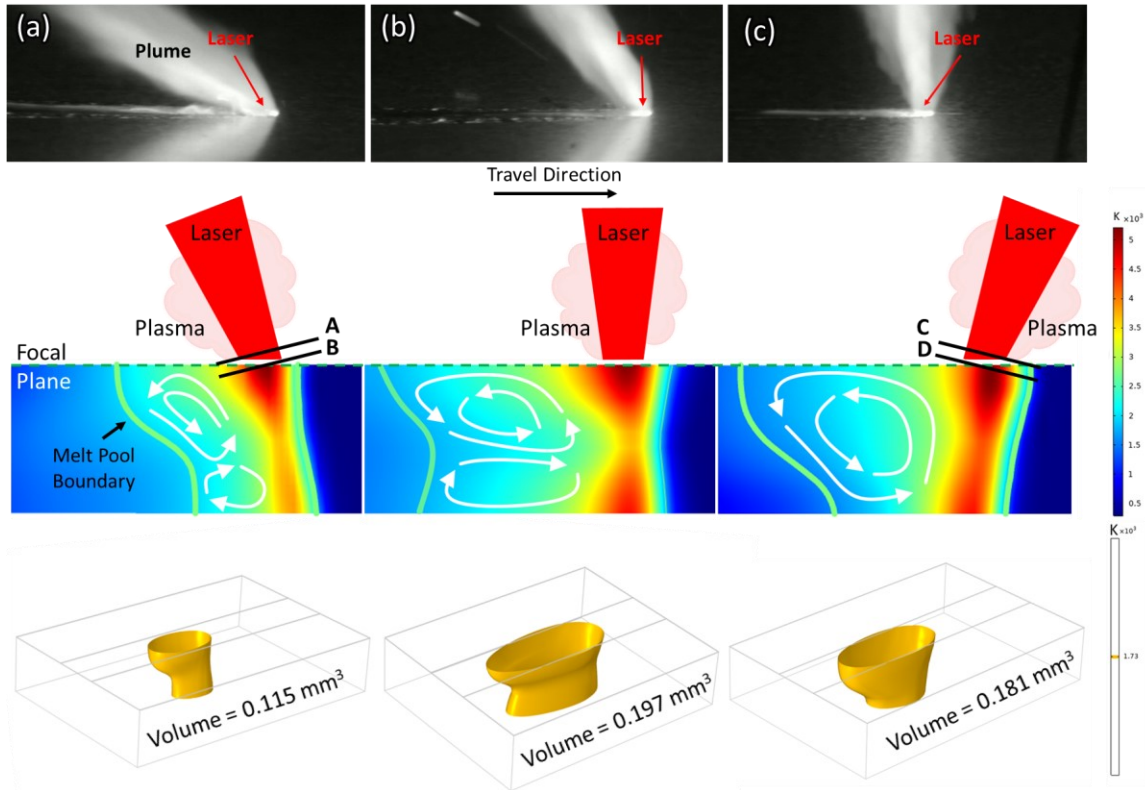


Figure 31: Respective still images of the LW process with images of the longitudinal cross-section of the temperature distribution along with the isothermal view of the molten weld pool boundary in the (a) TBC, (b) PBC, and (c) LBC. The green lines indicate the predicted boundary of the melt pool and the schematic arrows show the predicted flow fields generated in the melt pool based on the CFD model developed by Courtois et al. [138,144]. It can be seen clearly in (a) and (b) that due to the shape, size and temperature of the keyhole combined with the geometry of the molten weld pool, specifically the large convex bend at the back wall, two distinct flows develop in the molten pool leading to the violent turbulence observed in Figure 28 and Figure 32. As the laser beam impingement angle changes to $+20^\circ$ (i.e., the LBC) as shown in (c), the keyhole shape changes which changes the temperature profile and the resulting melt pool geometry, stabilizing the molten liquid flow as shown in Figure 35.

3.5.1.3 Trailing beam configuration

For the second case analyzed as part of this study, the BIA of the laser was set to negative 20° from the normal (Figure 26 (a)) and the welding process was observed in the TBC with several still frames in sequence shown in Figure 32. The plasma plume ejection angle was smaller (Figure 32 (b)) compared to the plume angle observed in the PBC, which led to increased turbulence in the molten weld pool, causing the ejection of material in the form of spatter (Figure 32 (c-f)) and severe humping in the weld bead. Lin et al. showed that for a backward tilting keyhole, similar to what is shown in Figure 31 (a), the excessive weld pool volatility was attributed to the cyclic collapse of the molten material located at the front wall of the keyhole [145], which led to erratic fluid flow and severe turbulence in the melt pool. This problem was compounded by the fact that the angle at which the plasma was ejected from the keyhole (Figure 32 (b)) was smaller than what was observed in the PBC, exacerbating the cyclic, wave-like motion of the molten liquid with clearly visible valleys and peaks trailing the keyhole as seen in the welding video. This volatility led to significant loss of molten material from the top and bottom surfaces of the weld in the form

of excessive spattering from the top and material ejection from the bottom as confirmed by the weld cross-section in Figure 30 (a).

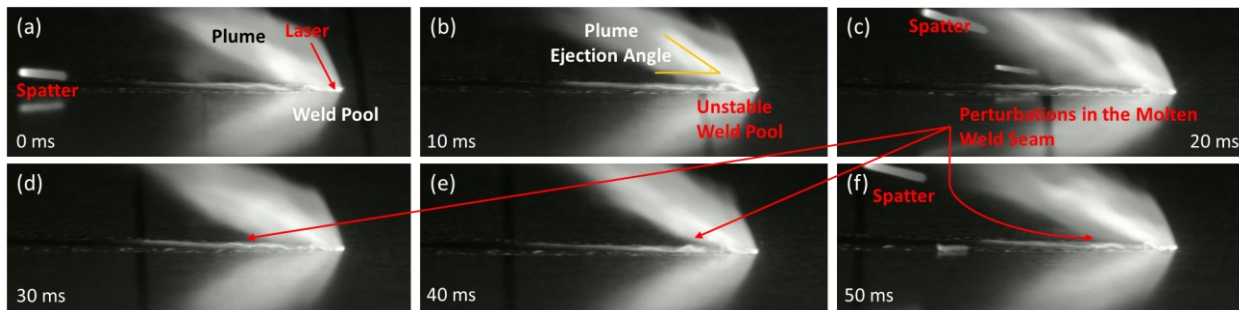


Figure 32: Still images of the welding process using the TBC showing an unstable weld pool leading to perturbations in the molten weld seam and significant spattering which causes defects such as weld humping and high concavity.

Furthermore, in the TBC, the backward tilt of the laser relative to the direction of motion changed the shape of the beam spot from circular to elliptical which caused an uneven delivery of power to the workpiece with less power being delivered to the back of the keyhole and more power being delivered to the front. By observing the location of the transverse planes along the beam focus (planes A and B shown in Figure 31 (a)), it was clear that the focal point of the beam was inside the keyhole and the point of interaction at the back of the keyhole was closer to the laser which meant that the intensity at that point was less than that at the leading edge. In other words, the intensity in plane A was less than that in plane B, causing a shrinkage in the size of the melt pool as there was less heat delivered to the back wall of the keyhole which decreased the overall temperature of the system. This resulting in a decrease in the total volume of the molten liquid present in the weld pool, as confirmed by the weld pool volume predicted by the FE model shown in Figure 31 (a). The smaller volume of molten liquid available and the angled keyhole caused the fluid to flow violently from around the front wall of the keyhole towards the back which led to severe turbulence in the melt pool causing visible humping as observed in Figure 32.

Due to the elliptical shape of the beam spot which delivered less power to the trailing end of the keyhole at the top surface, which decreased the size of the melt pool combined with the presence of the angled keyhole decreased the length of the plasma column, causing the plasma to overheat which inadvertently reduced the heat input into the weld [63] as less power was delivered to the bottom surface, which consequently caused the melt pool to be smaller (0.115 mm^3) with a V-shaped weld geometry, as shown by the weld cross-section in Figure 30 (a). Since the keyhole was highly distorted for the TBC relative to the PBC, it caused the rapid movement of molten liquid upward and outward along the back wall of the keyhole as shown by the schematic in Figure 31 (a), which led to severe turbulence in the weld pool as observed in Figure 32. The instability in the molten weld pool led to significant loss of material which caused observable FZ concavity as shown by the 3D surface profile of the top and bottom of the weld surface in Figure 33 (a) and (b),

respectively. It was also observed that the HAZ was the narrowest for the TBC mostly due to the fact that a significant amount of energy available from the laser was wasted due to the excessive heating of the plasma plume and the large volume of molten material that was ejected away as spatter. The 3D surface profiles clearly showed significant loss of material from the weld zone, with the concavity in the top surface measuring at around 150 μm (12.5% of the sheet thickness) while much more severe concavity was observed in the bottom surface measuring at around 300 μm (25% of the sheet thickness).

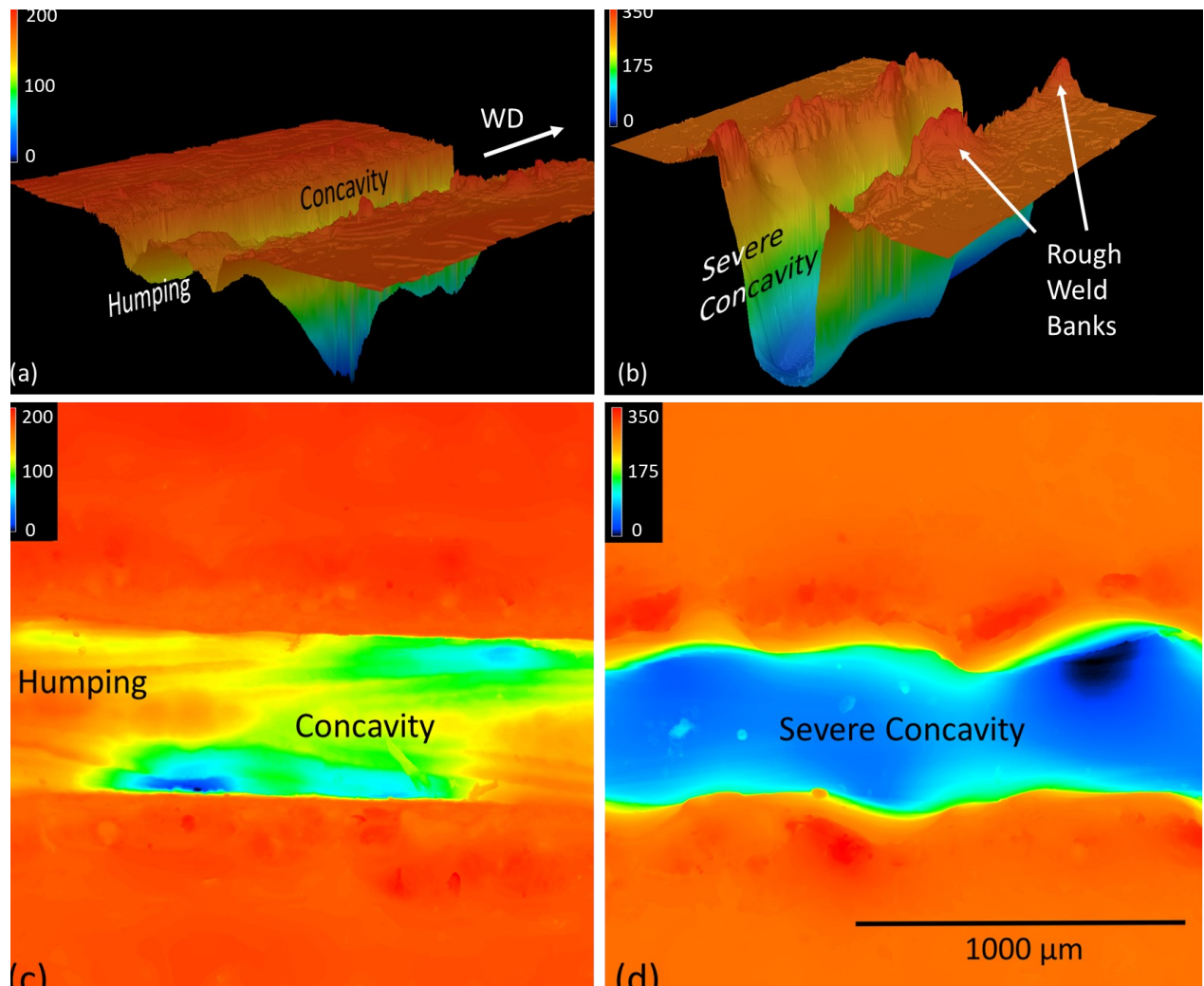


Figure 33: 3D laser profile of the (a) top and (b) bottom surfaces of the weld in the TBC showing severe concavity and loss of material from within the weld seam. The loss of material was attributed to the high level of spattering observed during the welding process which could be a result of the serious turbulence and humping phenomenon observed in the molten weld pool that was captured using the welding camera. The concavity was much more severe at the bottom surface ($\approx 300 \mu\text{m}$) compared to the top surface ($150 \mu\text{m}$). 2D height maps of the (a) top and (b) bottom surfaces of the weld in the TBC showing the severe loss of material from the weld seam. Color scale bars have a unit of μm . (WD: Welding Direction)

The 2D height maps for the top and bottom surfaces shown in Figure 33 (c) and (d), respectively, confirmed the loss of material observed using the 3D surface profiles, while making it easy to observe the cyclic nature of the fluid flow by clearly showing that the humping phenomenon was also observed when welding in the TBC – although the concavity defects were much more severe. The humping phenomenon was caused by a combination of the backward tilting angle of the keyhole (Figure 31 (a)) and the angle of ejection of the plasma plume (Figure 32 (b)), which resulted in the cyclic humping of the molten fluid as was observed during the welding process. The severe concavity was a consequence of the relatively smaller size of the melt pool, while the turbulent fluid flow was a direct result of the backward tilted keyhole which caused

the ejection of molten material which further reduced the amount of molten material available in the weld bead. Figure 34 (a) and (b) shows the cross-sectional profile of the top and bottom surface of the weld in the TBC superimposed on the cross-section of the weld in the PBC configuration, respectively. The yellow-colored line traces the profile of the weld in the TBC while the red-colored line traces the profile of the weld in the PBC. Figure 34 clearly shows that the weld geometry in the TBC is significantly worse compared to the PBC with the red regions highlighting how much material is missing from the weld zone in the TBC relative to the PBC.

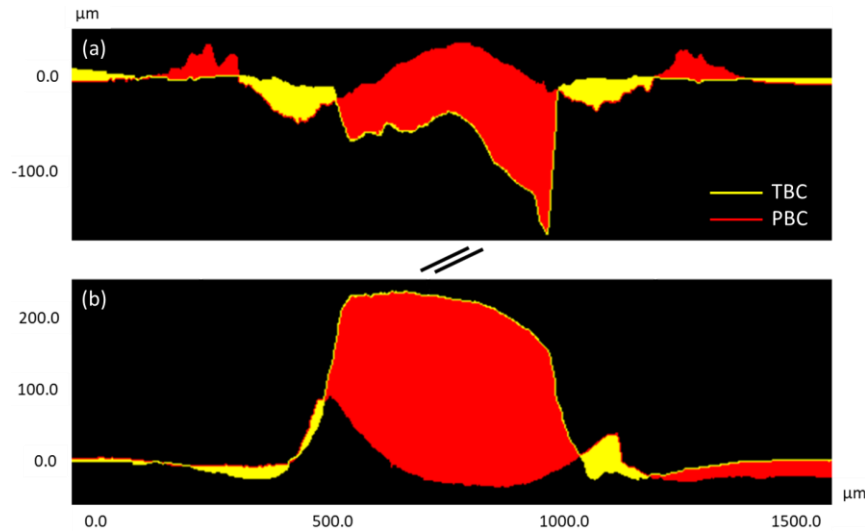


Figure 34: Comparison of the cross-section of the weld profiles made in the trailing (shown by the yellow line) and perpendicular beam (shown by the red line) configurations for the (a) top and (b) bottom surfaces. The red region highlights the material that is missing the TBC compared to the PBC which clearly shows the severe concavity observed when welding in the TBC. The yellow region shows the material that is present in the welds made in the TBC and missing in the PBC; it is clear to see that no undercut is present in the TBC, but it is a serious problem in the PBC.

3.5.1.4 Leading beam configuration

The third case that was analyzed as part of this study was the LBC where the BIA was set to positive 20° from the normal (Figure 26 (c)). Welding in the LBC displayed the most stable welding process as shown by several still frames in sequence in Figure 35. There was no observable spattering, humping or weld pool instability. The 3D surface profile of the top and bottom surface of the weld showed that the weld profile was slightly convex with no observable surface defects as shown in Figure 36 (a) and (b), respectively. The improved weld geometry for the LBC can be seen clearly in the micrograph of the FZ cross-section as shown in Figure 30 (c).

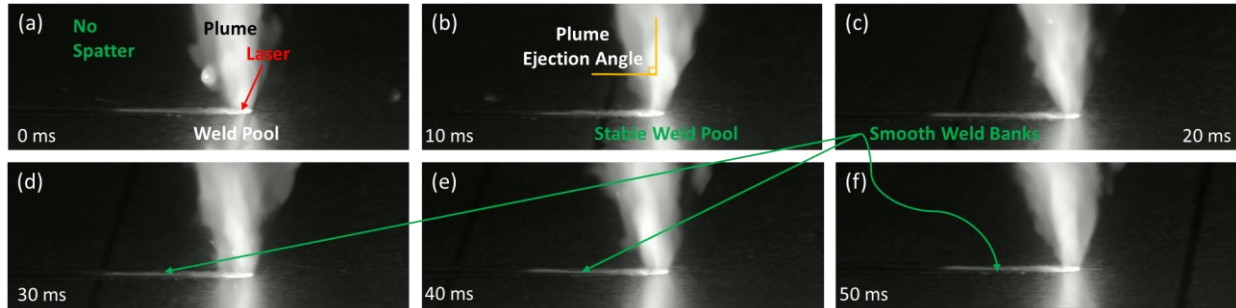


Figure 35: Still images of the welding process using the LBC showing a very stable weld pool with almost no visible perturbations in the molten weld seam.

The reason for the improved weld pool stability and the convex profile of the weld was a direct consequence of the BIA and the resulting forward tilting keyhole as shown in Figure 31 (c). The BIA changed the beam spot shape from circular to elliptical which changed the delivery of power to the workpiece as shown by the transverse planes C and D in Figure 31 along the beam focus. In this case, the point of interaction at the front of the keyhole was closer to the laser, which meant that the intensity at this point was less than that at the trailing edge – i.e., higher power was delivered to the back of the keyhole and lower power was delivered to the front. This change in the delivery of power, and the resulting orientation of the keyhole, ensured that the size of the molten weld pool increased but its geometry changed from an X-shape that was previously observed to a Y-shape, as shown in Figure 31 (c). In fact, the predicted volume of the molten weld pool was around 0.181 mm^3 for the LBC, which was significantly higher than 0.115 mm^3 for the TBC, and slightly less than the volume predicted for the PBC. It was observed that the HAZ for the weld made using the LBC was relatively narrower compared to the PBC because the energy available from the laser was being used more effectively due to the nature in which power was being delivered to the workpiece.

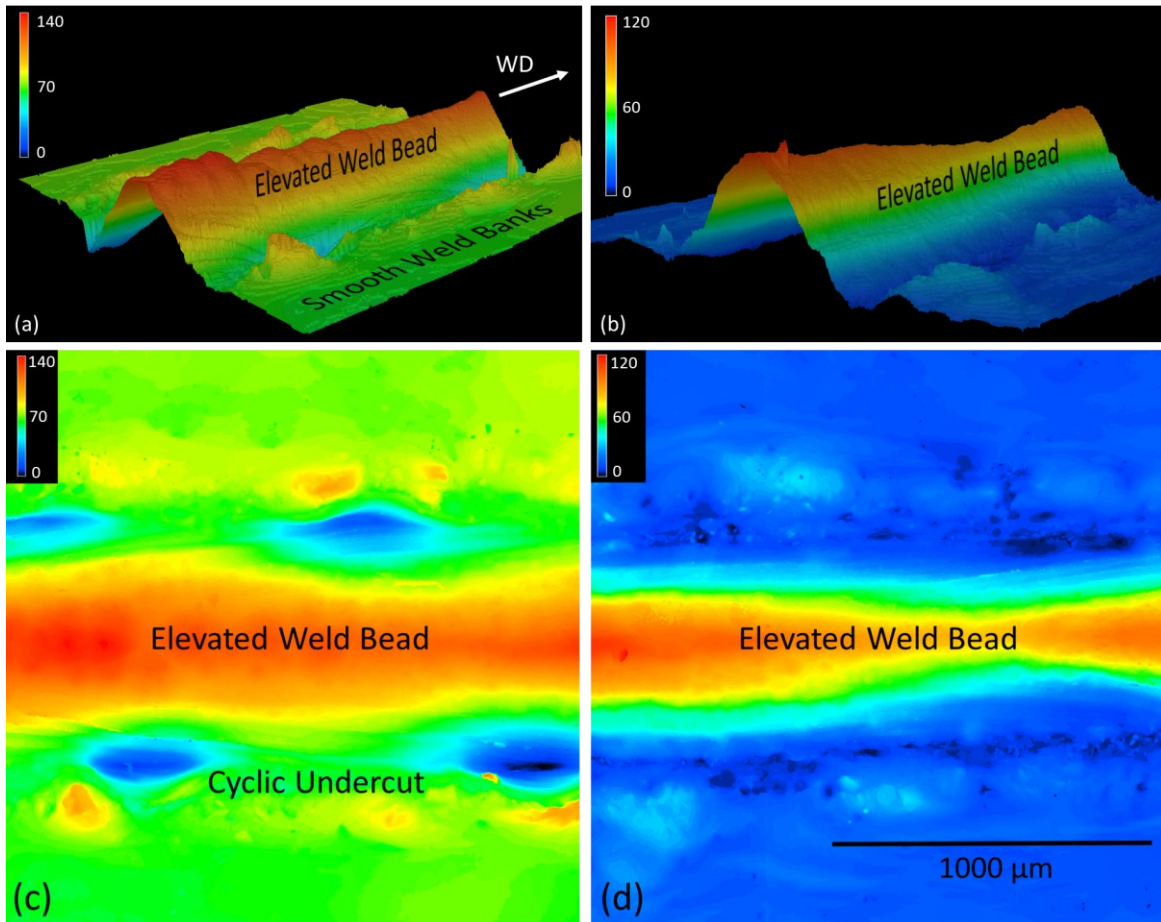


Figure 36: 3D laser profile of the (a) top and (b) bottom surfaces of the weld in the LBC showing a weld profile that is free of any serious concavity or undercut defects. In fact, the 3D profiles of the weld suggest that the fluid flow generated in this beam configuration is such that more molten material is deposited and retained in the molten weld seam which causes the weld bead to have a convex profile at the top and bottom surfaces. Despite this accumulation of excess material in the weld bead, very minimal undercut was observed at the top surface ($< 30 \mu\text{m}$) and no undercut was observed at the bottom. 2D height maps of the (c) top and (d) bottom surfaces of the weld in the LBC showing the elevated weld beads with some cyclic undercut at the top surface and no surface defects at the bottom surface. Color scale bars have a unit of μm . (WD: Welding Direction)

The forward tilting keyhole stabilized the fluid flow at the back wall by reducing the angle at which the molten fluid rose towards the surface. This change in the orientation of the keyhole was confirmed by the much larger angle of plasma ejection (essentially perpendicular to the workpiece) observed in the welding videos, as shown in Figure 35 (b). It was also important to note that the humping phenomenon was not observed in the LBC as it was in the other cases. Since it has been shown that the frequency and amplitude of humping is directly related to the plasma ejection angle [60], which in this case was much greater than the other two cases, resulting in the complete elimination of any humping in the weld profile. The result of these changes to the beam profile and the shape and size of the melt pool was that the liquid flow in the weld was much more stable when compared to the TBC and the PBC. As the molten liquid flowed from the front of the weld pool towards the back, there was a larger volume of molten material available in a less

turbulent weld pool which quickly solidified, leading to a convex weld profile at the top and bottom surface as shown by the 2D height maps in Figure 36. Figure 37 (a) and (b) show the cross-section of the top and bottom surface profiles of the weld in the LBC superimposed on the cross-section of the weld in the PBC configuration, respectively. The yellow-colored line traces the profile of the weld in the LBC while the red-colored line traces the profile of the weld in the PBC. The yellow region shows the convex profile of the weld in the LBC relative to the PBC and it is clear to see from the cross-sections that the weld geometry was significantly improved, with the severe undercut observed in the PBC being completely eliminated from the weld profile in the LBC.

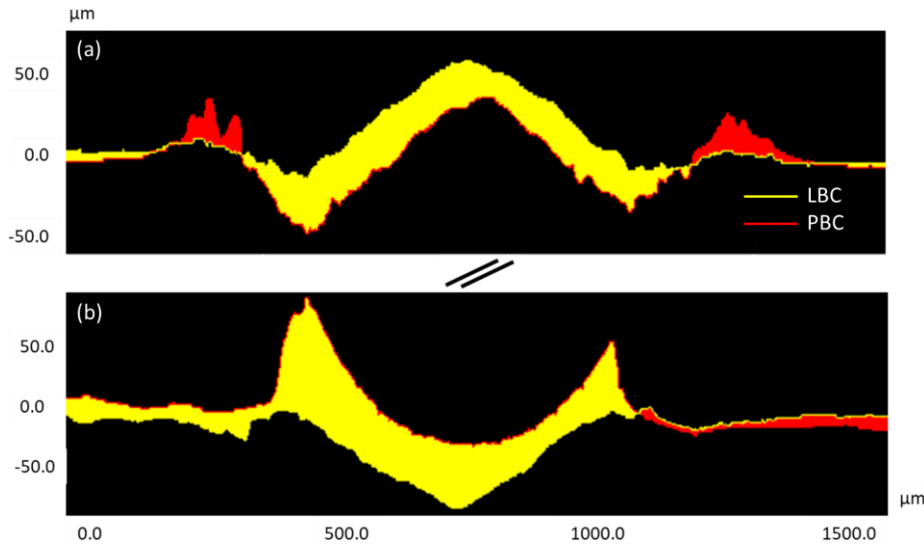


Figure 37: Comparison of the cross-section of the weld surface profiles made in the leading (shown by the yellow line) and perpendicular beam (shown by the red line) configurations for the (a) top and (b) bottom surfaces. The yellow region shows the material that is present in the weld seam for the LBC compared the material that is missing in the PBC. The severe undercut that was observed in the PBC was entirely mitigated when welding in the LBC. The red region in (a) shows the elevated weld banks in the PBC that were not present when welding in the LBC.

3.5.1.5 Conclusions

This study investigated the effect of the beam impingement angle during open keyhole mode, high-speed laser welding of thin-gauge AHSSs on the process stability and the resulting weld geometry using numerical modelling and experimental observations. Three different beam impingement angles were analyzed as part of this study: perpendicular, negative 20° from the normal (referred to as the trailing beam configuration), and positive 20° from the normal (referred to as the leading beam configuration). The following conclusions can be made from the study:

1. The process was observed to be the most stable when a beam impingement angle of positive 20° (i.e., LBC) was used with no turbulence in the molten weld pool, no observable spattering, no humping, and a stable plasma plume. On the other hand, the beam impingement angle of negative 20° (i.e., TBC) was the most unstable with severe turbulence in the molten weld pool, significant spattering and humping and an unstable plasma plume.

2. The weld geometry was the worst when a beam impingement angle of negative 20° was used, giving a V-shaped FZ, with severe concavity being observed in both the top and bottom surface as well as humping being observed in the top surface.
3. The weld geometry improved significantly when the beam impingement angle was set perpendicular to the workpiece (i.e., PBC), giving an X-shaped FZ, with minimal humping and mild undercut being observed in the top surface and severe but cyclic undercut being observed at the bottom surface.
4. The weld geometry was the best when the beam impingement angle was set to positive 20° with no defects being observed at either the top or the bottom surface of the weld. The FZ had a Y-shaped profile indicating that the energy available from the laser was being most effectively used.
5. The increase in process stability when welding in the LBC was attributed to several reasons: the change in the shape of the beam spot that is caused by changing the beam impingement angle, the tilt angle of the keyhole relative to the direction of welding, the plasma plume ejection angle, the shape, size and orientation of the molten weld pool, and the resulting changes in the fluid flow caused by the combination of the listed factors.

In conclusion, it is recommended that for high-speed laser welding applications, the BIA should be considered as a parameter of consequence and should be optimized to ensure better process stability and improved weld geometry.

3.5.2 Effect of laser beam defocusing on process optimization

To investigate the effect of laser defocusing on keyhole stability, weld pool volatility, and the resulting FZ geometry, a set of BOP welds were made by defocusing the laser beam by moving the laser head towards the sheet surface (i.e., negative defocusing) from the fully focused condition. The open keyhole mode (OKM) laser welding process is shown in Figure 38 (a). A schematic of the weld pool cross-section and the associated liquid flow in the weld pool is shown for the fully focused and defocused condition in Figure 38 (b) and (c), respectively. No shielding gas was used during welding. Full penetration welds were obtained in the fully focused condition with a beam spot size of 0.3 mm, while welding in the fully defocused condition with a beam spot size of 0.5 mm yielded partial penetration welds. To observe the material-laser interaction, the welding process was recorded from the side at a speed of 90 fps using an XIRIS XVC-1000 welding camera equipped with UV and IR filters. This camera observed the melt pool and plasma plume at an angle of $\sim 45^\circ$. Still images from the videos showing a few representative frames are presented to show differences in process stability with and without laser defocusing. Weld cross-sections were prepared using standard metallography techniques for grinding, polishing, and etching the specimen to clearly show the changes in the FZ profile, which evolve from a characteristic “X” shape to a “Y” shape as the beam goes from a fully focused to a fully defocused

condition as shown in Figure 38 (b) and (c). The details of the finite element model used in this study can be found in Ref. [63].

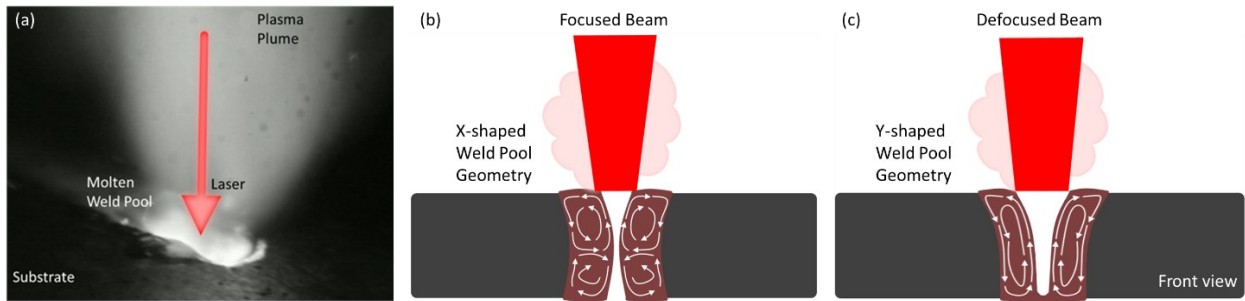


Figure 38: (a) Still image of the OKM laser welding process showing the keyhole surrounded by the molten weld pool. (b) and (c) show the schematic of the weld cross-section for the fully focused and defocused conditions, respectively.

The thermal distribution of three different welding conditions was modelled starting from the fully focused beam condition with an effective spot size of 0.3 mm which modelled the OKM welding process to a fully defocused beam condition with an effective spot size of 0.5 mm which modelled the CKM welding process as shown in Figure 39 (a) and (c), respectively.

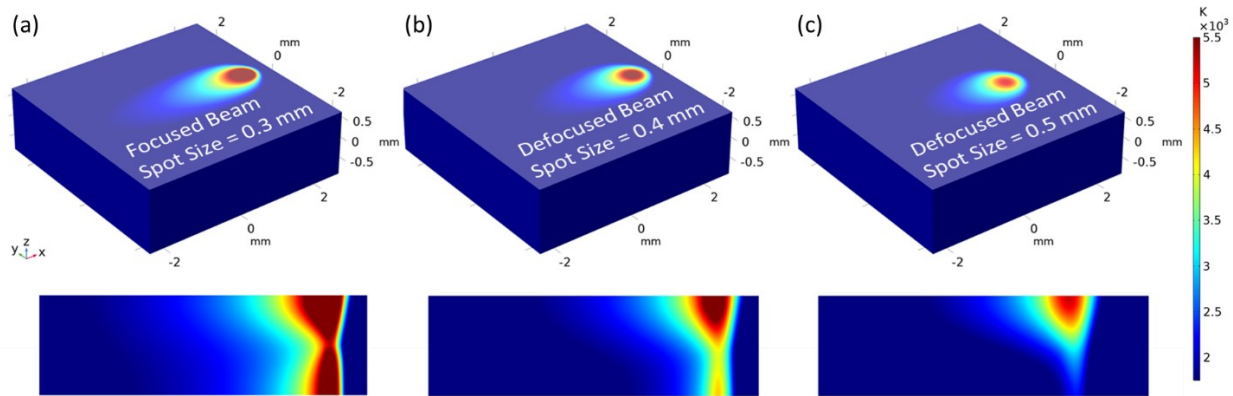


Figure 39: Isometric views along with the respective longitudinal cross-section of the temperature distribution in the (a) fully focused beam condition with a spot size of 0.3 mm, the (b) partially defocused beam condition with a spot size of 0.4 mm, and the (c) fully defocused beam condition with a spot size of 0.5 mm, showing clearly how the melt pool geometry changes as the laser beam is defocused going from full penetration welding in (a) to partial penetration in (c).

The results of the simulations using these models were compared to the experimental results, as shown in Figure 40, where it can be seen that the numerical model was in excellent agreement with the geometry observed in cross-sectional images of the weld. The DCG heat source was found to be capable of modelling the effect of laser beam defocusing on melt pool geometry for both X-shaped welds made using OKM laser welding, and Y-shaped welds made using CKM laser welding. A good representation of the morphology of partial penetration welds was also obtained from these simulations. The model confirms that, as the laser beam is defocused, the resulting increase in the beam spot size decreases the power density delivered to the substrate

which then produces a change in the shape and size of the keyhole, as shown schematically in Figure 38.

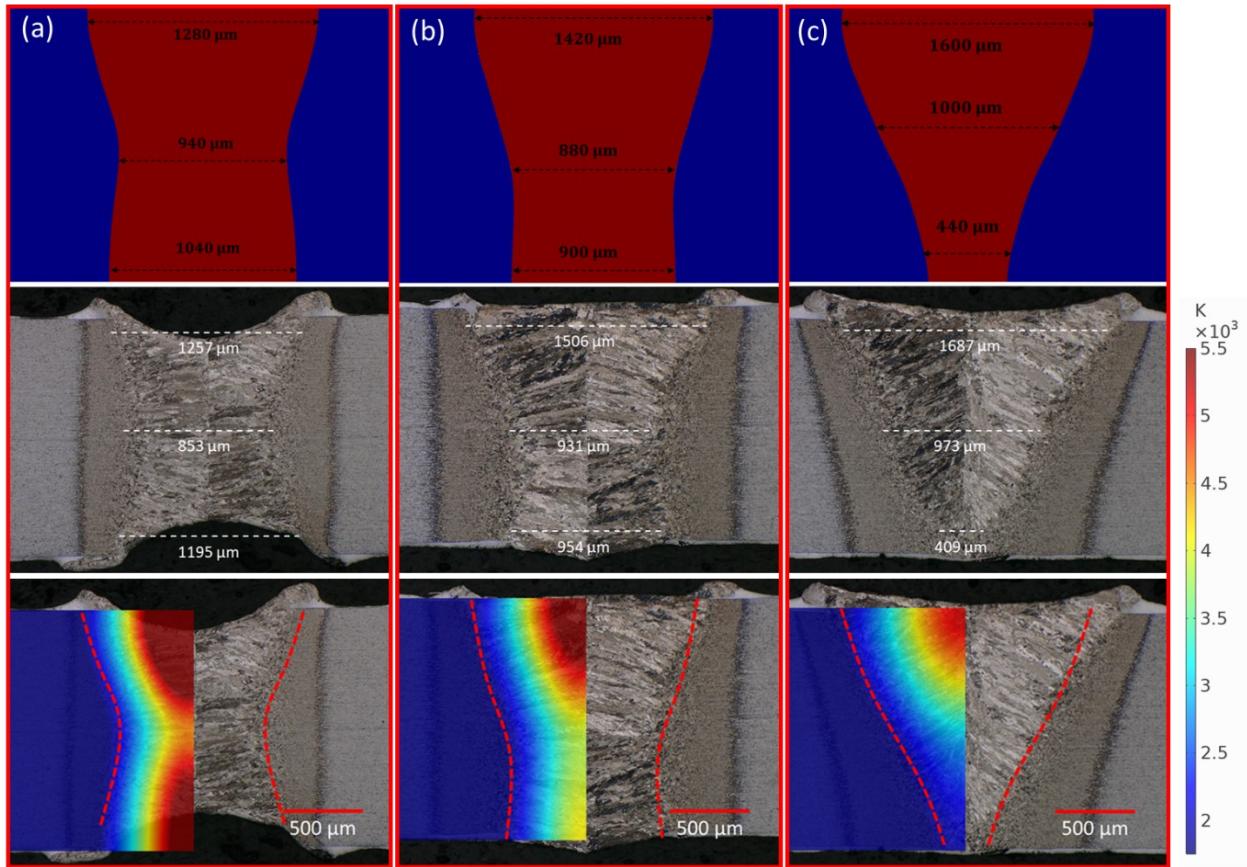


Figure 40: Comparison of the cross-section of the weld pool geometry given by the numerical model with the experimental results for the (a) fully focused beam condition with a spot size of 0.3 mm showing the X-shaped profile of the FZ, while the (b) partially defocused beam condition with a spot size of 0.4 mm, and the (c) fully defocused beam condition with a spot size of 0.5 mm, showed the Y-shaped profile of the FZ, respectively. The dashed lines show that there is an excellent match between the fusion boundary location predicted by the FE model compared to the actual weld cross-sections.

The dynamics of the welding process were observed using a special welding camera and nine sequential frames are shown in Figure 41 under conditions where the effective beam spot size on the surface of the substrate was ~ 0.3 mm. It can be seen that the plume and molten weld pool are noticeably unstable (Figure 41 (b to h)). This produces turbulence in the weld pool which causes the ejection of molten liquid leading to severe concavity as shown in the weld cross-sections in Figure 42 (a). Ejected liquid from the melt pool is present along the edge of the weld as recast material resembling elevated weld banks. The instability lasts for about 0.1s and is then followed by a period of stability before the cycle begins again. The weld pool volatility observed in Figure 41 can be attributed to the high beam intensity (55 kW/mm^2) which results in heating of the plasma inside the keyhole. This causes much of the incident power to be used up in the heating of the keyhole plasma. As the plasma is heated and expands, material is ejected from the keyhole. The

pressure wave associated with this expansion destabilizes the flow of liquid on the sides of the keyhole and suppresses the formation of a steady weld pool as shown in Figure 6. Liquid droplets are also ejected from the keyhole and further destabilize the welding process when they absorb power and scatter radiation from the incident laser beam. As the vaporized material dissipates, the incident laser beam can once again fully penetrate into the keyhole re-establishing the stable conditions required for deep penetration welding. These conditions are maintained until further instabilities arise in the laser and plasma plume interaction causing the cycle to be repeated [37].

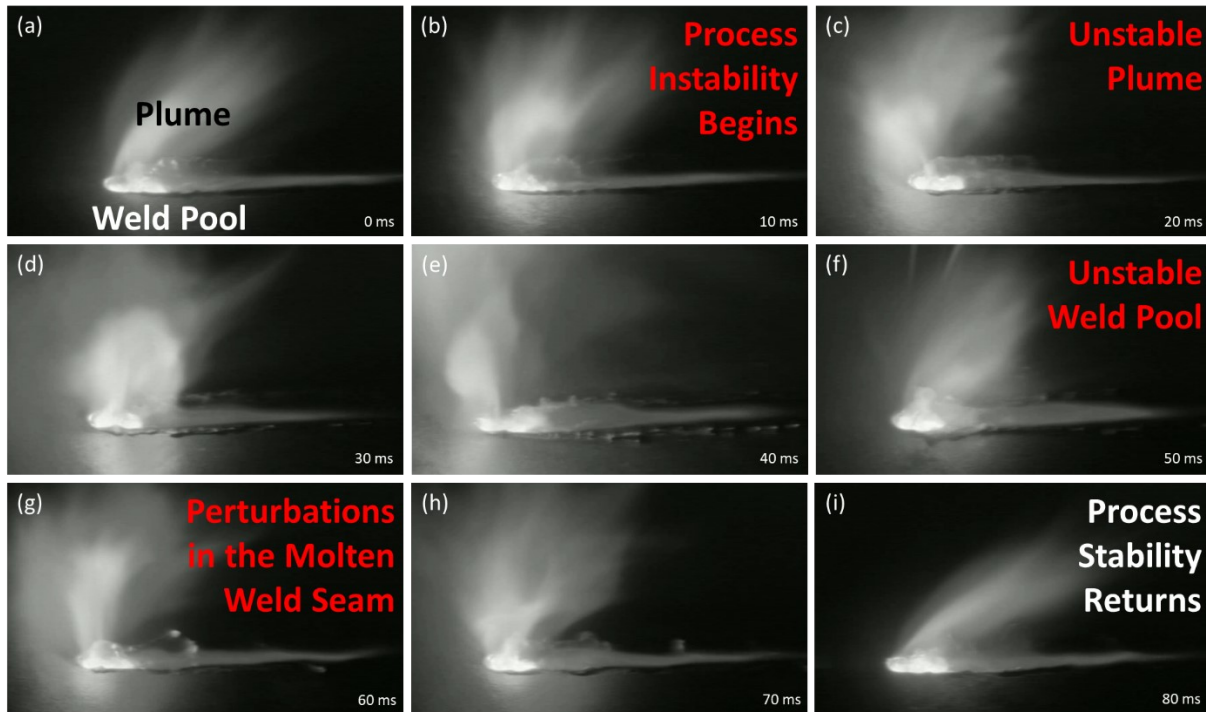


Figure 41: Still images of the weld zone using the focused beam condition showing a larger, unstable melt pool, some spattering, instability in the weld plume and perturbations in the weld seam. The size of the plasma plume at the top surface is noticeably smaller as some of the plasma escapes through the bottom of the keyhole.

Lin et al. [146] studied the effect of laser power and travel speed on the shape and size of the keyhole and the resulting geometry of the FZ, and reported that an X-shaped weld geometry (Figure 42 (a-e)) was a direct consequence of OKM welding using high laser power (3 kW) while a Y-shaped weld geometry (Figure 42 (f-h)) can be attributed to the use of low laser power (1 kW) as in CKM welding. The results from this study show that the weld pool geometry can be changed from an X- to a Y-shape by simply defocusing the laser beam (Figure 42) without changing laser power. A change in laser power would likely require an associated change in laser travel speed to optimize the process and ensure that welding defects are avoided which would hamper process efficiencies.

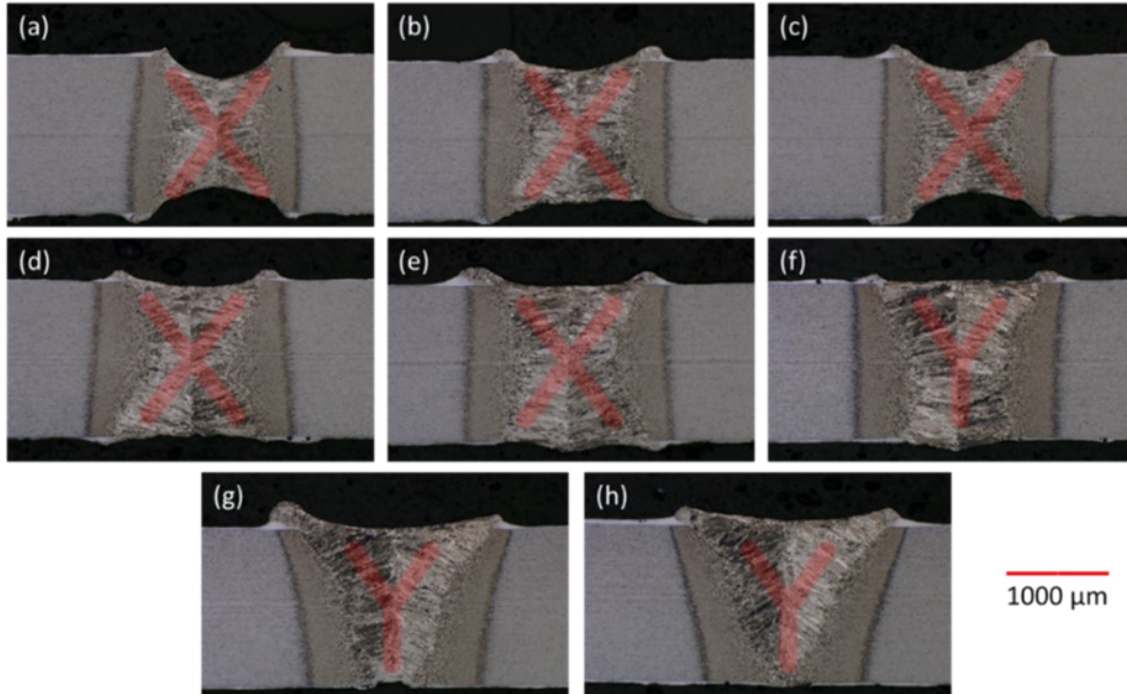


Figure 42: Optical Micrographs showing the improvement in weld geometry with severe concavity being observed in the (a) fully focused condition with a beam spot size of 0.3 mm, the concavity improving (b-d) as the laser beam is defocused by increasing the effective spot size, with almost no concavity (e and f) being observed at a defocusing distance where the beam spot size is about 0.4 mm. As the defocusing distance increases to a point where the spot size is greater than 0.5 mm (g and h), the total energy delivered to the work piece decreases, and partial penetration welds are observed.

For welding in the OKM, the vapor column extends through the full length of the keyhole as shown in the schematic in Figure 38 (b). The shape of this vapor column resembles a catenoid [142] which results from a balance between the forces that act to keep the keyhole open and those that tend to constrict its geometry. The keyhole is formed along the laser beam axis when sufficient energy per unit area is delivered by the laser to the substrate which leads to a thin vapor cavity being drilled into the surface due to the constant and even vaporization of the material. This vaporization produces a gas in the keyhole, which is then further heated by the incident laser beam to create a plasma [37]. Expansion of the plasma helps keep the keyhole open but also introduces absorbing material that attenuates the laser beam as it enters the keyhole leading to an inherent instability.

The catenoid shape of the keyhole is attributed to the vapor-induced recoil pressure generated by vaporized metal that forces the keyhole to remain open. This pressure is balanced by surface tension that tries to collapse the keyhole. In order to ensure a stable keyhole with a consistent geometry, the laser must vaporize enough material to generate a high enough vapor pressure, P_v , inside the keyhole to counteract the surface tension pressure, P_γ , acting along the keyhole wall [147]. It is important to note that P_v is dependent on the temperature at the keyhole

wall (T) while P_γ changes as the radius, a , of the keyhole varies [148]. The X-shaped weld pool geometry predicted by the model and confirmed experimentally (Figure 40 (a)), is a direct consequence of the catenoid shape of the keyhole during OKM laser welding in the fully focused condition.

The random instability observed during the fully focused laser welding condition is also related to liquid flow in the molten weld pool as shown schematically in Figure 43. In laser welding, convection in the weld pool is driven by Marangoni flow and is a function of the surface tension (γ) and the local temperature (T) [25,32,119]. If $\frac{\partial\gamma}{\partial T}$ is negative, then the molten material at the center of the weld pool first rises to the surface and then flows to the weld boundaries where it sinks to form a loop-like flow profile [122]. On the other hand, if $\frac{\partial\gamma}{\partial T}$ is positive, then the molten material rises along the fusion boundary and flows to the center of the weld pool [122].

It is well documented that γ is negative for liquid steels [120], implying that liquid flow driven by the Marangoni effect during laser welding of steels causes liquid metal to rise at the periphery of the keyhole where the local temperature is highest. It then moves to the outside of the weld pool and follows the boundary of the FZ as the local temperature diminishes [25]. Based on the CFD model developed by Courtois et al. [138] which predicted liquid flow in OKM laser welding of thin-gauge automotive steels, flow in the molten weld pool can become turbulent due to the generation of two opposing flow systems centered at opposite ends of the catenoid-shaped keyhole. As each liquid flow component loops and flows along the outside wall of the molten weld pool, the colliding liquid currents give rise to instabilities that interrupt the deposition of laser power as shown, for example, in Figure 41 (f). When this occurs, molten material is ejected from the weld forming concavities and defects in the weld bead as shown in Figure 42 (a).

This effect of counter propagating flows is shown schematically in Figure 38 (b) and a detailed simulation for three different focus settings can be seen in Figure 43. These simulations show that the flow in the melt pool separates into two counter propagating currents when the keyhole is open at the bottom surface of the sheet. As this liquid makes a loop and flows along the outside wall of the molten weld pool, the opposing liquid collides with it and causes severe turbulence as shown in Figure 41 (f). This phenomenon disappears when the far end of the keyhole constricts as the laser beam is defocussed, limiting the ejection of gas from the bottom of the keyhole. Under these conditions, liquid flow in the weld pool is limited to a single circulating current (Figure 43 b and c), and the molten weld pool appears to be significantly more stable as shown in Figure 44.

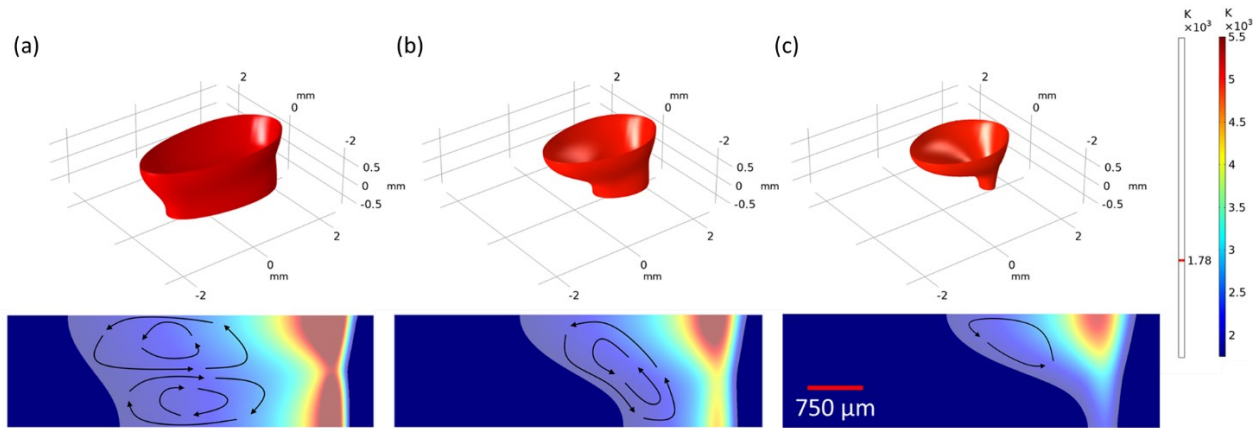


Figure 43: Isothermal view of the molten weld pool boundary along with the respective longitudinal cross-section of the temperature distribution with arrows showing the flow fields generated due to the Marangoni convection flow based on the CFD model developed by Courtois et al. [138] in the (a) fully focused beam condition with a spot size of 0.3 mm, the (b) partially defocused beam condition with a spot size of 0.4 mm, and the (c) fully defocused beam condition with a spot size of 0.5 mm. It can be seen clearly in (a) that due to the shape, size and temperature of the keyhole combined with the geometry of the molten weld pool two distinct flows develop in the molten pool leading to the violent turbulence observed in Figure 41. As the laser beam is defocused as shown in (b) and (c), the spot size increases, the power density of the laser decreases, and the keyhole shape changes as the temperature decreases. This decreases the effect of the Marangoni convection flow and the liquid in the molten pool becomes less turbulent. As the size of the molten weld pool becomes smaller the liquid flow stabilizes as observed in Figure 44.

In the partially defocused beam condition when the laser head is moved closer to the substrate, the effective spot size increases to 0.4 mm (Figure 44), and the process remains stable throughout the welding cycle. By defocusing the laser, the beam delivers a power density of about 32 kW/mm^2 . The increase in process stability can be attributed to the larger effective spot size which decreases the power density delivered to the substrate and stabilizes the keyhole, reducing turbulence in the melt pool. As the defocusing distance increases so that the focal point moves deeper into the plate, the length of the plasma column inside the keyhole increases. This implies that the beam intensity decreases towards the bottom surface of the plate and welding evolves from an OKM to a CKM causing the weld to change from an X-shape to a Y-shape.

In the defocused beam condition, the hottest plasma is located closer to the top surface of the sheet and attenuation of the beam reduces power dissipation deeper in the keyhole. Due to the beam intensity decreasing towards the bottom surface of the plate and most ejecta material exiting through the top of the keyhole, the weld becomes wider at the top while it closes in at the bottom, as shown schematically in Figure 38 (c) and confirmed by the micrographs and the simulation results shown in Figure 40 (c). In order to simulate the widening effect for the defocused beam condition in the numerical model, the selection of higher enhancement factors of anisotropic thermal conductivity in the y-direction is reasonable and can be justified by the fact that a larger melt pool width was observed when the beam was defocused. The simulation results and the weld cross-sections were in excellent agreement as shown in Figure 40. It is also important to note that a significantly larger weld plume that adversely affects the energy delivery to the material [149–

151], also helps in stabilizing the process by reducing the power density in the laser beam. The improvement in process stability translates into an improvement in weld geometry, with virtually no defects being observed in the weld cross-section as shown in Figure 42 (e and f).

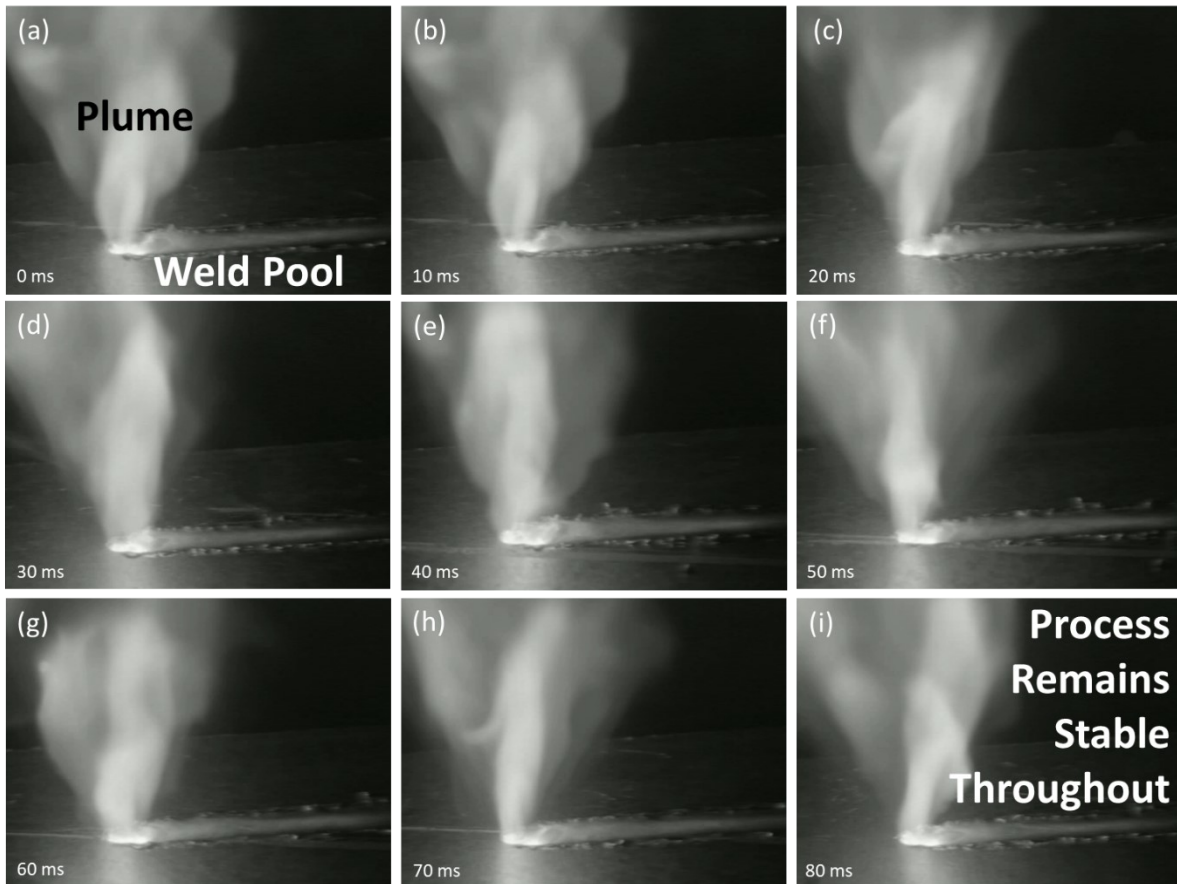


Figure 44: Still images of the weld zone using the partially defocused beam condition with a beam spot size of 0.4 mm showing a smaller melt pool, drastic reduction in process instabilities and an increase in the size of the weld plume as no vapor escapes from the bottom of the keyhole.

These results indicate that, as the focus changes, the length of the absorbing plasma column also changes. If this column is too small, the plasma overheats and reduces heat input into the weld while producing an excess of vaporized metal that depletes the weld yielding severe concavity accompanied by a large amount of recast material. Optimum results occur near the point where the plasma column has a length that maximizes heat input into the weld while maintaining full penetration. This condition gives the weld structure and morphology that is shown in Figure 40 (b) and the micrographs in Figure 42 (e) and (f). Under these conditions best use is being made of power available from the laser and the largest FZ cross-sectional area is observed at 1.76 mm^2 , compared to 1.35 mm^2 and 1.63 mm^2 for the fully focused and fully defocused conditions, respectively. The results also show that by optimally defocusing the laser, the peak load-bearing capacity of the joint can be improved by about 8% for the welded samples in the hot-stamped condition (Figure 45). Westerbaan et al. [46] showed that the peak load-bearing capacity of thin-

gauge advanced high strength steels was reduced by about 6.7% for welded samples that had a concavity of about 20% and they recommended that the welding speed should be reduced in order to correct for this concavity. This work shows that the same improvement in peak load bearing capacity can be achieved without any compromise in production efficiency by simply defocusing the laser beam to the optimal position.

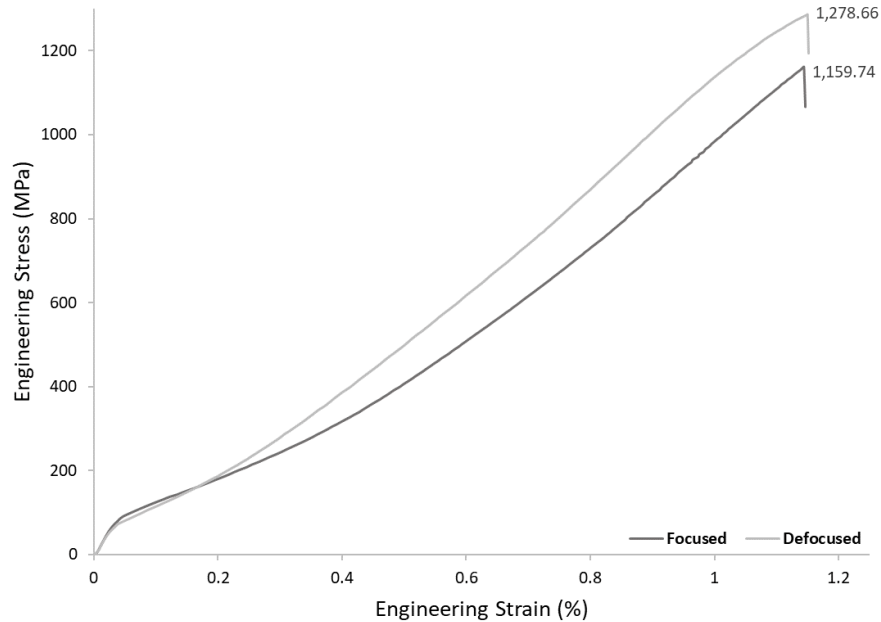


Figure 45: Flow curves for the base metal, and the welds made in the defocused and focused condition showing an improvement of about 8% in the peak load, respectively.

The results of this study showed that laser beam defocusing can be used as an effective method to optimize the laser welding of thin-gauge Al-Si coated 22MnB5 PHS used for automotive applications by controlling the fluid dynamics in the molten weld pool and improving the weld geometry. By way of FE numerical modelling and a detailed experimental study, it was shown that laser defocusing can be used as a control variable in the process optimization of laser welding applications as it allows the control of energy input into the substrate which leads to an observable improvement in the weld geometry and mechanical properties. It was observed that by defocusing the laser beam, the focal intensity of the beam can be controlled which can be used to change the length of the plasma column present in the sheet during welding.

The FE numerical model used to simulate the effect of defocusing the laser beam had an excellent agreement with the experimental results showing a near-perfect match between the weld geometry predicted by the model and the geometry that was observed experimentally. The numerical model can be used to optimize existing welding schedules by identifying the optimal defocusing distance that allows for an increase in welding speed without compromising the mechanical integrity of the joint, which can prove to be extremely beneficial in large-scale

manufacturing endeavours in the automotive industry. A similar methodology can be applied to improving the laser welding process efficiency for other applications and industries.

By optimally defocusing the laser beam, a plasma column can be achieved that has a length that maximizes the heat input into the weld while maintaining full penetration into the sheet. Under these optimal conditions, the FZ cross-sectional area is the largest, and the most effective use is being made of the power available from the laser. Defocusing the laser beam during the laser welding of thin-gauge coated steels can be used as an additional control parameter to stabilize the welding process, improve the liquid flow in the molten weld pool, and eliminate any surface or internal defects from the weld to achieve a weld geometry that is near-perfect. It was shown as part of this study that the peak load bearing capacity of the joint was improved by about 8% when the beam was optimally defocused.

In general, the optimization studies showed that by changing the impingement angle (i.e., LBC of + 20°) and defocusing the laser beam, the laser welding parameters could be kept constant for every study presented henceforth while minimizing the formation of any defects that could adversely affect the mechanical integrity of the joint. By utilizing this type of experimental methodology and process optimization, we drastically increased the reported accuracy of our results and ensured that these results were not affected by geometrical factors that tend to increase the error associated with the advanced metallurgical and mechanical characterization of laser welded joints. The results presented in this chapter show that by properly optimizing the laser welding process using FE modelling and experimental validation, the appropriate processing conditions can be acquired to ensure that welding defects are almost completely eliminated to the extent that they do not have a significant effect on the mechanical properties of the laser welded FZ produced using the techniques described in the following chapters. The ability to utilize a fully optimized laser welding process was deemed critical to the success of this research as any significant geometrical defects in the welded samples would make it extremely challenging to properly investigate the metallurgical and mechanical effects that have been explored in the upcoming chapters.

4 Suppressing α -ferrite by simultaneous in-situ ablation of the Al-Si coating and in-situ alloying of the FZ with carbon

* This chapter is composed of a published research paper [152] as outlined in the Statement of Contributions.

It has been reported that TWBs made from PHSs have practical use only in the press-hardened condition because the high strength of the BM is achieved due to the hot-stamping (i.e., heat treatment and subsequent die-quenching and stamping) process [25]. Therefore, FZ morphology, mechanical properties and the overall performance of the joint must be evaluated in the as-received-welded then hot-stamped (ARWHS) condition rather than the as-received welded (ARW) condition. This study investigated the effect of welding Al-Si coated 22MnB5 PHS through pure colloidal graphite coatings of different thicknesses in the ARWHS condition, on the change in FZ alloying chemistry, specifically, the Al and C content in the weld, which changed the FZ microstructure and the resulting mechanical properties of the joint. The results were compared to the base condition where no graphite coating was used during the welding process. It was observed that the FZ Al content decreased, and the C content increased as the graphite coating thickness increased. The study evaluated the impact of these changes on the mechanical performance of the hot-stamped joints, and the results show that by welding Al-Si coated 22MnB5 PHS through a colloidal graphite coating of a particular thickness, the α -ferrite phase concentration in the hot-stamped FZ was significantly reduced so that the mechanical strength of the joint was improved, and failure was shifted from the FZ, where it normally occurs, to the BM. Furthermore, the study proposed a new mechanism for in-situ ablation of the Al-Si coating during welding which has not been observed or achieved before. The findings of this work have a high impact potential [153] as the proposed method eliminates the need to remove the Al-Si coating prior to welding, which is the method currently employed in industry and is known to be time-consuming and costly.

4.1 Experimental details

1.5 mm thick Al-Si coated 22MnB5 PHS was used in the present study and the BM chemical composition is shown in Table 4. Bead-on-plate (BOP) welds were made perpendicular to the rolling direction of the steel on 200 mm by 200 mm sized samples using a laser power of 4 kW and a welding speed of 6 m/min with a defocused laser beam to reduce the weld concavity to under 5%. The samples were hot stamped following welding by heating them in a furnace for 6 minutes to an austenitization temperature of 930°C and then quenching them using a water-cooled die at a cooling rate of approximately 30°C/s, which resulted in a fully martensitic microstructure in the HSBM.

Pure colloidal graphite suspended in an isopropanol (IPA) base was applied to the area being welded. As the IPA base evaporated, a pure colloidal graphite coating was left behind as shown in Figure 46. BOP welds were made through the coating after which the samples were hot stamped. This condition is referred to as the welded with graphite and then hot stamped (WGHS) condition. The graphite coating thickness was varied from 5 μm to 130 μm and the coating thickness was measured prior to welding using a Veeco Profilometer to ensure a coating thickness accuracy of within $\pm 5\mu\text{m}$ for each condition.

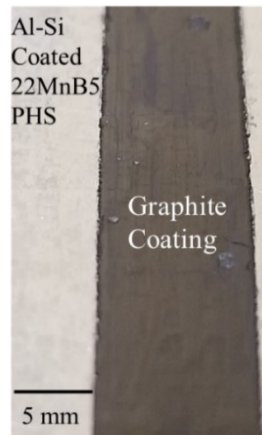


Figure 46: Image showing the graphite coating applied to the surface of the Al-Si coated 22MnB5 PHS, and the welds were made through the coated area.

The Zeiss UltraPlus field emission scanning electron microscope (SEM) was used to capture high magnification images of the microstructure and fracture surfaces of the welds to clearly observe the changes in FZ morphology and the variations in fracture mode for the ARWHS and WGHS conditions. Clemex Vision Lite Image Analysis software (v. 8.0.197) was used to analyze the FZ and BM microstructure to quantify the phase concentration of ferrite and martensite. Elemental analysis to determine the Al and C content in the FZ of the various welds was done using the JEOL JXA-8230 electron probe micro-analyzer (EPMA). The weight percentage of C and Al was measured in the regions shown in Figure 52 (a) and the average of these values was considered to be the bulk content of the given element in the FZ. The DB-100 Infrared Reflectometer was used to measure the emissivity of the substrate and the graphite coating in accordance to ASTM E408 [154]. The in-situ ablation process was observed at 1000 fps using the FASTCAM Mini UX100 high speed camera with a hard-coated 394 nm center wavelength bandpass filter with a full-width at half-maximum length of 10 nm. The high dynamic range XIRIS XVC-1000 welding camera with additional ultraviolet, near-infrared and neutral density filters was used to film the entire welding process at 90 fps.

4.2 Mechanism for in-situ ablation of the Al-Si coating

Welding Al-Si coated 22MnB5 PHS through a colloidal graphite coating decreased the Al content while increasing the C content in the FZ. The elemental analysis showed that the bulk Al

content of the weld decreased from 1.02 wt.% in uncoated (i.e., no graphite coating) welds, to 0.62 wt.% when welding through the maximum graphite coating thickness of 130 μm . Conversely, FZ C content increased from 0.23 wt.% in the uncoated case to about 0.34 wt.% when the maximum graphite coating thickness was used. Interestingly, Al content decreased approximately linearly with increasing graphite thickness until a coating thickness of 40 μm , after which FZ Al content did not decrease further, whereas C content continually increased with increasing graphite thickness. The change in FZ Al and C contents relative to graphite thickness can be found in Figure 47. The reason for the reduction in Al content was initially attributed to a theory proposed by Duley [37] that suggested that due to the darker color of the graphite coating – which has a lower reflectivity (0.23 @ 800K) compared to the substrate (0.82 @ 800K) – the laser absorptivity can be improved which increases the heat input into the weld. The higher heat input would potentially lead to greater vaporization of the Al-Si coating, resulting in a lower Al content in the FZ.

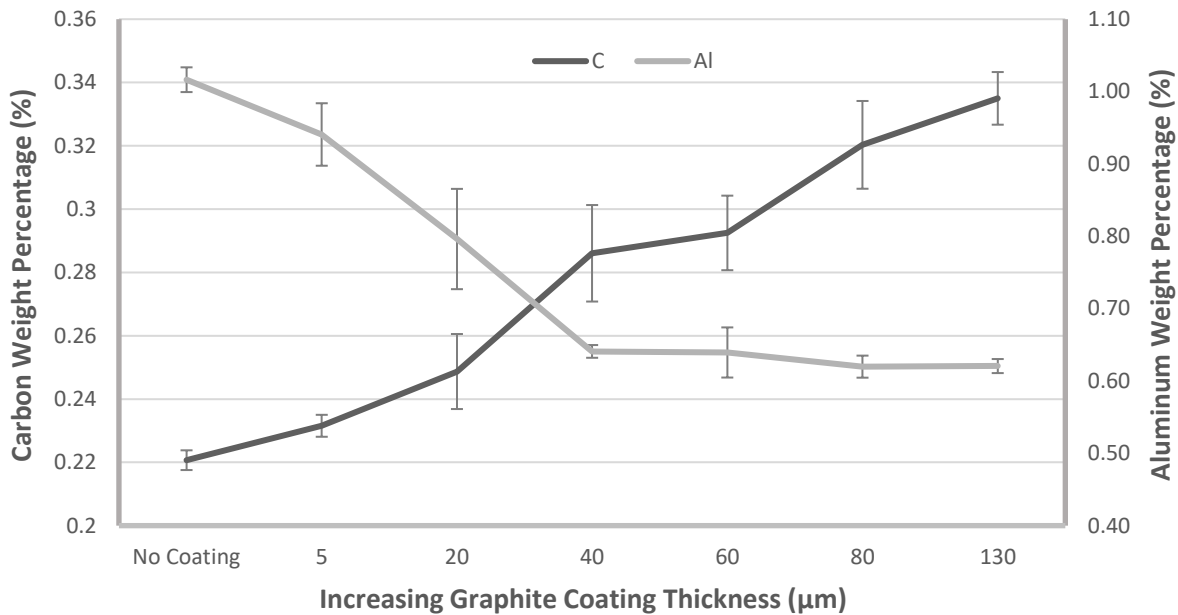


Figure 47: EPMA data showing that the Al-content in the FZ decreases as the graphite coating thickness increases, however, C-content increases at higher coating thicknesses

However, a clear limitation to this line of reasoning is that even if the Al-Si coating is more readily vaporized, it is still covered by a solid graphite coating which will hinder the removal of the vaporized Al-Si. Therefore, in order to understand the mechanism of in-situ ablation of the Al-Si coating during the welding process, the process itself was closely observed as shown in Figure 48. Lin et al. [103] suggested in an illustration that there was a layer of molten Al that floats on top of the molten weld pool during the laser welding of Al-Si coated 22MnB5 PHS. Figure 48 confirms that a small amount of molten Al-Si can be observed along the length of the weld bank on the surface of the molten weld pool. This molten layer of Al that floats on the surface of the

substrate surrounding the weld pool holds the key to understanding how the Al-content in the weld decreases when welding through a graphite coating.

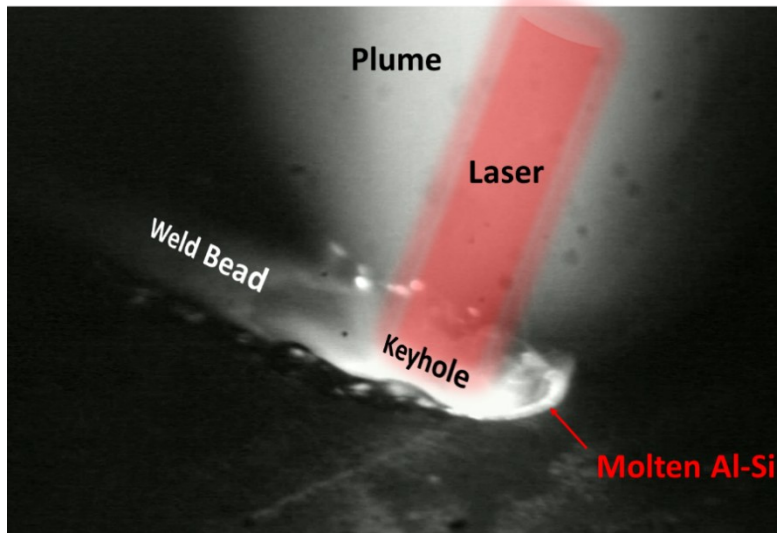


Figure 48: Zoomed in image of the weld zone showing the outer boundary of the molten weld pool surrounded by the molten Al-Si coating which has a much lower melting point as compared to the substrate.

The mechanism of in-situ ablation of the Al-Si coating can be explained effectively using the schematic shown in Figure 49. In the absence of a graphite coating, all the molten Al-Si coating surrounding the weld pool dilutes into the FZ as the molten weld traverses the length of the workpiece. However, when welding the Al-Si coated steel through a graphite coating, the Al-Si coating (which has a low melting point of ~ 580 °C) becomes sandwiched between the graphite coating (which does not melt) and the substrate (which has a much higher melting temperature of ~ 1540 °C). In fact, the graphite coating acts as a heat insulator and a physical barrier that entraps the molten Al-Si coating which ensures that the heat generated from the laser begins to liquefy a larger amount of the Al-Si coating, as shown in Figure 49 (b). As the laser continues to move forward, the molten liquid becomes pressurized as shown in Figure 49 (c). As the pressure builds up, the Al-Si coating eventually “explodes” through the thin graphite coating and is ejected away from the molten weld pool as shown in Figure 49 (d).



Figure 49: Schematic showing the mechanism of removal of Al-Si coating during the laser welding of graphite coated 22MnB5 steel where (a) is the welding process with no graphite coating, (b) is the process with the graphite coating showing an increase in the amount of molten Al-Si coated sandwiched between the graphite coating and the substrate, and (c and d) is showing how the molten Al-Si coating becomes pressurized and explodes through the graphite coating, respectively.

The primary evidence for the proposed mechanism for in-situ ablation was derived by the use of camera imaging with special filters, and a sequence of the welding process is shown in Figure 50, which clearly shows the ejection of material from the vicinity of the molten weld pool as the laser transitions from the non-coated substrate to the graphite coated substrate. The in-situ ablation process was observed using a special hard-coated 394 nm center wavelength bandpass filter with a full-width at half-maximum length of 10 nm to ensure that only light radiation emitted from molten or vaporized Al was captured, confirming that the “spatter” in Figure 50 (d), was mostly pure Al being ejected away from the surface of the weld. The proposed mechanism is given further validity by the EPMA data shown in Figure 47 that confirms that the reduction in Al content is proportional to the thickness of the graphite coating up to a maximum thickness of 40 μm (i.e., the thicker the graphite coating the higher the reduction in the Al content), after which no further reduction in Al content is observed. This means that as the graphite coating gets thicker, a larger volume of Al-Si becomes molten, which increases the internal pressure of the system, causing more molten material to be ejected away from the weld. The reason why no further reduction in

Al content was observed after a graphite coating thickness of 40 μm is due to the removal of all the Al-Si from the top surface. However, due to the liquid flow generated around the keyhole during laser welding, Al enters the molten weld pool from both the top and the bottom surfaces of the substrate [25], so even if all the Al is eliminated at the top surface, it continues to flow into the weld from the bottom. This means that the in-situ ablation effect of the graphite coating may not be enough to suppress the formation of ferrite in the FZ, and a supplementary strengthening effect may be required to improve the joint efficiency. The simultaneous increase in FZ C-content due to an increase in the graphite coating thickness holds the potential to further mitigate the formation of ferrite since it is well known that relatively small increases in the C-content tend to significantly improve the hardenability of steels [155].

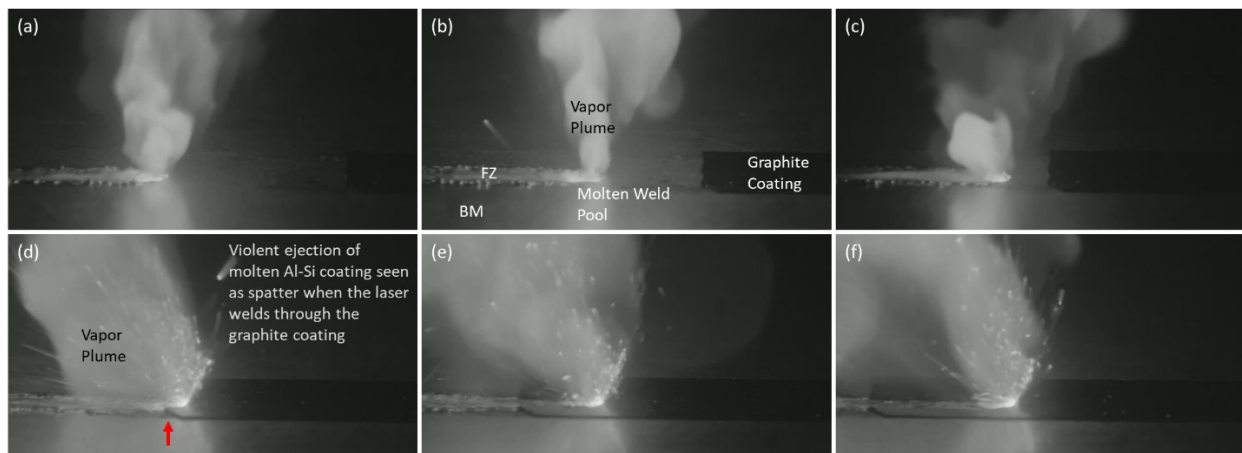


Figure 50: Still images from the welding video showing (a-c) the welding process in the absence of graphite coating, and (d-f) the welding process with the graphite coating, clearly showing the violent ejection of the molten Al-Si coating away from weld pool. The red arrow shows the deformation of the graphite coating due to the internal build-up of pressure that causes the ejection of the molten Al-Si coating.

4.3 Microstructural analysis

The effect of changing the C and Al content in the FZ using the aforementioned method has a significant effect on the microstructure of the weldment as shown by the SEM micrographs in Figure 51 (a) and (d). The BM surrounding the FB is purely martensitic for both the ARWHS and WGHS conditions, but the FZ looks drastically different. The FZ in the ARWHS condition is characterized by large martensite islands interspersed with almost equally sized ferrite grains as shown in Figure 51 (b) and (c). On the other hand, the FZ in the WGHS condition is almost purely martensitic with a few small grains of ferrite ($< 3 \mu\text{m}$) observed along the FB and even fewer grains dispersed through the weldment as shown in Figure 51 (e) and (f).

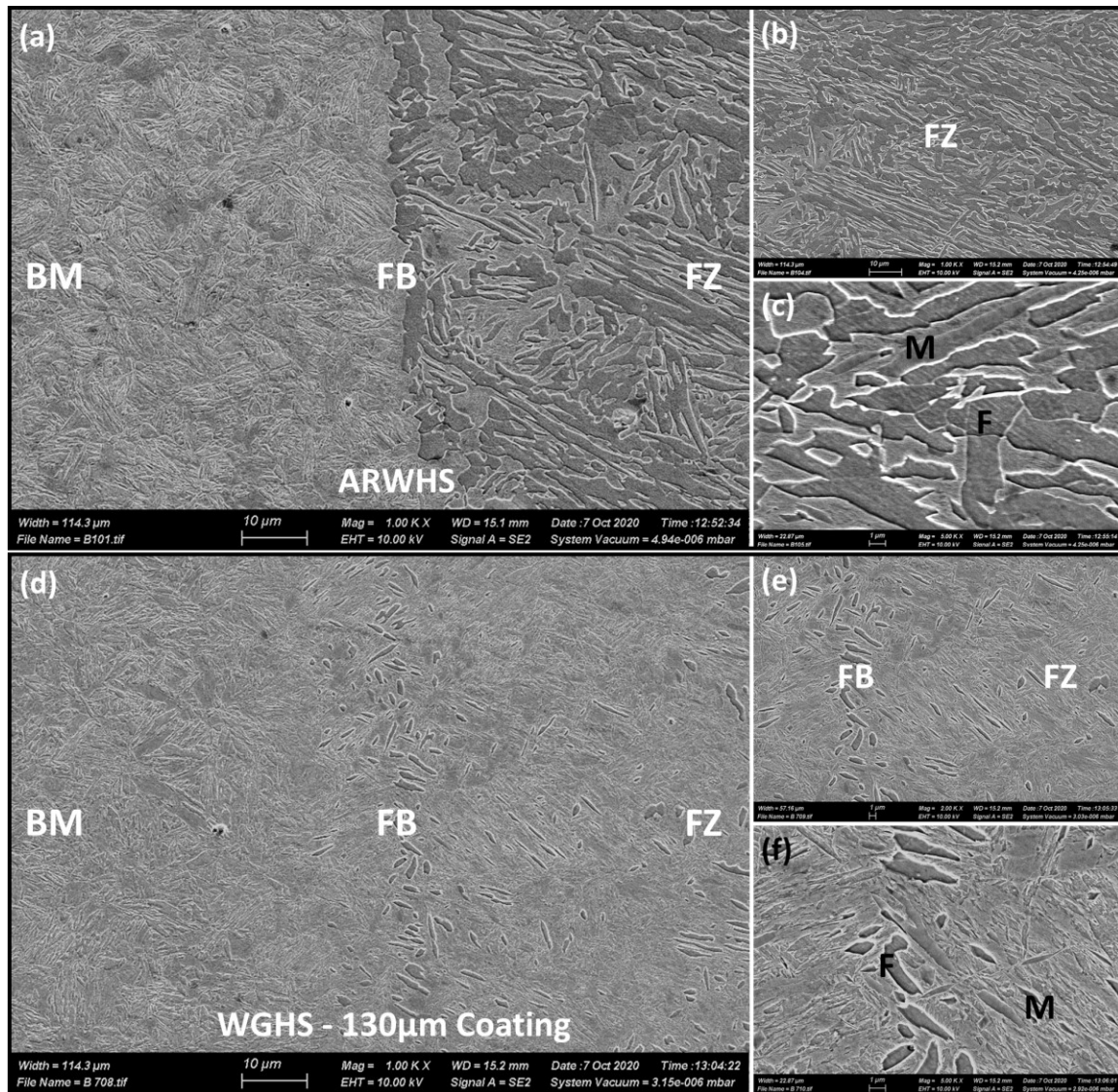


Figure 51: High magnification SEM images of the (a) BM, FB, and FZ in the ARWHS condition showing the difference between the morphology of the BM (which has a fully martensitic microstructure) and the FZ, with (b) and (c) showing magnified images of the dual-phase ferrite-martensite microstructure in the FZ; (d) shows the BM, FB, and FZ in the WGHS condition, with (e) and (f) showing magnified images of the FB and FZ showing significantly reduced ferrite phase concentration in the weld (M: Martensite, F: Ferrite). [Note: (a) is reprinted from Ref. [156], with permission of the American Welding Society (AWS), Miami, FL.]

Image analysis was used to identify the volume fraction of each phase present in the weld as the graphite coating thickness was increased (Figure 52). When no graphite coating was used, it was found that the FZ had a ferrite volume fraction of about 40 (± 3) %, shown by the brown phase in Figure 52 (a), with the remainder being martensite, shown by the green phase. These results are similar to those reported previously by Saha et al. [74]. When analyzing the welds made through the graphite coating, it was noted that the ferrite phase concentration decreased consistently as the graphite coating thickness increased as shown by the graph in Figure 53, with

the ferrite volume fraction being reduced to about 2 (± 2) % when the maximum graphite coating thickness of 130 μm was used, as shown in Figure 52 (c).

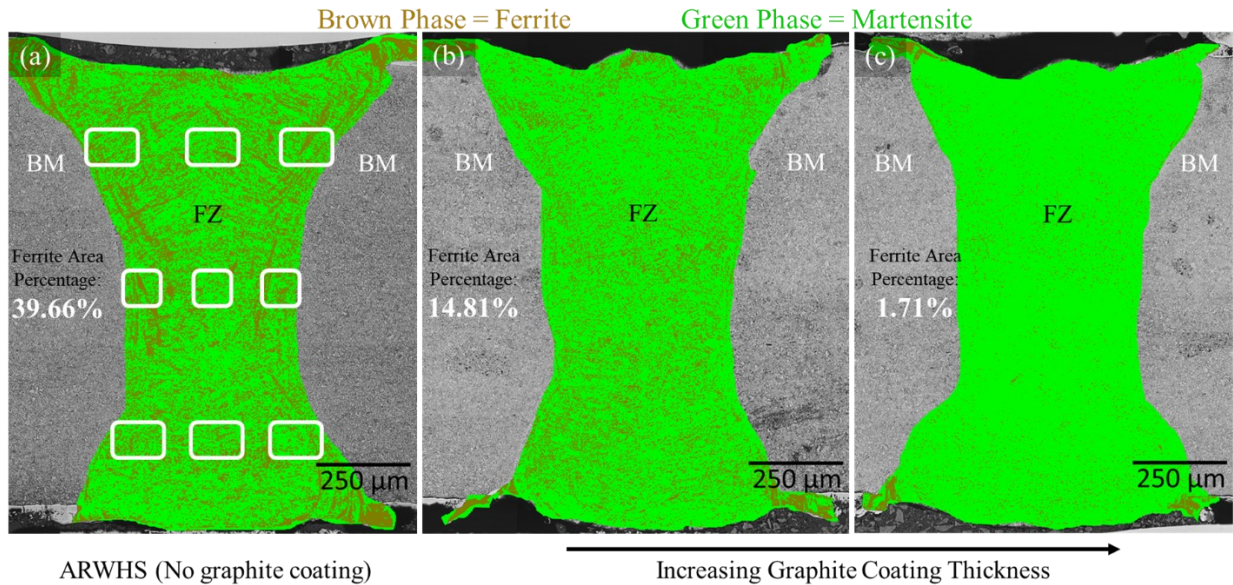


Figure 52: Image analysis of optical micrographs using Clemex Vision Lite showing the phase fraction of ferrite (brown color) and martensite (green color) in the weld microstructure for the (a) ARWHS condition, (b) WGHS condition with a coating thickness of 60 μm , and (c) WGHS condition with a coating thickness of 130 μm . The insets in (a) show the regions where EPMA area scanning was performed to measure the C and Al content in the FZ.

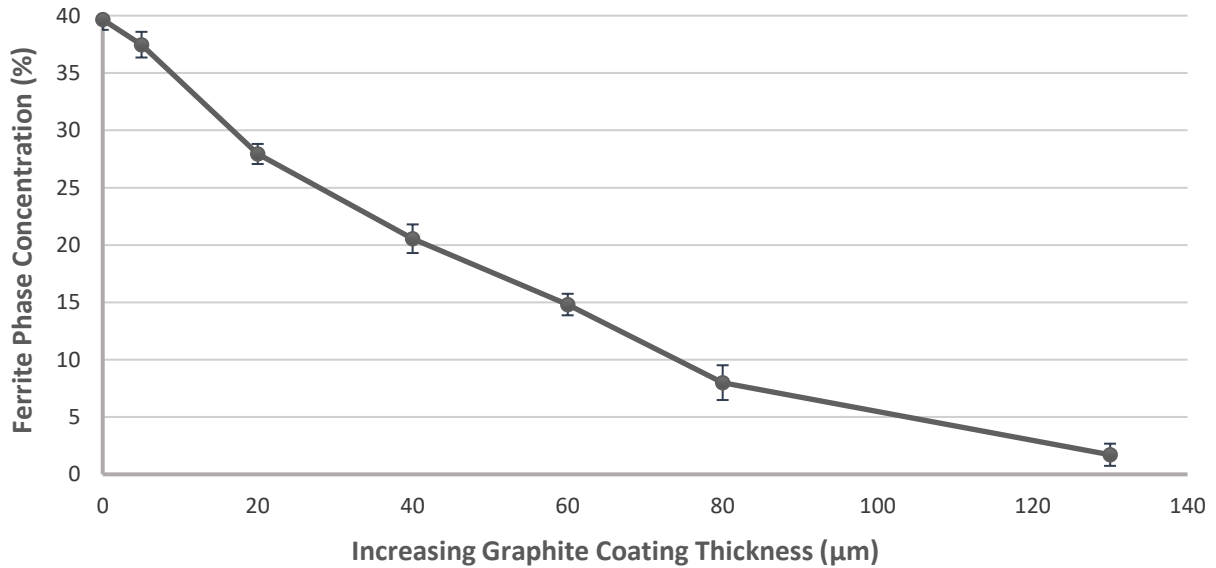


Figure 53: Graph showing the decrease in ferrite phase fraction in the FZ as the graphite coating thickness increases.

Martín et al. [117] have shown that increasing the Al content in a steel significantly increases the A_{c3} temperature, confirming that Al is a strong ferrite stabilizer. The predicted Fe-Al phase diagram for the ARWHS FZ composition shows that the FZ with a bulk Al content of about 1 wt.% comprises of austenite and ferrite at the austenitization temperature of 930 $^{\circ}\text{C}$ (Figure

54 (a)) which explains the dual-phase ferrite-martensite microstructure observed in the weld as shown in Figure 51 (b and c). On the other hand, C is known as an austenite stabilizer, which means that as the C content in the FZ increases and the Al content decreases, the austenite phase is stabilized which can be seen by the expansion of the single-phase austenite region in the predicted phase diagram shown in Figure 54 (b). This leads to a significant reduction in the ferrite phase fraction, as was confirmed by the micrographs in Figure 52.

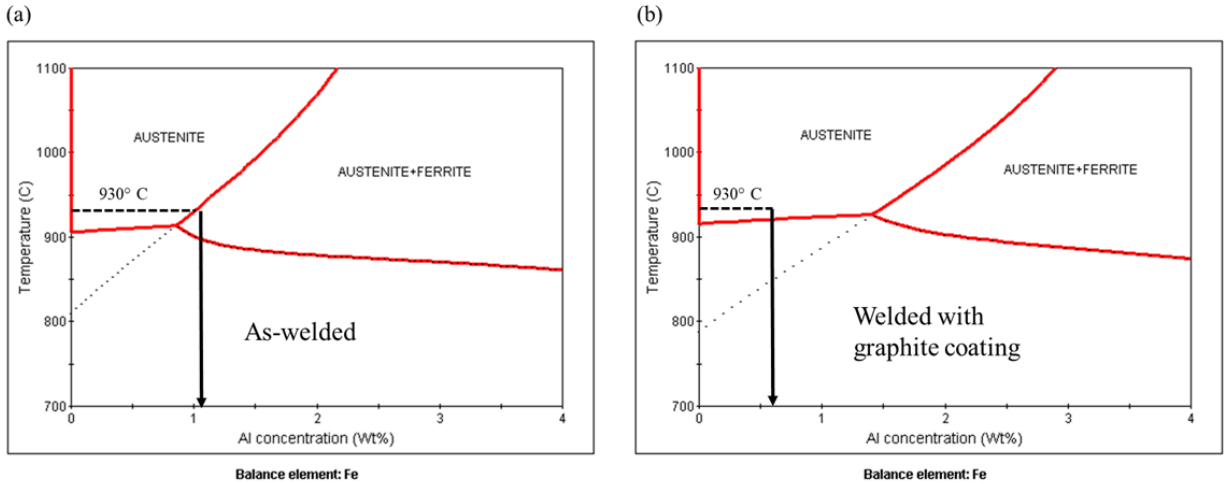


Figure 54: Fe-Al phase diagrams generated using JMatPro (v. 11.2) for (a) the ARWHS FZ composition showing that at the austenitization temperature of 930°C and an Al content of about 1 wt.% the FZ comprises of austenite and ferrite, and (b) the WGHS FZ composition showing that the addition of C and removal of Al stabilizes the single-phase austenite-region thereby increasing the phase concentration of the martensite at the end of the hot stamping process and the arrow is showing that the FZ microstructure at 930°C and the measured Al content of about 0.6 wt.% is fully austenitic.

The increase in the size of the single-phase austenite region ensures that during austenitization at a temperature of 930°C, the FZ microstructure is completely austenitic in the welded with graphite coating condition compared to the dual-phase ferritic and austenitic microstructure observed in the ARW condition. Therefore, the results clearly show that by welding Al-Si coated 22MnB5 PHS through a pure colloidal graphite coating, the austenite phase is stabilized due to the in-situ alloying of C and removal of Al from the FZ, which leads to a reduction in the α -ferrite phase concentration that is observed in the weldment after hot-stamping.

4.4 Mechanical properties

As the α -ferrite content in the FZ of the WGHS condition is significantly lower compared to the FZ of the ARWHS condition, a noticeable improvement in the mechanical properties of the weld was observed. Microhardness maps were generated for the BM and FZ of the ARWHS and WGHS conditions to observe the changes in FZ hardness as shown in Figure 55. The average BM hardness was measured at about 480 HV which falls within the range reported previously by Saha et al. [74], Yoon et al. [126], and Lin et al. [102]. The average FZ hardness for the ARWHS condition was measured at about 320 HV, which was significantly lower than the BM hardness as

shown in Figure 55 (a), due to the presence of a high phase concentration of α -ferrite. However, due to the reduction in the ferrite phase concentration in the FZ of the WGHS samples, the average FZ hardness increased from around 320 HV when no coating was used to about 540 HV at the maximum coating thickness of 130 μm , indicating that the average FZ hardness increases as the graphite coating thickness increases.

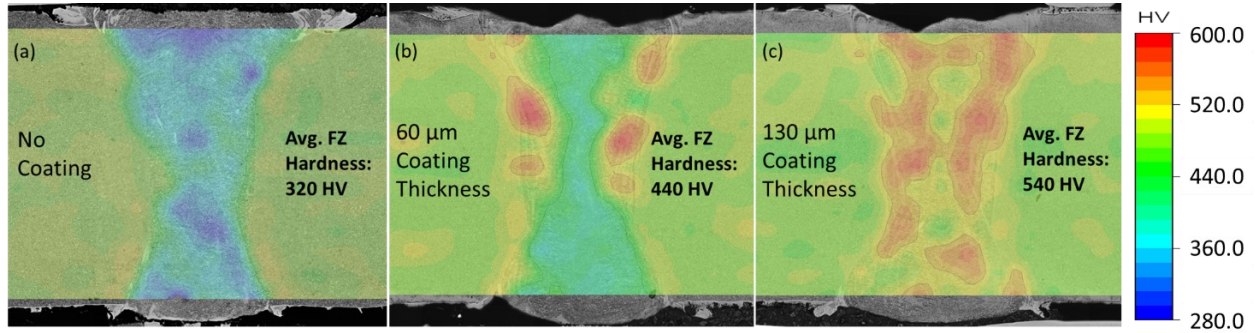


Figure 55: Hardness maps for the BM and FZ of the (a) ARWHS condition showing a significantly softer FZ as compared to the BM, and of the WGHS condition with a (b) 60 μm and (c) 130 μm coating thickness showing that the average FZ hardness increases as the coating thickness increases.

Due to the relatively lower hardness of the FZ and the high ferrite phase concentration, the weld strength in the ARWHS condition was measured at about 1249 ± 15 MPa and sudden fracture was observed along the length of the FB as shown by the red dotted line in Figure 56 (a), which agrees with the data reported by Saha et al. [74], Yoon et al. [126], and Lin et al. [102]. The fracture surface for this sample shows catastrophic rupture and it is clear to see that failure occurred by cleavage, confirming that the fracture was brittle as shown in Figure 57 (a-d). The fracture morphology corresponds well to the flow curve for this sample (Figure 57 (e)), which shows that abrupt failure happened in the joint relatively quickly after the onset of plastic deformation during the tensile test.

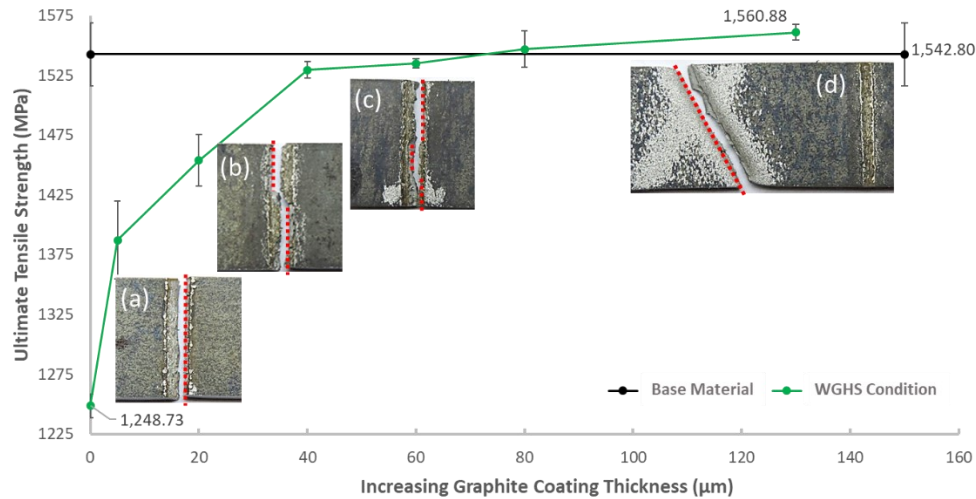


Figure 56: Graph showing the increase in UTS for the WGHS condition as the coating thickness increases with complete strength recovery when a coating thickness of 130 µm is used. Insets are showing the failure location in the FZ due to the high phase concentration of α -ferrite when (a) no graphite coating is applied, (b) 20 µm coating thickness is used, and (c) 60 µm coating thickness is used, respectively; (d) shows the failure location in the BM of the WGHS sample with 130 µm coating thickness. Fracture surfaces for (a), (c) and (d) are shown in Figure 57.

As the graphite coating thickness increases and the ferrite phase concentration decreases – which subsequently leads to an improvement in the FZ hardness – the UTS for these samples also increases as shown in Figure 56 (b) and (c), with the latter showing signs of banding along the FB, indicating that the weld strength is approaching that of the BM. Although the failure continues to be observed in the FZ for these samples, the key difference is that the fracture path changes direction abruptly as it propagates through the weld and has a jagged profile, as shown by the red dotted lines, indicating that fracture propagation through the weld was difficult due to the lower ferrite phase concentration. The fracture surface for the sample shown in Figure 56 (c), shows a combination of ductile and brittle fracture as shown by the small dimples (average size: $0.24 \mu\text{m}^2$) interspersed with regions of cleaved fracture faces as shown in Figure 57 (f-i). The flow curve for this sample (Figure 57 (j)), shows that the joint exhibited higher strength and elongation compared to the ARWHS sample due to the reduction in ferrite phase concentration, which allowed for the sample to undergo more stable plastic deformation during the tensile test (as shown by the arrow pointing to the lighter region in Figure 57 (f)), which allowed more time for voids to nucleate and grow, shown by the dimples on the fracture surface. However, since the UTS and fracture point of this sample was the same (as shown by the tensile curve in Figure 57 (j)), the fracture mode is still characterized by sudden brittle failure through the FZ.

At the maximum coating thickness of 130 µm, the UTS of the weld matches that of the BM at around 1561 ± 7 MPa and failure in these samples occurred in the BM with the crack propagating at an angle showing the plane of maximum shear stress as shown in Figure 56 (d). The sample showed clear signs of banding around the fracture which is indicative of necking and ductile failure. The fracture surface for this sample was characterized by large dimples (average size: 0.76

μm^2) and no cleavage-like features were observed as shown in Figure 57 (k-n), confirming that the fracture mode in this case was purely ductile. The flow curve for this sample (Figure 57 (o)), shows that the joint exhibited the highest strength and elongation compared to the other samples, with a clear separation between the UTS and fracture point which indicates that this sample underwent necking that led to the coalescence of microvoids which resulted in significantly larger dimples observed on the fracture surface.

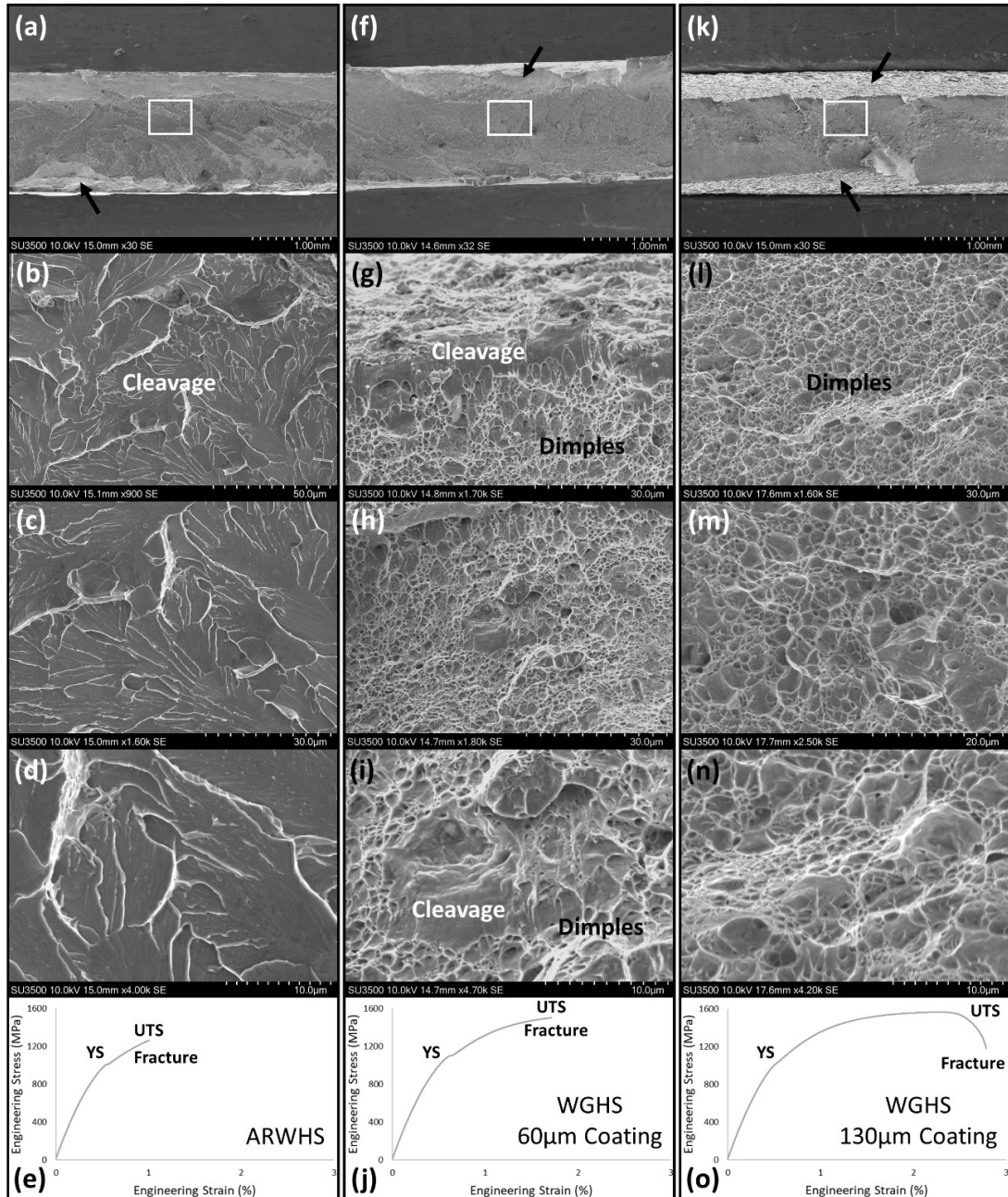


Figure 57: SEM micrographs of the fracture surface of the samples shown in Figure 56. (a) shows the fracture surface of the weld for the ARWHS condition, with (b-d) showing magnified images from within the region outlined in (a), confirming that brittle fracture occurred in this sample by cleavage, which corresponds well to the tensile curve for this sample as shown in (e). (f) shows the fracture surface of the weld for the WGHS condition with a coating thickness of 60 μm , with (g-i) showing magnified images from within the region outlined in (f), confirming that a combination of ductile and brittle fracture occurred in this sample as shown by the small dimples interspersed with cleavage faces, which corresponds well to the tensile curve for this sample as shown in (j). (k) shows the fracture surface of the BM for the WGHS condition with a coating thickness of 130 μm , with (l-n) showing magnified images from within the region outlined in (k), confirming that ductile failure occurred in this sample due to the presence of numerous and relatively larger dimples, which corresponds well to the tensile curve for this sample as shown in (e). The lighter regions in (a), (f), and (k) shown with arrows represent the relative area of the fracture surface that experiences stable plastic deformation before failure. (YS: Yield Strength)

4.5 Conclusions

The presented study analyzed the effect of changing the alloying chemistry of the FZ by welding Al-Si coated 22MnB5 PHS through a layer of pure colloidal graphite coating on the resulting microstructure and mechanical properties of the weldment. The following conclusions can be made from this work:

1. Welding Al-Si coated 22MnB5 PHS through a graphite coating changed the alloying chemistry of the FZ by decreasing the Al and increasing the C content in the weld which stabilized the austenite phase at elevated temperatures causing an increase in the martensite phase fraction after hot-stamping and improving the mechanical properties of the joint.
2. The Al content in the FZ decreased as the graphite coating thickness increased due to the in-situ ablation of the molten Al-Si coating.
3. It was observed that the ferrite phase concentration in the FZ decreased continuously from about 40% when no graphite coating was used during welding to about 2% when the maximum graphite coating thickness of 130 μm was used.
4. By reducing the ferrite phase concentration in the FZ, the average FZ hardness was effectively increased.
5. The reduction in the ferrite phase concentration and the subsequent improvement in the FZ hardness led to a direct improvement in the mechanical strength of the laser welded joints. It was observed that the welds made through the maximum graphite coating thickness of 130 μm had a UTS that matched the strength of the BM, and failure for these samples was successfully shifted from the FZ, where it normally occurs, to the BM.

Therefore, it can be concluded that by welding Al-Si coated 22MnB5 PHS through a graphite coating of a given thickness, the microstructure of the FZ can be controlled so that the mechanical properties of the weldment can be improved without requiring the laser ablation of the Al-Si coating prior to welding. As a concluding remark, it is worth noting that the discovery presented in this chapter was granted an international patent [153] in 2021.

5 Optimizing FZ mechanical properties by modifying the Al-Si coating using electro-spark deposition to achieve in-situ alloying during laser welding

* This chapter is composed of a published research paper [157] as outlined in the Statement of Contributions.

Using colloidal graphite as a potential solution to the FZ-softening issue was shown to be quite effective in the BOP configuration but differentiating between the effect of coating ablation and C-alloying on the strengthening of the FZ was deemed to be quite challenging. Furthermore, applying and maintaining the appropriate graphite coating thickness on a large-scale using pre-existing infrastructure and built-in automation tools was found to be significantly difficult. The coating was problematic to apply in the butt-joint configuration due to its low viscosity which caused the coating to run into the gap leading to much higher levels of C-alloying in the FZ, which resulted in excessive brittleness in the weld.

Therefore, a different approach was employed in which the Al-Si coating was modified using electro-spark deposition (ESD) prior to welding. The study presented in this chapter investigated the effect of laser welding ESD-modified Al-Si coated 22MnB5 PHS using tungsten-carbide (WC) and Inconel-625 (In625) in the ARWHS condition to evaluate the changes in FZ alloying chemistry, which modified the microstructural morphology, the phase fraction, and the resulting mechanical properties of the joints. The samples welded with the WC-modified and In625-modified ESD-coatings are referred to as the as-welded with WC then hot-stamped (WWCHS) and the as-welded with In625 then hot-stamped (WIHS) samples. The WWCHS and WIHS samples were compared to two base conditions: the hot-stamped BM (HSBM) with no weld, and the ARWHS condition where no ESD-modified coating was used during the welding process. The in-situ alloying of WC and In625 in the FZ of laser-welded Al-Si coated 22MnB5 PHS significantly decreased the α -ferrite phase concentration in the hot-stamped FZ such that the mechanical strength of the joints was considerably improved, and failure was shifted from the FZ, where it normally occurs, to the BM. The findings of this study hold a significant relevance in the fully-automated manufacturing of TWBs, as well as other applications for functionally-graded components, where highly controlled in-situ modification of the processed zone is required to achieve tailored properties.

5.1 Experimental details

FE-SEM (JEOL7000F) equipped with an electron back-scattered diffraction (EBSD) detector was used to characterize the microstructure of the fusion boundary. After conventional sample preparation and polishing, the EBSD samples were prepared with vibratory polishing using OP-S solution. The pattern acquisition was performed with a high-speed Hikari CCD camera with 2 x 2 binning which provided appropriate indexing. Data was recorded using a 0.2 μm step size. High energy synchrotron X-ray diffraction was performed at the beamline P07 at DESY and was used to probe the existing phases across the welded joints. With a beam energy of 87.1 keV (wavelength of 0.14235 \AA), transmission-mode measurements were acquired with a beam size of 50 x 50 μm with a 50 μm step between consecutively analyzed spots. Processing of the raw diffraction data was performed using a proprietary software that relied on the use of calibrant powder (LaB_6) to determine the sample-to-detector distance, instrumental peak broadening, and other detector-dependent information. A 2D PerkinElmer detector was used to capture the Debye-Scherrer rings.

Electro-spark deposition operates by discharging a capacitor through a conductive electrode and substrate, forming a short duration arc and transferring small droplets of material from the electrode to the surface of the substrate in the form of a “splat” [158,159]. Electro-spark deposition was used in this study to manually apply In625 and WC-10%Co coatings to Al-Si coated 22MnB5 steel, as shown in Figure 58 (a) and (b), respectively. The voltage, capacitance, and frequency process parameters used for WC depositions were 120 V, 200 μF , and 150 Hz, respectively, while the process parameters for In625 were 100 V, 80 μF , 150 Hz, respectively. Electrode sizes differed between the two, with a diameter of 8 mm for the WC-10%Co and a diameter of 3.2 mm for the In625. Four passes with the electrodes were used to provide an average coating thickness of about 45 μm for the In625 coating and 55 μm for the WC-10%Co coating, measured using 3D surface profilometry. All coatings were applied with an ultra high-purity argon cover gas delivered coaxially around the electrode. The modified In625 ESD coating had an average chemical composition of 41.7 wt.% Ni, 25.0 wt.% Al, 15.1 wt.% Fe, 14.3 wt.% Cr, 2.1 wt.% Ti, and 1.8 wt.% Si. The modified WC-10%Co ESD coating had an average chemical composition of 60.5 wt.% W, 11.1 wt.% Al, 19.7 wt.% Fe, 6.0 wt.% Co, 1.9 wt.% Mn, and 0.8 wt.% Si. The compositions were measured using EDS and EPMA and the results are shown in Figure 61.

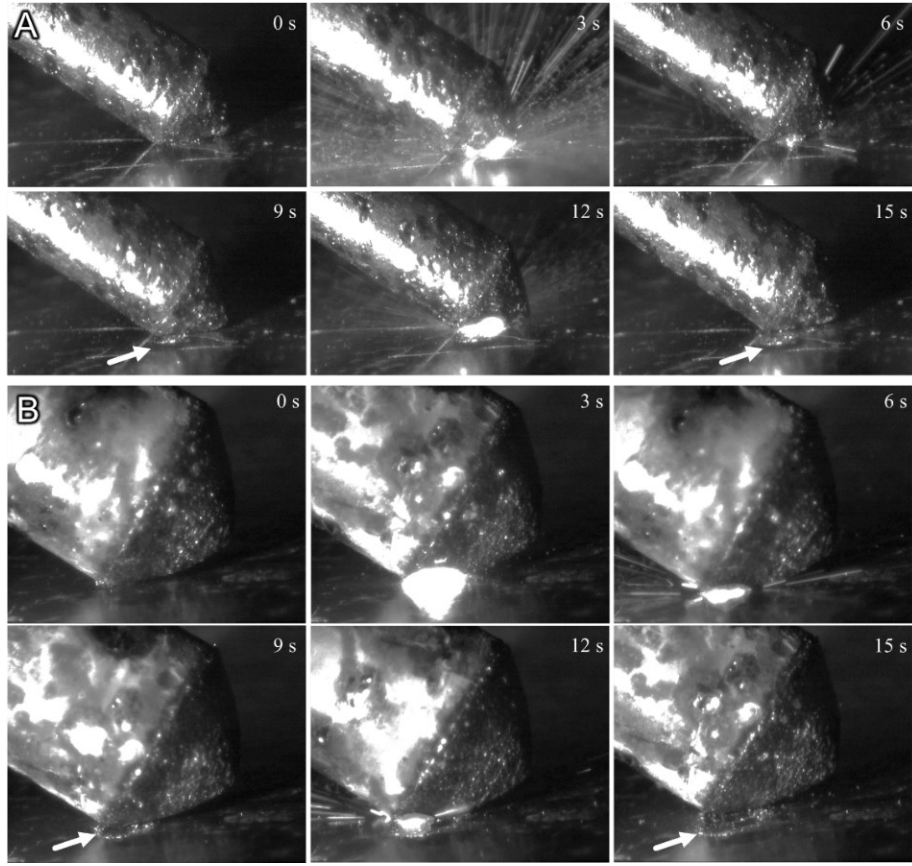


Figure 58: Electro-spark deposition of (a) In625 and (b) WC-10%Co on Al-Si coated 22MnB5 steel in the as received condition. “Splats” of material are deposited from the electrode on to the substrate as the electrode tip rotates and makes contact with the surface, with the white arrows show the coating that has already been deposited.

The in-situ alloying of the FZ was achieved by producing BOP welds on the substrate through the ESD-modified coatings, perpendicular to the rolling direction of the steel using a laser power of 4 kW and a welding speed of 6 m/min using a laser defocusing distance of 4 mm, and a positive beam impingement angle of 20° to reduce the weld concavity to under 5% [58,61,63], as shown in Figure 59. The samples were welded and then hot-stamped by heating them in a furnace for 6 minutes to an austenitization temperature of 930°C and then quenched instantaneously using a water-cooled die at a cooling rate of approximately 30°C/s , to ensure a fully martensitic microstructure in the as-received HSBM. A high dynamic range XIRIS XVC-1000 welding camera with additional ultraviolet, near-infrared, and neutral density filters was used to film the entire welding process at 90 fps, as shown in Figure 59.

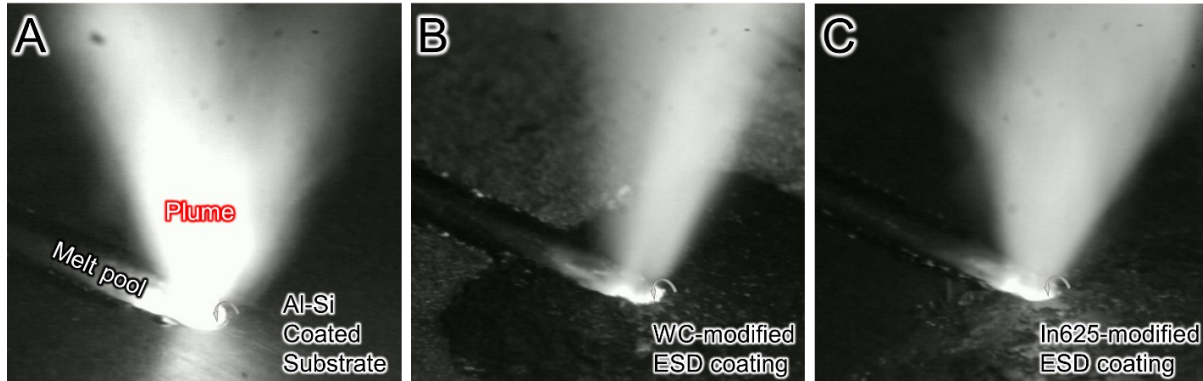


Figure 59: Still images of the laser welding process for the (a) Al-Si, (b) WC, and (c) In625 coated 22MnB5 steel, clearly showing that the plume size gets smaller when welding through the higher melting temperature secondary coatings. The gray colored arrows are showing how the Al-Si and ESD-modified coatings melt around the molten weld pool and mix into the fusion zone.

5.2 In-situ alloying of the FZ

The FZ alloying composition was changed by welding directly through the ESD-modified coatings, as shown by the arrows in Figure 59 (b) and (c), and the bulk compositions of the FZ, as measured using EPMA, is summarized in Table 7. The dilution effect of the Al-Si coating during welding has been studied in significant detail in the literature [25,74,125,160,161], and as such will be taken as the base condition in this study. It is well-established that the dilution of the Al-Si coating (Figure 61 (a)) into the molten weld pool increases the local Al content above 1 wt.%, which significantly increases the A_{c3} temperature [117] and causes the shrinkage of the single-phase austenite (γ) region while expanding the dual-phase $\gamma + \delta$ -ferrite region in the Fe-Al phase diagram [156], which results in the formation of a dual-phase ($\gamma + \delta$) microstructure at high temperature. During hot-stamping, two things happen simultaneously: (i) the Al trapped at the FB diffuses through the FZ increasing the average Al content in the bulk structure and, (ii) the martensite in the dual-phase FZ decomposes, which relieves the compressive stresses acting on the high-temperature δ -phase, facilitating the formation of a more abundant unstressed α -ferrite phase by way of recrystallisation [25]. The effect of increasing the Al-content in the bulk FZ and the transformation of δ -ferrite at the FB leads to an overall increase in the phase concentration (PC) of α -ferrite in the FZ. The continuous cooling transformation (CCT) diagram for the bulk composition of the FZ of the ARWHS sample is shown in Figure 60 (a), clearly predicting that quenching the sample from 930 °C at a cooling rate of 30 °C/s, would lead to a martensite-ferrite dual-phase microstructure.

Table 7: Bulk chemical composition of the weld fusion zone in the ARWHS, WWCHS, and WIHS conditions (in wt.%).

Sample Condition	C	Mn	B	Si	Cr	Ti	Mo	W	Co	Ni	Al	Fe
ARWHS	0.23	1.22	0.0032	0.27	0.20	0.04	0.02	0.00	0.00	0.00	1.53	bal.
WWCHS	0.36	1.22	0.0032	0.27	0.20	0.04	0.02	2.60	0.39	0.00	1.13	bal.
WIHS	0.23	1.22	0.0032	0.27	0.65	0.05	0.02	0.00	0.00	1.89	1.32	bal.

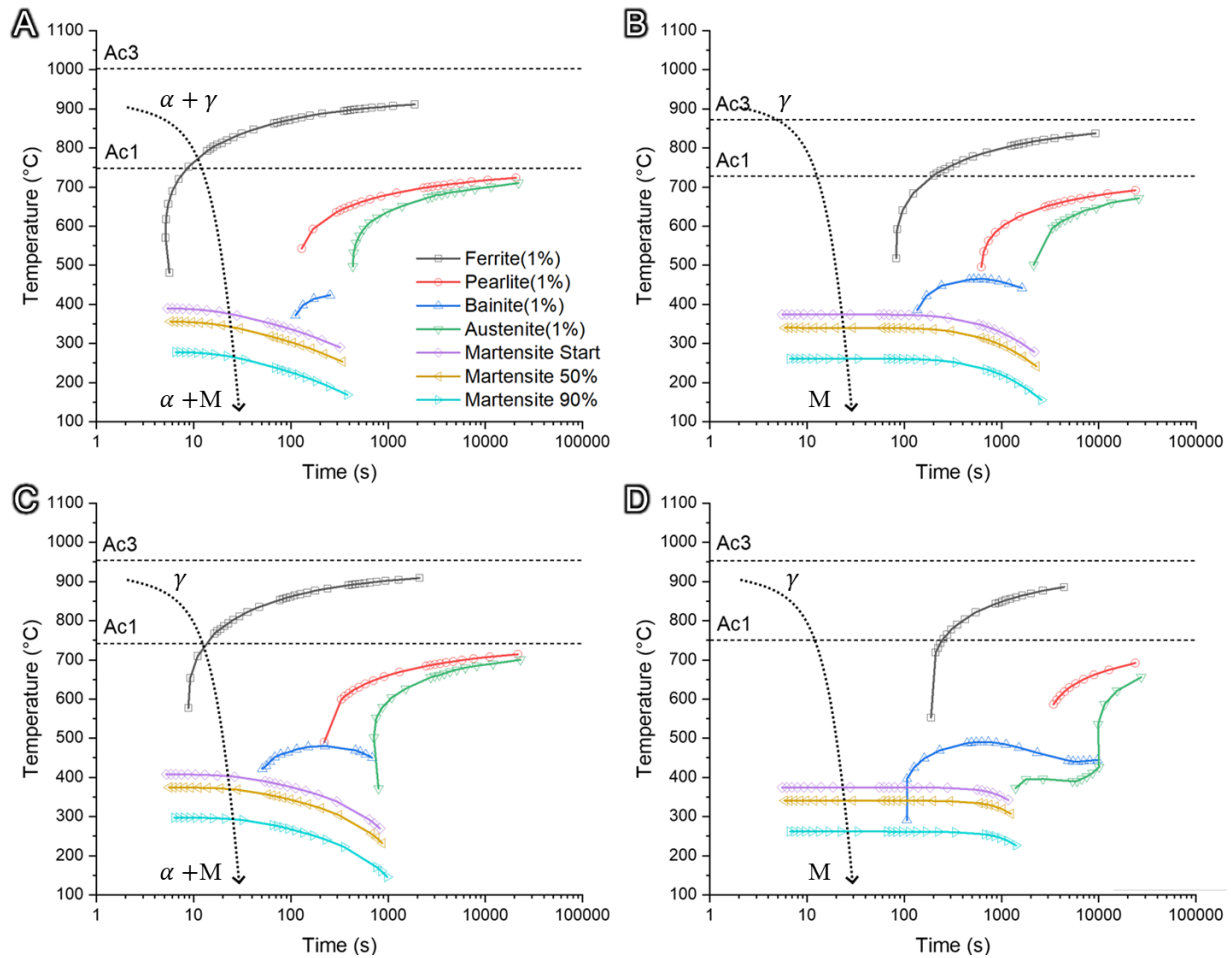


Figure 60: CCT diagrams for the bulk composition of the FZ of the (a) ARWHS and (b) WIHS samples. (c) and (d) show the predicted CCT diagrams for the bulk composition of the center of the FZ, and the FB of the WWCHS sample, respectively. The dotted arrow represents a cooling rate of 30 °C/s, with the starting and ending phases observed in each case also shown next to the dotted arrow. Although the Ac_1 and Ac_3 values were almost identical for the FZ and FB regions of the WWCHS sample, the starting microstructure in the FZ post-welding had a fully martensitic morphology because the Al that was diluting into the weld pool was trapped at the FB, which also had a higher W- and C-content that suppressed the formation of ferrite. Therefore, it can be assumed that during austenitization the FZ microstructure was purely austenitic leading to a fully martensitic microstructure after quenching. (M: Martensite)

The microstructure and measured composition of the as-received In625 and WC-10%Co ESD coatings are shown in Figure 61 (c-d) and (e-f), respectively – with the hot-stamped coating morphology shown in Figure 61 (g) and (h), respectively. The ESD-modified coating morphology and local composition was complex due to the nature of the ESD process which deposits “splats” of coating material onto the substrate surface [162]. Since the coating electrode was rotating at a high velocity during deposition, it scraped the surface of the substrate upon contact (Figure 58) mixing the Al-Si coating, the steel and the material being deposited from the electrode. The ESD-modified coatings in the as-coated condition (Figure 61 c-f) were characterized by significant cracks and discontinuities. However, the coating quality was significantly improved in the hot-stamped condition which allowed the cracks and discontinuities in the coating to be recovered, as shown in Figure 61 (g-h). Khan et al. [156] showed that the α -ferrite PC in the FZ could be significantly lowered when welding Al-Si coated 22MnB5 through an adhesively applied 50 μm thick pure Ni-coating (Chapter 6). However, one of the major issues with adhesively applied coatings for laser welding applications is that the coatings can have a tendency to delaminate when exposed to elevated temperatures, so using ESD coatings to achieve in-situ alloying in the FZ can be an effective technique to eliminate the risk of coating delamination, as shown in Figure 59.

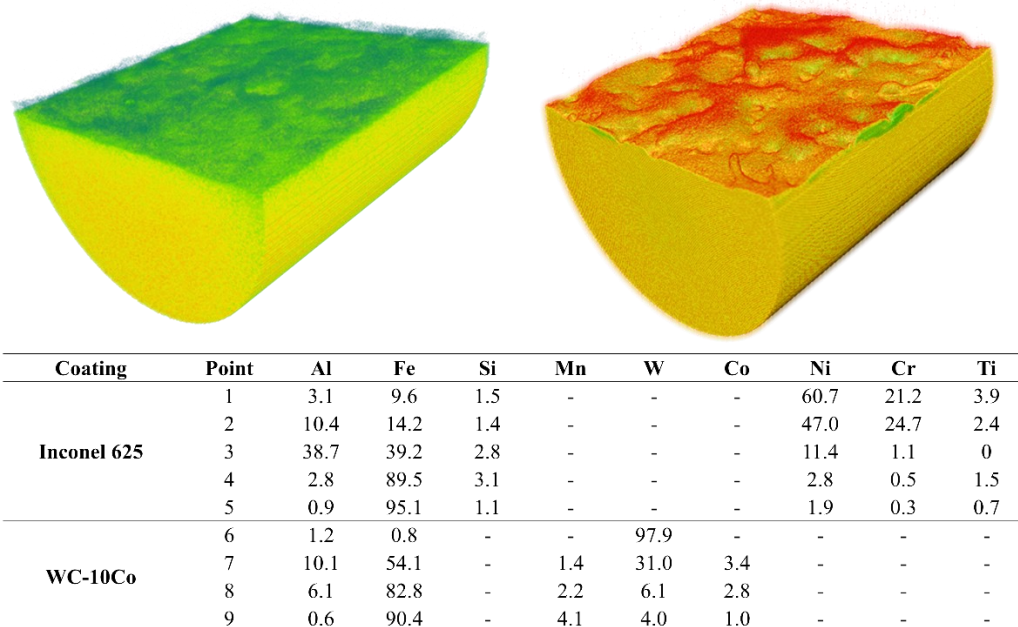
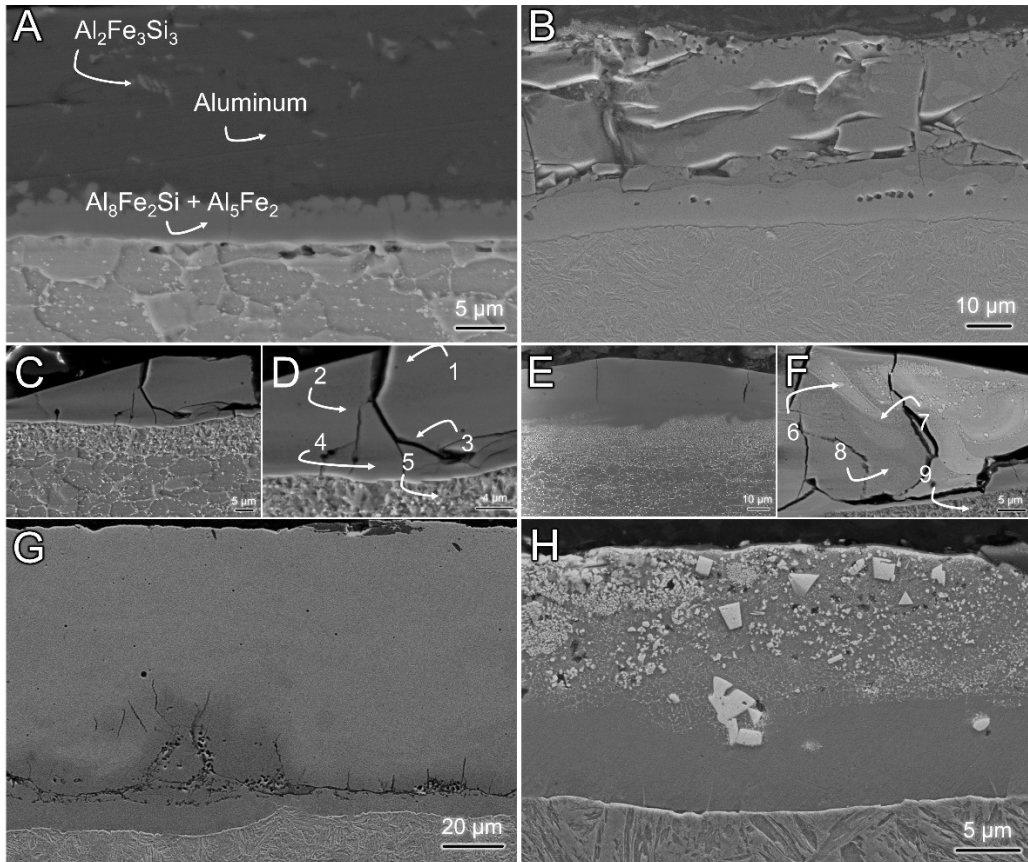


Figure 61: FE-SEM images of the (a, b) Al-Si, (c-d, g) In625, and (e-f, h) WC coatings in the as-received and press-hardened state, respectively, along with the corresponding EDS data for the regions specified in (d) and (f). Computerized tomography (CT) scan images of the Inconel and WC coated samples is also shown to highlight the tomographical differences between the coatings' relative surface texture. The known phases of the as-received Al-Si coating are identified in (a).

The chemical composition of the regions identified in Figure 62 (a) was measured using EPMA, and the average of these regions was considered to be the bulk composition of the entire FZ. The bulk Al-content in the FZ of the ARWHS sample was measured to be around 1.53 wt.% which was slightly lower than the theoretical maximum Al-content that could be present in the weld if 100% of the Al-Si coating diluted into the molten weld pool. Khan et al. [156] showed in a separate study that some of the coating tends to vaporize during laser welding, resulting in a slightly smaller amount of Al diluting into the weld pool.

The bulk alloying content of the FZ of the WWCHS condition was relatively inhomogeneous compared to the other samples. Three distinct regions in the FZ were identified, as shown by the dotted lines in Figure 62 (a). The region within the white dotted lines (representing ~19% of the total area of the FZ) was rich in nanosized WC particles and had a W content of about 7.50 wt.%. The region within the red dotted lines (representing ~32% of the total area of the FZ) showed no traces of WC particles and had a W content of about 0.25 wt.%. The remaining area of the FZ had a W content of about 2.28 wt.%, with significantly smaller area fraction of WC particles being observed (i.e., ~ 73% less than the region shown by the white dotted lines). The average bulk alloying content of the FZ for C, W, and Co was about 0.36, 2.60, and 0.39 wt.%, respectively, which represented an alloying composition that was 88% of the theoretical maximum had no vaporization of the coating occurred during welding. The WIHS sample showed a bulk increase in the Cr and Ni content of about 0.65 and 1.89 wt.%, respectively, which represented an alloying composition that was ~79% of the theoretical maximum. The difference in the lower levels of dilution for the In625 coating compared to the WC-10%Co coating was because the latter has a higher melting and boiling temperature compared to the former leading to less vaporization of the coating during laser welding, as confirmed by the observable size of the plasma plume in Figure 59.

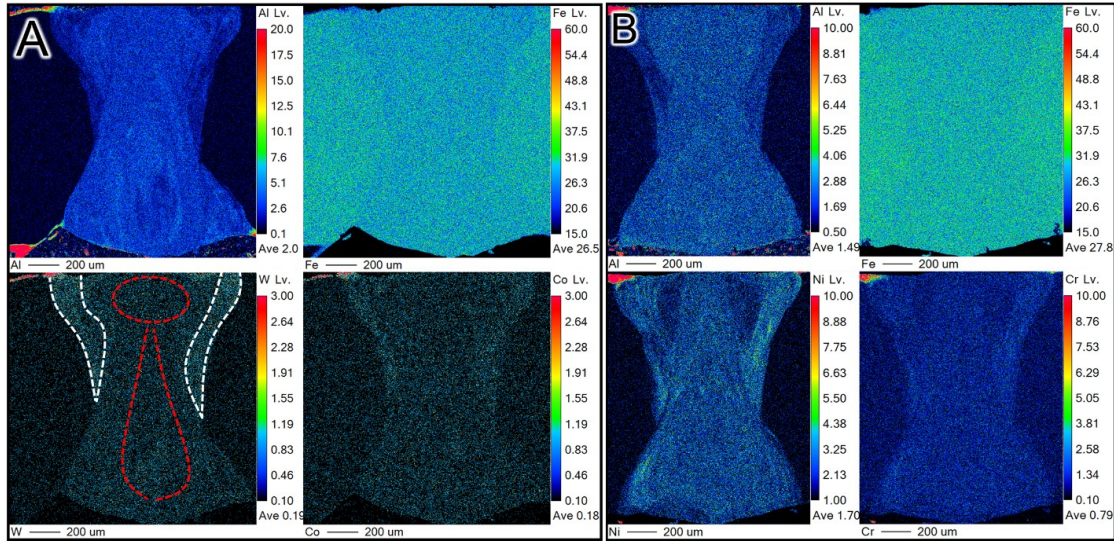


Figure 62: EPMA maps showing the elemental distribution of Al, Fe, W, Co, Ni, and Cr in the (a) WWCHS, and the (b) WIHS samples, respectively. Insets are showing the regions where elemental distribution was measured and the average of these regions has been considered the bulk composition of the sample. The white and red dotted lines in (a) are showing the regions where the largest concentration of WC particles and no WC particles were found, respectively.

5.3 Microstructural analysis

The optical micrographs for the ARWHS, WWCHS, and the WIHS samples are shown in Figure 63 (a-c), respectively. The PC was measured using image analysis; the detailed methodology has been explained in previous work [156]. It was observed that the ARWHS samples had a dual-phase microstructure with an average PC of about 68% martensite and 32% α -ferrite, which is within the range reported in the literature [74,103,125,152,156,160]. There was a significant decrease in the average α -ferrite PC for the WWCHS and WIHS samples, being measured at about 8% and 2%, respectively. The micrographs for the WWCHS and WIHS samples shown in Figure 63 clearly indicate the martensitic morphology in the FZ was visibly different than that of the BM. Specifically, the WIHS sample was under-etched at the FB due to the higher Ni- and Cr-content, which are known to improve the corrosion resistance of steel, whereby making the steel more difficult to etch [163]. To characterize the key morphological differences in the microstructures of the different samples, the regions of interest (shown by the white insets in Figure 63) were investigated at higher magnification using FE-SEM and EBSD techniques and the different phases were identified using SXRD analysis.

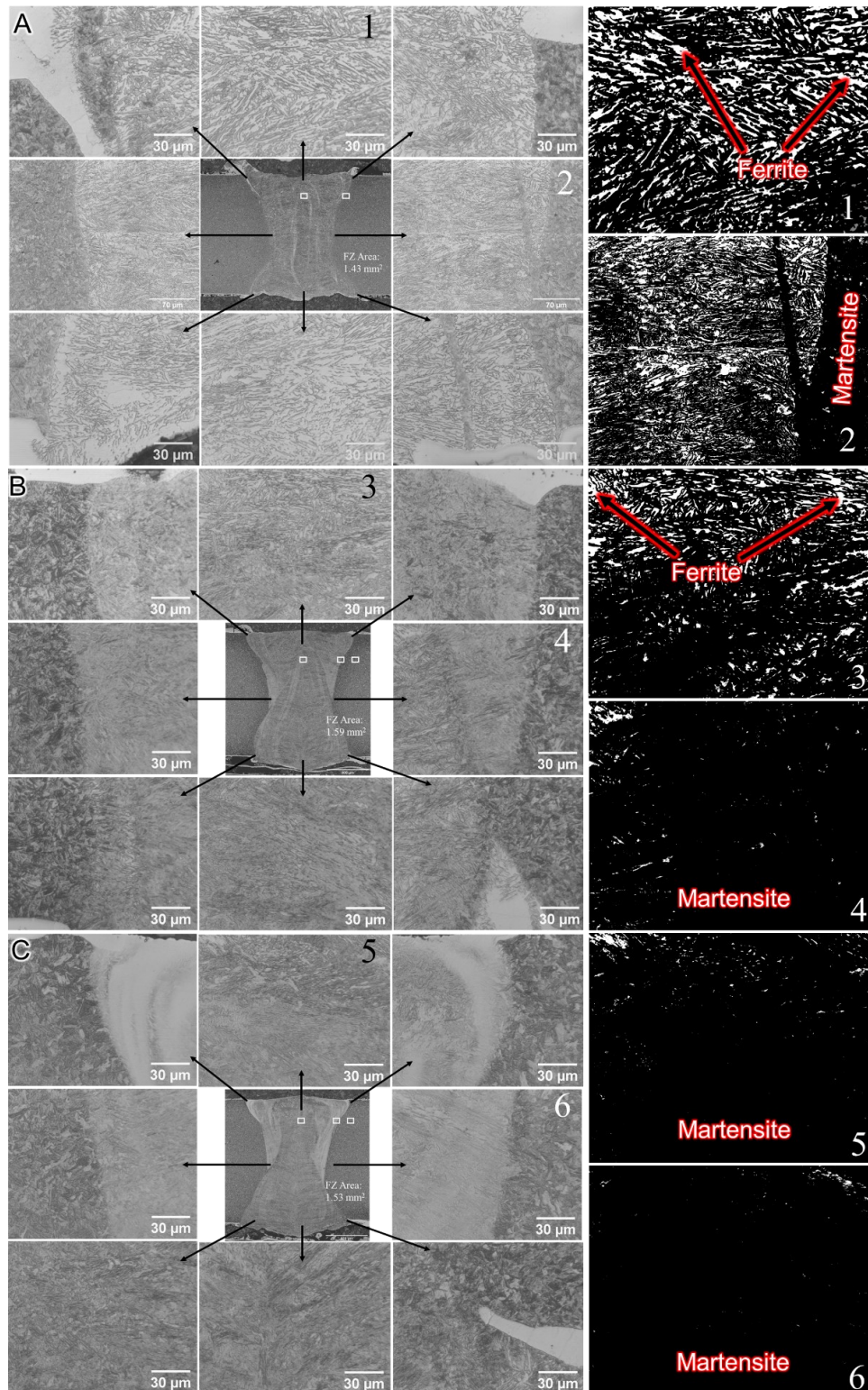


Figure 63: Optical microscopy showing the differences in microstructure for the (a) ARWHS, (b) WWCHS, and the (c) WIHS samples. The black arrows indicate the regions where high magnification images were taken from and the white insets show the regions of interest that were investigated further using FE-SEM. The figures shown with an associated number were analyzed using image analysis to measure the phase volume fraction of martensite (shown as the black phase) and α -ferrite (shown as the white phase).

The HSBM microstructure in all the samples was found to be lath martensite (LM), with islands of lower bainite (LB) and traces of acicular bainite (AB) (similar to the morphological features observed and characterized by Zhao et al. [164]), as shown in Figure 64 (b). The dual-phase microstructure, that was predicted by the CCT diagram shown in Figure 60 (a) was confirmed by the micrographs of the FZ of the ARWHS sample, shown in Figure 64. This dual-phase ferrite/martensite morphology of the ARWHS sample was characterized in a detailed study by Saha et al. [125]. The micrograph shown in Figure 64 (d) shows α -ferrite grains which formed by way of nucleation and grain growth during the hot-stamping heat treatment [125]. There were small traces of cementite (θ) found in some of the α -ferrite grains, while the LM matrix appeared to be free of any autotempered carbides, on account of the lower martensite start temperature due to the higher Al-content in the weld [125]. It was observed from the micrographs that the martensitic matrix was characterized by the presence of martensitic-austenitic (MA) constituents and large blocky martensite with a smooth surface, resembling similar morphological features that have been reported in the literature [165,166]. The smoother surface of this type of martensite was because it contained more supersaturated carbon and as a result it was more difficult to etch [167].

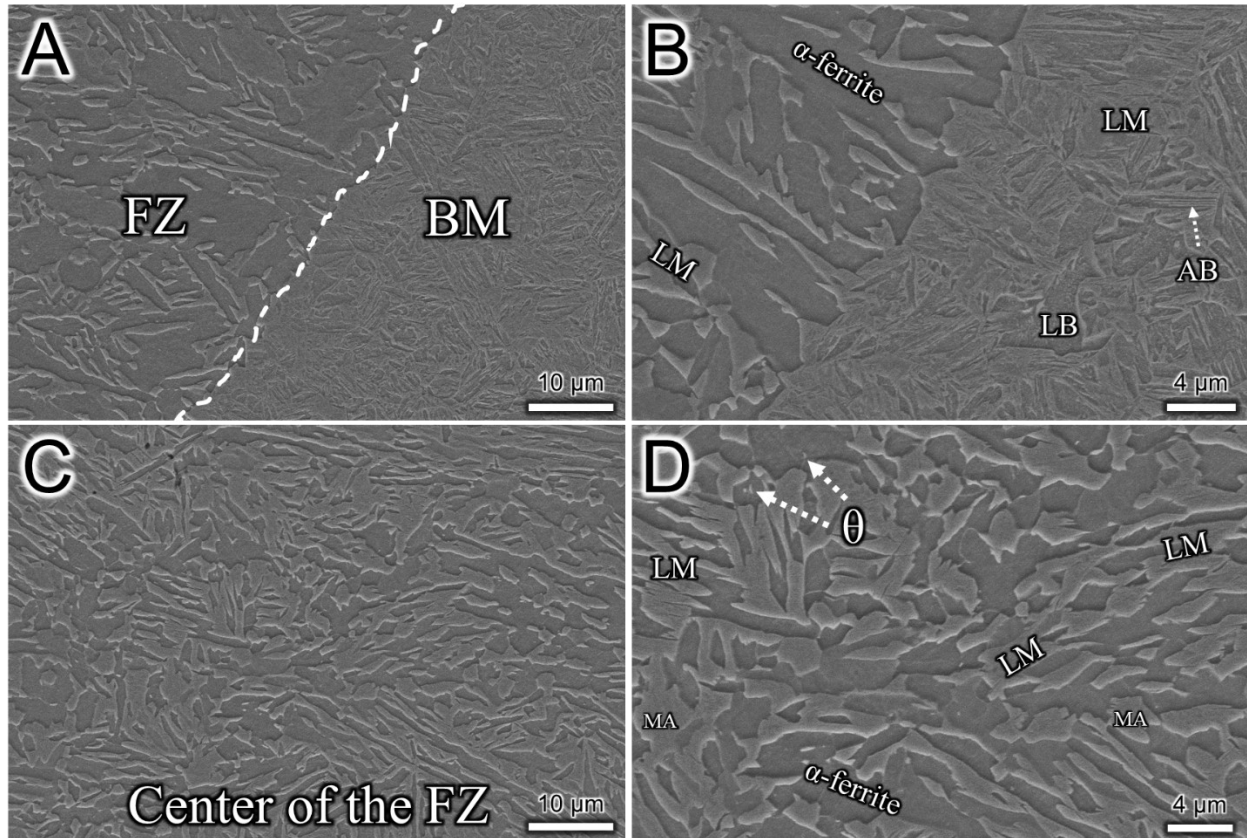


Figure 64: High magnification FE-SEM images of the ARWHS sample at the (a, b) fusion boundary and at the (c, d) center of the weld clearly showing the dual phase ferrite-martensite morphology of the FZ. (LM: lath martensite, LB: lower bainite, AB: acicular bainite, θ : cementite, PAGB: prior austenite grain boundary, MA: Martensite-austenite constituent)

The high-magnification FE-SEM images of the microstructure from the FB and center of the FZ of the WWCHS sample, identified by the insets shown in Figure 63 (b), are shown in Figure 65. The microstructure at the FB showed that α -ferrite formation had been completely suppressed, and the morphology was characterized by highly refined laths of martensite, with some islands of LB and AB. During laser welding, nanosized WC particles were diluted into the FZ, based on the Marangoni flow which has been discussed in detail elsewhere [25]. The WC particles were dispersed randomly along the length of the FB, as shown in Figure 65 (b). No WC nanoparticles were found in the region enclosed by the red-dotted lines shown in Figure 62, confirming that the WC particles flowed into the weld along the FB during laser welding and became trapped as the weld pool quickly solidified [121]. It is worth noting that during laser welding, the WC particles in the ESD-modified coating that were in direct contact with the laser beam would have melted and decomposed, increasing the dissolved tungsten and carbon content at the FB which diffused into the FZ during hot-stamping. Consequently, the average W- and C-content at the center of the FZ was higher (about 0.25 and 0.26 wt.% for W and C, respectively) compared to the ARWHS condition, resulting in a reduction in the α -ferrite PC which was measured to be around 13%. The dual-phase microstructure observed at the center of the FZ was characterized by sparsely dispersed

α -ferrite islands embedded in a martensitic matrix, as shown in Figure 65 (h). The CCT diagram for this composition, shown in Figure 60 (c), predicted that upon quenching, the microstructure at the center of the FZ would be a dual-phase mixture of martensite and ferrite, similar to what was observed. The martensitic matrix was characterized by the presence of MA constituents and large blocky martensite with a smooth surface, similar to what was observed in the LM matrix of the ARWHS sample.

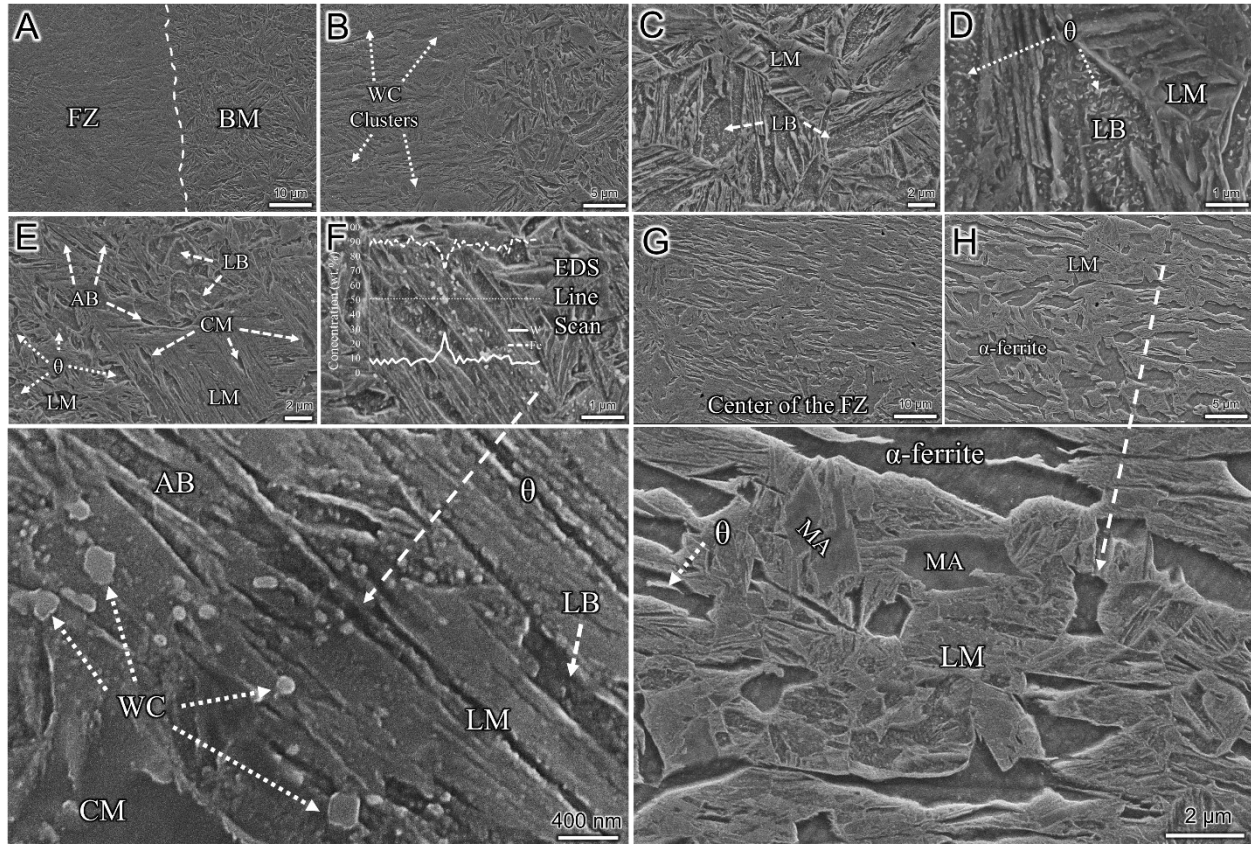


Figure 65: High magnification FE-SEM images of the WWCHS sample showing the (a, b) fusion boundary, the (c, d) base material to the right of the fusion boundary, the (e, f) edge of the FZ close to the fusion boundary, and the (g, h) center of the FZ. The high magnification inset shows the abundant presence of nanosized WC particles found in the FZ along the FB. The other high magnification inset shows the sparse presence of the ferrite phase dispersed in the martensitic matrix at the center of the FZ. Finally, the inset of an EDS line scan is shown in (f) to confirm the presence of WC nanoparticles at the FB. (LM: lath martensite, LB: lower bainite, CM: coalesced martensite, AB: acicular bainite, θ : cementite, M*: plate martensite, MA: martensite-austenite constituent)

The complete suppression of α -ferrite at the FB, as shown in Figure 65 (e), was achieved due to two main reasons. The first was a direct consequence of the increase in the local W- and C-content present as solid-solution in the Fe-matrix and the second reason was due to the abundant presence of nanosized WC particles, which had a total phase fraction of about 8% in the FZ. The majority of WC nanoparticles were found in the FB region (shown by the white dotted lines in Figure 62), which had a measured W content of about 7.5 wt.%, with a WC nanoparticle phase fraction of about 5%. This meant that about 4.8 wt.% of the W present in the FB region was tied

up in the WC, since it is known that WC has a mass distribution of 94 wt.% W and 6 wt.% C. This means that the average W- and C-content dissolved in the FB region of the WWCHS sample was about 2.70 and 0.42 wt.%, respectively.

The CCT diagram for this alloying composition, showed that the increase in dissolved W- and C-content pushed the ferrite nose to the right so that on quenching at 30 °C/s, the microstructure would be completely martensitic, as shown in Figure 60 (d). Khan et al. [152] reported in a separate study (Chapter 4) that an increase in the average C-content in hot-stamped 22MnB5 steel stabilized the single-phase γ -region in the Fe-Al phase diagram which led to a reduction in the observed α -ferrite content, which is in agreement with the observations made here. In addition to the change in the solid-solution composition, the presence of the nanosized WC particles had a profound effect on the microstructural morphology of the FB region as well. The presence of these nanoparticles helped to refine the morphology of the martensite at the FB, significantly increasing the hardness of this region, as clearly shown by the microhardness map in Figure 70 (b). The presence of numerous nanosized WC particles randomly dispersed at the FB significantly inhibited γ grain growth during the heating stage of hot-stamping, due to the grain boundary pinning effect [168–174], which effectively states that the presence of an inclusion/particle in the plane of a grain boundary, acts as a discontinuity which forces the creation of the missing portion of the boundary by pushing it away from the particle. Ray et al. [171] showed that it was the energy needed to create the missing segment of the boundary that was responsible for the impediment to the growth of γ grains.

The presence of the WC particles led to highly refined lath martensite by limiting the growth of the γ grains during austenitization at 930 °C, as shown in Figure 65 (e). The finer martensitic laths were punctuated by islands of coalesced martensite (CM). Bhadeshia and others have shown that under special circumstances, adjacent martensitic or bainitic plates that share the same habit plane and variant of the orientation relationship with the prior γ tend to coalesce to form coarser microstructures [175–177]. Therefore, as the martensitic laths become finer, the stress acting on individual plates increases during the quenching stage of the heat treatment, increasing the propensity for these plates to combine and coalesce [178,179]. Similar CM structures were observed and analyzed in detail by Pous-Romero and Bhadeshia [180]. The FB microstructure also showed the presence of LB and traces of AB, which has been shown to form at lower temperatures, nucleating inside the grains rather than at the grain boundaries in highly stressed microstructures [164].

EBSA analysis of the microstructure at the FB of the WWCHS has been shown in Figure 66. Based on the image quality and phase (IQP) map (Figure 66 (a)), the WWCHS sample showed a fully martensitic microstructure with extremely fine lath morphology, similar to what was observed in the FE-SEM micrographs. Further confirmation of the fully martensitic microstructure was provided by the inverse pole figure (IPF) map, which revealed fine martensite laths within the

martensite blocks, as shown in Figure 66 (b). The presence of the nanosized WC particles prevented the coarsening of γ grains, which restricted the size of the martensitic packets and blocks [181], leading to highly refined laths in the microstructure. The presence of the refined martensitic laths, led to the coalescence of some of these laths to relieve some of the internal stress in the microstructure, as shown in Figure 66 (a). The presence of the lesser strained CM was confirmed using the grain reference orientation deviation (GROD) map which is a grain-based misorientation parameter used to illustrate the strain-induced changes in microstructure [182], as shown in Figure 66 (c). The martensite morphology was further characterized by using the local average misorientations (LAM) map which determined the misorientation angle of grain boundaries by calculating the average angle of all the neighboring points, as shown in Figure 66 (d). According to the LAM map, the martensitic lath interface displayed a high degree of local misorientation. Since the γ to martensite transformation results in an approximate volume expansion of about 4% within the microstructure [183], geometrically necessary dislocations (GNDs) are formed between the lath interfaces to maintain the continuity of the lattice. Indeed, it is the presence of these GNDs which are responsible for the high LAM value observed at the lath interfaces, as shown in Figure 66 (d). The $\{100\}$ pole figure (PF) acquired from several individual grains in the microstructure at the FB have been shown in Figure 66, which combined with the IPF map confirms that the microstructure in the FZ of this sample was randomly textured because the presence of the WC nanoparticles restricted the size and shape of the martensitic packets and blocks, resulting in highly strained and somewhat misoriented martensitic laths.

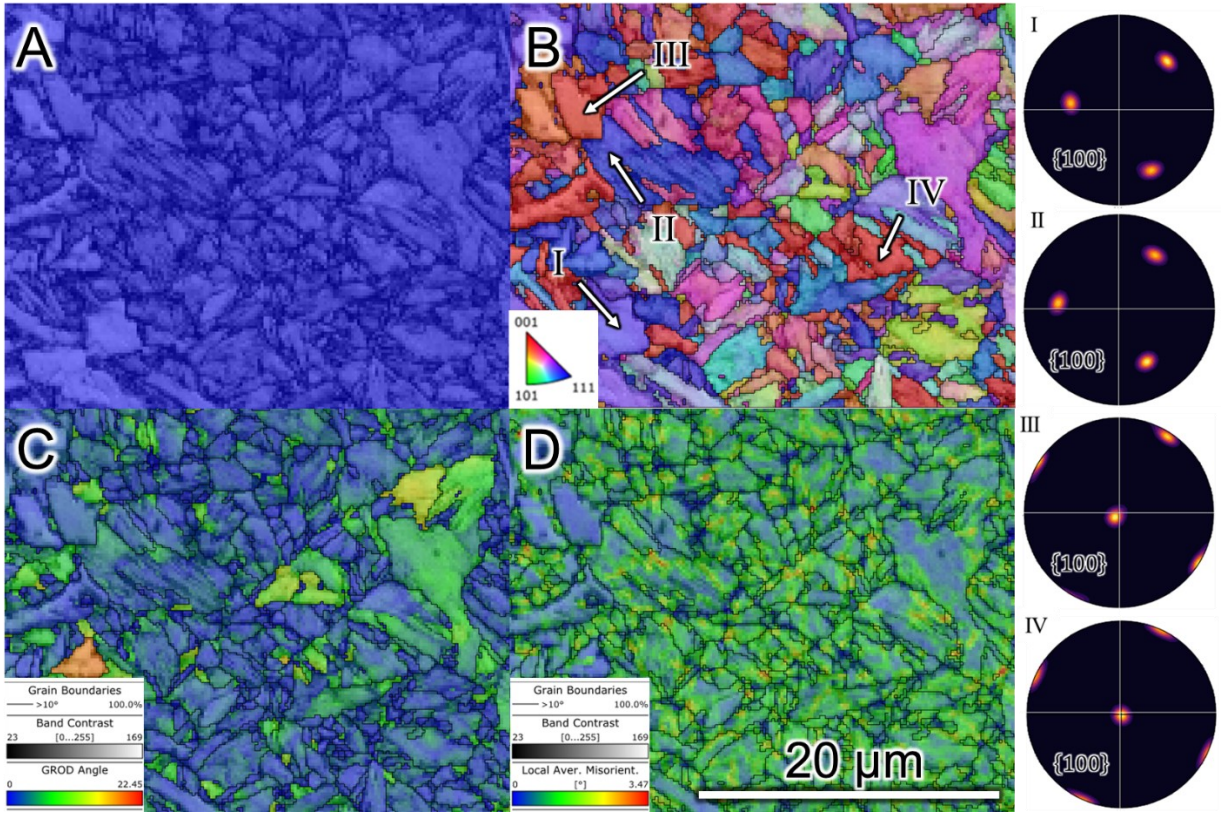


Figure 66: EBSD analysis showing the (a) IQP map, (b) IPF, (c) GROD, and (d) LAM maps of the FB region of the WWCHS sample. The PFs for several individual grains along {100} are also shown.

The microstructure of the WIHS sample was relatively homogenous (Figure 67) compared to the other two samples because there were no traces of α -ferrite observed in the weld microstructure. In fact, the CCT diagram shown in Figure 60 (b), predicted that the morphology of the steel with a Ni-rich alloying composition would be purely martensitic when quenched at 30 °C/s. At the FB, there was a 4-6 μm thick region that had a relatively higher Ni- and Cr-content which made this region highly resistant to etching, and consequently, revealing the microstructure was challenging, as shown in Figure 67 (e). The microstructure at the FB adjacent to the under-etched region is shown in Figure 67 (f).

Increasing the Ni-content of the FZ had a profound effect on the microstructure and mechanical properties. It has been shown that Ni stabilizes the γ -phase by enlarging the γ -phase region, resulting in the inhibition of ferritic and bainitic transformation [184]. Consequently, the FB microstructure was fully martensitic with several types of different martensite morphologies being observed, as shown by the high magnification inset in Figure 67 (f). The presence of numerous small, concave grains of coarse martensite (CM*) was observed in the microstructure. Tian et al. [159] and Yao et al. [184] have also observed the presence of CM* but referred to it as athermal and prior martensite, respectively, which is thought to form at the beginning of the

cooling stage of the quenching process. It has been reported that CM* has a lower C-content which decreases its hardness but improves the toughness properties [166,184].

The solid-solution strengthening effect of the alloying elements increases the internal stresses in the untransformed γ [185] which leads to the formation of significantly refined LM and plate martensite (PM). On the other hand, the microstructure at the center of the FZ had very few grains of CM* because the Ni-content at the center of the weld was relatively lower than at the FB. Instead, there was a large PC of LB that was observed which likely formed due to the presence of dissolved Cr from the ESD-modified coating which is known to shrink the γ -phase region in the Fe-Al phase diagram while promoting bainitic transformation [186]. The presence of AB was also observed, surrounded by refined LM. There were traces of lenticular martensite (shown with * in Figure 67) observed adjacent to several LM grains, which is a known type of martensite that forms in Ni-rich steels [187].

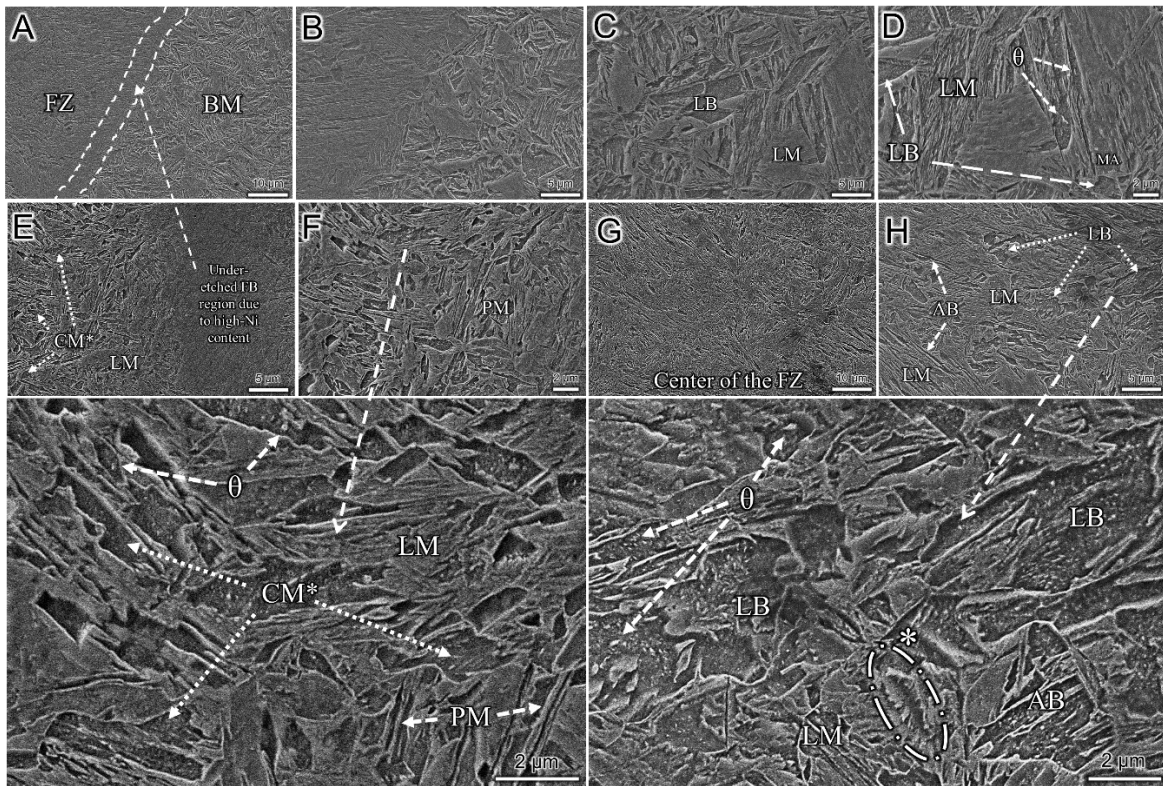


Figure 67: High magnification FE-SEM images of the WIHS sample showing the (a, b) fusion boundary, the (c, d) base material to the right of the fusion boundary, the (e, f) right edge of the FZ close to the fusion boundary, and the (g, h) center of the FZ. The high magnification inset shows the abundant presence of coarse and lath martensite found in the FZ along the FB. The other high magnification inset shows a complex phase morphology at the center of the FZ with the presence of lath martensite, various different types of bainite and traces of cementite. (LM: lath martensite, LB: lower bainite, CM*: coarse martensite, AB: acicular bainite, θ : cementite, PM: plate martensite, MA: martensite-austenite constituent, Region shown with the dotted line and marked with an * is lenticular martensite)

The EBSD maps for the WIHS sample are shown in Figure 68. It is evident from the IQP map (Figure 68 (a)) that the grain structures for this sample are much larger compared to the

WWCHS specimen because the addition of Ni as a solid-solution in the microstructure stabilizes and promotes the growth of the γ -grains, resulting in the formation of larger martensite packets and blocks as clearly confirmed by the IPF in Figure 68 (b). The GROD map indicates that there are significantly more regions with high local misorientations compared to the WWCHS sample, which can be attributed to the solid-solution strengthening effect of the alloying elements. The LAM map showed the maximum local grain boundary misorientation angle was significantly lower ($\sim 3.13^\circ$) for the WIHS sample compared to what was observed in the WWCHS sample ($\sim 3.47^\circ$), clearly demonstrating the differences in martensitic morphology of the different samples. The $\{100\}$ PF acquired from several individual grains in the microstructure at the FB are shown in Figure 68, which combined with the IPF map confirms that most of the grains have a preferred texture along $\{100\}$ due to the presence of Ni that promoted the growth of the γ -phase allowing the martensite to have a more homogenized texture.

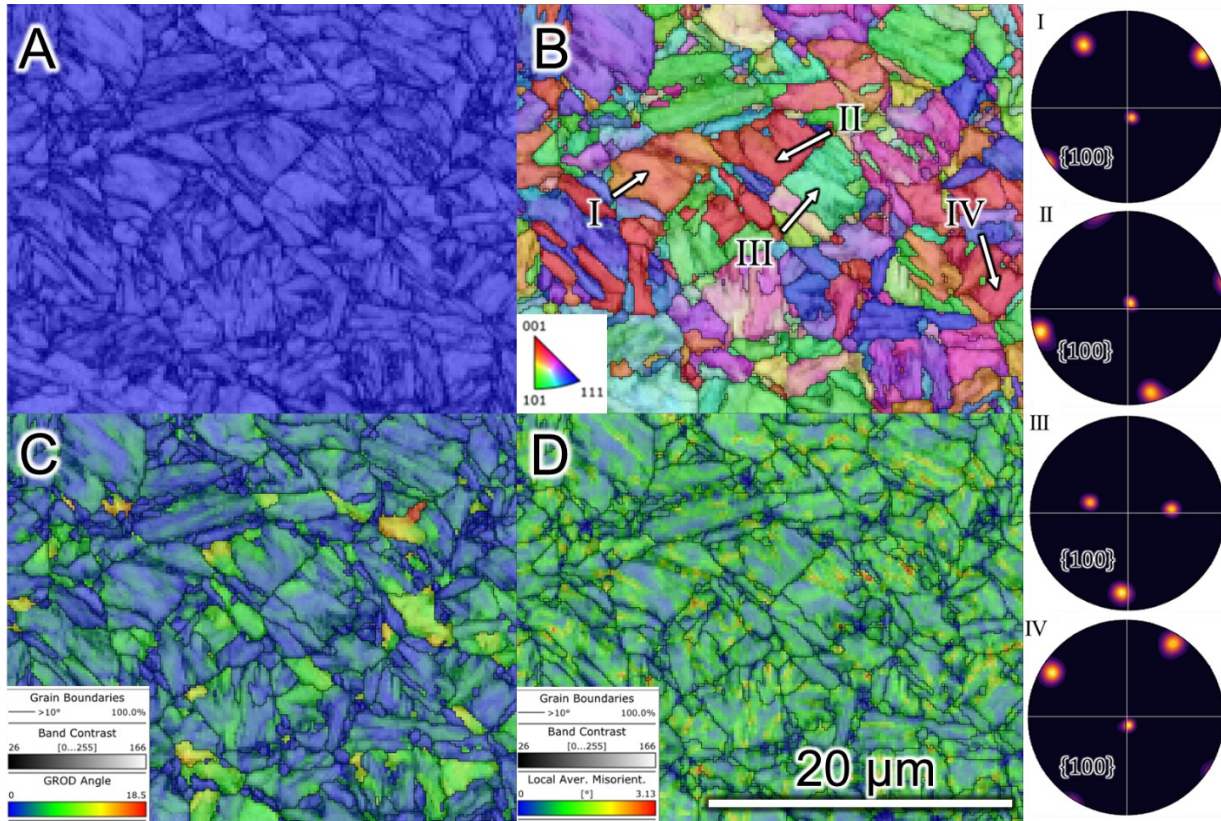


Figure 68: EBSD analysis showing the (a) IPF map, (b) IPF, (c) GROD, and (d) LAM maps of the FB region of the WWCHS sample. The PFs for several individual grains along $\{100\}$ are also shown.

The SXR analysis across the entire length of the WWCHS and WIHS samples, going from the HSBM on one side, then through the FZ, to the HSBM on the other side is shown in Figure 69 (a) and (b), respectively. The data confirms the presence of the different phases that were identified in the microstructure of the different regions of the samples. Most importantly, the SXR data confirms that almost no WC nanoparticles were observed at the center of the FZ of the

WWCHS sample, confirming that the WC nanoparticles were added into the molten weld pool during laser welding and became trapped at the FB during solidification, based on the Marangoni flow in the FZ during welding. At the end of the hot-stamping process, the FB was composed of refined martensite littered with an abundance of nanosized WC particles, some retained γ that was supersaturated in C, and with cementite (θ) being found in the LB and AB grains. The center of the FZ was composed of coarser martensite islands that were populated by MA constituents, and the SXRD confirmed the presence of trace amounts of cementite and Al_4C_3 particles, which would most likely be found in the α -ferrite grains and at the boundaries of the LM, acting as nucleation sites for the phases during quenching.

The SXRD data of the WIHS sample showed that the FZ matrix was composed almost entirely of martensite with traces of retained γ and θ . There were traces of several types of intermetallic compound (IMC) particles (i.e., Al_5Fe_3 , $AlNi_3$, and Al_3Ni) that were identified by SXRD which most likely formed during the deposition of the ESD-modified In625 coating on the Al-Si coated substrate. However, these IMCs weren't observed in the SEM micrographs, indicating that their volume fraction was extremely low. The WIHS sample had a much more uniform distribution of phases compared to the WWCHS sample because the alloying elements present in the Inconel coating dissolved into the Fe-matrix during welding and these elements were able to diffuse into the FZ freely during hot-stamping creating a much more homogenous microstructure in the weld.

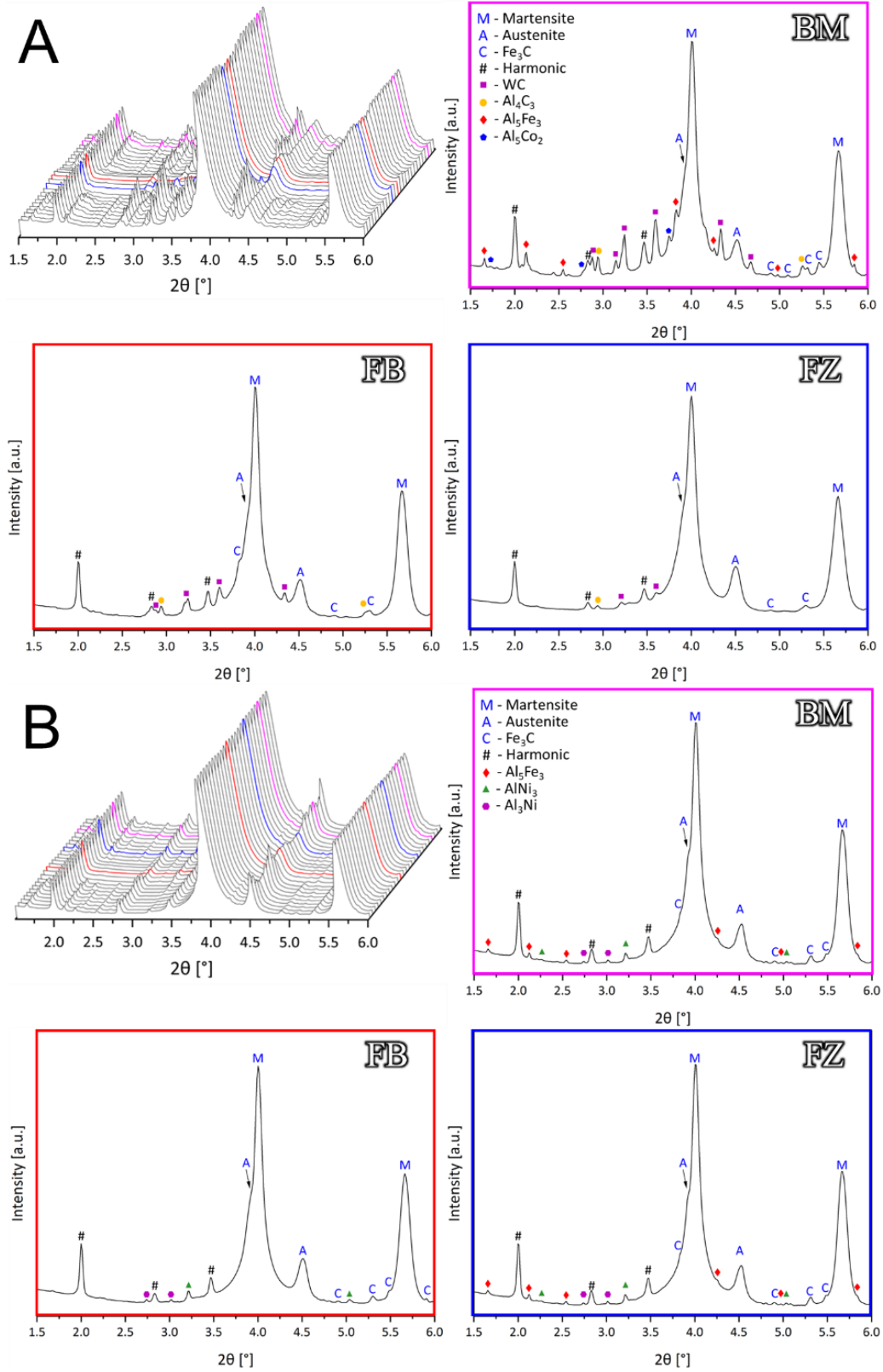


Figure 69: SXR data from the BM, FB, and center of the FZ identifying the different phases observed in these regions for the (a) WC- and (b) Inconel-coated samples.

5.4 Mechanical properties

The reduction in α -ferrite PC in the WWCHS and WIHS samples had a remarkable effect on the mechanical properties and load bearing performance of the welded joints. The differences in microhardness properties of the welds are illustrated by the microhardness maps shown in Figure 70. The dual-phase FZ of the ARWHS sample had an average hardness of 387 HV, which was significantly lower than that of the HSBM which had an average hardness of about 520 HV. The lower bulk hardness of the FZ in the ARWHS sample was attributed to the significantly lower hardness of the α -ferrite phase which was measured using nanoindentation to be around 5.31 GPa, compared to the nanoindentation hardness of 7.38 GPa of the surrounding LM (labelled as α'), as shown in Figure 70 (a). The nanoindentation load vs. depth (P-h) graphs in Figure 70 showed the differences between the mechanical response of the different phases during indentation. The α -ferrite phase (gray curve) deviated from the Hertzian elastic solution – which represents the start of fully plastic deformation – at a depth of about 67 nm during loading, which was greater than the depth at which the surrounding LM deviated from the Hertzian elastic solution. This is a reasonable observation given the known morphology and mechanical properties of the α -ferrite phase, which is softer and significantly more ductile compared to LM. On the other hand, the LM in the FZ of the ARWHS sample (red curve), showed the beginning of fully plastic deformation behavior at a much smaller depth of about 48 nm, given the excessive hardness and low ductility of this phase, exacerbated by the high MA-constituent fraction.

The presence of the WC nanoparticles, and the higher solid-solution W- and C-content along the FB of the WWCHS samples significantly increased the local microhardness at the FB to about 720 HV, while the average hardness at the center of the FZ was measured to be about 475 HV, as shown by the line scan and hardness map in Figure 70 (b). The effect of WC nanoparticles on the hardening of the microstructure can be calculated using the rule of mixtures [188,189] proposed by Kim [190], which states that:

$$\bar{H}_{EST} = f_h H_h + f_s H_s \quad (13)$$

where, \bar{H} represents the effective hardness of the composite material strengthened by a secondary phase, based on an equal strain treatment which represents the upper bound of hardness. f_h and f_s represent the volume fraction, and H_h and H_s represent the known hardness values of the hard and soft phases respectively.

The phase fraction of the WC particles at the FB was measured to be around 0.08 with the remainder assumed to be LM. Accordingly, the effective hardness of the WC-rich microstructure was calculated to be approximately 655 HV which was about 70 HV lower than the measured value. The remaining difference in hardness can, therefore, be attributed to the increase in the dissolved W- and C-content in the weld, that effectively suppressed the formation of α -ferrite and increased the maximum hardness of the martensite after quenching. The nanoindentation hardness

results of the LM at the FB showed a hardness increase to about 8.45 GPa and the P-h graph (blue curve) showed that the phase displayed fully plastic deformation at a depth of about 39 nm, confirming that the presence of the WC particles and the local increase in W- and C-content helped to significantly increase the hardness of the LM, but at the same time decreased its toughness, making it more susceptible to brittle failure.

The Ni-rich WIHS sample had an average FZ microhardness of about 557 HV which was very close to the microhardness of the HSBM. It was observed that the nanoindentation hardness of the Ni-rich martensite at the FB was about 6.32 GPa, which was higher than that of the α -ferrite but lower than that of the LM found in the ARWHS and WWCHS samples. Perhaps the most interesting finding was that the P-h graph (green curve) showed that the Ni-rich martensite in the WIHS sample displayed fully plastic behavior at a depth of about 89 nm, higher than all the other phases investigated as part of this study.

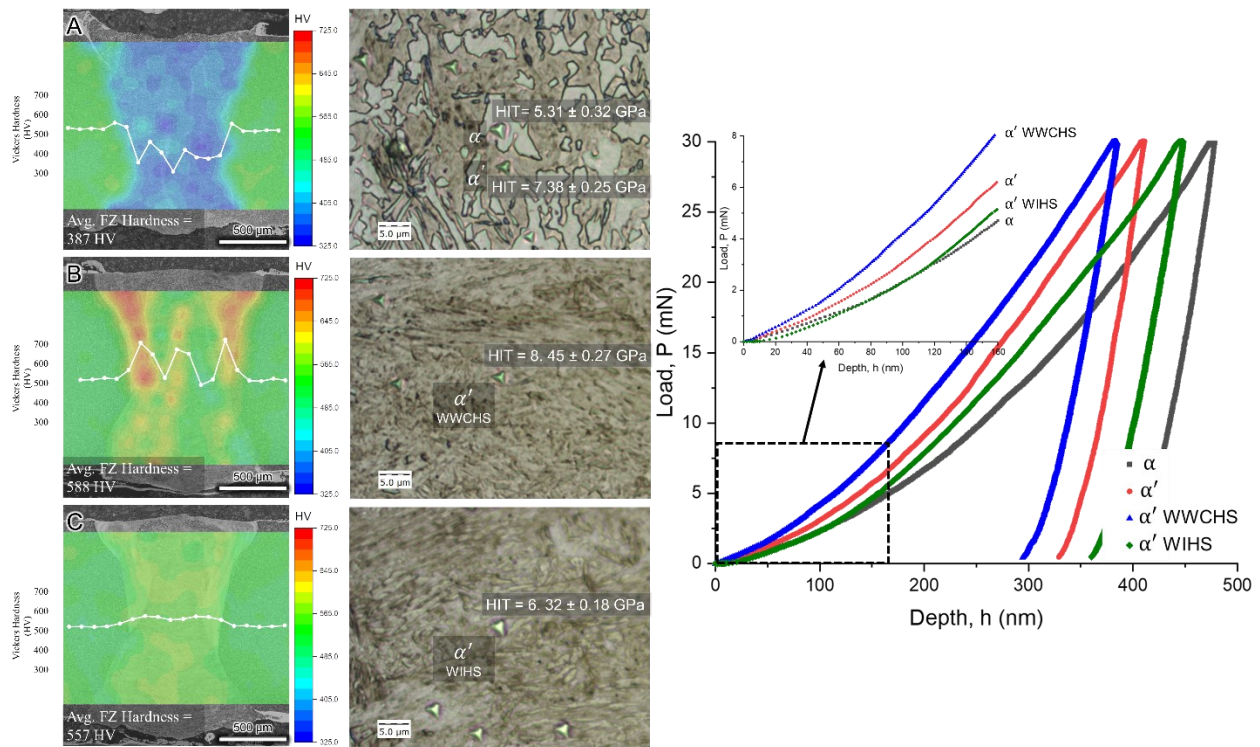


Figure 70: Microhardness maps and line scans, along with the nanoindentation results for the (a) ARWHS, (b) WWCHS, and the (c) WIHS samples. The graph shows the Load vs. Depth graph for the nanoindentation results which provides insight into the mechanical behavior of a given type of phase as it transitions from fully elastic to fully plastic deformation behavior.

The characteristic flow curve for hot-stamped 22MnB5 steel is shown in Figure 71, which had a UTS of about 1505 ± 27 MPa, falling within the range that has been reported in the literature [74,152,156]. The fracture surface of this sample showed characteristic signs of ductile failure with large dimples being observed, as shown in Figure 72 (a). The fractured sample showed clear signs of banding around the fracture region (shown by the white arrow in Figure 71) and the fracture

surface was characterized by a large region showing the occurrence of stable plastic deformation during tensile testing (shown by the white arrow in Figure 72 (a)).

Since the average FZ microhardness of the ARWHS sample was significantly lower due to the dual-phase microstructure, it is not surprising that the tensile strength of the weld was measured to be around 1231 ± 35 MPa, with sudden catastrophic brittle failure being observed in the weld at the FB, as shown by the red arrow in the inset in Figure 71, which agrees with the data and observations reported in the literature [74,126,152,156]. The fractography analysis of this sample showed that the material underwent brittle failure by way of catastrophic rupture as shown by the cleavage-like appearance of the fracture surface and the large abundance of intergranular cracks in Figure 72 (b), with no signs of stable plastic deformation being observed at the fracture surface. Analysis of the fracture cross-section, shown in Figure 73 (e), confirmed that the crack propagated along the FB inside the FZ, following a path through the martensitic islands with a high abundance of the MA-constituent. MA is a high-hardness constituent composed of martensite and austenite containing carbon-enriched untransformed austenite [191]. The PC of the MA constituent has a strong influence on the ductile-to-brittle transition temperature (DBTT) making the steel excessively brittle if the PC is too high [191,192]. In fact, the large difference in hardness between MA and the surrounding matrix means that cracks are easily initiated and propagated in steels containing MA [193]. Therefore, it is reasonable to see that the crack in these samples propagated through the MA-enriched martensitic islands.

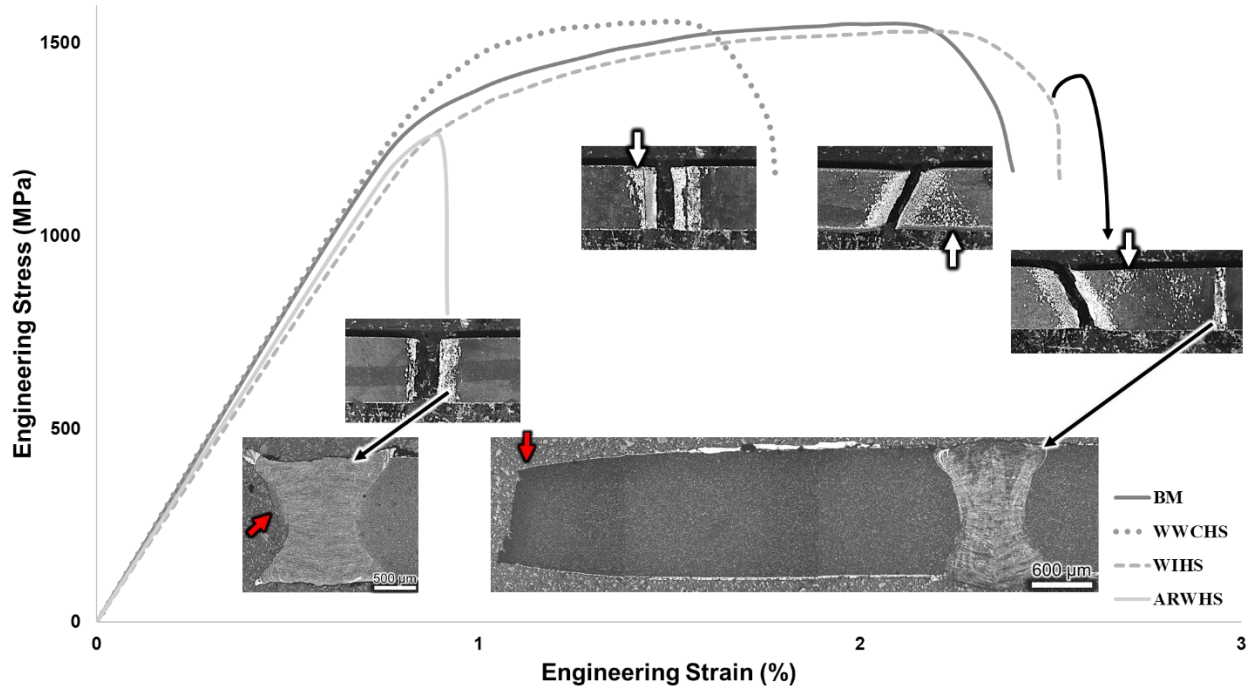


Figure 71: Characteristic flow curves for the HSBM, ARWHS, WWCHS, and the WIHS samples. The insets show the fracture location for the tested samples along with the OM images of the fractured samples, showing that the ARWHS sample failed catastrophically along the FB while the WIHS sample failed far from the weld in the BM by way of ductile failure, as shown by the red arrows. The white arrows show clear signs of banding on the tensile coupons, clearly indicating that these sample had undergone necking and therefore, failed in a ductile manner.

The samples with the ESD-modified coatings showed a significant improvement in the tensile properties of the weld compared to the ARWHS condition by successfully shifting failure from the FZ to the BM, as shown in Figure 71. The WWCHS sample had a UTS of about 1531 ± 51 MPa, with a significantly lower engineering strain, compared to the HSBM. The reason for this was that the failure in WWCHS sample occurred in the BM adjacent to the FZ, with the crack initiating at the weld toe where the steel was extremely hard (> 730 HV), due to the formation of extremely hard and brittle carbide phases, as shown in Figure 73 (a) and (b). The presence of these extremely brittle phases at the toe, surrounded by a softer BM on one side and a relatively harder FB region on the other side (strengthened by the presence of the WC nanoparticles) created a metallurgical notch [194], which made the microstructure at this location prone to cracking. During tensile testing, when the surrounding BM close to the metallurgical notch had yielded, the brittle toe region continued to get strained until it finally cracked – well beyond the UTS of the HSBM.

Since the crack initiated at the toe of the weld, it had to propagate through the thickness of the sample, either by propagating through the FB or through the adjacent BM. Due to the presence of a large volume fraction of WC particles along the FB of the weld which offered significant hindrance to the propagation of cracks through this microstructure, along with the significantly higher hardness of the FB martensite (which gave the microstructure at this location a higher yield point compared to the HSBM), crack propagation through the FB would be highly unlikely because

the microstructure would be resistant to yielding. On the other hand, the BM surrounding the weld had already yielded (i.e., plastic deformation had been initiated and void nucleation had occurred in the microstructure), as confirmed by the flow curve and clear signs of banding on the tensile coupon as shown by the white arrow in the inset in Figure 71. Therefore, the crack that initiated at the brittle toe region of the weld had the path of least resistance through the yielded BM that was undergoing void nucleation as the sample continued to plastically deform. Consequently, the fractured samples of the WWCHS condition showed a mixture of brittle and ductile failure, as shown by the fracture cross-sections in Figure 73 (c) and (d), respectively. The fractography analysis revealed that the fracture sample shown in Figure 72 (c) had very little stable plastic deformation in the tensile sample as compared to what was observed in the HSBM. However, the presence of dimples at the fracture surface clearly indicated that the BM had formed microvoids before final failure, resulting in partially ductile failure which can be confirmed by the fracture morphology shown in Figure 73 (d).

Finally, the WIHS samples showed the highest combination of strength and ductility, with the UTS being measured at about 1497 ± 32 MPa, and the highest engineering strain being recorded for these samples. The failure in these samples was far from the FZ in the BM and had characteristic features of a fully ductile fracture, as shown in Figure 71. The fractography analysis revealed the presence of numerous dimples across the fracture surface and the fracture samples showed the largest region of stable plastic deformation before failure, as shown by the white arrow in Figure 72 (d).

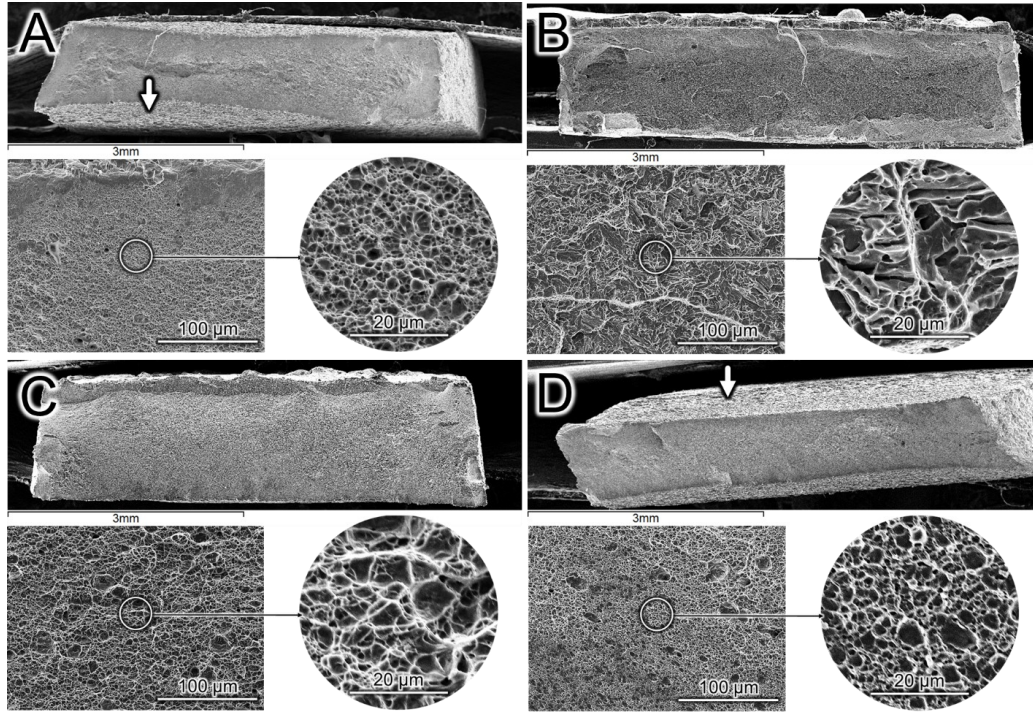


Figure 72: Fracture surface analysis of the (a) BM, (b) ARWHS, (c) WWCHS, and the (d) WIHS samples. The white arrows show the regions of the fracture sample that underwent stable plastic deformation before failure.

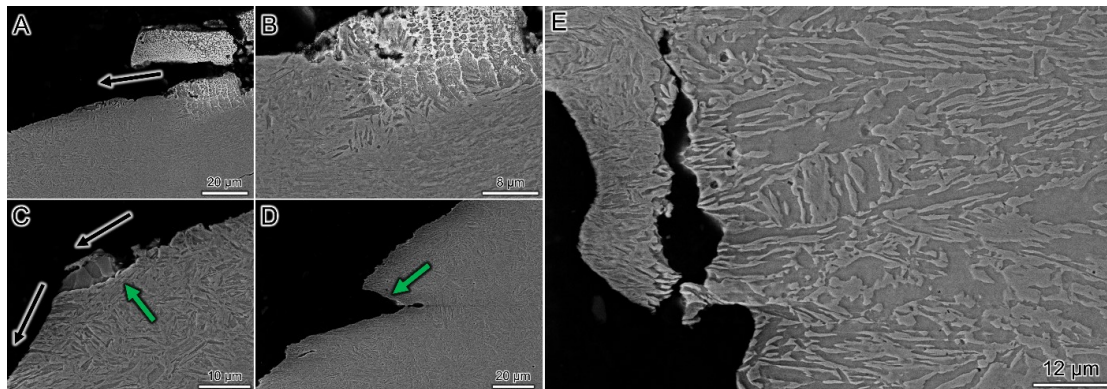


Figure 73: Cross-sectional images of the (a-d) WWCHS, and (e) ARWHS fractured samples. (a) shows that the fracture was initiated at the brittle (b) toe region, with (c) and (d) showing fracture features indicative of brittle and ductile failure, respectively, as shown by the green arrows, confirming that the WWCHS samples underwent a combination of brittle and ductile failure. (e) shows that the crack propagated through the martensitic islands in the FZ of the ARWHS sample that were rich in MA-constituents.

5.5 Conclusions

The presented study analyzed the effect of in-situ alloying of the FZ of laser-welded Al-Si coated 22MnB5 steel by welding through a WC and In625 ESD-modified coating on the resulting microstructure and mechanical properties of the weldment. The results showed that the addition of dissolved W and C in the FZ stabilized the austenite loop which led to a reduction in the α -ferrite phase concentration, but the increased austenite stability was still insufficient to result in a fully

as-quenched martensitic structure. However, the addition of WC nanoparticles reinforced the martensitic matrix by way of dispersion strengthening, thereby moving the failure location from the FZ to the BM when the weld was loaded. On the other hand, the addition of dissolved Ni and Cr in the FZ stabilized the austenite loop and significantly decreased the A_{c3} temperature which led to complete suppression of the α -ferrite phase formation in the weld, and again, moved the failure location from the FZ to the BM when loaded. The following conclusions can be made from this work:

- 1) Welding 22MnB5 steel through an ESD-modified WC coating changed the alloying chemistry of the FZ by increasing the volume fraction of WC nanoparticles at the FB of the weld. The WC particles were diluted into the molten weld pool based on the Marangoni flow, where they became trapped as the weld pool solidified.
- 2) The WC nanoparticles restricted the growth of the γ -phase, causing the formation of highly refined and randomly textured martensite. The large volume fraction of the WC particles increased the hardness of the microstructure at the FB which helped improve the mechanical properties of the joint.
- 3) During welding, some of the WC present in the ESD-modified coating melted and the decomposed W and C dissolved into the molten weld pool increasing the local content of these elements in the FZ. During subsequent hot-stamping, the W and C diffused through the weld, and during quenching, these elements played a critical role in suppressing the formation of the α -ferrite phase by stabilizing the γ -phase.
- 4) By reducing the α -ferrite PC in the FZ and improving the mechanical properties of the weld by way of WC dispersion strengthening, the failure in these samples was successfully shifted from the FZ to the surrounding BM.
- 5) Welding 22MnB5 steel through an ESD-modified In625 coating changed the alloying chemistry of the FZ by increasing the Ni- and Cr-content in the weld. The increase in Ni-content, which is a known γ -stabilizer, led to the complete suppression of α -ferrite phase in the weld.
- 6) The addition of Ni and Cr to the FZ helped refine the martensitic morphology such that the mechanical properties of the FZ were superior to the surrounding BM. Consequently, the tensile samples showed the best mechanical properties, with failure in these samples happening in a completely ductile manner in the BM, far away from the FZ.

Therefore, it can be concluded that by welding Al-Si coated 22MnB5 steel through an ESD-modified coating with a known alloying composition and thickness, the microstructure of the FZ can be controlled so that the mechanical properties of the weldment can be improved without requiring the laser ablation of the Al-Si coating prior to welding. The technique being proposed as part of this study goes beyond its relevance to the manufacturing of TWBs and instead, opens several new avenues for future research regarding the production of highly novel functionally-graded components that can be used in advanced manufacturing in different industries.

6 Suppressing α -ferrite and strengthening the FZ microstructure through in-situ alloying with nickel

* This chapter is composed of a published research paper [156] as outlined in the Statement of Contributions.

The previous chapter made it abundantly clear that the in-situ alloying of the FZ during laser welding is not just achievable but also an extremely effective method to improve the mechanical properties of the joint. The WIHS sample was particularly effective because the tensile performance showed that the microstructure in the FZ was stronger than the hot-stamped BM. However, due to the complex alloying chemistry of In625, a deeper investigation into the effect of specific alloying elements on the morphology and mechanical properties of the FZ was quite challenging. Therefore, a study was designed in which the effect of welding Al-Si coated 22MnB5 steel through a pure nickel coating on the microstructure and mechanical properties of the weld in the hot-stamped condition was investigated. This condition will be referred to as the welded with Ni and then hot stamped (WNHS) condition. The results were compared to the base condition where no nickel coating was used during the welding process, with the base condition being referred to as the ARWHS condition. This work showed that alloying Ni to the FZ of laser welded Al-Si coated 22MnB5 steel by welding through a pure Ni coating of a specified thickness, ferrite formation in the FZ was suppressed, whereby improving the mechanical integrity of the weld and successfully shifting failure from the FZ, where it normally occurs, to the base material. This work showed that by laser welding Al-Si coated 22MnB5 steel through a Ni coating completely eliminated the need to mechanically or chemically remove the Al-Si coating prior to welding.

6.1 Experimental details

The presented study was carried out on 1.5 mm thick Al-Si coated 22MnB5 PHS. Bead-on-plate (BOP) welds were made on 200 mm by 200 mm sized samples using an IPG Photonics YLS6000 Fiber Laser mounted to the Panasonic TA1600 6-axis robot. All welds were made perpendicular to the rolling direction of the steel using a laser power of 4 kW (as shown on the laser controller) and a welding speed of 6 m/min. The laser was defocused and had a positive BIA to ensure that weld concavity was minimized to < 5%. A 50 μ m thick pure Ni shim was applied to the area being welded using an adhesive, as shown in Figure 74 (g). BOP welds were made through the nickel coating as shown by the still images in Figure 74 (a – f) captured using the XIRIS XVC1000 welding camera at 90 fps. The samples were HS following welding, where they were heated in a furnace for 6 minutes to an austenitization temperature of 930°C and then quenched

using a water-cooled die at a cooling rate of approximately 30°C/s, which resulted in a fully martensitic microstructure in the as-received BM, as shown by the high magnification SEM images shown in Figure 78 (b) and Figure 80 (b).

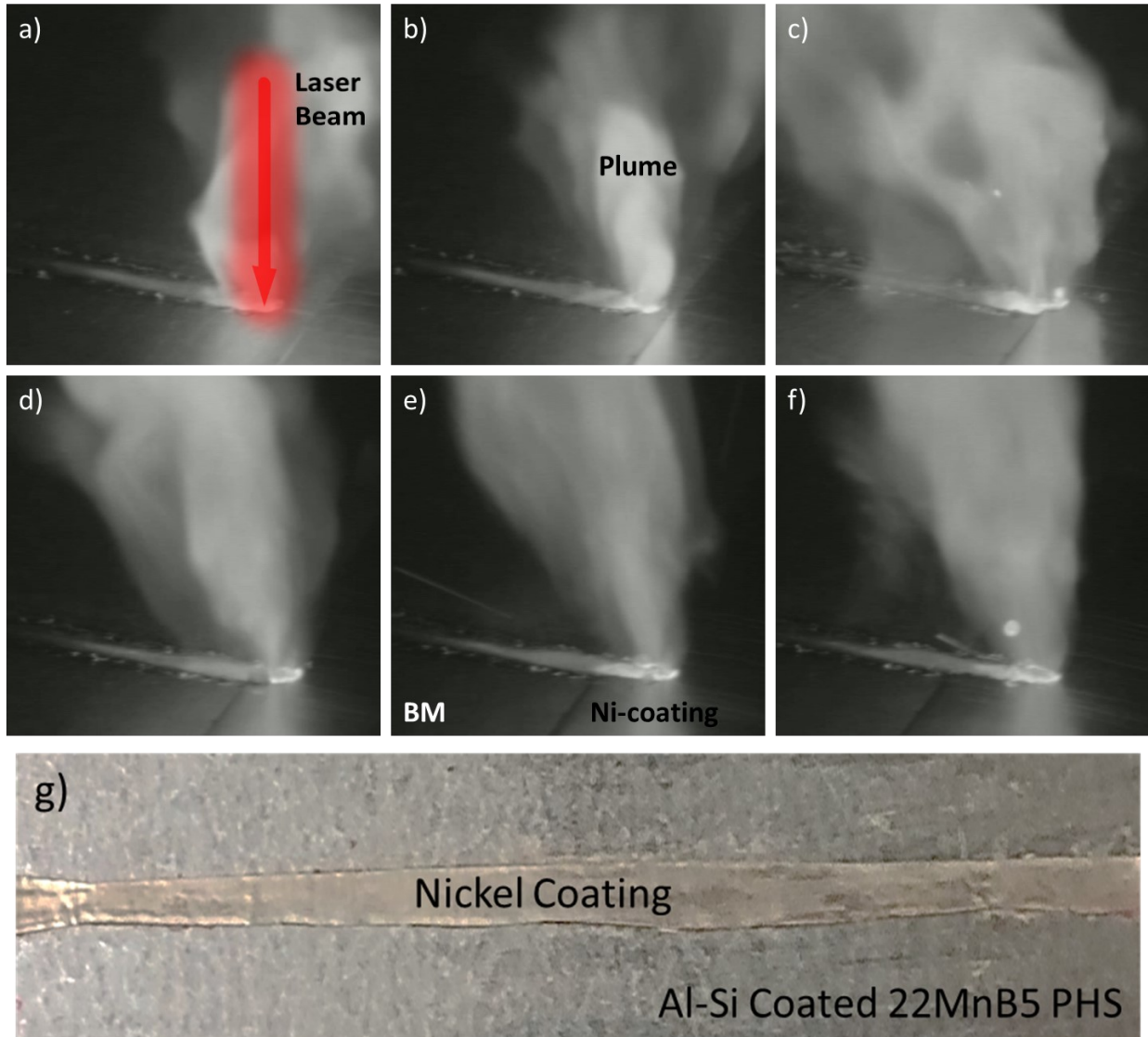


Figure 74: Frame-by-frame images of the welding process showing the weld being made as the laser travels from the non-coated substrate (a, b) to the Ni-coated substrate (c-f). The final image (g) is showing how the Ni-coating was applied to the Al-Si coated 22MnB5 PHS. The weld was made through the area that is covered by the Ni-coating.

The FZ and BM microstructure was analyzed using the Clemex Vision Lite Image Analysis software (v. 8.0.197) to measure the phase concentration (PC) of ferrite and martensite in the FZ. In order to validate the image analysis results, two separately welded samples for each condition were analyzed. Image analysis for the first set of samples was done for the entire FZ as shown in Figure 76. For the second set of samples, 3 regions of interest located at the FB and the center of the FZ were selected and image analysis was performed at these regions at high magnification to

measure the ferrite and martensite PC, as shown in Figure 77 and Figure 79, respectively. The ferrite PC for these regions was averaged and compared to the first set of samples to verify that the image analysis results were accurate. The Zeiss UltraPlus field emission scanning electron microscope (FESEM) was used to capture high magnification images of the BM, FB, and FZ to clearly identify the different phases.

Elemental analysis to determine the Al content in the ARWHS condition and the Ni content in the WNHS condition was done using the JEOL JXA-8230 electron probe micro-analyzer (EPMA). Hardness was measured using the Clemex CMT (v. 8.0.197) with a 200 gf and a 10 s dwell time. Hardness maps were constructed using OriginPro. Tensile coupons were first cut from the 200 mm by 200 mm sample using a water jet cutter and then machined in accordance with the ASTM E8/E8M standard with a gauge length of 50 mm. Each individual tensile coupon was pulled using the Instron 4206 at a crosshead speed of 1 mm/minute and an optical extensometer was used to measure the strain. A total of 4 tensile coupons were pulled for each condition.

6.2 Microstructural analysis

EPMA analysis showed that the FZ of the ARWHS sample had an Al content of 1.02 wt.% with no traces of Ni being found as shown in Table 8. The local Ni content in the FZ of the WNHS condition ranged from about 1.5 wt.% at the center of the FZ to 15 wt.% at the FB. The average bulk Ni content in the entire weld was found to be around 3.5 wt.% due to the dilution of the Ni-coating into the FZ during the welding process. The cross-sectional area of the FZ was measured at approximately 1.16 mm² and the cross-sectional area of the applied Ni-coating was approximately 0.055 mm² which means that theoretically, if all of the Ni-coating was to be diluted into the FZ, a bulk Ni content of about 4.74 wt.% would be expected which is higher than the measured value of 3.5 wt.%. The low Ni content in the FZ can mainly be attributed to the partial vaporization of the Ni-coating when it encounters the laser beam. The partial vaporization can be confirmed by the increase in the size of the vapor plume as the laser goes from the region of the substrate with no Ni-coating (Figure 74b) to the Ni-coated region (Figure 74c). The elemental map for Fe shows that the concentration of Fe is lower in the FB where the concentration of Ni is the highest, as shown in Figure 75 (a) and (b), respectively.

Table 8: Chemical composition of the weld fusion zone in the ARWHS and WNHS conditions (in wt.%).

Sample Condition	C	Mn	B	Si	Cr	Ti	Mo	P	Ni	Al	Fe
ARWHS	0.23	1.22	0.0032	0.27	0.20	0.04	0.02	0.01	0.00	1.02	bal.
WNHS	0.23	1.22	0.0032	0.27	0.20	0.04	0.02	0.01	3.52	0.73	bal.

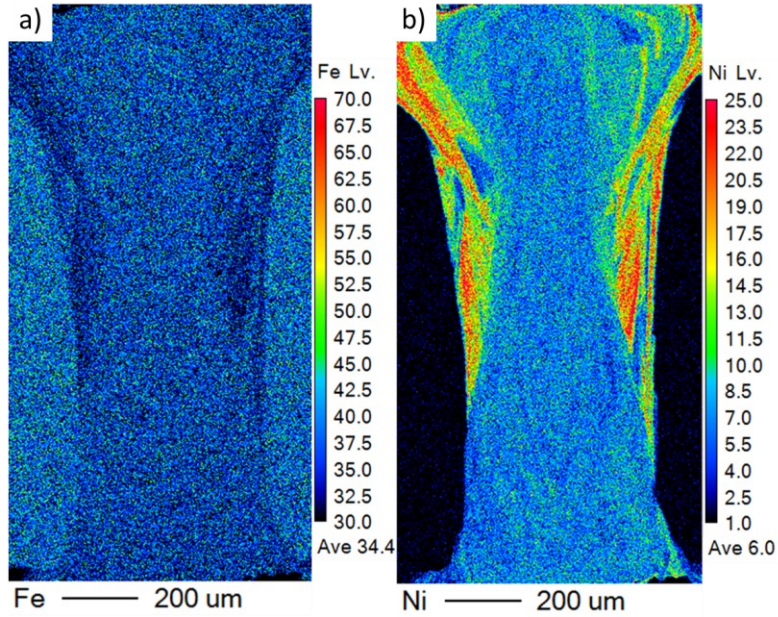


Figure 75: EPMA elemental maps for (a) Fe, and (b) Ni showing the dilution of the Ni coating into the FZ for the WNHS condition with the highest concentration of Ni found at the FB whereas the bulk of the FZ has a more even distribution of Ni content.

Image analysis was used to identify the PC of each phase present in the weld, as shown in Figure 76. When no Ni-coating was used, it was found that the FZ had a ferrite PC of 35.4%, shown by the gray phase in Figure 76 (c), and a martensite PC of 64.6%, shown by the green phase. These results are similar to those reported by Saha et al. for phase concentrations of the two phases present in the FZ of the ARWHS condition [74], and verified in separate independent studies by Khan et al. [152,157]. Alternatively, when analyzing the weld using the Ni-coating, the ferrite PC was reduced to 4.2% with the remainder being made up of martensite as shown in Figure 76 (d) and these results have been summarized in Table 9.

Table 9: Summary of the ferrite PC found in the ARWHS and WNHS conditions measured using image analysis for the entire FZ.

Sample Condition	Ferrite Phase Concentration	Martensite Phase Concentration
ARWHS	35.4%	bal.
WNHS	4.2%	bal.

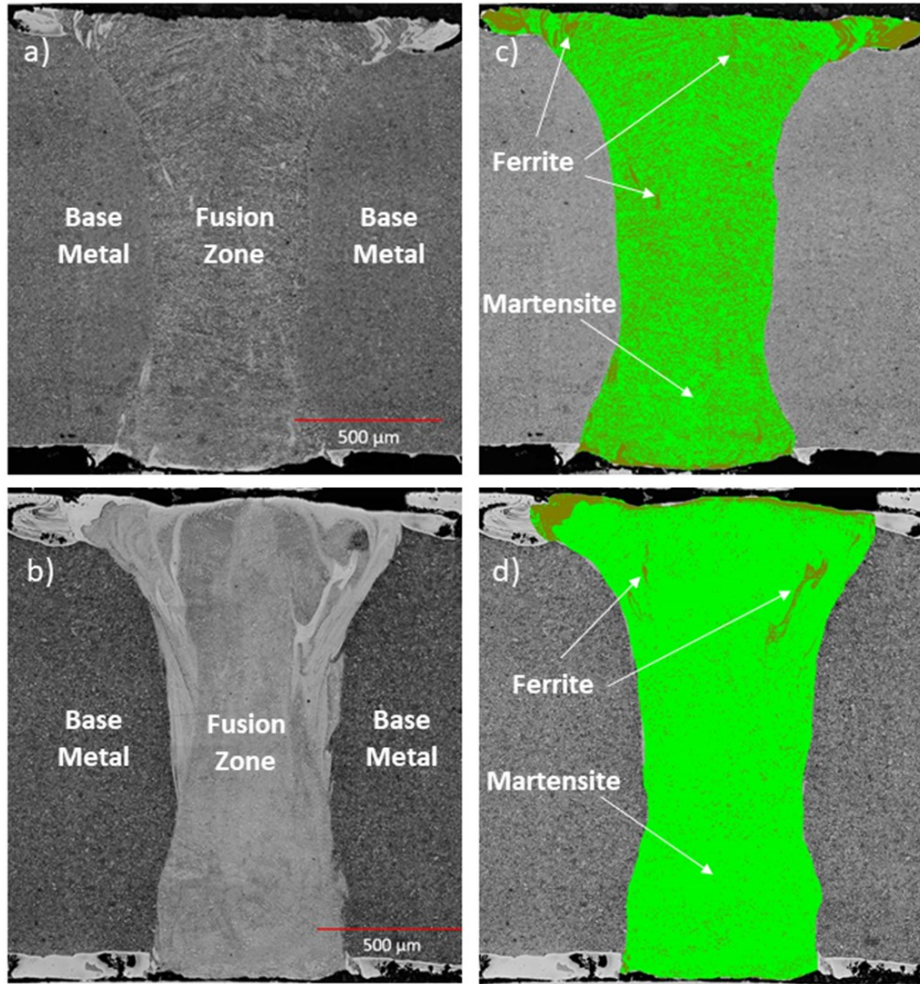


Figure 76: Optical micrographs of the (a) weld microstructure with no Ni addition, (b) Weld microstructure with Ni-coating, and image analysis using Clemex Vision Lite showing the PC of ferrite (gray color) and martensite (green color) in (c) and (d) for both conditions, respectively.

In order to verify the image analysis results shown in Figure 76, a second set of identical welds were prepared in the ARWHS and WNHS conditions and the micrographs of the weld cross-sections are shown in Figure 77 (a) and Figure 79 (a), respectively. Three regions of interest located at the left-side FB, right-side FB and the center of the FZ (shown as regions b, c, and d in Figure 77 and Figure 79) were selected so that the microstructure could be observed at higher magnification and image analysis could be performed for these regions. The measured PC of ferrite for each respective region from the ARWHS and WNHS condition is shown in Table 10. The average ferrite PC for these regions was calculated as 38.1% and 3.0%, respectively, which shows excellent agreement with the image analysis results for the entire FZ as measured for the first set of samples.

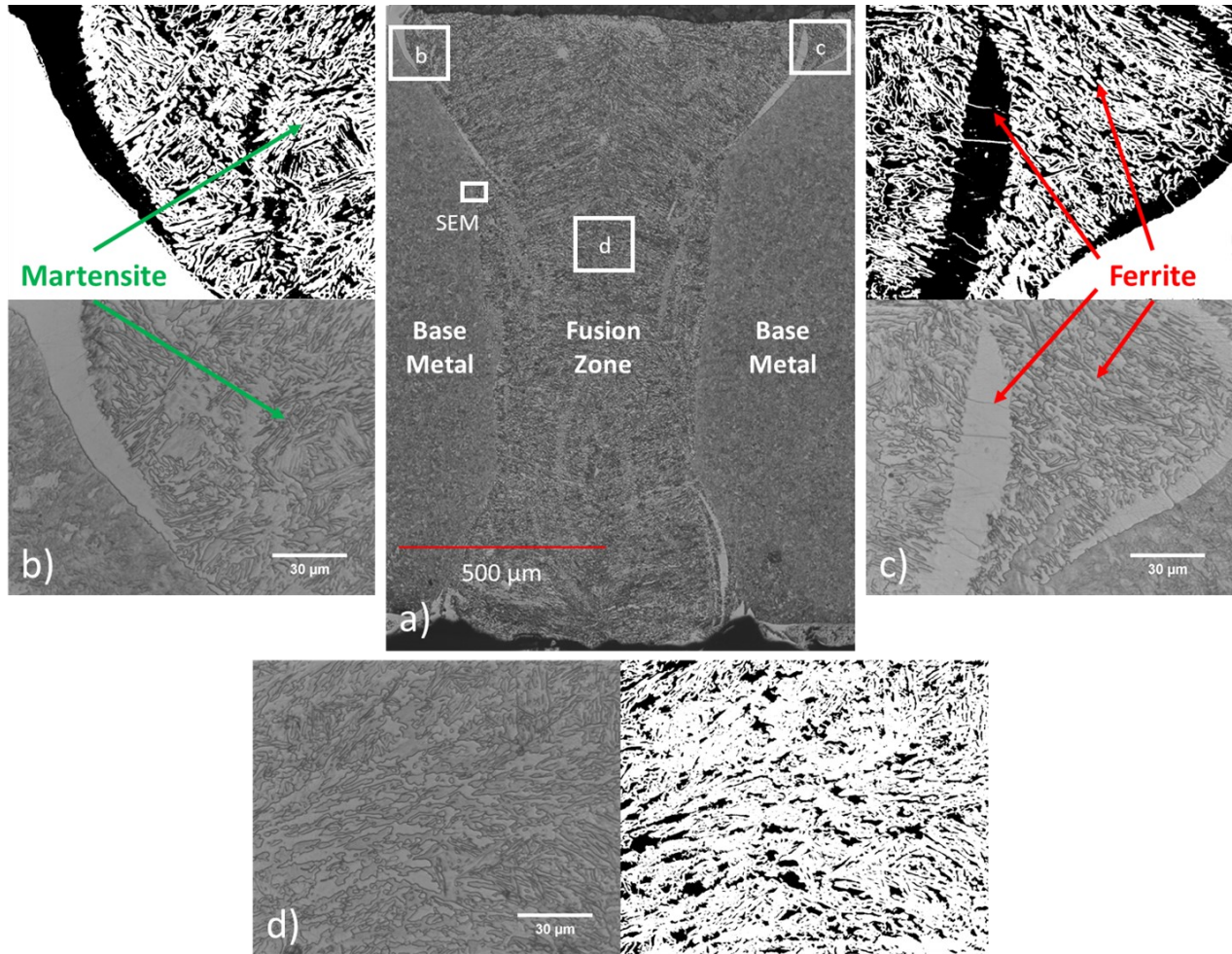


Figure 77: Optical micrographs of the (a) weld microstructure with no Ni addition, with high magnification images of the (b) left-side fusion boundary, (c) right-side fusion boundary, and the (d) center of the fusion zone with corresponding images showing the PC of ferrite (black color) and martensite (white color).

High magnification SEM images of the FB region for the ARWHS and WNHS condition are shown in Figure 78 (a) and Figure 80 (a), respectively. The SEM images confirm that the BM in both the ARWHS and WNHS conditions is fully martensitic as shown in Figure 78 (b) and Figure 80 (b), respectively. However, the microstructure morphology is significantly different for the FZ in the ARWHS and WNHS condition. The FZ in the ARWHS condition is characterized by the darker ferrite islands embedded in a martensitic matrix as shown in Figure 78 (c), which is similar to what has been shown in other studies [74,125]. The FZ in the WNHS condition is fully martensitic characterized by large grains of coarse martensite (CM) embedded in a lath martensite (LM) matrix, as shown by Figure 78 (c). Tian et al. [159] and Yao et al. [184] have also observed the presence of CM but referred to it as athermal and prior martensite, respectively [157]. Yao et al. [184] showed that CM had a lower carbon content as it formed at higher temperatures which would potentially give it better toughness properties compared to LM. Furthermore, they showed

that the CM etched easily, was darker in its appearance, and its microstructural morphology was concave similar to what has been shown in Figure 80 (c).

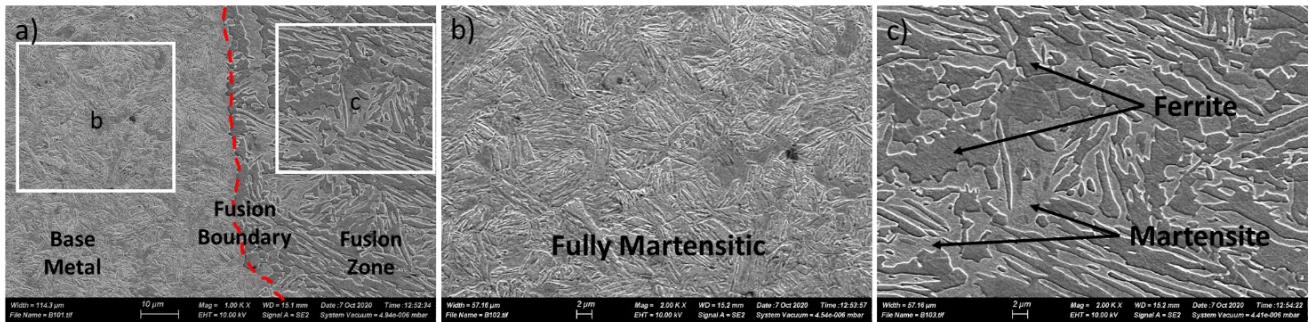


Figure 78: SEM images of the (a) fusion boundary of the ARWHS condition at the location specified in Figure 77 as well as high magnification images of the (b) base metal showing a fully martensitic microstructure, and the (c) fusion zone showing the ferrite phase embedded in a martensitic matrix.

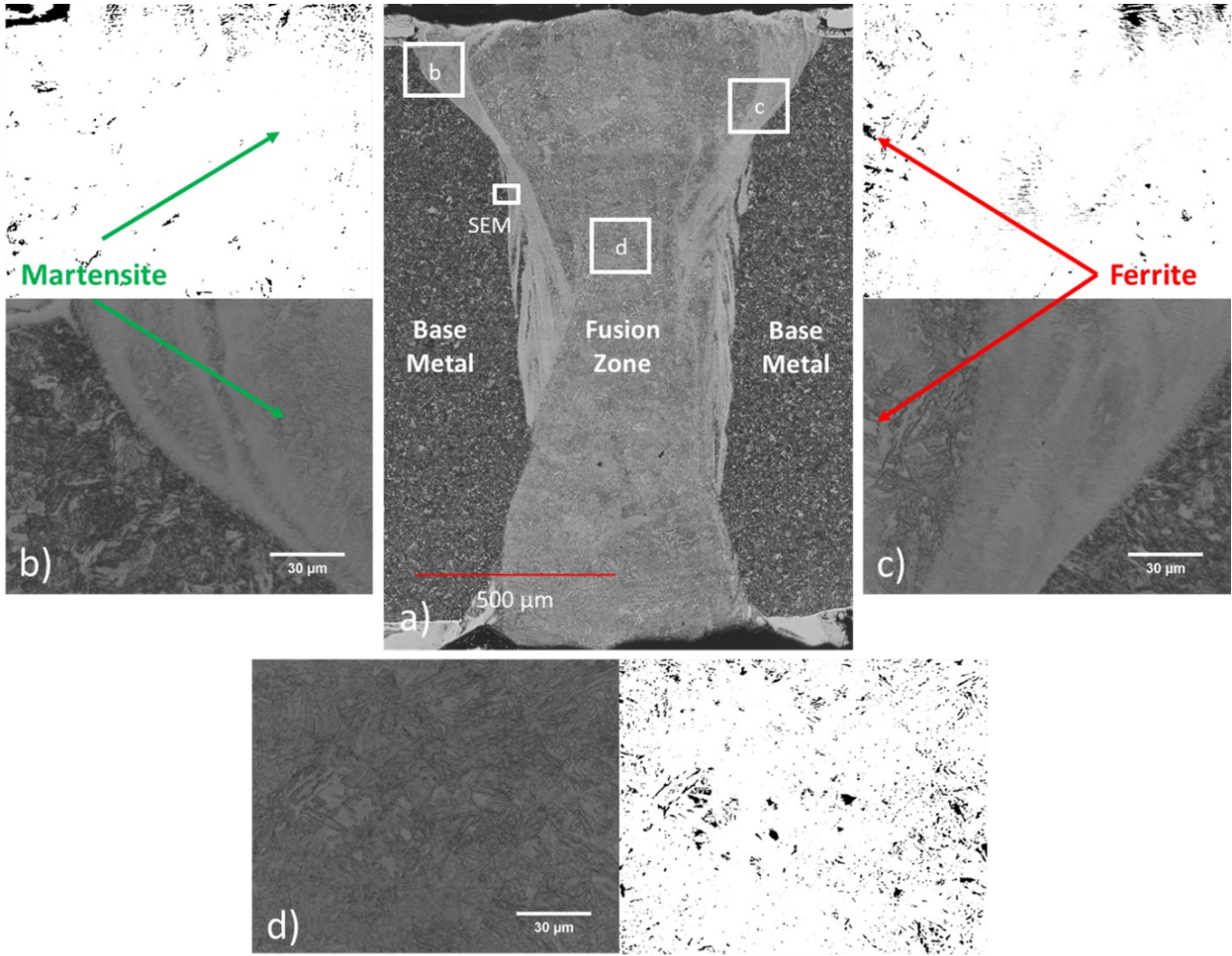


Figure 79: Optical micrographs of the (a) weld microstructure with Ni-coating, with high magnification images of the (b) left-side fusion boundary, (c) right-side fusion boundary, and the (d) center of the fusion zone with corresponding images showing the PC of ferrite (black color) and martensite (white color).



Figure 80: SEM images of the (a) fusion boundary of the WNHS condition at the location specified in Figure 79 as well as high magnification images of the (b) base metal showing a fully martensitic microstructure, and the (c) martensitic fusion zone showing a combination of prior martensite characterized by the darker concave morphology and fresh martensite characterized by the lighter convex morphology.

Table 10: Summary of the ferrite PC found in the ARWHS and WNHS conditions measured using image analysis for 3 distinct regions of interest at high magnification.

Sample Condition	Ferrite PC Region b	Ferrite PC Region c	Ferrite PC Region d	Average Ferrite PC	Martensite PC
ARWHS	43.3%	49.5%	21.5%	38.1%	bal.
WNHS	2.2%	2.1%	4.8%	3.0%	bal.

Martin *et al.* confirmed that aluminum is a strong ferrite stabilizer that reduces the size of the single-phase austenite region in the Fe-Al phase diagram [117]. It can be clearly seen that the addition of Ni into the FZ stabilizes the austenite phase by expanding the size of the single-phase austenite region when compared to the size of the single-phase austenite region in the Fe-Al phase diagram generated using JMatPro (v. 11.2) for the ARWHS FZ composition, as shown in Figure 81. The increase in the size of the single-phase austenite region ensures that during austenitization at a temperature of 930°C, the FZ microstructure is completely austenitic in the welded with Ni coating condition compared to the dual-phase ferritic and austenitic microstructure observed in the ARW condition as shown in Figure 81 (a). Therefore, it can be said that the addition of Ni into the FZ stabilizes the austenite phase leading to a direct reduction in α -ferrite PC that is observed in the weldment.

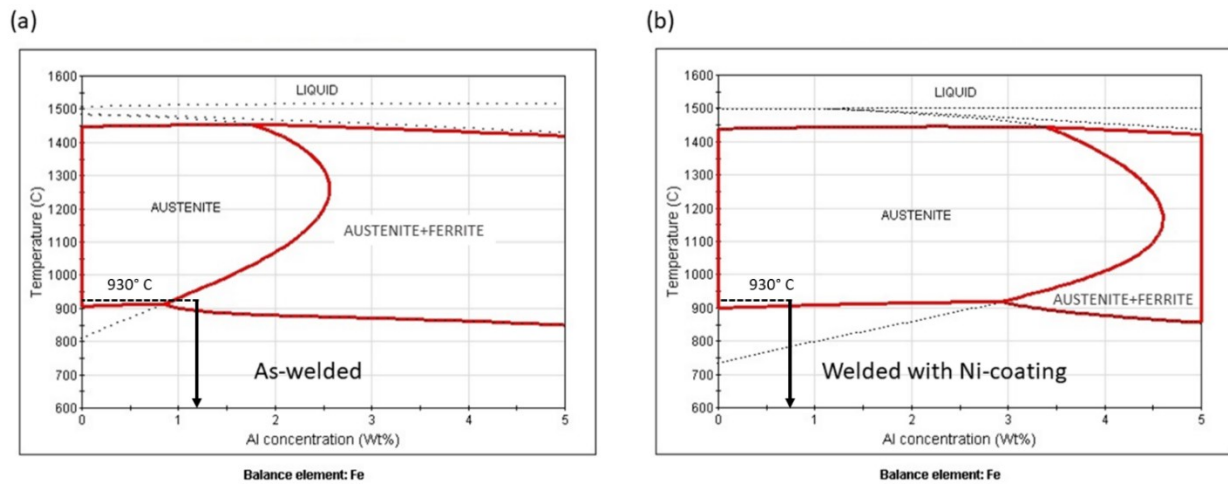


Figure 81: Fe-Al phase diagrams generated using JMatPro (v. 11.2) for (a) the ARWHS FZ composition in which there is no Ni and the arrow is showing that at the austenitization temperature of 930°C the FZ microstructure comprises of austenite and ferrite, and (b) the WNHS FZ composition showing that the addition of Ni stabilizes the single-phase austenite-region thereby increasing the PC of the martensite at the end of the hot stamping process and the arrow is showing that the FZ microstructure at 930°C is fully austenitic.

CCT curves generated using JMatPro (v. 11.2) predicted that at a cooling rate of about 30°C/s, the microstructure of the FZ in the ARWHS condition would be a mixture of ferrite and martensite as shown in Figure 82 (a), which agrees with the PC results shown in Table 9 and in

Table 10. Conversely, the CCT diagram for the FZ of the WNHS condition predicted that the weld would have a fully martensitic microstructure as shown in Figure 82 (b). However, the ferrite PC of the FZ in the WNHS condition was shown to be about 3-4%, with the remainder being made up of martensite. The small disagreement between the ferrite PC observed in the image analysis results and the CCT diagram can be explained by recognizing that the CCT diagram has been generated for a fixed bulk material chemical composition while in reality the local chemical composition in certain parts of the FZ may be different than the bulk chemical composition. For this reason, very small amounts of ferrite may still be found in the FZ. The CCT diagrams can be used in conjunction with the Fe-Al phase diagrams to confirm that as the Ni content in the weld increases, the α -ferrite PC decreases, leading to an almost fully martensitic microstructure in the FZ upon cooling.

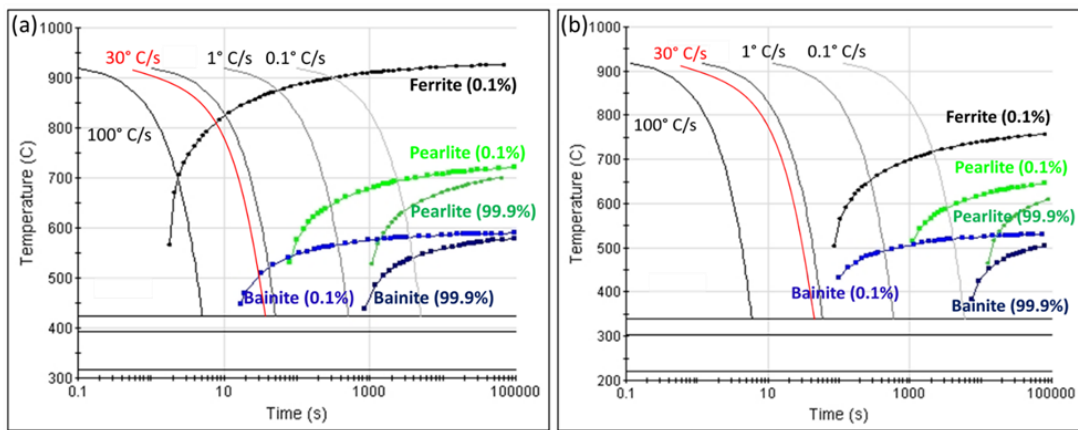


Figure 82: Predictive CCT diagrams for the (a) ARWHS FZ composition showing that at a 30°C/s cooling rate the weld microstructure is expected to be a combination of ferrite and martensite, and for the (b) WNHS FZ composition showing that the weld microstructure is expected to be purely martensitic at a 30°C/s cooling rate.

6.3 Mechanical properties

As the α -ferrite content in the weldment is significantly lower in the WNHS condition compared to the ARWHS condition, the difference leads to an observable effect on the mechanical properties of the weld. 299 microhardness indents were made in the BM and FZ of the ARWHS and WNHS conditions to generate hardness maps, as shown in Figure 83. The BM hardness was measured at about 500 HV which falls within the range reported in previous research [74,102,126]. The average FZ hardness for the ARWHS condition was measured at about 350 HV, which was significantly lower than the BM hardness as shown in Figure 83 (a), which agrees with the data reported by Saha et al. who showed that the difference in hardness was due to the presence of α -ferrite [74]. However, due to the reduced ferrite PC in the FZ of the WNHS condition, the average hardness was measured to be around 500 HV, which is the same as the BM hardness.

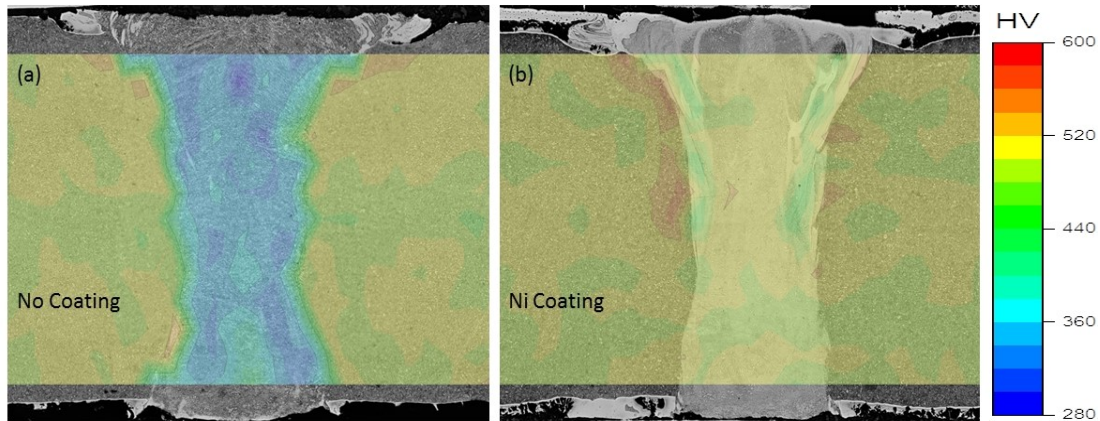


Figure 83: Hardness maps for the (a) BM and FZ of the ARWHS condition showing a significantly softer FZ as compared to the BM, and for the (b) BM and FZ of the WNHS condition showing that the average FZ hardness is the same as that of the BM.

Due to the high ferrite PC present in the FZ and the relatively lower hardness, the weld strength in the ARWHS condition was measured at about 1276 ± 11 MPa and sudden fracture was observed in the FZ, which agrees with the literature [74,96,102,103]. However, due to the reduction in ferrite PC and the subsequent improvement in FZ hardness, the UTS for the WNHS condition matches that of the BM at around 1562 ± 5 MPa and failure in these samples occurred in the BM, far away from the weld, with the fracture occurring on an angle showing the plane of maximum shear stress as shown in Figure 84.

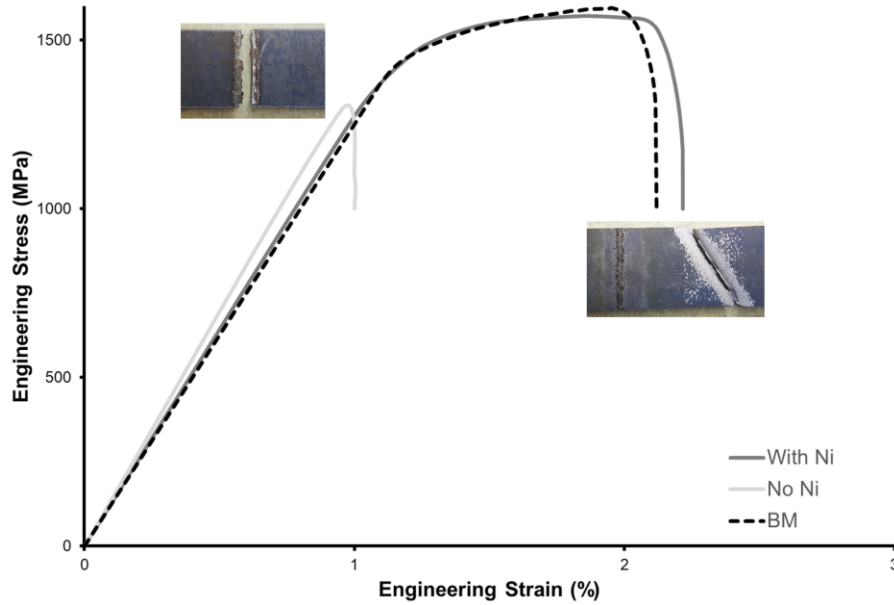


Figure 84: Flow curves for the hot-stamped BM, ARWHS condition, and WNHS condition with inserts showing the failure location of the ARWHS samples along the FB due to the high PC of α -ferrite present in the FZ, and the failure location of the WNHS samples in the BM.

6.4 Conclusions

By welding Al-Si coated 22MnB5 PHS through a pure Ni coating followed by a hot stamping process, the strength of the welds was increased to that of the hot-stamped BM, and the failure location was shifted from the FZ to the BM. Prior to welding, a 50 μm Ni-shim was applied using an adhesive to 1.5 mm thick Al-Si coated 22MnB5 steel and fiber-laser welds were then produced through the Ni-coating. This condition was compared to the condition in which welds were made with no Ni-coating applied as well as the non-welded BM and all the samples were hot-stamped using identical conditions. It was found that by welding Al-Si coated 22MnB5 steel through a Ni-coating, the Ni-content in the weld increased which suppressed the formation of α -ferrite. This improved the hardness and the UTS of the FZ to match that of the BM. Therefore, it can be concluded that the aforementioned method can be used to improve the mechanical properties of Al-Si coated TWBs without requiring the prior removal of the Al-Si coating by mechanical, chemical or laser ablation methods which can be costly and time-consuming.

7 Effect of nickel on the morphology, crystallography, and mechanical properties of hot-stamped 22MnB5

* This chapter is composed of a published research paper [195] as outlined in the Statement of Contributions.

In the previous chapters the in-situ alloying of the FZ of laser-welded 22MnB5 has been studied to show that it can be used as an effective tool to improve the mechanical performance of the joint. The results have shown that by properly optimizing the chemical composition of the FZ and its microstructural morphology, the mechanical properties that can be achieved are superior to the HSBM [152,156,157]. This final chapter considers the effect of alloying 22MnB5 with Ni on the resulting morphology and crystallography of the lath martensitic microstructure of the steel. The goal of this study was to go beyond the practical solutions proposed in the previous chapters and adopt a fundamental materials science focused approach to fully develop the relationship between the processing-microstructure-properties of the given system to offer recommendations on how the BM used for this study could potentially be improved in other broad steel-making applications.

High-strength martensitic steels have been employed extensively for centuries. Early applications included structural components, tools, and weapons, and now they are being used for applications within the automotive, shipbuilding, construction, defense, and other important industries that require components with load-bearing, high-fatigue, and high-wear resistant properties [152,153,157,196–198]. Martensitic steels have had a remarkable evolution through the years, with regular and clear-cut improvements being made to optimize the mechanical properties of these steels by carefully adjusting the alloying chemistry and processing techniques to control the martensitic transformation and refine its morphology. The quenching of a fully austenitic parent phase with a face-centered cubic (fcc) crystal structure at a cooling rate high enough (which provides a sufficient degree of undercooling below a specific transformation temperature) triggers the formation of the martensite crystals by way of a “displacive” or “diffusionless” shear transformation [155].

Several different types of martensite morphologies have been reported in the literature [199,200], with “lath martensite” (sometimes known as dislocated martensite) and “plate martensite” being used to describe the two most widely observed martensitic morphologies in steels. According to Owen et al. [201], lath martensite has an extremely fine microstructure and forms in low-carbon (C) alloys of iron, maintaining a relatively uniform body-centered cubic (bcc) structure, while plate martensite is primarily found in high-C, high-nickel and high-nitrogen binary

alloys which introduces a tetragonality to the crystal giving it a body-centered tetragonal (bct) structure. Sherby et al. [202] referred to the results presented by Fink and Campbell [203], which were separately verified by Ohman [204], to show that the tetragonality of Fe-C steels was very small for a C-content less than 0.6 wt.%. The c/a ratio (defined as the ratio between the lattice parameters in martensite) for these low-C steels was shown to be approximately equal to unity. The c/a ratio changes abruptly to about 1.02 when the C-content is equal to 0.6 wt.%, and further increasing the carbon content stabilizes the bct structure with the c/a ratio increasing proportionally as the C-content increases [202,205].

Lath martensite is well known to be of significant importance in commercially available structural grades of high strength steels, given its contribution to strengthening the microstructural constituents in complex-phase, hot-stamped, and martensitic steels [206–209]. The useful combination of high strength and toughness of lath martensitic steels is attributed to its complex morphology [210], which can be controlled most effectively by changing the C-content. However, an increase in the C-content of high strength steels can lead to excessive brittleness which can significantly deteriorate their mechanical properties. Other elements like Mn [211,212] and Ni [213,214] are known to affect the morphology of lath martensitic steels but the scope of the studies is somewhat limited. To investigate the effect of morphological changes on the mechanical properties by way of adjusting the alloying composition of the steel, the microstructure and crystallography of the material needs to be understood. Morito et al. [212,215] and Kitahara et al. [216] provided a comprehensive crystallographic investigation to show that the orientation relationship (OR) between lath martensite (α') and austenite (γ) can be expressed through the well-known Kurdjumov–Sachs (K-S) model [212,215–217]:

$$(111)_{\gamma} // (011)_{\alpha'} \quad [\bar{1}01]_{\gamma} // [\bar{1}\bar{1}1]_{\alpha'}$$

It has been shown in several different studies that the habit plane of the laths is $\{557\}_{\gamma}$ which is close to $\{111\}_{\gamma}$ when the direction is along $\langle 111 \rangle_{\alpha'}$ [212,218–220]. The crystallography of lath martensite has a distinct morphological hierarchy [221]: a single crystal of γ can evolve into 24 equivalent crystallographically distinct lath martensite variants (V1 – V24) based on the symmetry of the cubic system. These 24 crystallographic variants can be grouped into a maximum of 4 distinct structures (known as packets) because γ has four close-packed (CP) $\{111\}$ planes (i.e., 6 variants for each $\{111\}$ plane). The variants in a given packet organize themselves as variant-pairs in structures known as “blocks”, which are distinct platelet-like structures separated by high-angle boundaries, and low-misoriented laths [222]. For highly refined structures, the blocks are sometimes referred to as sub-blocks where each sub-block represents a single martensitic variant containing a few irregularly shaped martensitic laths with a similar orientation [213]. In other words, martensitic blocks contain laths that have almost the same known orientation, while martensitic packets are defined as a group of blocks with laths that share almost the same habit plane [198,215,223]. Takayama et al. [193,224] redefined blocks and packets based on the variants

that were found in them. Accordingly, a packet could, therefore, be defined as a region containing a group of 6 distinct variants that belong to the same CP group and share the same parallel relation of close-packed planes (CPPs), e.g., CP group 2 (i.e., CP2) is made up of variants V7-V12 and CP group 4 (i.e., CP4) is made up of variants V19-V24, etc. A block was redefined as a region that consisted of a variant-pair in each CP group that belonged to the same Bain group (B) which represents all the possible combinations of CP parallel directions. Consequently, the variants belonging to the same Bain group have very small misorientation angles relative to each other [224]. For example, a packet composed of the variants in the CP3 group could be divided into three Bain groups, i.e., B1: V13/V16, B2: V15/V18, and B3: V14/V17, where B denotes a given Bain group. The crystallographic relationship of the 24 martensitic variants and their organization into CP and Bain groups has been summarized in Table 11.

There is significant interest in understanding the hierarchical nature of the martensitic microstructure, and its effect on the mechanical properties of lath martensitic steels [221]. Maki et al. [206] originally showed that the block and packet sizes were directly proportional to the prior austenite grain (PAG) size (PAGS), which has been confirmed in several later studies [198,225,226], while it is generally believed that the lath width does not change appreciably with a change in PAGS [223,226]. It has been well-known for many years that the strength of martensite is related to the lattice-invariant deformations and the structural changes produced in the lattice during the martensitic transformation [218]. Traditionally, it had been recognized that since the crystallographic orientation of the martensitic crystal in a packet remains constant, the packet size (PS) was the effective grain size of the martensitic microstructure, controlling its associated strength and toughness [198,208]. This view was strengthened by the fact that the size of cleavage facets produced during brittle transgranular failure were directly related to the PS given the abundance of $\{100\}_{\alpha'}$ cleavage planes in parallel laths that compose a given packet [198]. In fact, it was definitively shown by Wang et al. [227] that packet boundaries strongly hinder fracture propagation and as such, PS should be taken as the de facto grain size that affects the toughness and DBTT behaviour of low-C lath martensitic steels. However, exhaustive work by Morito et al. [228] showed that the yield strength (YS) of martensite shows a significantly higher dependence on the block size (BS) in comparison to the PS. This finding has been confirmed in several recent studies [181,213,229].

It has been well-established that the alloy composition of a given steel has a significant effect on the martensitic morphology and its hierarchy [230–234]. Although, this effect has been studied in significant detail for the C-content in a given steel, studies focusing on other important alloying elements (i.e., Mn, Ni, N, Al, and other austenite- or ferrite-stabilizing elements) are relatively limited in their scope, primarily because designing steels with a specific alloying composition to single out the effect of a particular alloying element can be challenging and costly [235]. Consequently, there is an urgent need to investigate the effect of different alloying elements on the morphology and mechanical properties of lath martensite to improve its performance for

advanced applications. Understanding of the role of non-C alloying in martensitic structures is especially important to recent lightweighting design efforts, specifically in the automotive industry where this is needed to promote the electrification of modern vehicles and other decarbonization efforts. This study provides a comprehensive investigation on the effect of Ni on morphology, crystallography, microstructural refinement, internal transformational strain, and the mechanical properties of coarse and lath martensite in 22MnB5; the most widely used grade of press-hardened (or hot-stamped) steel (PHS) in the automotive industry. 22MnB5 is an ultra-high strength steel that has the unique property of having low strength and high ductility in the as-received condition due to its ferrite/pearlite microstructure but transforms into an ultra-high strength martensitic microstructure following a press-hardening heat treatment, which makes this steel ideal for the production of highly optimized, functionally graded components [20].

The results of this study were acquired using advanced analytical tools at the meso-, nano-, and atomic-scales to offer insights that have so far been lacking in the literature by showing that the addition of Ni increased the PAGES for the same hot-stamping heat-treatment, while simultaneously refining the PS, block width, and the width of individual laths in a given block. The addition of Ni promoted a relatively ideal martensitic transformation such that the majority of PAGES in the bulk microstructure were found to be composed of all 4 CP groups with a relatively homogenous distribution of the martensitic variants. The addition of Ni lowered the martensite start (M_s) temperature and strengthened the γ -matrix at lower temperatures [236,237] by way of solid-solution strengthening which resulted in the refinement of the PS and BS to self-accommodate the transformational strain, whereby significantly decreasing the internal strain in the microstructure. The addition of Ni induced the formation of interspersed coarse martensite (CM) laths which were significantly larger than the fine lath martensite crystals that made up the bulk structure, and these CM laths were more prone to autotempering during the quenching stage of hot stamping. The results of this study showed that alloying lath martensitic steels with Ni can prove to be an effective method to refine the hierarchical structures in a way that can be used to improve the mechanical properties of these steels.

Table 11: 24 crystallographically distinct variants of the K-S orientation relationship, showing that 6 unique variants form on each of the four $\{111\}$ planes found in the austenite grain [216]. The associated organization of variants into CP and Bain groups is shown to make their identification in packet and block structures simpler to understand. Note that the Bain correspondence can be found in Ref. [224]. The color in brackets represents the color for that CP group used for EBSD analysis, as shown in Figure 89.

Variant	Parallel Plane	Parallel Direction	CP Group	Bain Group
V1		$[\bar{1}01]_{\gamma} // [\bar{1}\bar{1}1]_{\alpha}$		B1
V2		$[\bar{1}01]_{\gamma} // [\bar{1}1\bar{1}]_{\alpha}$		B2
V3	$(111)_{\gamma} // (011)_{\alpha}$	$[01\bar{1}]_{\gamma} // [\bar{1}\bar{1}1]_{\alpha}$	CP1	B3
V4		$[01\bar{1}]_{\gamma} // [\bar{1}1\bar{1}]_{\alpha}$	(Blue)	B1
V5		$[1\bar{1}0]_{\gamma} // [\bar{1}\bar{1}1]_{\alpha}$		B2
V6		$[1\bar{1}0]_{\gamma} // [\bar{1}1\bar{1}]_{\alpha}$		B3
V7		$[10\bar{1}]_{\gamma} // [\bar{1}\bar{1}1]_{\alpha}$		B2
V8		$[10\bar{1}]_{\gamma} // [\bar{1}1\bar{1}]_{\alpha}$		B1
V9	$(1\bar{1}1)_{\gamma} // (011)_{\alpha}$	$[\bar{1}\bar{1}0]_{\gamma} // [\bar{1}\bar{1}1]_{\alpha}$	CP2	B3
V10		$[\bar{1}\bar{1}0]_{\gamma} // [\bar{1}1\bar{1}]_{\alpha}$	(Orange)	B2
V11		$[011]_{\gamma} // [\bar{1}\bar{1}1]_{\alpha}$		B1
V12		$[011]_{\gamma} // [\bar{1}1\bar{1}]_{\alpha}$		B3
V13		$[0\bar{1}1]_{\gamma} // [\bar{1}\bar{1}1]_{\alpha}$		B1
V14		$[0\bar{1}1]_{\gamma} // [\bar{1}1\bar{1}]_{\alpha}$		B3
V15	$(\bar{1}11)_{\gamma} // (011)_{\alpha}$	$[\bar{1}0\bar{1}]_{\gamma} // [\bar{1}\bar{1}1]_{\alpha}$	CP3	B2
V16		$[\bar{1}0\bar{1}]_{\gamma} // [\bar{1}1\bar{1}]_{\alpha}$	(Yellow)	B1
V17		$[110]_{\gamma} // [\bar{1}\bar{1}1]_{\alpha}$		B3
V18		$[110]_{\gamma} // [\bar{1}1\bar{1}]_{\alpha}$		B2
V19		$[\bar{1}10]_{\gamma} // [\bar{1}\bar{1}1]_{\alpha}$		B3
V20		$[\bar{1}10]_{\gamma} // [\bar{1}1\bar{1}]_{\alpha}$		B2
V21	$(11\bar{1})_{\gamma} // (011)_{\alpha}$	$[0\bar{1}\bar{1}]_{\gamma} // [\bar{1}\bar{1}1]_{\alpha}$	CP4	B1
V22		$[0\bar{1}\bar{1}]_{\gamma} // [\bar{1}1\bar{1}]_{\alpha}$	(Green)	B3
V23		$[101]_{\gamma} // [\bar{1}\bar{1}1]_{\alpha}$		B2
V24		$[101]_{\gamma} // [\bar{1}1\bar{1}]_{\alpha}$		B1

7.1 Experimental details

The base metal (BM) for this study was 1.5 mm thick Al-Si coated 22MnB5 steel. The BM composition was adjusted by processing the steel using a pure Ni-coating and a high-powered fiber laser traversing the length of the steel samples. The laser melted the Ni-coating which alloyed with the molten substrate in the processed zone (PZ), based on the fluid flow constraints defined by the Marangoni convection flow [25]. A high dynamic range XIRIS XVC-1000 camera with additional ultraviolet, near-infrared, and neutral density filters was used to film the in-situ alloying process at 90 fps, as shown in Figure 85. The laser processing parameters were adjusted to ensure no defects were created in the PZ by moving the laser along the surface of the substrate through the adhesively applied Ni-coating, perpendicular to the rolling direction of the steel using a laser power of 4 kW and a travel speed of 6 m/min with a laser beam diameter of 0.4 mm using a laser defocusing distance of 4 mm, and a positive beam impingement angle of 20° to induce the most stable melt pool during laser processing [62,63]. Further details regarding the laser processing system can be found elsewhere [132]. After laser processing, the samples were hot-stamped by heating them in a furnace for 6 minutes, which was set to an austenitization temperature of 930 °C, and then quenched instantaneously using a water-cooled die at a cooling rate of approximately 30 °C/s, to replicate the press-hardening heat treatment employed in the production of functionally graded tailor blanks [25].

The chemical composition of the BM and the Ni-alloyed BM (NABM) is shown in Table 12. The samples were prepared for metallographic analysis using conventional grinding and polishing to a final 1 μm diamond polishing finish, and the samples were etched with 2.5% Nital solution. Preliminary characterization of the microstructure was done using the Keyence VK-X250 laser scanning confocal microscope (LSCM) in high-resolution laser scanning and differential interference contrast (DIC) modes to identify the key differences in the morphology of the steels. The Zeiss UltraPlus field emission scanning electron microscope (FE-SEM) was used to investigate the steel morphology at high magnification. The JEOL JXA-8230 electron probe micro-analyzer (EPMA) was used for elemental analysis to determine the local chemistry of the PZ, and the reported weight percentage for the elements of interest in the area outlined in Figure 85 (e) is shown in Table 12. The raw thermodynamic data for the phase transformations during austenitization and quenching was acquired using the commercially available CALPHAD software JMatPro (v. 11.2) for the chemical compositions presented in Table 12, and the data was plotted using OriginPro 2021b (v. 9.85). The phase evolution during quenching was predicted for a cooling rate of 30 °C/s to mimic the cooling rate during the quenching stage of hot-stamping.

FE-SEM (JEOL7001F) equipped with an electron back-scattered diffraction (EBSD) detector was used to characterize the microstructure of the BM and the NABM. After conventional sample preparation and polishing, the EBSD samples were prepared with vibratory polishing using active oxide polishing suspension (OP-S) solution to produce a mirror finish on the sample

surfaces to achieve >93% indexing of the martensitic microstructure. A high-speed Hikari CCD camera was used for pattern acquisition ranging from 0.25-0.1 μm step size. The raw EBSD data was analyzed using the MTEX toolkit in MATLAB [238]. For each set of EBSD data, the toolkit was utilized to reconstruct the inverse pole figures (IPFs), grain reference orientation deviation (GROD) maps, and the grain orientation spread (GOS) maps to thoroughly characterize the microstructure of the different samples. The MTEX toolkit in MATLAB was also used to reconstruct the primary austenite grains based on the crystallographic K-S OR between austenite and martensite. A description of the steps and algorithms involved in the reconstruction of the parent grains using MTEX have been explained in Ref. [239].

Samples for transmission electron microscope (TEM) analysis were prepared using a focused ion beam (FIB) Zeiss NVision 40 FIB-SEM. The target location was coated with ion-beam-induced deposition of tungsten for protection throughout the FIB process. The target location was extracted from the specimen and attached to a copper FIB grid using a conventional FIB milling and lift-out procedure. The thinning was performed with the ion beam using milling lines of progressively smaller beam currents on each side down to 40 pA. Final cleaning steps were performed with the ion beam voltage at 10 kV and 5 kV using a glancing angle raster box with the stage tilted 7° below the tilt angle of the thinning step. The FIB-prepared foil was examined using a scanning TEM (Thermo Fisher Scientific Talos 200X) and an analytical TEM (Thermo Fisher Scientific Talos L120C) equipped with EDS X-ray spectrometer and electron-energy-loss spectroscopy (EELS). High-angle annular dark-field (HAADF) imaging was performed with a spot size less than 1 nm and a convergence semi-angle of 10.5 mrad. EELS experiments were performed using a Gatan CMOS detector with a dispersion of 0.75 eV and an energy resolution of around 2 eV.

Table 12: Chemical composition of the base material and the Ni-alloyed BM used in the present work (in wt.%).

Sample	C	Mn	B	Si	Cr	Ti	Mo	P	Al	Ni	Fe
22MnB5	0.23	1.22	0.0032	0.27	0.20	0.04	0.02	0.01	0.04	0.00	bal.
Ni-Rich 22MnB5	0.23	1.22	0.0032	0.41	0.20	0.04	0.02	0.01	1.13	8.30	bal.

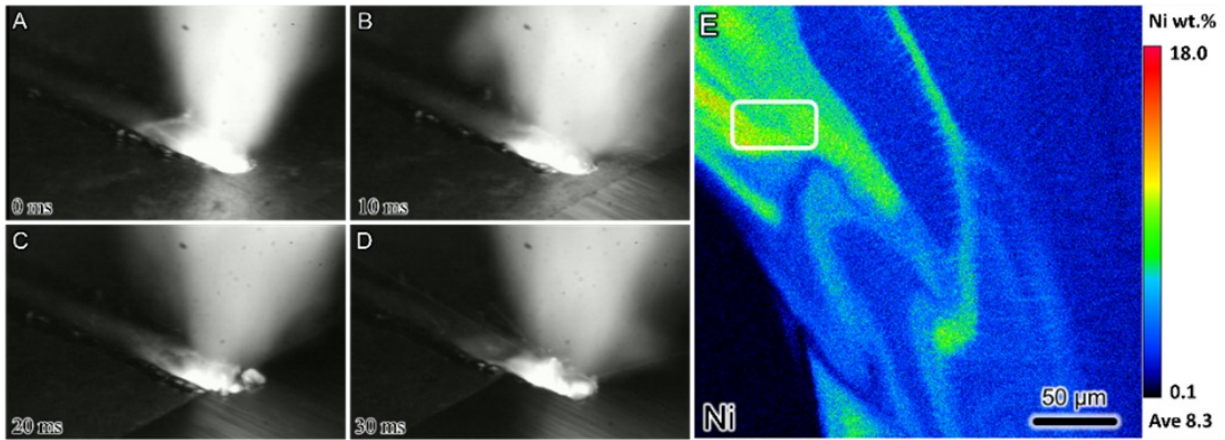


Figure 85: (a-d) In-situ alloying of pure Ni using a high-powered fiber laser to dilute the molten Ni coating into the processed melt pool. The molten Ni flows into the melt pool along the boundary based on the Marangoni convection flow. During the heating stage of hot-stamping, a relatively homogenous distribution of Ni is achieved at the center of the processed zone as the Ni-content gradually increases towards the periphery. (e) EPMA results showing the elemental map of Ni. The Ni content was measured to be ~2 wt.% at the center of the PZ, with a maximum of ~18 wt.% measured at the periphery. The bulk average Ni-content of the entire processed zone was measured to be ~4 wt.%. The outlined region shown in (e) had an average Ni-content of ~8.3 wt.% and was chosen as the region of interest for investigation.

The hardness of the different phases was measured using an Anton Parr RST3 and a NHT3 nanoindentation tester. Nanoindentation hardness measurements were made with a standard Berkovich tip under the load control mode with a maximum load of 30 mN. The loading and unloading rates were set to 60 mN/min with a dwell time of 5 s for each indent. Each phase was indented at least 3 times and the average hardness values have been reported. All errors have been reported as a confidence interval with a significance of 0.05 (i.e., a confidence level of 95%) for the mean value for each condition.

7.2 CALPHAD predications and microstructural analysis

22MnB5 is well-known to have a martensitic microstructure with traces of lower bainite (LB) in the press-hardened condition [83]. This morphology can be seen clearly in the micrographs shown in Figure 86 (a) and (b). During the austenitization heat treatment, the as-received (AR) bulk microstructure consisting of ferrite and pearlite would be transformed into a fully austenitic microstructure, as predicted by the thermodynamic results shown in Figure 86 (c). When a hypoeutectoid steel is heated and the temperature is raised above A_{c1} , the pearlitic structure transforms to austenite first, as confirmed by the thermodynamic results shown in Figure 86 (c). As the pearlitic to austenitic transformation is completed, the remaining ferrite begins partial transformation to austenite when the temperature is still between A_{c1} and A_{c3} – with the transformation reaching completion when the temperature is above A_{c3} . The fully austenitic microstructure then undergoes a predominantly displacive transformation during the subsequent quenching and stamping of the steel resulting in a bulk microstructure composed of about 94%

martensite (labelled as α'_1 to indicate lath martensite in the BM) and 6% LB, as shown in the micrographs and confirmed by the thermodynamic prediction in Figure 86 (d).

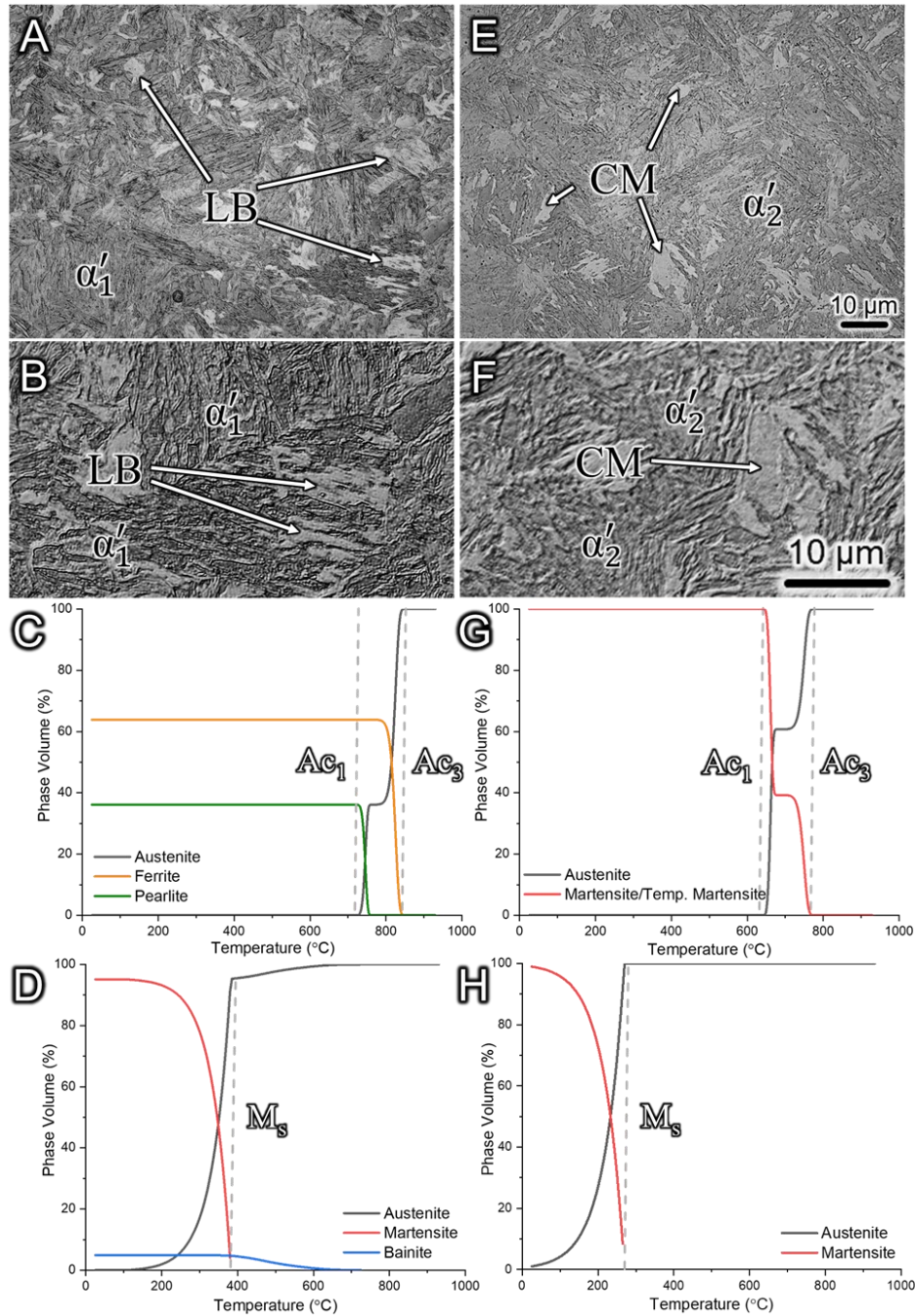


Figure 86: LSCM and high magnification differential interference contrast (DIC) images showing the difference in the morphology and phase distribution of the bulk microstructure of the (a-b) BM and (e-f) NABM samples. The CALPHAD predicted phase volume fraction has been shown for the (c-d) BM and (g-h) NABM chemistry shown in Table 12 during the heating and quenching stages of hot-stamping, respectively.

When the AR BM was processed to achieve in-situ alloying with Ni followed by the press-hardened heat treatment, the microstructure in the PZ was fully martensitic (labelled as α'_2 to

signify the difference in lath morphology between the NABM and the BM) with a significantly more refined lath morphology and traces of CM grains interspersed through the matrix, as shown in Figure 86 (e) and (f). Due to the extremely high cooling rate experienced by the PZ during in-situ alloying, the PZ was fully martensitic prior to austenitization, as shown in Figure 86 (g). The thermodynamic results showed that the addition of Ni lowered the Ac_1 and Ac_3 temperatures of the NABM, which is well within the reported range for Fe-9%Ni steels [214]. This resulted in larger austenite grains compared to the BM at the completion of the austenitization process. Upon subsequent quenching and stamping of the steel, the thermodynamic results predicted that the fully austenitic microstructure was transformed completely into martensite, as shown in Figure 86 (h), which was also confirmed by the morphology shown in the micrographs.

The thermodynamic results also show that the addition of Ni lowered the martensite start temperature (M_s) of the steel, despite an expected increase in the austenite grain size which is known to increase the M_s due to the larger grain boundary area that offers more nucleation sites for the transformation of the martensitic crystals [240]. This decrease in the M_s can be attributed to two main reasons: first is the known austenite-stabilizing effect of Ni which delays the decomposition of austenite to martensite and the second is the solid-solution strengthening effect of the additional Ni in the bulk matrix which makes it more difficult to plastically deform the austenite to accommodate the martensitic transformational strain which further drives down the M_s [214,237,241]. The lowering of the M_s can be used as an effective tool to refine the martensitic morphology. As the M_s is lowered, the austenite and martensite become more resistant to plastic deformation which causes them to simultaneously deform in order to accommodate the martensitic transformational strain, resulting in large elastic stresses that cause significant self-accommodation of the martensitic crystals in the microstructure, i.e., highly refined, favorable combination of variants are formed in the austenite grains to complete the austenite to martensite transformation [223].

High magnification FE-SEM images show clear differences in the martensitic morphology of the BM and the NABM. Image analysis of the microstructure at high magnification confirmed the CALPHAD-predicted volume fraction showing that the BM was composed of about 5% LB with the remaining being made up of martensite, as shown in Figure 87 (a). The lath morphology was visibly coarser in the BM, with a significant volume of martensite-austenite (MA) constituents (flat, dull features) visible inside large martensitic islands, as shown in Figure 87 (c). These MA constituents are a high-hardness morphological feature containing untransformed carbon-rich austenite which can make martensitic steels excessively brittle if their volume fraction is too high [192,193,242]. These MA constituents had a similar morphology to what has been observed in other bainitic/martensitic microstructures [165].

The martensitic morphology in the NABM was significantly more refined compared to the BM, with much finer features observed in the microstructure, as shown in Figure 87 (e). There was

no visible evidence of the presence of any MA constituents in the microstructure, which is not surprising because MA constituents tend to form in blockier crystals of martensite, so their formation was likely hindered by the abundance of finer martensitic crystals in the NABM. The microstructure also showed the presence of sparsely distributed martensitic crystals with a lenticular-like morphology with the presence of a clearly visible midrib, as shown in Figure 87 (f), which is commonly observed in Ni-rich steels. Finally, the last major morphological difference was the frequent presence of coarse martensite (CM) crystals, dispersed through the highly refined microstructure, as shown in Figure 87 (g) and (h). Similar CM features have been reported and studied extensively in the literature [209,222,243]. Morsdorf et al. [209] argued that since these CM crystals do not show the presence of any internal interfaces, they can be considered as the smallest sub-unit in the martensitic structural hierarchy and each individual crystal can, therefore, be referred to as “coarse laths”, noting that the CM laths did not always have the same size. For the sake of clarity, the same authors [209] defined conventional thin laths as having a thickness that ranged from $\sim 0.05 \mu\text{m}$ to $0.50 \mu\text{m}$, while CM laths had a wedge-like shape with a thickness of $\sim 3.5 \mu\text{m}$, embedded within the fine lath matrix.

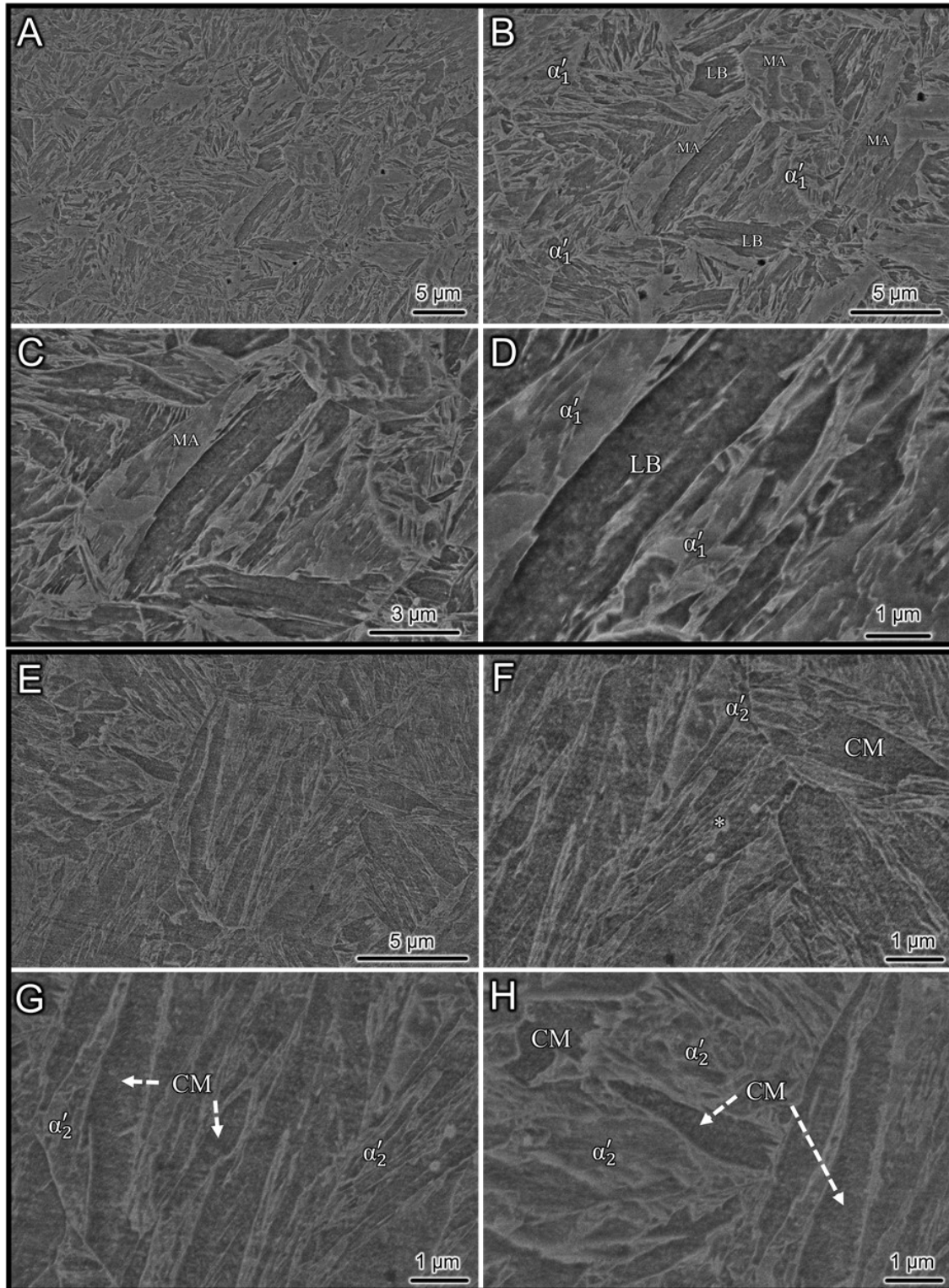


Figure 87: High magnification FE-SEM images showing the microstructure of the (a-d) BM, composed mainly of fine lath martensite (α'_1) with sparsely distributed islands of lower bainite, and the (e-h) NABM, showing the presence of coarse martensite grains distributed in a fine lath martensite (α'_2) matrix, respectively. (CM: Coarse martensite, LB: lower bainite, MA: martensite-austenite constituent, and the region marked with an * is lenticular martensite with a clearly visible midrib)

7.3 Effect of Ni on morphological hierarchy

The key differences in martensitic morphology and the effect of Ni on the morphological hierarchy of the martensite was investigated using a comprehensive EBSD analysis, as shown in Figure 88. The inverse pole figures (IPF) of the bulk microstructure clearly show the differences in the size distribution of the martensitic features for the BM and the NABM, as shown in Figure 88 (a) and (d), respectively. The results show that the PAGS was larger for the NABM compared to those in the BM due to the addition of Ni, which lowered the A_{c1} and A_{c3} temperatures, as shown in Figure 88 (b) and (e). Despite the larger PAGS, the packets and blocks were significantly more refined in the NABM compared to the BM, as shown in Figure 88 (c) and (f).

Qi et al. [244] showed that single-variant models of martensitic transformation did not produce orientations and habit planes commonly found in low-carbon martensite, so instead they developed the “composite Bain block with two-slip systems” model to show that the “ideal” martensitic transformation occurred when the PAGs transformed into four packets (CP1-CP4), with three blocks in each packet, and all of the 24 K-S variants having a relatively homogenous volume fraction in the microstructure. The solutions to the proposed model created twelve composite Bain blocks (i.e., three blocks in each of the four packets), with each block containing two K-S variants sharing the same Bain axis (Table 11). Each variant had an invariant plane that was parallel to the $\{111\}_\gamma$ plane which was parallel to the $\{011\}_\alpha$ planes of the two variants satisfying the K-S relationship. This ideal transformation ensured that the transformational strain was purely dilatational with no net shear, i.e., the parent γ grains were transformed entirely due to a volumetric change with no net shear stress being produced in the lattice, which would result in exceptional mechanical properties for these steels [244]. However, the authors note that these results only hold true if a PAG transforms into four packets because the uniaxial elongation in a packet is large enough to cause significant shape changes in the structure if fewer than four packets are formed. Kinney et al. [213] showed that the microstructure of a quenched 9Ni steel with very large PAGSs ranging from ~ 75 to $200 \mu\text{m}$ had a martensitic transformation that was very nearly ideal from a minimum transformational strain perspective.

The measurements of different morphological features in the observed microstructures are presented in Table 13. To compare the morphological features of the alloys used in this study, characteristic measurements of comparable steels (i.e., Fe-0.2C and Fe-0.2C-2Mn) were taken from the literature with similar PAGSs [228]. The average PAGS for the NABM was almost double compared to the BM for the same hot-stamping heat treatment. Based on the results reported by Morito et al. [228], it can be seen that an increase in the Ni content had a similar effect to an increase in the Mn content, such that the PS and block width become smaller. For almost similarly sized PAGs, however, the Ni-alloyed steel had the most refined PS (measuring at $2.99 \pm 0.17 \mu\text{m}$) and block width (measuring at $0.73 \pm 0.11 \mu\text{m}$). It is interesting to note that the average PS for the BM and NABM was about 63.5% and 23.6% of the PAGS, respectively, which shows

that the likelihood for an ideal martensitic transformation to occur in the BM was significantly lower compared to the NABM, simply based on geometric constraints. The average block width in either steel was small enough that 3 blocks could easily form in a given packet. Lath widths were measured from the TEM data presented in Section 7.6. It is well-known that fine laths can have widths ranging from ~ 0.05 to $0.50 \mu\text{m}$ [209], but it is generally well-accepted that the average lath width in low C steels is ~ 0.23 to $0.30 \mu\text{m}$ [228,245]. Although lath width is known to be independent of the PAGS [228], it tends to become finer as the C content increases [181]. The results presented in this study show a clear refinement in the average lath width due to an increase in the Ni content, most likely to further facilitate the self-accommodation required to achieve an ideal transformation.

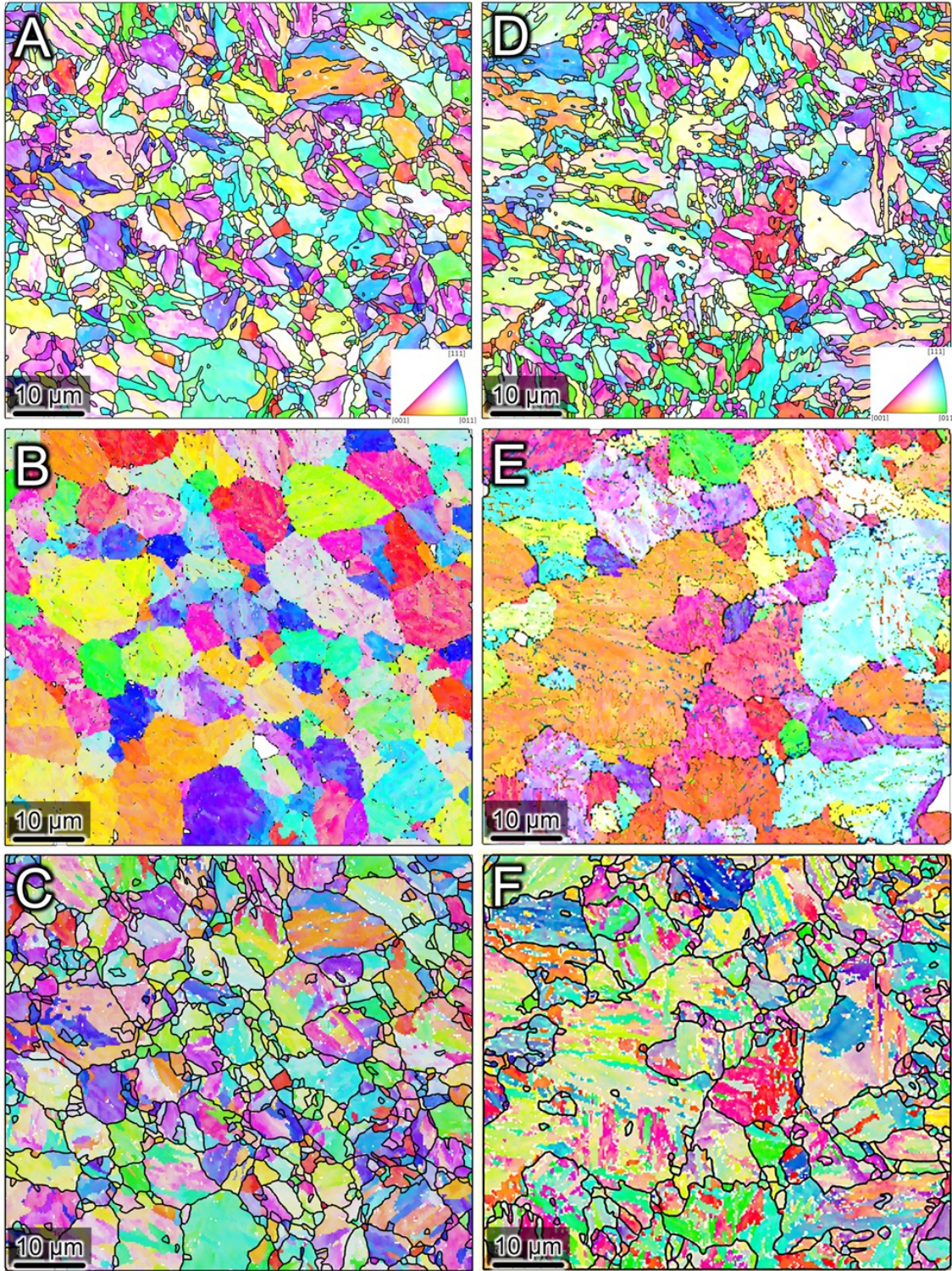


Figure 88: EBSD-IPF maps showing the differences in crystal morphology of the (a) BM and the (d) NABM microstructure, reconstructed using the MTEX toolbox in MATLAB. To predict and show the difference in the prior austenite grain (PAG) size, the EBSD data was plotted for the (b) BM and the (e) NABM samples using the standardized Fe-FCC crystal structure information, showing that the austenite grain sizes (AGS) were much larger for the NABM. The IPF figures with the predicted PAG boundaries are shown in (c) and (f) for the BM and the NABM sample, respectively.

Table 13: Measurements of PAGES, PS, block width, sub-block width, and lath width acquired from the EBSD and TEM data presented in this study. The measurements have been compared to the data presented for lath martensitic structures for similar PAGES in different steels given in Ref. [228]. The lath width for the 22MnB5 BM was measured from the TEM data presented in Ref. [125]. The measured values are reported with a confidence interval of 95%.

Sample	PAGS (μm)	PS (μm)	Block width (μm)	Sub-block width (μm)	Lath width (μm)
Fe-0.2C [228]	6.14	-	2.56	-	-
Fe-0.2C-2Mn [228]	6.14	3.72	1.05	0.70	0.23
22MnB5	6.42 ± 0.31	4.08 ± 0.23	1.10 ± 0.14	0.77 ± 0.05	0.22 ± 0.01
Fe-0.2C [228]	10.82	9.43	2.67	-	-
Fe-0.2C-2Mn [228]	13.99	5.53	1.21	-	0.23
22MnB5-8Ni	12.65 ± 0.49	2.99 ± 0.17	0.73 ± 0.11	0.49 ± 0.03	0.19 ± 0.02

7.4 Effect of Ni on variant-pairing and transformation mechanism

Using the MTEX toolbox, the microstructure in the BM and NABM samples was color-coded to show the distribution of packets in each PAG based on the CP parallel plane relationship (Table 11), as shown in Figure 89 (a) and (b), respectively. Figure 89 illustrates the packet ID distribution map where each color represents a single packet that forms along the same habit plane in a given PAG. The reconstructed maps show some white regions that indicate a mismatch between the austenite and martensite due to an assumed K-S OR that led to incomplete reconstruction. The results show that the majority of PAGs in the BM transformed into one or two packets, with very few PAGs showing the presence of all four packets. On the other hand, the majority of PAGs in the NABM transformed into all four packets. The addition of Ni ensured that all four packets evolved in a given PAG due to the refining effect of Ni on the hierarchical structures in the martensite, and there was a clear preference to the formation of CP1 (shown by the blue color) which is represented by the $(111)_\gamma // (011)_\alpha$ parallel plane OR, and CP4 (shown by the green color) which is represented by the $(11\bar{1})_\gamma // (011)_\alpha$ parallel plane OR.

The $\{001\}$ pole figures (PFs) for six individual PAGs from both samples are shown in Figure 89, showing the measured orientation of the martensitic crystals from each respective PAG, superimposed on the theoretical martensite variant orientations specific to the K-S model. The PFs in Figure 89 show the orientation spread from the ideal K-S variant orientations [216], clearly showing that the lath martensite structure in the BM and the NABM maintains the K-S OR. The results also show that the distribution of the orientation spread is not discrete as there is some clear deviation of the measured orientations from the ideal case.

The PFs show that the majority of PAGs in the BM did not show a full distribution of the 24 martensitic variants since each individual grain did not transform into all four packets. The NABM, on the other hand, showed an almost homogenous distribution of all 24 martensitic variants in each analyzed grain shown in Figure 89, primarily following from the composite Bain

block with two-slip systems model [244] that ensures an ideal martensitic transformation from a polygranular austenitic microstructure, resulting in a lath martensite hierarchical structure with minimal strain. This result is in complete agreement with Kinney et al. [213] who made the same observation for a 9Ni steel with significantly larger PAGSs (~200 μm). This result, therefore, leads to the conclusion that the alloying of Ni with steel to a bulk wt.% of ~8-9% leads to a martensitic microstructure that is extremely likely to show the presence of all 24 K-S variants in a given PAG, regardless of the grain size.

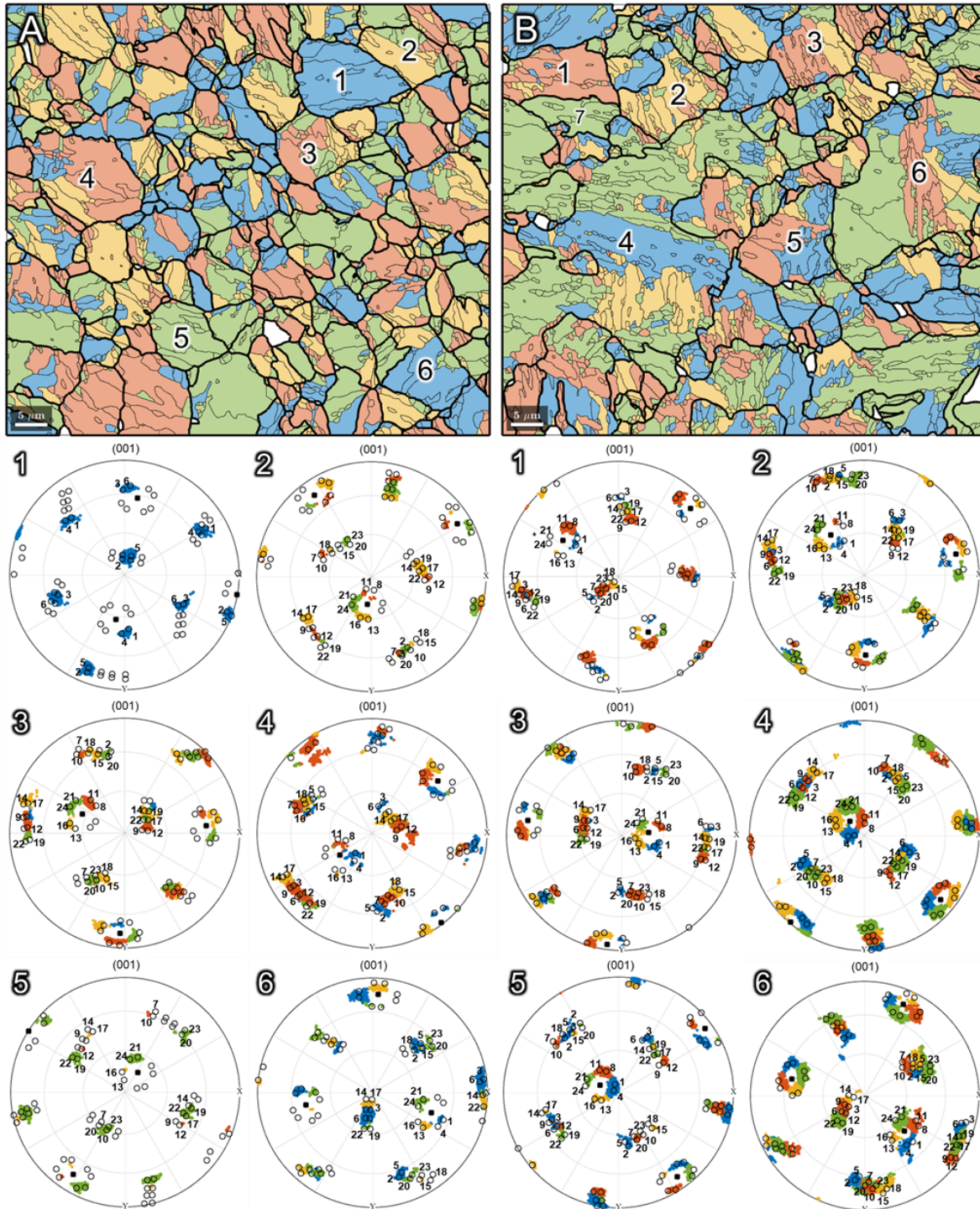


Figure 89: Reconstructed EBSD maps of the (a) BM and (b) NABM showing the packet distribution in the bulk microstructure based on the 4 possible parallel plane orientations that can exist in a given PAG, as summarized in Table 11. The pole figures for individually labelled PAGs were used to index the martensitic variants in each grain. The EBSD maps and the pole figures clearly showed that the NABM had a significantly more ideal martensitic transformation compared to the BM, as evident by the presence of a homogenous distribution of the 4 CP groups (representing individual packets) in each PAG analyzed in the NABM, with all 24 martensitic variants being indexed in each grain. The BM microstructure was composed of PAGs that had an average of about 2 CP groups in each grain and a significantly smaller number of variants were indexed in these grains.

The variant-pairing behavior of the lath martensite in the BM and the NABM was investigated by analyzing one single representative PAG from each sample (labelled as 1 in Figure 89 (a) and 1 & 7 in Figure 89 (b)), using high magnification and high-resolution EBSD analysis, as shown in Figure 90 (a) and (b), respectively. Each individual color in the IPF map represented a block based on the Bain groups shown in Table 11. A color variation in a given block showed its bi-variant nature. If the block had no color variation, it indicated the presence of a single-variant block, i.e., a sub-block. The (001) PF for grain 1 in the BM shows that only V1-V6 evolved in the microstructure since the entire grain had transformed into a single packet with a $(111)_\gamma // (011)_\alpha$ parallel plane relationship (i.e., CP1). The (001) PFs for the grain in the NABM shows that all 24 variants (i.e., V1-V24) evolved in the microstructure since the entire γ grain had undergone an ideal transformation to form all four packets, representing all the parallel plane CP group relationships, as shown in Table 11. Although, all 24 variants were indexed in the PAG, the PF clearly showed that certain variant groups formed in greater abundance compared to others. However, given the two-dimensional nature of the EBSD analysis, which considers the variant distribution at a discrete cross-section of a three-dimensional grain, it is difficult to say with certainty the actual distribution of the variant pairs. Based on the identification of the CP groups in the microstructure, it can be extrapolated that variants 1-6 and 19-24 are more likely to appear in the NABM compared to the BM which had a higher likelihood of variants 7-12 and 19-24 appearing in the microstructure. In any case, the results show that lath martensitic BM and its Ni-rich alloy both prefer to form martensitic variants 19-24 which belong to the $(11\bar{1})_\gamma // (011)_\alpha$ parallel plane relationship (i.e., CP4).

To accurately identify each variant present in the PAGs analyzed in Figure 90, $\{001\}$ PFs were generated for multiple randomly picked regions in each identified block to ensure statistical accuracy, and the indexed variants were superimposed on the ideal PF to identify the variant. The color of the indexed spots in the PFs correspond to the color of the CP group (Table 11) that each identified variant belongs to. The variant-pairing behaviour was observed to be very similar to what has been reported in the literature for low-C lath martensitic steels [210,212,215,216,246,247]. The PAG analyzed in the BM sample showed that the γ grain had evolved into a single packet belonging to CP1, with three distinct blocks clearly visible in the large packet (shown by the color purple, blue and orange), with each block containing two martensite variants belonging to the same Bain group and having a low misorientation (i.e., V1/V4, V2/V5, and V3/V6), as shown in Figure 90 (a). There were no sub-blocks (i.e., single-variant blocks) observed in the microstructure, most likely due to the coarser packet and block size in the BM, which did not rely on frequent self-accommodation that would force the formation of sub-blocks.

The PAG analyzed for the NABM was identified by the EBSD analysis as two separate grains (labelled as 1 and 7 in Figure 89 (b), and separated by a white dotted line in Figure 90 (b)) but it is clear from an inspection of the PFs shown in Figure 90 (b) that the structure is one coherent grain, confirming that this grain evolved into all four packets representing all the parallel plane

relationships for each CP group, with each packet being composed of three blocks. Each bi-variant block identified in the microstructure was composed of a variant pair belonging to the same Bain group (Table 11). The IPF map shows the presence of some highly refined single-variant sub-blocks (e.g., V11 and V22) that formed by way of self-accommodation to fill space in the microstructure and maintain its coherency. The EBSD data using PFs and stereographic projections show that the variant-pairing behaviour in lath martensitic 22MnB5 and its Ni-rich alloy follows the same rule for the combination of two variants which has been reported previously [215,216], i.e., variant-pairing occurs along a rotational axis of $\langle 011 \rangle$ at an angle of 10.53° , with bi-variant blocks in a given CP group having variants belonging to the same Bain group, as was shown in Table 11.

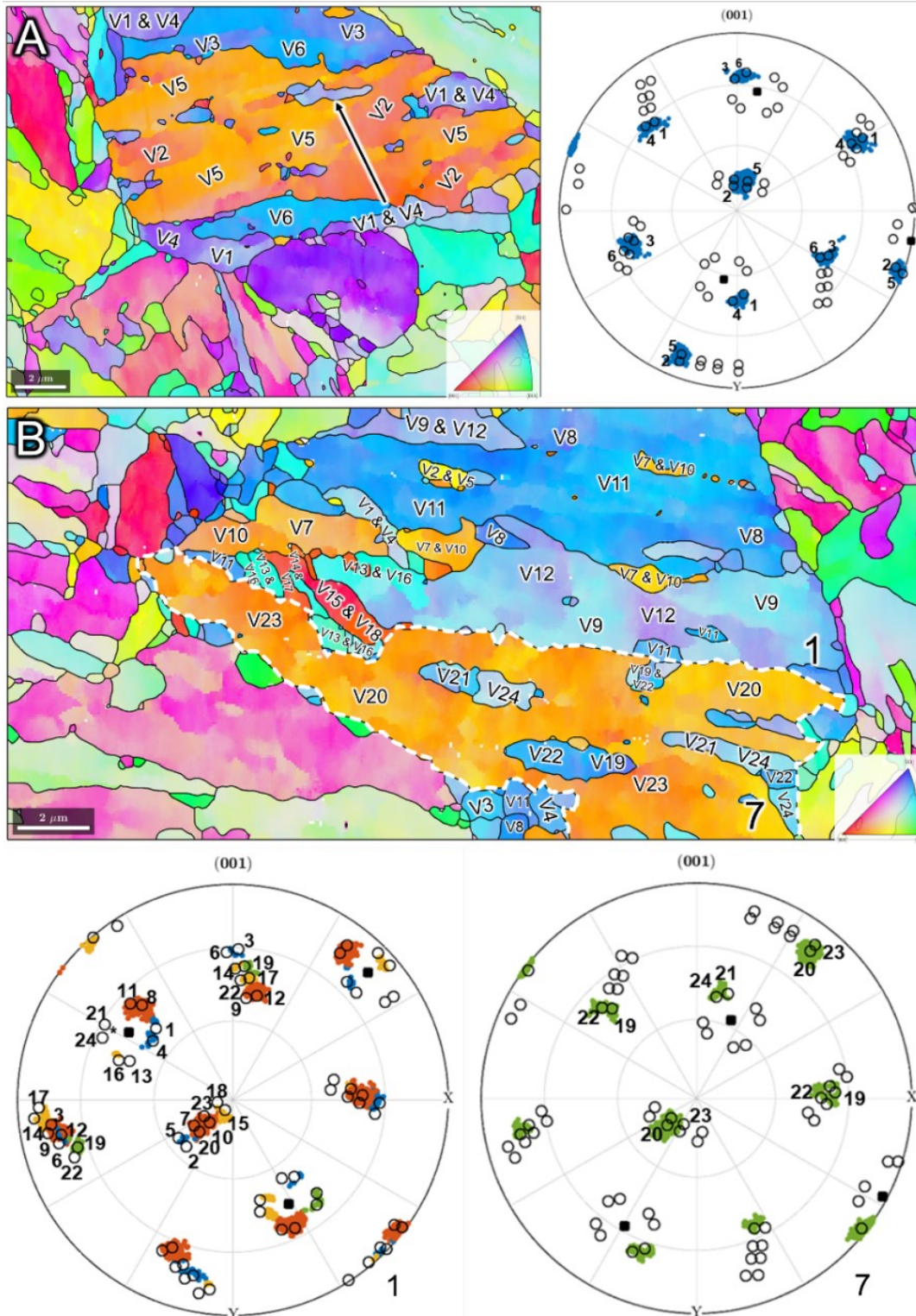


Figure 90: High-magnification IPF maps (and their respective pole figures) of a single austenite grain (labelled as grain 1 in Figure 6) from the (a) BM and (b) NABM, showing the variant-pairing behaviour and variant distribution in each respective grain. The {001} PFs clearly show that with the addition of Ni, the packet and block sizes are significantly more refined, with a much more homogeneous distribution of all 24 martensitic variants in each PAG indicating an ideal martensitic transformation with a net transformational strain that is almost purely dilatational.

7.5 Effect of Ni on grain orientation and internal strain during martensitic transformation

The grain reference orientation deviation (GROD) map shows the orientation heterogeneities that evolve during plastic deformation, making it an ideal tool to quantify internal strain during martensitic transformation. Each pixel in a given grain is colored based on its misorientation to the reference orientation of the grain it belongs to [248]. To minimize the effect of noise in the data which can be introduced by approaching the angular precision limit of the measurements [248], the grain orientation spread (GOS) map was used which is the average of the misorientation angles to the mean orientation of the grain, effectively measuring the relative spread in orientation for the whole grain.

The GROD map for the BM (Figure 91 (a)) shows that a significantly higher internal strain exists in the BM microstructure with a peak GROD angle of 15° . The GOS map for the BM (Figure 91 (c)) shows that a high percentage of martensitic blocks in the bulk microstructure had a high mean GOS value, indicating that these relatively larger sized blocks had high internal strain. These larger blocks exerted a much larger stress on the surrounding microstructure, resulting in a microstructure that showed severe orientation heterogeneities that evolved due to the plastic deformation associated with the martensitic transformation. The EBSD results showed that since the PAGs were unable to undergo an ideal transformation, i.e., the PAGs did not transform into all 4 packets based on the K-S OR [244], and the transformational strain was composed of a dilatational and shear strain which increased the plastic deformation of the martensitic structures, whereby increasing the internal strain.

The alloying of Ni in 22MnB5 had a profound effect on the morphology of the martensite and this resulted in a quantifiable effect on the observed grain orientation and internal strain in the microstructure due to the martensitic transformation. The GROD map for the NABM (Figure 91 (b)) shows a clear decrease in the mean and peak GROD, indicating that the microstructure has a noticeably reduced internal strain compared to the BM. This difference is even more noticeable by the decrease in mean GOS (Figure 91 (d)), which indicates that the newly formed martensitic microstructure is relatively strain-free with practically no orientation gradient. This significant decrease in the measured internal strain based on the grain orientation analysis confirms that the alloying of Ni in steel minimizes any transformational shear stress which reduces the internal strain of the microstructure, as proposed by Qi et al. [244], primarily due to the effective refinement of the blocks in the microstructure, which encourages self-accommodation of the martensitic crystals and is likely to improve the mechanical properties of the steel. Furthermore, it is well-known that the formation of lath boundaries is controlled by the lattice deformation during martensitic transformation [213,249], i.e., laths form to minimize the transformational strain energy, which explains the refinement in average lath width reported in Table 13 and observed in Section 7.6. The results definitively show that the addition of Ni in a given steel ensures that a fine-grained

polygranular austenitic microstructure can be fully transformed into martensite without any substantial internal strains being observed in the microstructure, indicating the likelihood that the refining effect of the Ni on the hierarchical structures making up the martensitic morphology (i.e., the packets, blocks, sub-blocks, and the laths) minimizes shear strains during transformation resulting in the overall strains being almost purely dilatational.

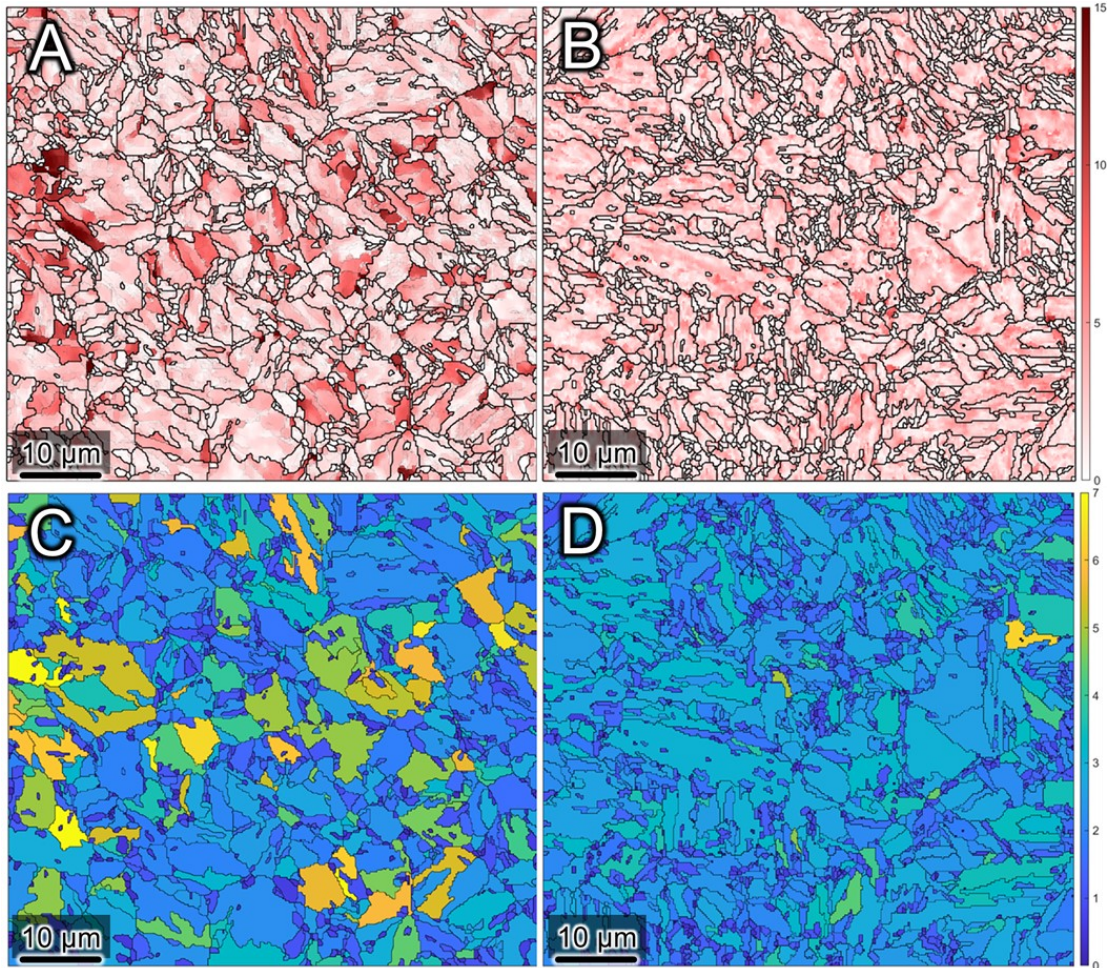


Figure 91: Grain reference orientation deviation (GROD) maps of the (a) BM and the (b) NABM showing the differences in orientation heterogeneities that evolve during plastic deformation with the addition of Ni. Grain orientation spread (GOS) maps of the (c) BM and the (d) NABM showing the differences in the average misorientation angles of the lath martensitic structures compared to the grain mean orientation. The strain maps clearly show that the addition of Ni significantly decreases transformational strains in the crystal lattice.

7.6 TEM analysis of lath and coarse martensite

The mesoscale investigation of the martensite morphology using EBSD shows clearly distinguishable differences between the microstructure of the BM and the NABM. However, an investigation using TEM is warranted to study the effect of Ni on the martensitic morphology at the nano- and atomic scale, with the low magnification HAADF and BF-TEM images of a characteristic FIB foil from the region of interest shown in Figure 92 (a) and (b), respectively. The

BM microstructure was not analyzed by TEM as lath martensitic 22MnB5 has been investigated in significant detail using TEM in other studies [250,251]. The martensitic morphology in the NABM was complex with the bulk microstructure being composed of fine needle-like laths (α_2'), with several large, interspersed CM laths, similar to the ones reported in the literature [209,222,243]. Due to the considerable variation in the size of the CM laths, ranging from a measured CM lath width of $\sim 0.62 \mu\text{m}$ to greater than $2 \mu\text{m}$ in some cases, these large laths were observed to be at different stages of autotempering, with some CM laths showing the presence of fine needle-like Fe_3C (θ)-carbides in the crystal (labelled as θ in Figure 94 (b)), while other CM crystals were completely carbide-free (labelled as CM* in Figure 92 (b)). These CM laths with carbides were smaller than the carbide-free CM laths which had a relatively high dislocation density in the crystal. The results showed that for the same hot-stamping heat treatment, the larger the size of the coarse lath, the lower the likelihood of fine needle-like θ -carbides nucleating in the crystal. The microstructure also showed the occasional presence of martensitic crystals with lenticular-like morphology (labelled with an * in Figure 92 (b)).

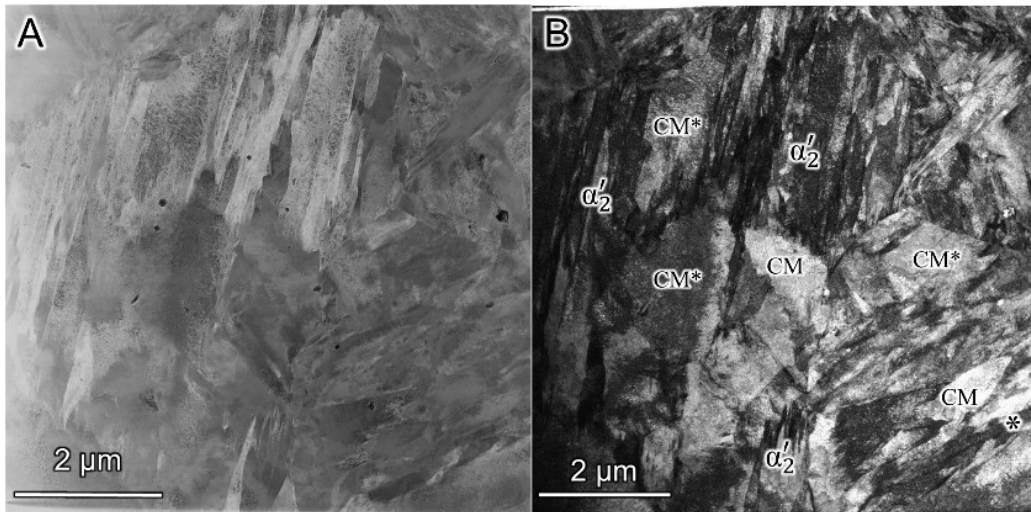


Figure 92: Low magnification (a) HAADF and (b) BF-TEM images of NABM showing the different types of martensitic morphology observed in the sample. (CM: coarse martensite, CM*: carbide-free coarse martensite, and the region marked with an * is lenticular martensite with a clearly visible midrib)

The low-magnification BF image (Figure 93 (a)) shows the microstructure of fine needle-like laths surrounding two carbide-free CM laths with different length scales. The BF image of the highly dislocated needle-like lath morphology is shown in high magnification in Figure 93 (b) and (c). Fine films of retained austenite (RA) were observed in between the martensitic laths using the dark field (DF) technique, as shown in Figure 93 (b₁) and (c₁), which would likely result in an improvement in the mechanical properties [252]. The presence of RA and the OR between the martensite and austenite was confirmed using the selected area diffraction (SAD) patterns shown in Figure 93 (c₂) with a zone axis of $[\bar{1}00]_{\alpha_{2,1}'} // [\bar{1}11]_{\alpha_{2,2}'} // [\bar{1}10]_{\gamma}$. The SAD pattern results confirm that the martensite and RA either had an OR close to K-S (i.e., $(111)_{\gamma} // (01\bar{1})_{\alpha_{2,2}'}$,

$[\bar{1}10]_{\gamma} // [\bar{1}11]_{\alpha_{2,2}'}$) or an OR close to Nishiyama-Wassermann (i.e., $(111)_{\gamma} // (011)_{\alpha_{2,1}'}$, $[\bar{1}10]_{\gamma} // [\bar{1}00]_{\alpha_{2,1}'}$) – although the match is closer to the K-S type OR, similar to what was shown by the EBSD results.

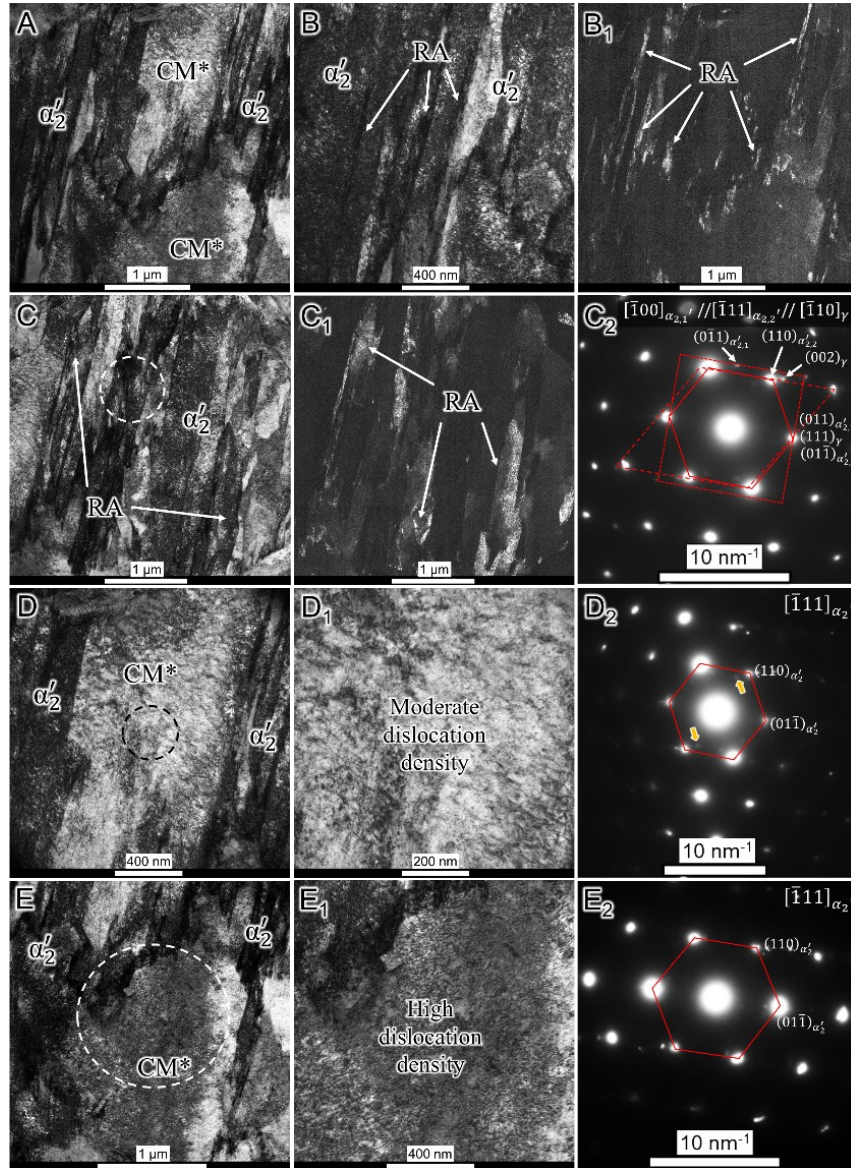


Figure 93: TEM micrograph at low magnification of the (a) BF image showing a region with several CM* crystals surrounded by fine lath martensite. High magnification BF- and DF images showing the lath martensite crystals on the (b, b₁) left and (c, c₁) right of the central CM* crystal, respectively. The DF images along with the SAD pattern shown in (c₂) confirms the presence of thin film-like RA between the martensite laths. The CM* crystal shown in (d) was smaller in size and had a relatively lower (d₁) dislocation density compared to the larger CM* crystal shown in (e), which had a significantly higher (e₁) dislocation density. The SAD patterns for these CM* crystals are shown in (d₂) and (e₂), respectively. The difference in dislocation density shows that these two coarse martensitic crystals are at different stages of autotempering, most likely due to their difference in size. Since the smaller crystal had autotempered more, faint diffraction spots corresponding to θ were observed as shown by the yellow arrows in (d₂). (CM*: carbide-free coarse martensite, RA: retained austenite, θ : cementite)

There were two types of carbide-free CM laths observed in the microstructure, as shown in Figure 93 (d) and (e). The first type (Figure 93 (d)) was a relatively smaller CM crystal which had a visibly lower dislocation density compared to the second type (Figure 93 (e)) of CM crystal which was larger and had a significantly higher dislocation density as shown in the high

magnification BF images in Figure 93 (d₁) and (e₁), respectively. Furthermore, the SAD pattern for the moderately-dislocated CM lath along the $[\bar{1}11]_{\alpha_2'}$ zone axis (Figure 93 (d₂)) showed the presence of faint diffraction spots that correspond to θ -carbides. The measured d-spacing of the faint spots from the SAD pattern was $d_{\text{measured}} \approx 2.52 \text{ \AA}$, which was in good agreement with the calculated value for the orthorhombic Fe₃C structure (i.e., $d_{211} \approx 2.54 \text{ \AA}$) with lattice parameters: $a = 5.091 \text{ \AA}$, $b = 6.744 \text{ \AA}$, and $c = 4.527 \text{ \AA}$. On the other hand, the SAD pattern for the highly-dislocated CM lath along the $[\bar{1}11]_{\alpha_2'}$ zone axis (Figure 93 (e₂)) showed no extra diffraction spots confirming that no carbide particles had nucleated in the crystal. These results show that the size of CM laths is very important in controlling the microstructural evolution that occurs in these crystals during autotempering, i.e., the smaller the CM laths, the higher the likelihood of partial dislocation recovery by way of annihilation as the dislocation networks inside the crystal become untangled which can lead to the dissolution of planar defects in the crystal structure. The subsequent lowering of the dislocation density in the coarse lath increases the likelihood of needle-like θ -carbides to preferentially nucleate along dislocation lines still present in the crystal. Similar microstructural evolution of CM laths has been reported in studies that have investigated the tempering behavior of these coarse martensite crystals in significant detail [209,243].

CM laths with a much higher number of clearly visible fine needle-like θ -carbides and a bulk lattice structure with relatively low dislocation densities are shown in Figure 94 (a) and (c). The high-magnification BF image (Figure 94 (b)) along with the corresponding HAADF image (Figure 94 (b₁)) show the presence of θ -carbides in the crystal, with a clearly preferential nucleation behavior. The presence of the θ -carbides was confirmed using the SAD pattern shown in Figure 94 (b₂) along the $[\bar{1}00]_{\alpha_2'} // [1\bar{2}2]_{\theta}$ zone axis. Three types of martensitic morphologies, namely fine martensitic laths bordering a large CM crystal and a lenticular-like martensitic crystal, are shown in high magnification in Figure 94 (c). The SAD pattern along the $[3\bar{3}1]_{\alpha_2'} // [2\bar{4}1]_{\theta}$ zone axis (Figure 94 (c₁)) confirms the presence of θ -carbides in the CM lath shown in Figure 94 (c).

In general, the CM crystals that showed the presence of θ -carbides were measured to be less than half the size of the carbide-free CM crystals. The significant difference in size resulted in greater autotempering of the smaller crystals which annihilated the dislocation networks and promoted the nucleation of needle-like carbides in the lattice. Finally, it is important to note that the film-like RA was only observed at the boundaries between the fine laths with no RA found in the vicinity of the CM crystals. This suggests that the γ to martensite transformation sequence requires the fine laths to form first, causing thin films of RA to become trapped in the spaces between adjacent lens-shaped lath martensitic crystals, while the CM transformation happens as a final “space-filling” step where the remaining γ in a given PAG transforms into a single or several large CM crystals.

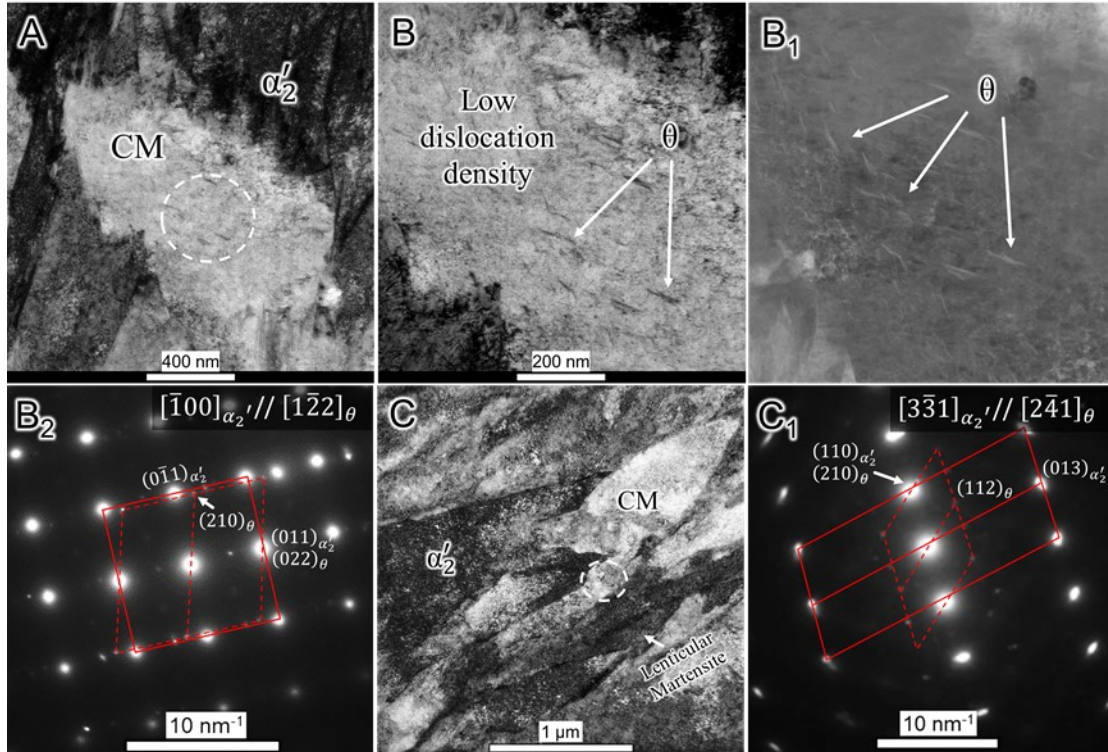


Figure 94: TEM micrographs at (a) Low and (b) high magnification BF and (b1) HAADF images showing the morphology of a single CM crystal that has a very low dislocation density and shows the presence of numerous needle-like θ carbides, as confirmed by the SADP shown in (b₂). (c) High magnification BF images of another CM crystal, with the associated (c₁) SADP confirming the presence of θ carbides. In general, the CM crystals were measured to be less than half the size of the CM* crystals resulting in greater autotempering of the crystals which results in dislocation recovery and encouraged the nucleation of needle-like carbides. (CM: coarse martensite, θ : cementite, CM*: carbide-free coarse martensite)

7.7 Effect of Ni on the hardness of the steel

Nanoindentation analysis was used to measure the hardness of the LB, and the different martensitic morphologies observed in the microstructure of the BM and NABM, as shown in Figure 95. Nanoindentation results showed that the alloying of Ni marginally reduced the hardness of the α_2' lath martensite in the NABM compared to the α_1' lath martensite found in the BM which had the highest measured hardness. This slight decrease in the nanohardness of the lath martensite in the NABM was most likely due to the refinement of the lath martensite crystals which promoted segregation of carbon from the bulk of the lath towards its boundaries during quenching [243], making the lattice slightly softer in comparison. It can also be argued that the addition of Ni minimized the internal strain in the bulk microstructure, which decreased the stress acting on neighboring martensitic blocks, which would also help decrease the bulk hardness of the microstructure. These results show that the solid-solution strengthening effect of the additional Ni in the lath martensite do not appear to have a significant effect on the hardness of the bulk microstructure, similar to what has been reported previously [156]. Combined with the refinement

of the PS, it can be expected that the toughness and the DBTT behavior of the steel would likely improve as a direct consequence of the alloying effect of Ni in 22MnB5.

The results also showed that the CM crystals found in the NABM had a lower hardness compared to the lath martensite found in either the BM or the NABM, which was most likely due to the autotempering of these large crystals during quenching that decreased the dislocation density in the crystal lattice resulting in a lower hardness. The LB found in the BM had the lowest measured hardness compared to the martensitic crystals. The nanohardness values of the martensite and LB reported in this study are well within the range that has been reported in the literature [121,125,157]. The load vs. depth (P-h) graph for α'_2 and the CM in the NABM (Figure 95) showed that although there was a significant difference in the initiation of plastic deformation for the two types of martensite at the beginning of the indentation test (with α'_2 and CM crystals showing the beginning of fully plastic deformation behavior at a depth of about 55 nm and 80 nm, respectively), the two graphs aligned almost perfectly at the later stages. This result confirms that CM crystals, although quite large compared to fine lath martensite, have mechanical properties that are quite similar to the surrounding bulk morphology.

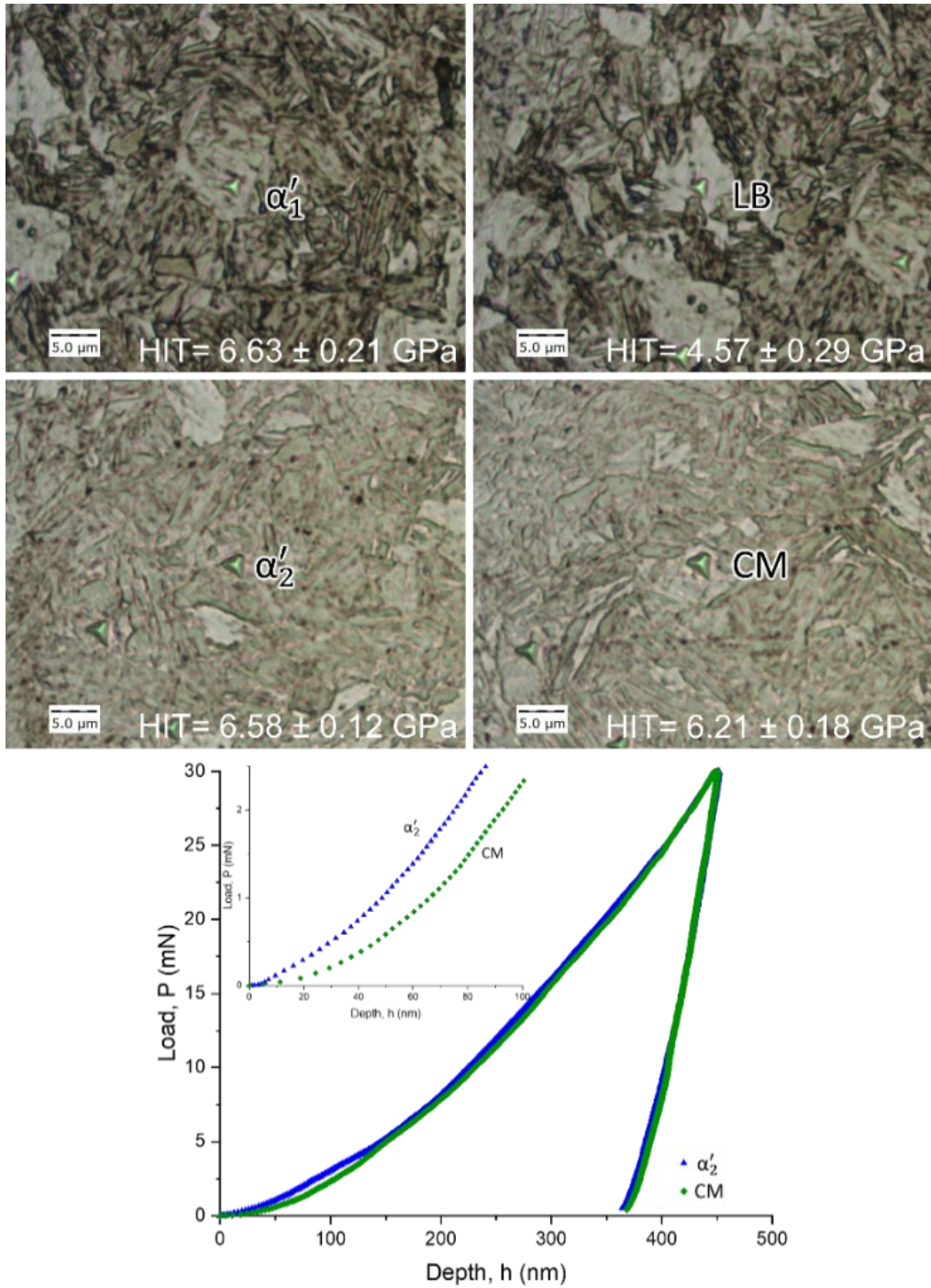


Figure 95: Nanoindentation data showing that the addition of Ni marginally reduced the hardness of the α'_2 lath martensite, compared to the α'_1 lath martensite found in the BM, most likely due to the decrease in size of the lath martensite crystals which promotes segregation of carbon from the bulk of the lath towards its boundaries making the lattice relatively softer in comparison. The CM crystals found in the NABM had a lower hardness compared to the lath martensite, most likely due to the autotempering of these large crystals that decreases the dislocation density resulting in a lower hardness. The LB found in the BM had the lowest measured hardness compared to the martensitic crystals. The P-h curve shows the deformation behavior response of the α'_2 and CM crystals during the indentation test.

7.8 Conclusions

This study provided a comprehensive investigation on the effect of alloying 22MnB5 steel with Ni to modify the martensitic morphology, crystallography, internal transformational strain, and mechanical properties of the lath martensite found in the bulk matrix. The results offer a tremendous insight into how martensitic morphology can be effectively controlled by alloying the steel with Ni. There are several key conclusions that can be made:

1. The additional of Ni increased the PAG size during the austenitization stage of hot-stamping while significantly refining the packet size, block width and the lath size.
2. The addition of Ni triggered an ideal martensitic transformation such that the majority of the austenite grains transformed into a total of four packets, with each packet representing a specific parallel plane OR as defined by the K-S model, and each packet was composed of three specific block structures with a homogenous distribution of all twenty-four martensitic variants regularly being observed in a given PAG.
3. The refinement of the hierarchical lath martensitic microstructure ensured frequent self-accommodation resulting in a transformational strain that was almost purely dilatational with very little strain being measured in the bulk microstructure of the NABM.
4. The refinement of the average lath width and average block width in the bulk microstructure due to the alloying effect of Ni would likely lead to an improvement in the yield strength of the NABM.
5. The NABM also showed the presence of significantly coarser martensite laths which were several times larger than the fine laths making up the bulk matrix.
6. CM laths formed as a final “space-filling” step during the martensitic transformation which facilitated self-accommodation of the crystals, helping minimize the transformational shear strain.
7. Depending on their size, the CM laths were observed to be at different stages of autotempering, with the largest CM crystals being the least likely to autotemper, as confirmed by their high dislocation density compared to smaller CM crystals.
8. The smallest CM crystals were more prone to tempering, having the lowest dislocation density and showing the presence of nanosized needle-like θ carbides embedded in the crystal that formed preferentially along dislocation lines in the lattice.
9. The different martensitic morphologies observed in the NABM had a lower hardness value compared to the lath martensite found in the BM, indicating that the addition of Ni would likely improve the toughness properties of fine-grained lath martensitic steels.

8 Conclusions and future work

8.1 Conclusions

The laser welding of Al-Si coated PHSs is problematic due to the dilution of the coating into the molten weld pool. This causes the formation of a dual phase ferrite-martensite microstructure in the FZ which is significantly weaker compared to the surrounding base material which is fully martensitic. The softer dual-phase FZ is prone to catastrophic brittle failure during loading of the welded sample. The research presented in this thesis aimed to solve the issue of FZ softening by achieving the following objective: to develop a fundamental understanding of the laser-substrate interaction during the LW of coated PHSs and investigating the effect of laser welding Al-Si coated 22MnB5 steel with various types of secondary/modified coatings on the microstructural evolution of the FZ and the resultant mechanical properties (i.e., establishing the relationships between the process-structure-properties of the given system).

The objective was achieved by optimizing the laser welding process to ensure that welding defects with the potential to negatively affect the mechanical properties of the studied laser welded joints were completely eliminated. A combination of numerical modelling and detailed experimental validation revealed the effects of laser defocusing and laser impingement angles on process stability which allowed for the process to be fully optimized without sacrificing process efficiency. Several different solutions to solve FZ softening in the joint were then developed. The results of the first study showed that a colloidal graphite coating could be used to achieve in situ ablation of the Al-Si coating with simultaneous in-situ alloying of the FZ with C to strengthen the weld beyond the nominal strength of the HSBM. The second study revealed that modification of the Al-Si coating using ESD was an effective method to strengthen the weld by way of in-situ alloying; although the results showed that solid-solution strengthening using Inconel was more effective compared to the dispersion strengthening effect achieved using WC nanoparticles. Finally, the effect of in-situ alloying of the FZ with pure Ni was considered which resulted in a fully martensitic microstructure and offered 100% joint efficiency. The effect of Ni on the morphology, crystallography, and mechanical properties of the lath martensitic steel was then investigated in thorough detail to provide insights on the strengthening effects of Ni on the microstructure of the HSBM. The results offered tremendous insights into how martensitic morphology could be effectively controlled by alloying the steel with Ni. This research offers several, highly novel solutions to the issue of FZ softening during laser welding of Al-Si coated 22MnB5, as validated by the international patent awarded to the authors for the discovery outlined

in Ref. [153]. The main conclusions from the research presented in this thesis are described in detail below:

1. Defocusing the laser beam and changing its impingement angle can be used as an effective tool to minimize/eliminate welding defects during high-speed laser welding without sacrificing process efficiency. By defocusing the beam, a plasma column can be achieved that has a length that maximizes the heat input into the weld while maintaining full penetration into the sheet to provide the largest cross-sectional area of the FZ by ensuring that the most effective use is being made of the power available from the laser. Defocusing the laser beam during the laser welding of thin-gauge materials can be used as an additional control parameter to stabilize the welding process, improve the liquid flow in the molten weld pool, and eliminate any surface or internal defects from the weld to achieve a weld geometry that is near-perfect. A leading beam impingement angle was shown to provide the most ideal weld geometry with the most stable melt pool for high-speed laser welding applications due to several reasons: the change in the shape of the beam spot that is caused by changing the beam impingement angle, the tilt angle of the keyhole relative to the direction of welding, the plasma plume ejection angle, the shape, size and orientation of the molten weld pool, and the resulting changes in the fluid flow caused by the combination of the listed factors.

2. Welding Al-Si coated 22MnB5 PHS through a graphite coating changed the alloying chemistry of the FZ by decreasing Al and increasing C in the weld which stabilized the austenite phase at elevated temperatures causing an increase in the martensite phase fraction and a reduction in the ferrite phase fraction after hot-stamping which improved the mechanical properties of the joint. It was observed that the welds made through the maximum graphite coating thickness of 130 μm had a UTS that matched the strength of the BM, and failure for these samples was successfully shifted from the FZ, where it normally occurs, to the BM.

3. Laser welding Al-Si coated 22MnB5 steel through a WC and In625 ESD-modified coating had a significant effect on the resulting microstructure and mechanical properties of the weldment. The results showed that the addition of dissolved W and C in the FZ stabilized the austenite loop which led to a reduction in the α -ferrite phase concentration, but the increased austenite stability was still insufficient to result in a fully as-quenched martensitic structure. However, the addition of WC nanoparticles reinforced the martensitic matrix by way of dispersion strengthening, thereby moving the failure location from the FZ to the BM when the weld was loaded. On the other hand, the addition of dissolved Ni and Cr in the FZ stabilized the austenite loop and significantly decreased the A_{c3} temperature which led to complete suppression of the α -ferrite phase formation in the weld, and again, moved the failure location from the FZ to the BM when loaded. The mechanical properties of the joints produced with the In625-modified coating were found to be superior to the WC-strengthened samples as the dispersion strengthening effect at the toe of the weld made this region excessively brittle.

4. By welding Al-Si coated 22MnB5 PHS through a pure Ni coating followed by a hot stamping process, the formation of ferrite in the FZ was completely suppressed and the strength

of the welds surpassed that of the hot-stamped BM, with the failure location being shifted from the FZ to the BM.

5. The addition of Ni increased the PAG size during the austenitization stage of hot-stamping while significantly refining the packet size, block width and the lath size. The refinement of the hierarchical lath martensitic microstructure ensured frequent self-accommodation resulting in a transformational strain that was almost purely dilatational with very little strain being measured in the bulk microstructure of the NABM. The results showed that the addition of Ni triggered an ideal martensitic transformation such that the majority of the austenite grains transformed into a total of four packets, with each packet representing a specific parallel plane OR as defined by the K-S model, and each packet was composed of three specific block structures with a homogenous distribution of all twenty-four martensitic variants regularly being observed in a given PAG. The refinement of the average lath width and average block width in the FZ microstructure due to the alloying effect of Ni led to an improvement in the yield and UTS of the martensite which made the Ni-alloyed FZ stronger than the surrounding BM.

The conclusions listed above directly satisfy the objectives outlined in Section 1.2 in the first chapter of this thesis. The studies presented in this thesis give several clear directions for future research, as discussed in the following section.

8.2 Direction for future research

There are three main directions for future research that can be highlighted as a consequence of this work. Firstly, it can be noted that there are very serious limitations in regard to the usage of the Al-Si coating, and none of the other Zn-based coatings used to protect 22MnB5 PHS provide a universal solution to corrosion and oxidation-related issues either. It can be concluded that almost all of the mechanical and metallurgical issues found with 22MnB5 PHS stem from the interaction of the coating with the substrate during the HS process – namely, LME cracking when using Zn-based coatings – or during the laser-welding process where the dilution of the Al-Si coating leads to severe FZ softening. Therefore, it is recommended that considerable efforts should be made in developing new coating technologies and/or improving the state of the art of existing coating technologies for HS applications.

Secondly, despite the existence of fully functional solutions to the problem of FZ softening in TWBs due to the dilution of the Al-Si coating into the FZ during laser welding, there exists a space in which newer and better solutions can be found that are more practical, more affordable, and easier to implement than the solutions currently being used. Several of these methods have been developed and discussed in this thesis (as described in the previous section) where the primary goal was to propose methodologies that achieved 100% joint efficiency without having to ablate the Al-Si coating prior to welding. Still, there is room to develop other process methodologies in which in-situ coating ablation can be achieved as a consequence of the reaction between the laser and the coating surface, similar to what has been proposed with the colloidal

graphite coating method. What other types of coatings might be a feasible option to achieve similar results? The mechanism of in-situ ablation due to secondary coatings is still in the early stages of discovery and requires further investigation. This could potentially be investigated by modifying the surface properties of the coating to change its emissivity properties or by adding a secondary coating that induces a reaction with the existing coating upon contact with the laser by way of which the problematic coating can be removed.

Thirdly, it can be noted that careful alterations in the chemical composition of the FZ by alloying different elements (i.e., Mn, Ni, or C) will give much better insight into how the mechanical and metallurgical properties of the FZ can be controlled. Studies of this sort may pave the way for future BM engineering (similar to what has been shown in Chapter 7), or it may open the door to developing newer coating technologies as our collective understanding of the material science that governs this problem improves. In the short-run, it may just help to solve the problem of FZ weakening due to the dilution of the coating into the molten weld pool. The in-situ modification of protective coatings using methods like ESD has been shown to be highly effective as it ensures that the coating is not removed prior to processing which improves the corrosion behavior of the final components. It is recommended that other methods of modifying as-received Zn and Al-based coatings like cold spraying etc. would be explored to investigate the added benefits of local coating modification techniques for industrially relevant processes like laser welding, resistance spot welding, and others.

Although the studies presented in this thesis have provided a comprehensive investigation on the effect of in-situ alloying of certain elements and compounds on the mechanical properties of laser welded joints, the morphology and microstructure were investigated in detail only for Ni-alloyed 22MnB5. It is also recommended that this type of analysis be expanded to include a thorough investigation on the effect of C and WC-alloyed 22MnB5 on the morphology and its resulting mechanical properties. The scale and scope of mechanical testing should be expanded to incorporate fatigue testing and formability testing (i.e., dome and punch tests) of the laser welded joints to develop a more comprehensive understanding of the mechanical properties of these joints. Finally, it is highly recommended that the scope of this work is expanded to an investigation on the similar and dissimilar butt-joining of 22MnB5 with other gauge lengths and grades of PHSs to further increase the practical relevance of the fundamental results presented in this thesis.

9 Research contributions (Ph.D. work)

9.1 Journal publications

1. **M. Shehryar Khan**, J. Lourenço, M. Faria, P. Enrique, G. Song, Y. Zhou, Improving the corrosion resistance of Inconel 52M laser-cladded steel by controlling the clad morphology, Under Review, *Journal of Manufacturing Processes* (2023)
2. **A.G. Kalashami**, **M. Shehryar Khan**, F. Goodwin, Y.N. Zhou, Investigating the mechanism of zinc-induced liquid metal embrittlement initiation in austenitic steel, Under Review, *Acta Materialia* (2023)
3. **S. Akbarian**, **M. Shehryar Khan**, O. Sherepenko, M.Y. Lee, P. Wanjara, E. Biro, Effect of heat source and Zn-coating type on the geometry and morphology of laser brazed thin-gauge steels, Under Review, *Journal of Manufacturing Processes* (2023)
4. **M. Shehryar Khan**, Y.N. Zhou, Weld-brazing or welding-brazing: Addressing the inconsistency in the naming convention used for this transformative non-fusion joining technique, *Manufacturing Letters* (2023), [10.1016/j.mfglet.2023.02.002](https://doi.org/10.1016/j.mfglet.2023.02.002)
5. S.S. Ghahfarokhi, **M. Shehryar Khan**, Y.-H Cho, M.Y. Lee, M.J. Benoit, Y.N. Zhou, The impact of heat input on the microstructural evolution and interfacial morphology of laser- and arc-brazed ZnAlMg coated steel, *Journal of Materials Processing Technology* (2023): 117943. [10.1016/j.jmatprotec.2023.117943](https://doi.org/10.1016/j.jmatprotec.2023.117943)
6. **M. Shehryar Khan**, **Y.-H. Cho**, F. Goodwin, Y.N. Zhou, Recent advances in weld-brazing to join thin-gauge alloys used in the automotive industry, *Advanced Joining Technologies for Automotive Lightweight Structures*, Book Chapter, TMS 2023, [10.1007/978-3-031-22524-6_40](https://doi.org/10.1007/978-3-031-22524-6_40)
7. Y.-H. Cho, **M. Shehryar Khan**, A. Midawi, S. Zhang, F. Goodwin, Y.N. Zhou, Effect of gap clearance on the mechanical properties of weld-brazed lap joints, *Manufacturing Letters* 35 (2023), [10.1016/j.mfglet.2022.11.002](https://doi.org/10.1016/j.mfglet.2022.11.002)
8. **M. Shehryar Khan**, Y.-H. Cho, S. Zhang, F. Goodwin, E. Biro, Y.N. Zhou, The effect of zinc coating type on the morphology, joint geometry, and mechanical properties of Si-Bronze arc brazed thin-gauge automotive steel, *Metallurgical and Materials Transactions A* 54 (2023), [10.1007/s11661-022-06857-1](https://doi.org/10.1007/s11661-022-06857-1)
9. A.G. Kalashami, **M. Shehryar Khan**, F. Goodwin, Y.N. Zhou, Investigating zinc-assisted liquid metal embrittlement in ferritic and austenitic steels: Correlation between crack susceptibility and failure mechanism, *Materials Characterization* 195 (2023), [10.1016/j.matchar.2022.112502](https://doi.org/10.1016/j.matchar.2022.112502).
10. **M. Shehryar Khan**, A.G. Kalashami, X. Wang, E. Biro, Y.N. Zhou, Refining the hierarchical structure of lath martensitic steel by in-situ alloying with nickel: morphology, crystallography, and mechanical properties, *Journal of Materials Science* (2022), [10.1007/s10853-022-07916-z](https://doi.org/10.1007/s10853-022-07916-z)

11. A. Ghatei-Kalashami, **M. Shehryar Khan**, M. Lee, Y.N. Zhou, High-temperature phase evolution of the ZnAlMg coating and its effect on mitigating liquid-metal-embrittlement cracking, *Acta Materialia*, 229 (2022). [10.1016/j.actamat.2022.117836](https://doi.org/10.1016/j.actamat.2022.117836)
12. **M. Shehryar Khan**, From dropout to Ph.D., *Science*, 377 6609 (2022), doi.org/10.1126/science
13. **M. Shehryar Khan**, P. Enrique, A. Ghatei-Kalashami, J.G. Lopes, N. Schell, J.P. Oliveira, E. Biro, Y.N. Zhou, (2022), The influence of in-situ alloying of electro-spark deposited coatings on the multiscale morphological and mechanical properties of laser welded Al-Si coated 22MnB5, *Materials Science and Engineering: A*. 839 (2022), [10.1016/j.msea.2022.142830](https://doi.org/10.1016/j.msea.2022.142830)
14. Y-H. Cho, **M. Shehryar Khan**, F. Goodwin, Y.N. Zhou, Effect of torch angle and position on bead geometry and joint strength during arc brazing of thin-gauge dual-phase steel, *International Journal of Advanced Manufacturing Technology*, (2022), [10.1007/s00170-022-09309-7](https://doi.org/10.1007/s00170-022-09309-7)
15. **M. Shehryar Khan**, S. Ali, D. Westerbaan, W. Duley, E. Biro, Y.N. Zhou, The effect of laser impingement angle on the optimization of melt pool geometry to improve process stability during high-speed laser welding of thin-gauge automotive steels, *Journal of Manufacturing Processes*, 78 (2022) 242–253. [10.1016/j.jmapro.2022.04.022](https://doi.org/10.1016/j.jmapro.2022.04.022)
16. **M. Shehryar Khan**, Y.-H. Cho, M. Alfano, F. Goodwin, E. Biro, Y.N. Zhou, A systematic study on the effect of coating type and surface preparation on the wettability of Si-Bronze brazing filler material on GI and GA- coated DP600, *Surface and Coatings Technology*, 425 (2021) 127735 [10.1016/j.surfcoat.2021.127735](https://doi.org/10.1016/j.surfcoat.2021.127735)
17. **M. Shehryar Khan**, M.H. Razmpoosh, A. Macwan, E. Biro, Y. Zhou, Optimizing weld morphology and mechanical properties of laser welded Al-Si coated 22MnB5 by surface application of colloidal graphite, *Journal of Materials Processing Technology*, 293 (2021) 117093. [10.1016/j.jmatprotec.2021.117093](https://doi.org/10.1016/j.jmatprotec.2021.117093)
18. **M. Shehryar Khan**, E. Biro, A. Macwan, Y.N. Zhou, α -ferrite Suppression during Fiber Laser Welding of Al- Si Coated 22MnB5 Press-Hardened Steel, *Welding Journal*, 100 (2021). [10.29391/2021.100.018](https://doi.org/10.29391/2021.100.018)
19. M.H. Razmpoosh, **M. Shehryar Khan**, A. Ghatei Kalashami, A. Macwan, E. Biro, N.Y. Zhou, Effects of laser beam defocusing on high-strain-rate tensile behavior of press-hardened Zn-coated 22MnB5 steel welds, *Optics and Laser Technology*, 141 (2021) 107116. [10.1016/j.optlastec.2021.107116](https://doi.org/10.1016/j.optlastec.2021.107116)
20. **M. Shehryar Khan**, S.I. Shahabad, M. Yavuz, W.W. Duley, E. Biro, Y. Zhou, Numerical modelling and experimental validation of the effect of laser beam defocusing on process optimization during fiber laser welding of automotive press-hardened steels, *Journal of Manufacturing Processes*, 67 (2021) 535–544. [10.1016/j.jmapro.2021.05.006](https://doi.org/10.1016/j.jmapro.2021.05.006)
21. **M. Shehryar Khan**, P. Enrique, G. Song, M.I.S.T. Faria, Y. Zhou, Laser-assisted wire cladding using a retrofitted laser welding system, *Surface Engineering* 37 (2021) [10.1080/02670844.2020.1820266](https://doi.org/10.1080/02670844.2020.1820266)
22. **M. Shehryar Khan**, M.H. Razmpoosh, E. Biro, Y. Zhou, A review on the laser welding of coated 22MnB5 press-hardened steel and its impact on the production of

tailor-welded blanks, *Science and Technology of Welding and Joining*, 25 (2020) 447–467. [10.1080/13621718.2020.1742472](https://doi.org/10.1080/13621718.2020.1742472)

23. J. Cheng, G. Song, Z. Zhang, **M. Shehryar Khan**, X. Dong, L. Liu, Investigating the multiscale effects of a novel post-weld composite processing treatment on minimizing weld softening in AA6061-T6 Al-alloy, *Journal of Materials Research and Technology*, (2022), [10.1016/j.jmrt.2022.09.020](https://doi.org/10.1016/j.jmrt.2022.09.020)
24. J. Cheng, G. Song, Z. Zhang, **M. Shehryar Khan**, Z. Liu, L. Liu, Improving heat-affected zone softening of aluminum alloys by in-situ forced cooling and post-weld rolling, *Journal of Materials Processing Technology*, 117639 (2022) [10.1016/j.jmatprotec.2022.117639](https://doi.org/10.1016/j.jmatprotec.2022.117639)
25. G. Song, S. Zhao, **M. Shehryar Khan**, J. Chen, M. Yao, Microscale bonding mechanism of Mg alloy and steel welded joint with nanoscale Al-based intermetallic compound interface layers, *Materials Today Communications*, 26 (2021) 101924. [10.1016/j.mtcomm.2020.101924](https://doi.org/10.1016/j.mtcomm.2020.101924)

9.2 Conference papers and presentations

1. **M. Shehryar Khan**, Y-H. Cho, F. Goodwin, Y.N. Zhou, Recent advances in the transformative non-fusion weld-brazing process used to join thin-gauge alloys used in the automotive industry, *TMS 2023: Advanced Joining Technologies for Automotive Lightweight Structures*, San Diego, CA, USA.
2. Y-H Cho, **M. Shehryar Khan**, B. Klassen, F. Goodwin, & Y. Zhou, Influence of surface treatment on joint strength during MIG brazing of GI and GA coated DP600. (2021) *Sheet Metal Welding Conference XIX*.
3. **M. Shehryar Khan**, D. Westerbaan, W.W. Duley, E. Biro, & Y.N. Zhou, The Impact of Laser Impingement Angle on Process Stability and Weld Geometry During High-Speed Laser Welding of Automotive Steels. (2021) *Sheet Metal Welding Conference XIX*.
4. **M. Shehryar Khan**, E. Biro and Y. Zhou (2020) Effects of Secondary Coatings on the ablation of Al-Si During Fiber Laser Welding of Al-Si Coated 22MnB5 Steel, Annual Innovation Seminar, Global R&D, ArcelorMittal Dofasco, Hamilton, ON, Canada
5. **M. Shehryar Khan**, E. Biro and Y. Zhou (2019) Effects of Colloidal Graphite Coating on Weld Properties During Fiber Laser Welding of Al-Si Coated 22MnB5 Steel, Annual Innovation Seminar, Global R&D, ArcelorMittal Dofasco, Hamilton, ON, Canada

9.3 Patents

1. Yunhong Zhou, Dulal Saha, Elliot Biro, Andrew Macwan, Adrian Gerlich, **M. Shehryar Khan**, (2021) Patent: WO / 2021/130524, Pre-Coated Steel Sheet Comprising an Additional Coating for Increasing the Mechanical Strength of the Weld Metal Zone of a Welded Steel Part Prepared from Said Pre-Coated Sheet, [patentscope.wipo.int/ WO2021130602](https://patentscope.wipo.int/WO2021130602)

References

- [1] M. Shehryar Khan, From dropout to Ph.D., *Science* 377 (2022) 1014. <https://doi.org/10.1126/science.caredit.ade5687>.
- [2] M. Ghosh, K. Kumar, R.S. Mishra, Friction stir lap welded advanced high strength steels: Microstructure and mechanical properties, *Mater. Sci. Eng. A.* 528 (2011) 8111–8119. <https://doi.org/10.1016/j.msea.2011.06.087>.
- [3] L. Mújica Roncery, S. Weber, W. Theisen, Welding of twinning-induced plasticity steels, *Scr. Mater.* 66 (2012) 997–1001. <https://doi.org/10.1016/j.scriptamat.2011.11.041>.
- [4] E. Billur, T. Altan, Three generations of advanced high strength steels for automotive applications, Part I, *Stamp. J.* (2014).
- [5] P. Kah, M. Pirinen, R. Suoranta, J. Martikainen, Welding of Ultra High Strength Steels, *Adv. Mater. Res.* 849 (2013) 357–365. <https://doi.org/10.4028/www.scientific.net/amr.849.357>.
- [6] S.S. Nayak, E. Biro, Y.N. Zhou, V.H. Baltazar Hernandez, E. Biro, Resistance Spot Welding of Dual-phase Steels: Heat affected zone softening and tensile properties, in: *Proc. 9th Int. Conf. Trends Weld. Res.*, Chicagi, Illinois, 2012: pp. 641–649. <https://www.researchgate.net/publication/258874522> (accessed March 8, 2020).
- [7] M. Xia, Z. Tian, L. Zhao, Y.N. Zhou, Metallurgical and Mechanical Properties of Fusion Zones of TRIP Steels in Laser Welding, *ISIJ Int.* 48 (2008) 483–488. <https://doi.org/10.2355/isijinternational.48.483>.
- [8] R. Ueji, N. Tsuchida, D. Terada, N. Tsuji, Y. Tanaka, A. Takemura, K. Kunishige, Tensile properties and twinning behavior of high manganese austenitic steel with fine-grained structure, *Scr. Mater.* 59 (2008) 963–966. <https://doi.org/10.1016/j.scriptamat.2008.06.050>.
- [9] P. Lan, J. Zhang, Tensile property and microstructure of Fe-22Mn-0.5C TWIP steel, *Mater. Sci. Eng. A.* 707 (2017) 373–382. <https://doi.org/10.1016/j.msea.2017.09.061>.
- [10] H. Liu, J. Liu, B. Wu, Y. Shen, Y. He, H. Ding, X. Su, Effect of Mn and Al contents on hot ductility of high alloy Fe-xMn-C-yAl austenite TWIP steels, *Mater. Sci. Eng. A.* 708 (2017) 360–374. <https://doi.org/10.1016/j.msea.2017.10.001>.
- [11] J.E. Jin, Y.K. Lee, Effects of Al on microstructure and tensile properties of C-bearing high Mn TWIP steel, *Acta Mater.* 60 (2012) 1680–1688. <https://doi.org/10.1016/j.actamat.2011.12.004>.
- [12] H. Karbasian, A.E. Tekkaya, A review on hot stamping, *J. Mater. Process. Technol.* 210 (2010) 2103–2118. <https://doi.org/10.1016/j.jmatprotec.2010.07.019>.
- [13] Z.H. Cai, H. Ding, R.D.K.K. Misra, Z.Y. Ying, Austenite stability and deformation behavior in a cold-rolled transformation-induced plasticity steel with medium manganese content, *Acta Mater.* 84 (2015) 229–236. <https://doi.org/10.1016/j.actamat.2014.10.052>.
- [14] J. Han, Y.-K.K. Lee, The effects of the heating rate on the reverse transformation

- mechanism and the phase stability of reverted austenite in medium Mn steels, *Acta Mater.* 67 (2014) 354–361. <https://doi.org/10.1016/j.actamat.2013.12.038>.
- [15] M. Abbasi, M. Naderi, A. Saeed-Akbari, Isothermal versus non-isothermal hot compression process: A comparative study on phase transformations and structure-property relationships, *Mater. Des.* 45 (2013) 1–5. <https://doi.org/10.1016/j.matdes.2012.08.062>.
- [16] P. Hein, J. Wilsius, Status and Innovation Trends in Hot Stamping of USIBOR 1500 P, *Steel Res. Int.* 79 (2008) 85–91. <https://doi.org/10.1002/srin.200806321>.
- [17] M. Maikranz-Valentin, U. Weidig, U. Schoof, H.-H. Becker, K. Steinhoff, Components with Optimised Properties due to Advanced Thermo-mechanical Process Strategies in Hot Sheet Metal Forming, *Steel Res. Int.* 79 (2008) 92–97. <https://doi.org/10.1002/srin.200806322>.
- [18] R. George, *Hot Forming of Boron Steels with Tailored Mechanical Properties: Experiments and Numerical Simulations*, University of Waterloo, 2011.
- [19] R. George, A. Bardelcik, M.J. Worswick, Hot forming of boron steels using heated and cooled tooling for tailored properties, *J. Mater. Process. Technol.* 212 (2012) 2386–2399. <https://doi.org/10.1016/j.jmatprotec.2012.06.028>.
- [20] M. Merklein, M. Wieland, M. Lechner, S. Bruschi, A. Ghiotti, Hot stamping of boron steel sheets with tailored properties: A review, *J. Mater. Process. Technol.* 228 (2016) 11–24. <https://doi.org/10.1016/j.jmatprotec.2015.09.023>.
- [21] B.T. Tang, Q.L. Wang, S. Bruschi, A. Ghiotti, P.F. Bariani, Influence of temperature and deformation on phase transformation and vickers hardness in tailored tempering process: Numerical and experimental verifications, *J. Manuf. Sci. Eng. Trans. ASME.* 136 (2014). <https://doi.org/10.1115/1.4027816>.
- [22] D.D. Múnera, A. Pic, D. Abou-Khalil, F. Shmit, F. Pinard, Innovative press hardened steel based laser welded blanks solutions for weight savings and crash safety improvements, *SAE Int. J. Mater. Manuf.* 1 (2009) 472–479. <https://doi.org/10.4271/2008-01-1076>.
- [23] D.D. Múnera, F. Pinard, L. Lacassin, Very and Ultra High Strength Steels based Tailored Welded Blanks: A step further towards crashworthiness improvement, in: *SAE Tech. Pap.*, SAE International, 2006. <https://doi.org/10.4271/2006-01-1213>.
- [24] H. Lindberg, Advanced high strength steel technologies in the 2016 Volvo XC90. Presented at: *Great Designs in Steel 2016*. Reproduced with permission from AISI – *Great Designs in Steel (GDIS)*, (2016).
- [25] M. Shehryar Khan, M.H. Razmpoosh, E. Biro, Y. Zhou, A review on the laser welding of coated 22MnB5 press-hardened steel and its impact on the production of tailor-welded blanks, *Sci. Technol. Weld. Join.* 25 (2020) 447–467. <https://doi.org/10.1080/13621718.2020.1742472>.
- [26] A.L. Schawlow, C.H. Townes, Infrared and optical masers, *Phys. Rev.* 112 (1958) 1940–1949. <https://doi.org/10.1103/PhysRev.112.1940>.
- [27] EINSTEIN, Albert, Strahlungs-Emission und -Absorption nach der Quantentheorie, *Verh. Deutsch. Phys. Gesell.* 18 (1916) 318–323.
- [28] E. Toyserkani, *Laser Cladding*, 2005. <https://doi.org/10.1017/CBO9781107415324.004>.
- [29] T.H. Maiman, Stimulated optical radiation in Ruby, *Nature.* 187 (1960) 493–494. <https://doi.org/10.1038/187493a0>.

- [30] W. Steen, J. Mazumder, *Laser material processing*, Springer Science & Business Media, 2010.
<https://books.google.com/books?hl=en&lr=&id=gPsq0HHAU4UC&oi=fnd&pg=PA1&dq=steen+laser+material+processing&ots=TI9k7xKLSx&sig=25y5T6oXe7N4ytoMocHwKhE-HE> (accessed March 10, 2020).
- [31] C. Dawes, *Laser welding: a practical guide*, Woodhead Publishing, 1992.
<https://books.google.com/books?hl=en&lr=&id=coWfkULEVPQC&oi=fnd&pg=PP13&dq=Laser+Welding+1992&ots=I4LQUGBkPi&sig=AiCs1EgrHUV592qAec1UqJGSF8M> (accessed March 10, 2020).
- [32] S. Kou, *Welding Metallurgy*, 2nd ed., John Wiley and Sons, Hoboken, NJ, 2003.
<https://doi.org/10.22486/iwj.v4i3.150243>.
- [33] S. Kou, Reprinted from *Welding Metallurgy*, 2nd ed, with permission from John Wiley and Sons, (2002).
- [34] M.N. Zervas, C.A. Codemard, High power fiber lasers: a review, *IEEE J. Sel. Top. Quantum Electron.* 20 (2014) 219–241. <https://ieeexplore.ieee.org/abstract/document/6808413/> (accessed March 11, 2020).
- [35] M.J. Cole, W.H. Loh, R.I. Laming, M.N. Zervas, S. Barcelos, Moving fibre/phase mask-scanning beam technique for enhanced flexibility in producing fibre gratings with uniform phase mask, *Electron. Lett.* 31 (1995) 1488–1490. <https://doi.org/10.1049/el:19950986>.
- [36] J.L. Archambault, S.G. Grubb, Fiber gratings in lasers and amplifiers, *J. Light. Technol.* 15 (1997) 1378–1390. <https://ieeexplore.ieee.org/abstract/document/618351/> (accessed March 11, 2020).
- [37] W. Duley, *Laser welding*, Wiley, 1999.
- [38] J. Dutta Majumdar, I. Manna, *Laser material processing*, *Int. Mater. Rev.* 56 (2011) 341–388. <https://doi.org/10.1179/1743280411Y.0000000003>.
- [39] J.M. Sánchez-Amaya, T. Delgado, J.J. De Damborenea, V. Lopez, F.J. Botana, Laser welding of AA 5083 samples by high power diode laser, *Sci. Technol. Weld. Join.* 14 (2009) 78–86. <https://doi.org/10.1179/136217108X347629>.
- [40] E. Assuncao, S. Ganguly, D. Yapp, S. Williams, Conduction mode-Broadening the range of applications for laser welding, in: *Proc. 63rd Annu. Assem. Int. Conf. Int. Inst. Weld.*, 2010: pp. 705–709. <https://dspace.lib.cranfield.ac.uk/handle/1826/7323> (accessed March 12, 2020).
- [41] E. Assuncao, S. Williams, D. Yapp, Interaction time and beam diameter effects on the conduction mode limit, *Opt. Lasers Eng.* 50 (2012) 823–828. <https://doi.org/10.1016/j.optlaseng.2012.02.001>.
- [42] Y. Kawahito, M. Mizutani, S. Katayama, High quality welding of stainless steel with 10 kW high power fibre laser, *Sci. Technol. Weld. Join.* 14 (2009) 288–294. <https://doi.org/10.1179/136217108X372531>.
- [43] S. Ramasamy, C.E. Albright, CO₂ and Nd-YAG laser beam welding of 5754-O aluminium alloy for automotive applications, *Sci. Technol. Weld. Join.* 6 (2001) 182–190. <https://doi.org/10.1179/136217101101538730>.
- [44] E. Assunção, L. Quintino, R. Miranda, Comparative study of laser welding in tailor blanks for the automotive industry, *Int. J. Adv. Manuf. Technol.* 49 (2010) 123–131.

- <https://doi.org/10.1007/s00170-009-2385-0>.
- [45] D. Westerbaan, *Fiber Laser Welding of Advanced High Strength Steels*, University of Waterloo, 2013.
- [46] D. Westerbaan, D. Parkes, S.S. Nayak, D.L. Chen, E. Biro, F. Goodwin, Y. Zhou, Effects of concavity on tensile and fatigue properties in fibre laser welding of automotive steels, *Sci. Technol. Weld. Join.* 19 (2014) 60–68. <https://doi.org/10.1179/1362171813Y.0000000163>.
- [47] D.T. Swift-Hook, A. E.F. Gick, Penetration Welding with Lasers, *Weld. J.* 52 (1973) 492s-499s. https://app.aws.org/wj/supplement/WJ_1973_11_s492.pdf (accessed March 15, 2020).
- [48] W.W. Duley, LASER MATERIAL INTERACTIONS OF RELEVANCE TO METAL SURFACE TREATMENT., in: NATO ASI Ser. Ser. E Appl. Sci., Martinus Nijhoff Publ, 1986: pp. 3–16. https://doi.org/10.1007/978-94-009-4468-8_2.
- [49] W.W. Duley, K. Grant, Laser surface treatment., U.S. Patent No. 4,972,061., 1990.
- [50] W. Steen, Z. Chen, D. West, Laser Surface Melting of Cast Irons and Alloy Cast Iron, *Ind. Laser Annu. Handb.* (1987) 80–96.
- [51] Z. Chen, LASER SURFACE MELTING AND ALLOYING OF CAST IRONS, Univeristy of London, 1987.
- [52] T.J. Wieting, J.L. Derosa, Effects of surface condition on the infrared absorptivity of 304 stainless steel, *J. Appl. Phys.* 50 (1979) 1071–1078. <https://doi.org/10.1063/1.326083>.
- [53] R. Weber, A. Michalowski, M. Abdou-Ahmed, V. Onuseit, V. Rominger, M. Kraus, T. Graf, Effects of radial and tangential polarization in laser material processing, *Phys. Procedia.* 12 (2011) 21–30. <https://doi.org/10.1016/j.phpro.2011.03.004>.
- [54] E. Kannatey-Asibu, Thermal aspects of the split-beam laser welding concept, *J. Eng. Mater. Technol.* 113 (1991) 215–221. <https://doi.org/10.1115/1.2903395>.
- [55] C. Glumann, J. Rapp, F. Dausinger, H. Hügel, Welding with combination of two CO₂-lasers - Advantages in processing and quality, in: *Int. Congr. Appl. Lasers Electro-Optics*, Laser Institute of America, 1993: pp. 672–681. <https://doi.org/10.2351/1.5058630>.
- [56] B. Hohenberger, C.-L. Chang, C. Schinzel, F. Dausinger, H. Hügel, Laser welding with Nd:YAG-multi-beam technique, in: *Int. Congr. Appl. Lasers Electro-Optics*, Laser Institute of America, 1999: pp. D167–D176. <https://doi.org/10.2351/1.5059218>.
- [57] Y. Sun, L. Wu, C. Tan, W. Zhou, B. Chen, X. Song, H. Zhao, J. Feng, Influence of Al-Si coating on microstructure and mechanical properties of fiber laser welded 22MnB5 steel, *Opt. Laser Technol.* 116 (2019) 117–127. <https://doi.org/10.1016/j.optlastec.2019.03.024>.
- [58] M.H. Razmpoosh, M. Shehryar Khan, A. Ghatei Kalashami, A. Macwan, E. Biro, Y. Zhou, Effects of laser beam defocusing on high-strain-rate tensile behavior of press-hardened Zn-coated 22MnB5 steel welds, *Opt. Laser Technol.* 141 (2021) 107116. <https://doi.org/10.1016/j.optlastec.2021.107116>.
- [59] X. Xu, G. Mi, L. Chen, L. Xiong, P. Jiang, X. Shao, C. Wang, Research on microstructures and properties of Inconel 625 coatings obtained by laser cladding with wire, *J. Alloys Compd.* 715 (2017) 362–373. <https://doi.org/10.1016/j.jallcom.2017.04.252>.
- [60] Y. Ai, P. Jiang, C. Wang, G. Mi, S. Geng, W. Liu, C. Han, Investigation of the humping formation in the high power and high speed laser welding, *Opt. Lasers Eng.* 107 (2018)

- 102–111. <https://doi.org/10.1016/j.optlaseng.2018.03.010>.
- [61] M. Shehryar Khan, D. Westerbaan, W. Duley, E. Biro, N.Y. Zhou, The Impact of Laser Impingement Angle on Process Stability and Weld Geometry During High-Speed Laser Welding of Automotive Steels, in: Sheet Met. Weld. Conf. XIX, Livonia, MI, 2021.
- [62] M. Shehryar Khan, S. Ali, D. Westerbaan, W. Duley, E. Biro, Y.N. Zhou, The effect of laser impingement angle on the optimization of melt pool geometry to improve process stability during high-speed laser welding of thin-gauge automotive steels, *J. Manuf. Process.* 78 (2022) 242–253. <https://doi.org/10.1016/j.jmapro.2022.04.022>.
- [63] M. Shehryar Khan, S.I. Shahabad, M. Yavuz, W.W. Duley, E. Biro, Y. Zhou, Numerical modelling and experimental validation of the effect of laser beam defocusing on process optimization during fiber laser welding of automotive press-hardened steels, *J. Manuf. Process.* 67 (2021) 535–544. <https://doi.org/10.1016/j.jmapro.2021.05.006>.
- [64] G.M. Eboo, Arc Augmented Laser Welding, University of London, 1979.
- [65] W.M. Steen, M. Eboo, Arc augmented laser beam welding, *Met. Constr.* (1979) 332–335.
- [66] W.M. Steen, Arc augmented laser processing of materials, *J. Appl. Phys.* 51 (1980) 5636–5641. <https://doi.org/10.1063/1.327560>.
- [67] W.M. Steen, Hybrid laser-Arc processing, in: 2nd Pacific Int. Conf. Appl. Laser Opt., Laser Institute of America, 2006: pp. 151–156. <https://doi.org/10.2351/1.5056917>.
- [68] F. Briand, O. Dubet, C. CHOVET, Process for laser-arc hybrid welding aluminized metal workpieces, U.S. Patent 9,616,527, 2017.
- [69] M. Kang, C. Kim, S.M. Bae, Laser tailor-welded blanks for hot-press-forming steel with arc pretreatment, *Int. J. Automot. Technol.* 16 (2015) 279–283. <https://doi.org/10.1007/s12239-015-0029-y>.
- [70] P. Ravier, L.G. Aranda, Y. Chastel, Hot stamping experiment and numerical simulation of pre-coated USIBOR1500 quenchable steels, in: SAE Tech. Pap., SAE International, 2003. <https://doi.org/10.4271/2003-01-2859>.
- [71] G. Tackle, K. Forch, A. Sartorius, Heat treatable and surface hardening steels for vehicle and machine construction, *Steel.* 2 (1993).
- [72] M. Naderi, Hot Stamping of Ultra High Strength Steels, RWTH Aachen, 2007.
- [73] H. Karbasian, A. Tekkaya, A review on hot stamping, Reprinted from *Journal of Materials Processing Technology*, 210/15, Pages 2103-2118, with permission from Elsevier, (2010).
- [74] D.C. Saha, E. Biro, A.P. Gerlich, Y.N. Zhou, Fiber Laser Welding of AlSi Coated Press Hardened Steel, *Weld. J.* 95 (2016) 147–156.
- [75] D.C. Saha, E. Biro, A.P. Gerlich, Y.N. Zhou, Fiber laser welding of AlSi coated press hardened steel, Reprinted with permission from the *Welding Journal*, Copyright American Welding Society, (2016).
- [76] J.E. Morral, J.B. Cameron, Boron hardenability mechanisms, in: *Boron in Steel*, 1979.
- [77] W.F. Jandeska, J.E. Morral, The distribution of boron in austenite, *Metall. Trans.* 3 (1972) 2933–2937. <https://doi.org/10.1007/BF02652863>.
- [78] D.A. Mortimer, M.G. Nicholas, Metal Science Surface and grain-boundary energies of AISI 316 stainless steel in the presence of boron, *Met. Sci.* 10 (1976) 326–332. <https://doi.org/10.1179/msc.1976.10.9.326>.

- [79] P. Maitrepierre, D. Thivellier, J.R. Vernis, Microstructure and hardenability of low alloy boron containing steels, hardenability concepts with applications to steel, in: Conf. Proceeding, Chicago, 1977: pp. 24–26.
- [80] R.C. Sharma, G.R. Purdy, NUCLEATION LIMITATION AND HARDENABILITY., *Met. Trans.* 5 (1974) 939–947. <https://doi.org/10.1007/BF02643152>.
- [81] B.M. Kapadia, Hardenability concepts with application to steel, in: AIME, 1978.
- [82] X.L. He, Y.Y. Chu, J.J. Jonas, Grain boundary segregation of boron during continuous cooling, *Acta Metall.* 37 (1989) 147–161. [https://doi.org/10.1016/0001-6160\(89\)90274-5](https://doi.org/10.1016/0001-6160(89)90274-5).
- [83] D.W. Fan, H.S. Kim, B.C. De Cooman, B.C. De Cooman, B.C. De Cooman, A review of the physical metallurgy related to the hot press forming of advanced high strength steel, *Steel Res. Int.* 80 (2008) 241–248. <https://doi.org/10.2374/SRI08SP131>.
- [84] L. Dosdat, J. Petitjean, T. Vietoris, O. Clauzeau, Corrosion resistance of different metallic coatings on press-hardened steels for automotive, *Steel Res. Int.* 82 (2011) 726–733. <https://doi.org/10.1002/srin.201000291>.
- [85] L. Vaissiere, J.P. Laurent, A. Reinhardt, Development of Pre-Coated Boron Steel for Applications on PSA Peugeot Citroën and RENAULT Bodies in White, in: SAE Trans., SAE International, 2002: pp. 909–917. <https://doi.org/10.2307/44718720>.
- [86] D.W. Fan, B.C. De Cooman, State-of-the-knowledge on coating systems for hot stamped parts, *Steel Res. Int.* 83 (2012) 412–433. <https://doi.org/10.1002/srin.201100292>.
- [87] M. Kobayashi, T. Saori, M. Okano, Hot-dip aluminized steel sheet, method of manufacturing the same and alloy-layer control apparatus, Patent No. 6,017,643, 2000.
- [88] R.W. Richards, R.D. Jones, P.D. Clements, H. Clarke, Metallurgy of continuous hot dip aluminising, *Int. Mater. Rev.* 39 (1994) 191–212. <https://doi.org/10.1179/imr.1994.39.5.191>.
- [89] S. Kobayashi, T. Yakou, Control of intermetallic compound layers at interface between steel and aluminum by diffusion-treatment, *Mater. Sci. Eng. A.* 338 (2002) 44–53. [https://doi.org/10.1016/S0921-5093\(02\)00053-9](https://doi.org/10.1016/S0921-5093(02)00053-9).
- [90] M. Shehryar Khan, Y.-H. Cho, M. Alfano, F. Goodwin, E. Biro, Y. Zhou, A systematic study on the effect of coating type and surface preparation on the wettability of Si-Bronze brazing filler material on GI and GA-coated DP600, *Surf. Coat. Technol.* 425 (2021) 127735. <https://doi.org/https://doi.org/10.1016/j.surfcoat.2021.127735>.
- [91] M. Shehryar Khan, Y.-H. Cho, S. Zhang, F. Goodwin, E. Biro, Y.N. Zhou, The Effect of Zinc Coating Type on the Morphology, Joint Geometry, and Mechanical Properties of Weld-Brazed Thin-Gauge Automotive Steel, *Metall. Mater. Trans. A Phys. Metall. Mater. Sci.* 54 (2023) 179–195. <https://doi.org/10.1007/s11661-022-06857-1>.
- [92] M.H. Razmpoosh, C. DiGiovanni, Y.N. Zhou, E. Biro, Pathway to understand liquid metal embrittlement (LME) in Fe-Zn couple: From fundamentals toward application, *Prog. Mater. Sci.* 121 (2021) 1–29. <https://doi.org/10.1016/j.pmatsci.2021.100798>.
- [93] A. Ghatei-Kalashami, M. Shehryar Khan, M.-Y.Y. Lee, Y.N. Zhou, High-temperature phase evolution of the ZnAlMg coating and its effect on mitigating liquid-metal-embrittlement cracking, *Acta Mater.* 229 (2022) 117836. <https://doi.org/10.1016/j.actamat.2022.117836>.
- [94] A. Ghatei-Kalashami, M. Shehryar Khan, F. Goodwin, Y.N. Zhou, Investigating zinc-

- assisted liquid metal embrittlement in ferritic and austenitic steels: Correlation between crack susceptibility and failure mechanism, *Mater. Charact.* 195 (2023) 112502. <https://doi.org/10.1016/j.matchar.2022.112502>.
- [95] D. Fan, B. De Cooman, State-of-the-Knowledge on Coating Systems for Hot Stamped Parts, Reprinted with permission from John Wiley and Sons, Copyright Steel Research International, (2012) 412–433.
- [96] W. Ehling, L. Cretteur, A. Pic, R. Vierstraete, Q. Yin, Development of a laser decoating process for fully functional Al-Si coated press hardened steel laser welded blank solutions, in: *Proc. 5th Int. WLT-Conference Lasers Manuf.*, Munich, Germany, 2009.
- [97] P. Drillet, D. Spehner, R. Kefferstein, Coated steel strips, methods of making the same, methods of using the same, stamping blanks prepared from the same, stamped products prepared from the same, and articles of manufacture which contain such a stamped product, U.S. Patent 8,307,680, 2012.
- [98] M. Suehiro, J. Maki, K. Kusumi, M. Ohgami, T. Miyakoshi, Properties of aluminized steels for hot-forming, in: *SAE Tech. Pap.*, SAE International, 2003: pp. 2003-01–2853. <https://doi.org/10.4271/2003-01-2853>.
- [99] D.W. Fan, H.S. Kim, J.-K.K. Oh, K.-G.G. Chin, B.C. De Cooman, Coating degradation in hot press forming, *ISIJ Int.* 50 (2010) 561–568. <https://doi.org/10.2355/isijinternational.50.561>.
- [100] F. Jenner, M.E. Walter, R. Mohan Iyengar, R. Hughes, Evolution of phases, microstructure, and surface roughness during heat treatment of aluminized low carbon steel, *Metall. Mater. Trans. A Phys. Metall. Mater. Sci.* 41 (2010) 1554–1563. <https://doi.org/10.1007/s11661-009-0105-x>.
- [101] D.W. Fan, B.C. De Cooman, Formation of an Aluminide Coating on Hot Stamped Steel, *ISIJ Int.* 50 (2010) 1713–1718. <https://doi.org/10.2355/isijinternational.50.1713>.
- [102] W. Lin, F. Li, D. Wu, X. Chen, X. Hua, H. Pan, Effect of Al-Si Coating on Weld Microstructure and Properties of 22MnB5 Steel Joints for Hot Stamping, *J. Mater. Eng. Perform.* 27 (2018) 1825–1836. <https://doi.org/10.1007/s11665-018-3259-0>.
- [103] W. Lin, F. Li, X. Hua, D. Wu, Effect of filler wire on laser welded blanks of Al-Si-coated 22MnB5 steel, *J. Mater. Process. Technol.* 259 (2018) 195–205. <https://doi.org/10.1016/j.jmatprotec.2018.04.041>.
- [104] M.H. Razmpoosh, A. Macwan, E. Biro, D.L. Chen, Y. Peng, F. Goodwin, Y. Zhou, Liquid metal embrittlement in laser beam welding of Zn-coated 22MnB5 steel, *Mater. Des.* 155 (2018) 375–383. <https://doi.org/10.1016/j.matdes.2018.05.065>.
- [105] R. Autengruber, G. Luckeneder, S. Kolnberger, J. Faderl, A.W. Hassel, Surface and coating analysis of press-hardened hot-dip galvanized steel sheet, *Steel Res. Int.* 83 (2012) 1005–1011. <https://doi.org/10.1002/srin.201200068>.
- [106] J. Kondratiuk, P. Kuhn, E. Labrenz, C. Bischoff, Zinc coatings for hot sheet metal forming: Comparison of phase evolution and microstructure during heat treatment, *Surf. Coatings Technol.* 205 (2011) 4141–4153. <https://doi.org/10.1016/j.surfcoat.2011.03.002>.
- [107] L. Cho, H. Kang, C. Lee, B.C. De Cooman, Microstructure of liquid metal embrittlement cracks on Zn-coated 22MnB5 press-hardened steel, *Scr. Mater.* 90 (2014) 25–28. <https://doi.org/10.1016/j.scriptamat.2014.07.008>.

- [108] C.W. Lee, W.S. Choi, L. Cho, Y.R. Cho, B.C. De Cooman, Liquid-Metal-Induced Embrittlement Related Microcrack Propagation on Zn-coated Press Hardening Steel, *ISIJ Int.* 55 (2015) 264–271. <https://doi.org/10.2355/isijinternational.55.264>.
- [109] Y.G. Kim, I.J. Kim, J.S. Kim, Y. Il Chung, D.Y. Choi, Evaluation of Surface Crack in Resistance Spot Welds of Zn-Coated Steel, *Mater. Trans.* 55 (2014) 171–175. <https://doi.org/10.2320/matertrans.M2013244>.
- [110] L.A. Roudabush, Zinc-Nickel Alloy Coatings—A Technical Review of Published Literature, *SAE Trans.* 99 (1990) 720–728. <https://doi.org/10.2307/44553749>.
- [111] S. Goedicke, S. Sepeur, G. Frenzer, C. Breyer, Wet chemical coating materials for hot sheet forming-anti scaling and corrosion protection, in: 1st Int. Conf. Hot Sheet Met. Form. High-Performance Steel, Kassel, Germany, 2008.
- [112] G. Berglund, The history of hardening of boron steel in northern Sweden, in: 1st Int. Conf. Hot Sheet Met. Form. High-Performance Steel, Kassel, Germany, 2008: p. (Vol. 175, 177).
- [113] X. Bano, J.P. Laurent, Heat treated boron steels in the automotive industry. In: 39th Mechanical Working and Steel Processing Conference, in: 39th Mech. Work. Steel Process. Conf., 1997: pp. 673–677.
- [114] F.G. Kerby, DIE-FORMED SHEET METAL STRUCTURES AND METHOD OF MAKING THE SAME, 3,159,419, 1964.
- [115] C. Kim, M.J. Kang, Y.D. Park, Laser welding of Al-Si coated hot stamping steel, *Procedia Eng.* 10 (2011) 2226–2231. <https://doi.org/10.1016/j.proeng.2011.04.368>.
- [116] D. Saha, E. Biro, A. Gerlich, N. Zhou, Fusion zone microstructure evolution of fiber laser welded press-hardened steels, Reprinted from *Scripta Materialia* (Copyright), 121, Pages 18-22, with permission from Elsevier, (2016).
- [117] D.S. Martín, Y. Palizdar, C. García-Mateo, R.C. Cochrane, R. Brydson, A.J. Scott, Influence of aluminum alloying and heating rate on austenite formation in low carbon-manganese steels, *Metall. Mater. Trans. A Phys. Metall. Mater. Sci.* 42 (2011) 2591–2608. <https://doi.org/10.1007/s11661-011-0692-1>.
- [118] T.J. Yoon, M.H. Oh, H. jeong Shin, C.Y. Kang, Comparison of microstructure and phase transformation of laser-welded joints in Al-10wt%Si-coated boron steel before and after hot stamping, Reprinted from *Materials Characterization*, 128:195-202, with permission from Elsevier, (2017).
- [119] K.C. Mills, B.J. Keene, R.F. Brooks, A. Shirali, Marangoni effects in welding, *Philos. Trans. R. Soc. A Math. Phys. Eng. Sci.* 356 (1998) 911–925. <https://doi.org/10.1098/rsta.1998.0196>.
- [120] I. Egry, E. Ricci, R. Novakovic, S. Ozawa, Surface tension of liquid metals and alloys-Recent developments, *Adv. Colloid Interface Sci.* 159 (2010) 198–212. <https://doi.org/10.1016/j.cis.2010.06.009>.
- [121] D.C. Saha, D. Westerbaan, S.S. Nayak, E. Biro, A.P. Gerlich, Y. Zhou, Microstructure-properties correlation in fiber laser welding of dual-phase and HSLA steels, *Mater. Sci. Eng. A.* 607 (2014) 445–453. <https://doi.org/10.1016/j.msea.2014.04.034>.
- [122] H. Du, L. Hu, J. Liu, X. Hu, A study on the metal flow in full penetration laser beam welding for titanium alloy, Reprinted from *Computational Materials Science*, 29(4), Copyright, with permission from Elsevier, (2004) 419–427.

- [123] M. Kang, Y.M. Kim, C. Kim, Effect of heating parameters on laser welded tailored blanks of hot press forming steel, *J. Mater. Process. Technol.* 228 (2016) 137–144. <https://doi.org/10.1016/j.jmatprotec.2015.06.028>.
- [124] H. Bhadeshia, R. Honeycombe, *Steels: microstructure and properties*, Butterworth-Heinemann, 2017.
- [125] D.C. Saha, E. Biro, A.P. Gerlich, N.Y. Zhou, Fusion zone microstructure evolution of fiber laser welded press-hardened steels, *Scr. Mater.* 121 (2016) 18–22. <https://doi.org/10.1016/j.scriptamat.2016.04.032>.
- [126] T.J. Yoon, M.H. Oh, H. Jeong Shin, C.Y. Kang, Comparison of microstructure and phase transformation of laser-welded joints in Al-10wt%Si-coated boron steel before and after hot stamping, *Mater. Charact.* 128 (2017) 195–202. <https://doi.org/10.1016/j.matchar.2017.02.007>.
- [127] W. Lin, F. Li, D. Wu, X. Chen, X. Hua, H. Pan, Effect of Al-Si Coating on Weld Microstructure and Properties of 22MnB5 Steel Joints for Hot Stamping, Reprinted by permission from Springer Nature, *Journal of Materials Engineering and Performance* (Copyright), (2018).
- [128] J.H. Moon, P.K. Seo, C.G. Kang, A study on mechanical properties of laser-welded blank of a boron sheet steel by laser ablation variable of Al-Si coating layer, *Int. J. Precis. Eng. Manuf.* 14 (2013) 283–288. <https://doi.org/10.1007/s12541-013-0039-5>.
- [129] C.W. Lee, S.Y. Kim, S.G. Jang, G.Y. Shin, J.H. Yoo, Fusion Zone Microstructural Evolution of Al-10% Si Coated Hot Stamping Steel during Laser Welding, *ISIJ Int.* 59 (2019) 136–143. <https://doi.org/10.2355/isijinternational.ISIJINT-2018-489>.
- [130] Q. Sun, H.S. Di, X.N. Wang, X.M. Chen, Suppression of δ -ferrite formation on Al-Si coated press-hardened steel during laser welding, *Mater. Lett.* 245 (2019) 106–109. <https://doi.org/10.1016/j.matlet.2019.02.111>.
- [131] ASTM E8, ASTM E8/E8M standard test methods for tension testing of metallic materials 1, *Annu. B. ASTM Stand.* 4. (2010) 1–27. <https://doi.org/10.1520/E0008>.
- [132] M. Shehryar Khan, P. Enrique, G. Song, M.I.S.T. Faria, Y. Zhou, Laser-assisted wire cladding using a retrofitted laser welding system, *Surf. Eng.* 37 (2021) 634–641. <https://doi.org/10.1080/02670844.2020.1820266>.
- [133] J. Rahman Chukkan, M. Vasudevan, S. Muthukumar, R. Ravi Kumar, N. Chandrasekhar, Simulation of laser butt welding of AISI 316L stainless steel sheet using various heat sources and experimental validation, *J. Mater. Process. Technol.* 219 (2015) 48–59. <https://doi.org/10.1016/j.jmatprotec.2014.12.008>.
- [134] P. Martinson, S. Daneshpour, M. Koçak, S. Riekehr, P. Staron, Residual stress analysis of laser spot welding of steel sheets, *Mater. Des.* 30 (2009) 3351–3359. <https://doi.org/10.1016/j.matdes.2009.03.041>.
- [135] K. Kim, J. Lee, H. Cho, Analysis of pulsed Nd:YAG laser welding of AISI 304 steel, *J. Mech. Sci. Technol.* 24 (2010) 2253–2259. <https://doi.org/10.1007/s12206-010-0902-6>.
- [136] C.S. Wu, H.G. Wang, Y.M. Zhang, A new heat source model for keyhole plasma arc welding in FEM analysis of the temperature profile, *Weld. J.* 85 (2006) 284.
- [137] A.M. Kamara, W. Wang, S. Marimuthu, L. Li, Modelling of the melt pool geometry in the laser deposition of nickel alloys using the anisotropic enhanced thermal conductivity

- approach, *Proc. Inst. Mech. Eng. Part B J. Eng. Manuf.* 225 (2011) 87–99. <https://doi.org/10.1177/09544054JEM2129>.
- [138] M. Courtois, M. Carin, P. Le Masson, S. Gaied, M. Balabane, Guidelines in the experimental validation of a 3D heat and fluid flow model of keyhole laser welding, *J. Phys. D. Appl. Phys.* 49 (2016) 155503. <https://doi.org/10.1088/0022-3727/49/15/155503>.
- [139] Heat Transfer Module User's Guide, COMSOL Multiphysics® v.5.6, COMSOL AB. (2015) 1–222.
- [140] S.I. Shahabad, Z. Zhang, A. Keshavarzkermani, U. Ali, Y. Mahmoodkhani, R. Esmailizadeh, A. Bonakdar, E. Toyserkani, Heat source model calibration for thermal analysis of laser powder-bed fusion, *Int. J. Adv. Manuf. Technol.* 106 (2020) 3367–3379. <https://doi.org/10.1007/s00170-019-04908-3>.
- [141] Z. Zhang, Y. Huang, A. Rani Kasinathan, S. Imani Shahabad, U. Ali, Y. Mahmoodkhani, E. Toyserkani, 3-Dimensional heat transfer modeling for laser powder-bed fusion additive manufacturing with volumetric heat sources based on varied thermal conductivity and absorptivity, *Opt. Laser Technol.* 109 (2019) 297–312. <https://doi.org/10.1016/j.optlastec.2018.08.012>.
- [142] I. Eriksson, J. Powell, A.F.H. Kaplan, Surface tension generated defects in full penetration laser keyhole welding, *J. Laser Appl.* 26 (2014) 012006. <https://doi.org/10.2351/1.4830175>.
- [143] R. Fabbro, S. Slimani, F. Coste, F. Briand, Study of keyhole behavior for full penetration Nd-YAG CW laser welding, *J. Phys. D. Appl. Phys.* 38 (2005) 1881. <https://doi.org/10.2351/1.5060302>.
- [144] M. Courtois, M. Carin, P. Le Masson, S. Gaied, M. Balabane, A complete model of keyhole and melt pool dynamics to analyze instabilities and collapse during laser welding, *J. Laser Appl.* 26 (2014) 042001. <https://doi.org/10.2351/1.4886835>.
- [145] R. Lin, H. ping Wang, F. Lu, J. Solomon, B.E. Carlson, Numerical study of keyhole dynamics and keyhole-induced porosity formation in remote laser welding of Al alloys, *Int. J. Heat Mass Transf.* 108 (2017) 244–256. <https://doi.org/10.1016/j.ijheatmasstransfer.2016.12.019>.
- [146] W. Lin, F. Li, X. Hua, Effect of keyhole mode on weld shape and mechanical properties of thin sheets of Al-Si coated 22MnB5 steel, *J. Laser Appl.* 30 (2018). <https://doi.org/10.2351/1.5052155>.
- [147] J. Volpp, F. Vollertsen, Modeling keyhole oscillations during laser deep penetration welding at different spatial laser intensity distributions, *Prod. Eng.* 9 (2015) 167–178. <https://doi.org/10.1007/s11740-014-0594-3>.
- [148] J.G. Andrews, D.R. Atthey, Hydrodynamic limit to penetration of a material by a high-power beam, *J. Phys. D. Appl. Phys.* 9 (1976) 2181.
- [149] M.H. Razmpoosh, A. Macwan, E. Biro, Y. Zhou, Effect of coating weight on fiber laser welding of Galvanneal-coated 22MnB5 press hardening steel, *Surf. Coatings Technol.* 337 (2018) 536–543. <https://doi.org/10.1016/j.surfcoat.2018.01.053>.
- [150] J. Greses, P.A. Hilton, C.Y. Barlow, W.M. Steen, Plume attenuation under high power Nd:YAG laser welding, in: *ICALEO 2002 - 21st Int. Congr. Appl. Laser Electro-Optics, Congr. Proc., Laser Institute of America, 2002: p. 47727.* <https://doi.org/10.2351/1.5065740>.

- [151] J. Zou, W. Yang, S. Wu, Y. He, R. Xiao, Effect of plume on weld penetration during high-power fiber laser welding, *J. Laser Appl.* 28 (2016) 022003. <https://doi.org/10.2351/1.4940148>.
- [152] M. Shehryar Khan, M.H. Razmpoosh, A. Macwan, E. Biro, Y. Zhou, Optimizing weld morphology and mechanical properties of laser welded Al-Si coated 22MnB5 by surface application of colloidal graphite, *J. Mater. Process. Technol.* 293 (2021) 117093. <https://doi.org/10.1016/j.jmatprotec.2021.117093>.
- [153] Y.N. Zhou, D.C. Saha, E. Biro, A. Macwan, A.P. Gerlich, M. Shehryar Khan, Pre-Coated Steel Sheet Comprising an Additional Coating for Increasing The Mechanical Strength of the Weld Metal Zone of a Welded Steel Part Prepared From Said Pre-Coated Sheet, WO / 2021/130524, 2021.
- [154] ASTM International, ASTM E408-13 (2019), Standard Test Methods for Total Normal Emittance of Surfaces Using Inspection-Meter Techniques, 2019. <https://doi.org/10.1520/E0408-13R19>.
- [155] H. Bhadeshia, R. Honeycombe, Formation of Martensite, 2017. <https://doi.org/10.1016/b978-0-08-100270-4.00005-6>.
- [156] M. Shehryar Khan, A. Macwan, E. Biro, Y. Zhou, α -ferrite Suppression during Fiber Laser Welding of Al-Si Coated 22MnB5 Press-Hardened Steel, *Weld. J.* 100 (2021). <https://doi.org/10.29391/2021.100.018>.
- [157] M. Shehryar Khan, P. Enrique, A. Ghatei-Kalashami, J.G. Lopes, N. Schell, J.P. Oliveira, E. Biro, Y. Norman Zhou, The influence of in-situ alloying of electro-spark deposited coatings on the multiscale morphological and mechanical properties of laser welded Al-Si coated 22MnB5, *Mater. Sci. Eng. A.* 839 (2022) 142830. <https://doi.org/10.1016/j.msea.2022.142830>.
- [158] G.. Pisarenko, G. V Samsonov, A.D. Verkhoturov, A.I. Bezykornov, B.A. Lyashenko, V. V Rishin, Y.M. Shemegan, The strength characteristics of layers produced by electrospark alloying of steels with refractory metals, *Strength Mater.* 5 (1973) 247–252.
- [159] R.N. Johnson, Coatings for fast breeder reactor components, *Thin Solid Films.* 118 (1984) 31–48. [https://doi.org/10.1016/0040-6090\(84\)90104-4](https://doi.org/10.1016/0040-6090(84)90104-4).
- [160] H. Yang, Y. Sun, C. Tan, X. Zhao, B. Chen, X. Song, W. Guo, J. Feng, Influence of Al–Si coating on microstructure and mechanical properties of fiber laser welded and then press-hardened 22MnB5 steel, *Mater. Sci. Eng. A.* 794 (2020) 139918. <https://doi.org/10.1016/j.msea.2020.139918>.
- [161] X.N. Wang, X.M. Chen, Q. Sun, H.S. Di, L.N. Sun, Formation mechanism of δ -ferrite and metallurgy reaction in molten pool during press-hardened steel laser welding, *Mater. Lett.* 206 (2017) 143–145. <https://doi.org/10.1016/j.matlet.2017.07.008>.
- [162] P.D. Enrique, Z. Jiao, N.Y. Zhou, E. Toyserkani, Dendritic coarsening model for rapid solidification of Ni-superalloy via electrospark deposition, *J. Mater. Process. Technol.* 258 (2018) 138–143. <https://doi.org/10.1016/j.jmatprotec.2018.03.023>.
- [163] X. Cheng, Z. Jin, M. Liu, X. Li, Optimizing the nickel content in weathering steels to enhance their corrosion resistance in acidic atmospheres, *Corros. Sci.* 115 (2017) 135–142. <https://doi.org/10.1016/j.corsci.2016.11.016>.
- [164] J. Zhao, X. Zhao, X. Zhao, C. Dong, S. Kang, Effects of nucleation site and morphology of carbide-free bainite on microstructures and properties of bainite/martensite multi-phase

- steels, *Mater. Sci. Eng. A*. 744 (2019) 86–93. <https://doi.org/10.1016/j.msea.2018.11.060>.
- [165] S.M. Hasan, S. Kumar, D. Chakrabarti, S.B. Singh, Understanding the effect of prior bainite/martensite on the formation of carbide-free bainite, *Philos. Mag.* 100 (2020) 797–821. <https://doi.org/10.1080/14786435.2020.1712486>.
- [166] J. Tian, G. Xu, M. Zhou, H. Hu, Refined Bainite Microstructure and Mechanical Properties of a High-Strength Low-Carbon Bainitic Steel Treated by Austempering Below and Above MS, *Steel Res. Int.* 89 (2018) 1–10. <https://doi.org/10.1002/srin.201700469>.
- [167] L. Zhao, L. Qian, J. Meng, Q. Zhou, F. Zhang, Below-Ms austempering to obtain refined bainitic structure and enhanced mechanical properties in low-C high-Si/Al steels, *Scr. Mater.* 112 (2016) 96–100. <https://doi.org/10.1016/j.scriptamat.2015.09.022>.
- [168] C. Fossaert, G. Rees, T. Maurickx, H.K.D.H. Bhadeshia, The effect of niobium on the hardenability of microalloyed austenite, *Metall. Mater. Trans. A*. 26 (1995) 21–30. <https://doi.org/10.1007/BF02669791>.
- [169] O.N. Dogan, G.M. Michal, H.W. Kwon, Pinning of austenite grain boundaries by AlN precipitates and abnormal grain growth, *Metall. Trans. A, Phys. Metall. Mater. Sci.* 23 A (1992) 2121–2129. <https://doi.org/10.1007/BF02646005>.
- [170] C.K. Lin, Y.H. Su, W.S. Hwang, G.R. Lin, J.C. Kuo, On pinning effect of austenite grain growth in Mg-containing low-carbon steel, *Mater. Sci. Technol. (United Kingdom)*. 34 (2018) 596–606. <https://doi.org/10.1080/02670836.2017.1421037>.
- [171] A. Ray, S. Kr. Ray, S.R. Mediratta, Effect of carbides on the austenite grain growth characteristics in 1Cr-1C and 6Cr-1Mo-1C steels, *J. Mater. Sci.* 25 (1990) 5070–5076. <https://doi.org/10.1007/BF00580131>.
- [172] F.B. Pickering, *Physical metallurgy and the design of steels*, Applied Science Publishers Ltd, London, 1978.
- [173] P. Michaud, D. Delagnes, P. Lamesle, M.H. Mathon, C. Levallant, The effect of the addition of alloying elements on carbide precipitation and mechanical properties in 5% chromium martensitic steels, *Acta Mater.* 55 (2007) 4877–4889. <https://doi.org/10.1016/j.actamat.2007.05.004>.
- [174] J. Adamczyk, E. Kalinowska-Ozgowicz, W. Ozgowicz, R. Wusatowski, Interaction of carbonitrides V(C,N) undissolved in austenite on the structure and mechanical properties of microalloyed V-N steels, *J. Mater. Process. Tech.* 53 (1995) 23–32. [https://doi.org/10.1016/0924-0136\(95\)01958-H](https://doi.org/10.1016/0924-0136(95)01958-H).
- [175] H.K.D.H. Bhadeshia, E. Keehan, L. Karlsson, H.O. Andrén, Coalesced bainite, *Trans. Indian Inst. Met.* 59 (2006) 689–694.
- [176] J.H. Pak, H.K.D.H. Bhadeshia, L. Karlsson, Mechanism of misorientation development within coalesced martensite, *Mater. Sci. Technol. (United Kingdom)*. 28 (2012) 918–923. <https://doi.org/10.1179/1743284712Y.0000000023>.
- [177] J.H. Pak, H.K.D.H. Bhadeshia, L. Karlsson, E. Keehan, Coalesced bainite by isothermal transformation of reheated weld metal, *Sci. Technol. Weld. Join.* 13 (2008) 593–597. <https://doi.org/10.1179/136217108X338926>.
- [178] H.K.D.H. Bhadeshia, S.A. David, J.M. Vitek, R.W. Reed, Stress induced transformation to bainite in Fe-Cr-Mo-C pressure vessel steel, *Mater. Sci. Technol. (United Kingdom)*. 7 (1991) 686–698. <https://doi.org/10.1179/mst.1991.7.8.686>.

- [179] J. Pak, D.W. Suh, H.K.D.H. Bhadeshia, Promoting the coalescence of bainite platelets, *Scr. Mater.* 66 (2012) 951–953. <https://doi.org/10.1016/j.scriptamat.2012.02.041>.
- [180] H. Pous-Romero, H. Bhadeshia, Coalesced martensite in pressure vessel steels, *J. Press. Vessel Technol. Trans. ASME.* 136 (2014) 1–6. <https://doi.org/10.1115/1.4026192>.
- [181] E.I. Galindo-Nava, P.E.J. Rivera-Díaz-Del-Castillo, A model for the microstructure behaviour and strength evolution in lath martensite, *Acta Mater.* 98 (2015) 81–93. <https://doi.org/10.1016/j.actamat.2015.07.018>.
- [182] M.N. Gussev, K.J. Leonard, In situ SEM-EBSD analysis of plastic deformation mechanisms in neutron-irradiated austenitic steel, *J. Nucl. Mater.* 517 (2019) 45–56.
- [183] A. Ghatei Kalashami, A. Kermanpur, E. Ghassemali, A. Najafizadeh, Y. Mazaheri, Correlation of microstructure and strain hardening behavior in the ultrafine-grained Nb-bearing dual phase steels, *Mater. Sci. Eng. A.* 678 (2016) 215–226. <https://doi.org/10.1016/j.msea.2016.09.108>.
- [184] Z. Yao, G. Xu, Z. Jiang, J. Tian, Q. Yuan, H. Ma, Effects of Ni and Cr on Cryogenic Impact Toughness of Bainite/Martensite Multiphase Steels, *Met. Mater. Int.* 25 (2019) 1151–1160. <https://doi.org/10.1007/s12540-019-00262-x>.
- [185] M. Zhou, G. Xu, H. Hu, Q. Yuan, J. Tian, The Effect of Large Stress on Bainitic Transformation at Different Transformation Temperatures, *Steel Res. Int.* 88 (2017) 1–7. <https://doi.org/10.1002/srin.201600377>.
- [186] J. Tian, G. Xu, M. Zhou, H. Hu, X. Wan, The effects of Cr and Al addition on transformation and properties in low-carbon bainitic steels, *Metals (Basel).* 7 (2017) 12–17. <https://doi.org/10.3390/met7020040>.
- [187] H. Sato, S. Zaeferrer, A study on the formation mechanisms of butterfly-type martensite in Fe-30% Ni alloy using EBSD-based orientation microscopy, *Acta Mater.* 57 (2009) 1931–1937. <https://doi.org/10.1016/j.actamat.2008.12.035>.
- [188] W. Voigt, Ueber die Beziehung zwischen den beiden Elasticitätsconstanten isotroper Körper., *Ann. Phys.* 274 (1889) 573–587.
- [189] A. Reuß, Berechnung der fließgrenze von mischkristallen auf grund der plastizitätsbedingung für einkristalle., *ZAMM-Journal Appl. Math. Mech. Für Angew. Math. Und Mech.* 9 (1929) 49–58.
- [190] H.S. Kim, On the rule of mixtures for the hardness of particle reinforced composites, *Mater. Sci. Eng. A.* 289 (2000) 30–33. [https://doi.org/10.1016/S0921-5093\(00\)00909-6](https://doi.org/10.1016/S0921-5093(00)00909-6).
- [191] Y. Kasamatsu, S. Takashima, T. Hosoya, Influence of Martensite-Austenite Constituent on the Heat Affected Zone Toughness of High Strength Weldable Structural Steels., *R D Res. Dev. Kobe Steel Eng. Reports.* 29 (1979) 48–52.
- [192] S.C. Wang, J.R. Yang, Effects of chemical composition, rolling and cooling conditions on the amount of martensite/austenite (M/A) constituent formation in low carbon bainitic steels, *Mater. Sci. Eng. A.* 154 (1992) 43–49. [https://doi.org/10.1016/0921-5093\(92\)90361-4](https://doi.org/10.1016/0921-5093(92)90361-4).
- [193] N. Takayama, G. Miyamoto, T. Furuhashi, Chemistry and three-dimensional morphology of martensite-austenite constituent in the bainite structure of low-carbon low-alloy steels, *Acta Mater.* 145 (2018) 154–164. <https://doi.org/10.1016/j.actamat.2017.11.036>.
- [194] G. Park, G. Bae, C. Lee, Characterization of Mechanical and Metallurgical Notch Effects

- of DP980 Steel Weld Joints in Fatigue Performance, *Metall. Mater. Trans. A Phys. Metall. Mater. Sci.* 50 (2019) 1294–1307. <https://doi.org/10.1007/s11661-018-5091-4>.
- [195] M. Shehryar Khan, A. Ghatei-Kalashami, X. Wang, E. Biro, Y.N. Zhou, Refining the hierarchical structure of lath martensitic steel by in situ alloying with nickel: morphology, crystallography, and mechanical properties, *J. Mater. Sci.* 57 (2022) 20867–20894. <https://doi.org/10.1007/s10853-022-07916-z>.
- [196] G.B. Olson, *Martensite*, ASM International, 1992.
- [197] L.S. Figiel, *On Damascus Steel*, Atlantis Arts Press, 1991.
- [198] G. Krauss, Martensite in steel: Strength and structure, *Mater. Sci. Eng. A.* 273–275 (1999) 40–57. [https://doi.org/10.1016/s0921-5093\(99\)00288-9](https://doi.org/10.1016/s0921-5093(99)00288-9).
- [199] G. Krauss, A.R. Marder, The morphology of martensite in iron alloys, *Metall. Trans.* 2 (1971) 2343–2357. <https://doi.org/10.1007/BF02814873>.
- [200] M. Umemoto, E. Yoshitake, I. Tamura, The morphology of martensite in Fe-C, Fe-Ni-C and Fe-Cr-C alloys, *J. Mater. Sci.* 18 (1983) 2893–2904. <https://doi.org/10.1007/BF00700770>.
- [201] W.S. Owen, E.A. Wilson, T. Bell, *High Strength Materials*, John Wiley and Sons, 1965.
- [202] O.D. Sherby, J. Wadsworth, D.R. Lesuer, C.K. Syn, The c/a Ratio in Quenched Fe-C and Fe-N Steels - A Heuristic Story, *Mater. Sci. Forum.* 539–543 (2007) 215–222. <https://doi.org/10.4028/www.scientific.net/msf.539-543.215>.
- [203] W.L. Fink, E.D. Campbell, The nature of the alloys of iron and chromium, *Trans. Am. Soc. Steel Treat.* 9 (1926) 717.
- [204] EINAR ÖHMAN, Crystal Structure of Martensite, *Nature.* 127 (1931) 270–272.
- [205] T.W. Liu, D.H. Ping, T. Ohmura, M. Ohnuma, Electron diffraction analysis of quenched Fe–C martensite, *J. Mater. Sci.* 53 (2018) 2976–2984. <https://doi.org/10.1007/s10853-017-1731-0>.
- [206] T. Maki, K. Tsuzaki, I. Tamura, The Morphology of Microstructure Composed of Lath Martensites in Steels, *Trans. Iron Steel Inst. Japan.* 20 (1980) 207–214. <https://doi.org/10.2355/isijinternational1966.20.207>.
- [207] H. Bhadeshia, R. Honeycombe, *Solutes that Substitute for Iron*, 2017. <https://doi.org/10.1016/b978-0-08-100270-4.00004-4>.
- [208] G. Krauss, Deformation and fracture in martensitic carbon steels tempered at low temperatures, *Metall. Mater. Trans. B Process Metall. Mater. Process. Sci.* 32 (2001) 205–221. <https://doi.org/10.1007/s11663-001-0044-4>.
- [209] L. Morsdorf, C.C. Tasan, D. Ponge, D. Raabe, 3D structural and atomic-scale analysis of lath martensite: Effect of the transformation sequence, *Acta Mater.* 95 (2015) 366–377. <https://doi.org/10.1016/j.actamat.2015.05.023>.
- [210] A. Stormvinter, G. Miyamoto, T. Furuhashi, P. Hedström, A. Borgenstam, Effect of carbon content on variant pairing of martensite in Fe-C alloys, *Acta Mater.* 60 (2012) 7265–7274. <https://doi.org/10.1016/j.actamat.2012.09.046>.
- [211] C.P. Scott, B. Shalchi Amirkhiz, I. Pushkareva, F. Fazeli, S.Y.P. Allain, H. Azizi, New insights into martensite strength and the damage behaviour of dual phase steels, *Acta Mater.* 159 (2018) 112–122. <https://doi.org/10.1016/j.actamat.2018.08.010>.
- [212] S. Morito, X. Huang, T. Furuhashi, T. Maki, N. Hansen, The morphology and

- crystallography of lath martensite in alloy steels, *Acta Mater.* 54 (2006) 5323–5331. <https://doi.org/10.1016/j.actamat.2006.07.009>.
- [213] C.C. Kinney, K.R. Pytlewski, A.G. Khachaturyan, J.W. Morris, The microstructure of lath martensite in quenched 9Ni steel, *Acta Mater.* 69 (2014) 372–385. <https://doi.org/10.1016/j.actamat.2014.01.058>.
- [214] R.W. Fonda, G. Spanos, Effects of Cooling Rate on Transformations in a Fe-9 Pct Ni Steel, *Metall. Mater. Trans. A Phys. Metall. Mater. Sci.* 45 (2014) 5982–5989. <https://doi.org/10.1007/s11661-014-2588-3>.
- [215] S. Morito, H. Tanaka, R. Konishi, T. Furuhashi, T. Maki, The morphology and crystallography of lath martensite in Fe-C alloys, *Acta Mater.* 51 (2003) 1789–1799. [https://doi.org/10.1016/S1359-6454\(02\)00577-3](https://doi.org/10.1016/S1359-6454(02)00577-3).
- [216] H. Kitahara, R. Ueji, N. Tsuji, Y. Minamino, Crystallographic features of lath martensite in low-carbon steel, *Acta Mater.* 54 (2006) 1279–1288. <https://doi.org/10.1016/j.actamat.2005.11.001>.
- [217] G. Kurdjumov, G. Sachs, Über den Mechanismus der Stahlhärtung, *Zeitschrift Für Phys.* 64 (1930) 325–343. <https://doi.org/10.1007/BF01397346>.
- [218] P.M. Kelly, J. Nutting, The Martensite Transformation in Carbon Steels, in: *Proc. R. Soc. London*, 1960: pp. 45–58.
- [219] A.R. Marder, G. Krauss, The Formation of Low-Carbon Martensite in Fe-C Alloys, *Trans. ASM.* 62 (1969) 957–963.
- [220] F.J. Schoen, J.L. Nilles, W.S. Owen, Crystallographic aspects of Fe-Ni and Fe-Ni-C dilute alloy martensites, *Metall. Trans.* 2 (1971) 2489–2494. <https://doi.org/10.1007/BF02814887>.
- [221] A. Chatterjee, A. Ghosh, A. Moitra, A.K. Bhaduri, R. Mitra, D. Chakrabarti, Role of hierarchical martensitic microstructure on localized deformation and fracture of 9Cr-1Mo steel under impact loading at different temperatures, *Int. J. Plast.* 104 (2018) 104–133. <https://doi.org/10.1016/j.ijplas.2018.02.002>.
- [222] L. Morsdorf, O. Jeannin, D. Barbier, M. Mitsuhashi, D. Raabe, C.C.C. Tasan, Multiple mechanisms of lath martensite plasticity, *Acta Mater.* 121 (2016) 202–214. <https://doi.org/10.1016/j.actamat.2016.09.006>.
- [223] S. Morito, H. Saito, T. Maki, T. Furuhashi, T. OGAWA, T. Furuhashi, T. Maki, Effect of Austenite Grain Size on the Morphology and Crystallography of Lath Martensite in Low Carbon Steels, *ISIJ Int.* 45 (2005) 91–94. <https://doi.org/10.2355/isijinternational.45.91>.
- [224] N. Takayama, G. Miyamoto, T. Furuhashi, Effects of transformation temperature on variant pairing of bainitic ferrite in low carbon steel, *Acta Mater.* 60 (2012) 2387–2396. <https://doi.org/10.1016/j.actamat.2011.12.018>.
- [225] J. Hidalgo, M.J. Santofimia, Effect of Prior Austenite Grain Size Refinement by Thermal Cycling on the Microstructural Features of As-Quenched Lath Martensite, *Metall. Mater. Trans. A Phys. Metall. Mater. Sci.* 47 (2016) 5288–5301. <https://doi.org/10.1007/s11661-016-3525-4>.
- [226] T. Hanamura, S. Torizuka, S. Tamura, S. Enokida, H. Takeuchi, Effect of austenite grain size on the mechanical properties in air-cooled 0.1c-5Mn martensitic steel, *ISIJ Int.* 53 (2013) 2218–2225. <https://doi.org/10.4028/www.scientific.net/msf.783-786.1027>.

- [227] C. Wang, M. Wang, J. Shi, W. Hui, H. Dong, Effect of microstructural refinement on the toughness of low carbon martensitic steel, *Scr. Mater.* 58 (2008) 492–495. <https://doi.org/10.1016/j.scriptamat.2007.10.053>.
- [228] S. Morito, H. Yoshida, T. Maki, X. Huang, Effect of block size on the strength of lath martensite in low carbon steels, *Mater. Sci. Eng. A.* 438–440 (2006) 237–240. <https://doi.org/10.1016/j.msea.2005.12.048>.
- [229] A. Shibata, T. Nagoshi, M. Sone, S. Morito, Y. Higo, Evaluation of the block boundary and sub-block boundary strengths of ferrous lath martensite using a micro-bending test, *Mater. Sci. Eng. A.* 527 (2010) 7538–7544. <https://doi.org/10.1016/j.msea.2010.08.026>.
- [230] N. Maruyama, S. Tabata, H. Kawata, Excess Solute Carbon and Tetragonality in As-Quenched Fe-1Mn-C (C:0.07 to 0.8 Mass Pct) Martensite, *Metall. Mater. Trans. A Phys. Metall. Mater. Sci.* 51 (2020) 1085–1097. <https://doi.org/10.1007/s11661-019-05617-y>.
- [231] H. Koohdar, P. Hakimipour, H.R. Jafarian, T.G. Langdon, M. Nili-Ahmadabadi, Engineering mechanical properties by controlling the microstructure of an Fe–Ni–Mn martensitic steel through pre-cold rolling and subsequent heat treatment, *Mater. Sci. Eng. A.* 804 (2021) 140760. <https://doi.org/10.1016/j.msea.2021.140760>.
- [232] A. Chakraborty, R.F. Webster, S. Primig, Lath martensite substructure evolution in low-carbon microalloyed steels, *J. Mater. Sci.* 57 (2022) 10359–10378. <https://doi.org/10.1007/s10853-022-07275-9>.
- [233] T.N. Durlu, Effects of high austenitizing temperature and austenite deformation on formation of martensite in Fe-Ni-C alloys, *J. Mater. Sci.* 36 (2001) 5665–5671. <https://doi.org/10.1023/A:1012582103327>.
- [234] K. Zhu, H. Shi, H. Chen, C. Jung, Effect of Al on martensite tempering: comparison with Si, *J. Mater. Sci.* 53 (2018) 6951–6967. <https://doi.org/10.1007/s10853-018-2037-6>.
- [235] A. Bandyopadhyay, K.D. Traxel, M. Lang, M. Juhasz, N. Eliaz, S. Bose, Alloy design via additive manufacturing: Advantages, challenges, applications and perspectives, *Mater. Today.* 52 (2022) 207–224. <https://doi.org/10.1016/j.mattod.2021.11.026>.
- [236] Y. Inokuti, B. Cantor, The formation of martensite in splat-quenched Fe-Mn and Fe-Ni-C alloys, *J. Mater. Sci.* 12 (1977) 946–958. <https://doi.org/10.1007/BF00540977>.
- [237] W.X. Zhang, Y.Z. Chen, Y.B. Cong, Y.H. Liu, F. Liu, On the austenite stability of cryogenic Ni steels: microstructural effects: a review, *J. Mater. Sci.* 56 (2021) 12539–12558. <https://doi.org/10.1007/s10853-021-06068-w>.
- [238] D. Mainprice, F. Bachmann, R. Hielscher, H. Schaeben, Descriptive tools for the analysis of texture projects with large datasets using MTEX: Strength, symmetry and components, *Geol. Soc. Spec. Publ.* 409 (2015) 251–271. <https://doi.org/10.1144/SP409.8>.
- [239] F. Niessen, T. Nyssönen, A.A. Gazder, R. Hielscher, Parent grain reconstruction from partially or fully transformed microstructures in MTEX, *J. Appl. Crystallogr.* 55 (2022) 180–194. <https://doi.org/10.1107/S1600576721011560>.
- [240] C. Celada-Casero, J. Sietsma, M.J. Santofimia, The role of the austenite grain size in the martensitic transformation in low carbon steels, *Mater. Des.* 167 (2019). <https://doi.org/10.1016/j.matdes.2019.107625>.
- [241] C. Capdevila, F.G. Caballero, C. Garcia de Andres, Determination of Ms Temperature in Steels: A Bayesian Neural Network Model, *ISI Int.* 42 (2002) 894–902.

- [242] D. Das, P.P. Chattopadhyay, Influence of martensite morphology on the work-hardening behavior of high strength ferrite-martensite dual-phase steel, *J. Mater. Sci.* 44 (2009) 2957–2965. <https://doi.org/10.1007/s10853-009-3392-0>.
- [243] L. Morsdorf, E. Emelina, B. Gault, M. Herbig, C.C. Tasan, Carbon redistribution in quenched and tempered lath martensite, *Acta Mater.* 205 (2021) 116521. <https://doi.org/10.1016/j.actamat.2020.116521>.
- [244] L. Qi, A.G. Khachaturyan, J.W. Morris, The microstructure of dislocated martensitic steel: Theory, *Acta Mater.* 76 (2014) 23–39. <https://doi.org/10.1016/j.actamat.2014.04.038>.
- [245] G. Krauss, Tempering of Lath Martensite in Low and Medium Carbon Steels: Assessment and Challenges, *Steel Res. Int.* 88 (2017) 1–18. <https://doi.org/10.1002/srin.201700038>.
- [246] T. Hayashi, S. Morito, T. Ohba, Local distribution of orientation relationship and microstructure evolution of lath martensite in an ultra-low-carbon steel, *Scr. Mater.* 180 (2020) 1–5. <https://doi.org/10.1016/j.scriptamat.2020.01.011>.
- [247] D. Sun, C. Li, X. Xue, Y. Liu, Z. Guo, J. Gu, Optimization scheme of the orientation relationship from crystallographic statistics of variants and its application to lath martensite, *Mater. Des.* 195 (2020) 109022. <https://doi.org/10.1016/j.matdes.2020.109022>.
- [248] S.I. Wright, S. Suzuki, M.M. Nowell, In Situ EBSD Observations of the Evolution in Crystallographic Orientation with Deformation, *JOM.* 68 (2016) 2730–2736. <https://doi.org/10.1007/s11837-016-2084-x>.
- [249] K. Iwashit, Y. Murata, Y. Tsukada, T. Koyama, Formation mechanism of the hierarchic structure in the lath martensite phase in steels, *Philos. Mag.* 91 (2011) 4495–4513. <https://doi.org/10.1080/14786435.2011.610763>.
- [250] L. Lin, B. shun Li, G. ming Zhu, Y. lin Kang, R. dong Liu, Effect of niobium precipitation behavior on microstructure and hydrogen induced cracking of press hardening steel 22MnB5, *Mater. Sci. Eng. A.* 721 (2018) 38–46. <https://doi.org/10.1016/j.msea.2018.02.021>.
- [251] L. Cho, P.E. Bradley, D.S. Lauria, M.L. Martin, M.J. Connolly, J.T. Benzing, E.J. Seo, K.O. Findley, J.G. Speer, A.J. Slifka, Characteristics and mechanisms of hydrogen-induced quasi-cleavage fracture of lath martensitic steel, *Acta Mater.* 206 (2021) 116635. <https://doi.org/10.1016/j.actamat.2021.116635>.
- [252] Z. Chai, Q. Lu, J. Hu, L. Wang, Z. Wang, J. Wang, W. Xu, Effect of retained austenite on the fracture behavior of a novel press-hardened steel, *J. Mater. Sci. Technol.* 135 (2023) 34–45. <https://doi.org/10.1016/j.jmst.2022.06.050>.